

Tunable Nano-Plasmonic Metamaterials at
Solid | Liquid and Liquid | Liquid Interfaces

Ye Ma

A thesis submitted in partial fulfilment of the requirement for the degree
of Doctor of Philosophy

Imperial College London, Department of Chemistry

August 2019

Declaration of Originality

I declare that the work presented in the following thesis is original and performed by myself; otherwise it is clearly cited and acknowledged.

Copyright Declaration

‘The copyright of this thesis rests with the author. Unless otherwise indicated, its contents are licensed under a Creative Commons Attribution-Non Commercial 4.0 International Licence (CC BY-NC). Under this licence, you may copy and redistribute the material in any medium or format. You may also create and distribute modified versions of the work. This is on the condition that: you credit the author and do not use it, or any derivative works, for a commercial purpose. When reusing or sharing this work, ensure you make the licence terms clear to others by naming the licence and linking to the licence text. Where a work has been adapted, you should indicate that the work has been changed and describe those changes. Please seek permission from the copyright holder for uses of this work that are not included in this licence or permitted under UK Copyright Law.’

All the copyright permission of the reprinted images cited in this thesis have been obtained from their publishers unless the documents are open access with a Creative Commons licence. It should be noted that the Figure 1.1 in this thesis is shared under a Creative Commons Attribution-NonCommercial-ShareAlike 4.0 International (CC BY-NC-SA 4.0) licence from the British Museum.

Abstract

Metamaterials have demonstrated their unusual optical properties, ranging from negative refractive index to optical nonlinearity. Real-time adjustment of these properties becomes critical for the next generation of ‘smart’ optical devices. In this thesis, different methods for actively tuning the structure and output of metamaterials are demonstrated. These metamaterials consist of metallic nanoparticles (NPs) at solid-liquid interfaces (SLIs) and liquid-liquid interfaces (LLIs).

Electrically, the assembly of gold NPs at a SLI is reversibly controlled by changing the potential of the solid substrate. As the interparticle distance is adjusted, the corresponding reflectance dip is modulated over the wavelength range 530–580 nm, with intensity changing from 93% to 1%. Moreover, the resulting ‘hot spots’ between adjacent NPs, and between the NP array and the metallic substrate, bring about a tunable surface-enhanced-Raman-scattering (SERS) enhancement of up to $\sim 10^5$ times.

Thermal tunability was achieved by constructing a nanoplasmonic optical switch, with poly(N-isopropylacrylamide) functionalized NPs on a metallic substrate. Within a 20–50 °C temperature window, the interparticle spacing and the separation between the NP array and the substrate can be simultaneously tuned in nanoscale.

Chemical bonding between the ligands on NPs and the heavy metal ions is also found to be able to adjust the interparticle distance of the NP array at LLI. For a glutathione functionalized NP array at LLI, an increase in the concentration of lead ions caused the reflectance peak to surge in intensity and to shift towards the red in wavelength. The fast dynamics (<1 min) and the low detection limit (ppb level) render this system an ideal candidate for the label-free detection of heavy metals.

These proof-of-principle methods demonstrated how electric, thermal and chemical effects could influence the nanoscale arrangement of NP assembly at SLI or LLI, which in return reforms the macroscale optical properties of these interfaces.

Table of Contents

Declaration of Originality	2
Abstract.....	3
Table of Contents	4
Acknowledgements	8
List of Abbreviations	9
1. Background	10
1.1. Nanoparticles	10
1.2. Basics of nano-plasmonics.....	11
1.3. Surface enhanced Raman scattering	13
1.4. Tunable metamaterials	15
1.4.1. Mechanical tuning.....	16
1.4.2. Thermal tuning.....	18
1.4.3. Chemical tuning.....	20
1.4.4. Electric related tuning	22
1.4.5. Optical tuning.....	24
1.5. Aims and objectives.....	25
1.6. References.....	26
2. Materials and methods	33
2.1. NP synthesis and functionalization.....	33
2.2. Film deposition	35
2.3. UV-Vis.....	36
2.4. Electron microscopy	37
2.5. Reflectance measurement	39
2.6. Effective medium theory.....	40

2.7.	Raman spectroscopy and SERS EF calculation	42
2.7.1.	SERS measurement.....	42
2.7.2.	Calculation of experimental SERS EF	43
2.7.3.	Calculation of theoretical SERS EF	44
2.8.	Electrochemical setup and measurement	44
2.8.1.	Electrochemical cell.....	44
2.8.2.	Capacitance measurement.....	44
2.9.	References.....	46
3.	Electric potential controlled switchable reflector at solid-liquid interface.....	48
3.1.	Abstract	48
3.2.	Introduction.....	49
3.3.	Experimental system and theoretical framework.....	51
3.3.1.	Electrochemical-optical cell.....	51
3.3.2.	Potential of zero charge and electrochemical window.....	53
3.3.3.	Optical reflectivity.	54
3.3.4.	Adsorption equilibria.	55
3.3.5.	Adsorption kinetics	56
3.4.	Results and discussions	57
3.4.1.	Assembly of NPs – the ‘absorber’ state	57
3.4.2.	Disassembly of NPs – the ‘mirror’ state	62
3.4.3.	Reversibility.....	64
3.5.	Conclusions.....	66
3.6.	References.....	67
4.	Electro-variable surface enhanced Raman spectroscopy at solid-liquid interface	71
4.1.	Abstract	71
4.2.	Introduction.....	72
4.3.	Results and discussions	72

4.3.1.	Working principle and experimental setup	73
4.3.2.	Potential dependant reflectance and SERS	76
4.3.3.	Dynamics of the electro-variable SERS.....	79
4.3.4.	Reversibility.....	81
4.4.	Conclusions.....	82
4.5.	References.....	82
5.	Thermo-responsive metasurface based on the coupling among metallic nanoparticle array and substrate.....	86
5.1.	Abstract.....	86
5.2.	Introduction.....	87
5.3.	Results and discussions.....	88
5.3.1.	Experimental setup and working principle	88
5.3.2.	Temperature dependence of reflectivity.....	91
5.3.3.	Kinetic response to thermal stimuli	93
5.3.4.	Reversible optical switching	96
5.4.	Conclusions.....	96
5.5.	References.....	97
6.	Label-free detection of lead employing nanoparticle self-assembly at liquid-liquid interface... 99	
6.1.	Abstract.....	99
6.1.	Introduction.....	100
6.2.	Results and discussions.....	101
6.2.1.	The working principle and experimental setup.....	101
6.2.2.	NPs functionalization and characterization in the bulk of aqueous solution	103
6.2.3.	LLI	105
6.2.4.	The effect of pH.....	106
6.2.5.	Sensing specificity	108
6.2.6.	Sensing dynamics.....	108

6.2.7.	Quantitative estimates and signal calibration.....	109
6.3.	Conclusions.....	113
6.4.	References.....	113
7.	Electrotunable nanoplasmonic liquid mirror.....	116
7.1.	Abstract.....	116
7.2.	Introduction.....	117
7.3.	Gold nanoparticles and electrochemical liquid-liquid cell.....	120
7.4.	Dynamics of assembly-disassembly of nanoparticle arrays.....	123
7.5.	Optical response during assembly/disassembly process.....	125
7.6.	Electrotuning of the optical metasurface.....	128
7.7.	Reversibility of the electrotuneable device.....	130
7.8.	Conclusion.....	131
7.9.	References.....	131
8.	Conclusions and outlook.....	134
8.1.	Tuning range.....	134
8.2.	Switching speed.....	135
8.3.	Reversibility.....	136
8.4.	References.....	136
Appendix	138
	List of publication during PhD study.....	138
	Certificates of copyright permission.....	139

Acknowledgements

The experience of my PhD study in Imperial College is valuable and unforgettable. First of all, I would like to express my deep and sincere gratitude to my supervisors: Professor Joshua Edel and Professor Alexei Kornyshev. Prof. Edel has provided me numerous experimental instructions and ideas, and Prof. Kornyshev is always ready to share with me his enthusiasm, theoretical insights and schemes for the interpretation of the data. Furthermore, meticulously editing every sentence of our joint papers, they gave me invaluable lessons on publications in high profile journals. Both have set role models for my future academia career.

I would reserve no efforts to thank my collaborators: Dr. Debabrata Sikdar, my brilliant theoretical companion, with whom we share ideas and finish every project together; Aleksandra Fedosyuk, my extremely helpful colleague and friend in experiments; Cristian Zagar, who contributed a lot in the kinetics and simulations; Danniell Klemme and Prof. Sang-Hyun Oh for their indispensable help with the substrates; Prof. Anthony Kucernak for his instructions on electrochemistry; Dr. Leonora Velleman for her professional tutorials about instruments. And many thanks to Xiaoyan Lin, William Pitchford, Ren Ren, Shenglin Cai, Liang Xue, Prof. Longhua Tang, Paolo Cadinu, Ivanov Aleksandar and Minggang Zhao who helped a lot in experiments and useful discussions.

Of course, I cannot forget those happy times with our group members and friends: James Million, Binoy Paulose Nadappuram, Yunuen Montelongo, Ben Edwards, Raquel Leh-na Fraccari, Oliver Robotham, Dominic Lee, and all the other members of Edel's and Kornyshev's groups. I am also very grateful for the hospitality from my landlord and landlady Mr and Mrs Behrens.

At last, I would thank my family. They are always encouraging me to cheer up, to move forward. They are one of the most important driving forces during my PhD study.

List of Abbreviations

AAS	atomic absorption spectrometry	NPoMS	nanoparticles deposited on metallic substrates
ALD	atomic layer deposition	PAL	naphthalene-based polyaromatic ligands
CTAB	cetrimonium bromide	PDMS	polydimethylsiloxane
DCE	1,2-dichloroethane	PEALD	plasma-enhanced atomic layer deposition
DI	deionized	PEG	polyethylene glycol
DLS	dynamic light scattering	pNIPAM	poly(N-isopropylacrylamide)
EF	enhancement factor	PS	polystyrene
EIT	electromagnetically induced transparency	PTFE	polytetrafluoroethylene
EMT	effective medium theory	PVP	polyvinylpyrrolidone
FEM	finite element method	PZC	potential of zero charge
GSH	glutathione	rcf	relative centrifugal force
HOMO	highest occupied molecular orbital	SAM	self-assembled monolayer
ICPMS	inductively coupled plasma mass spectrometry	SEF	surface enhanced fluorescence
ITIES	interface of two immiscible electrolytic solutions	SEM	scanning electron microscopy
ITO	indium tin oxide	SERS	surface enhanced Raman scattering
LCST	lower critical solution temperature	SHG	second-harmonic generation
LLI	liquid-liquid interface	SLI	solid-liquid interface
LOD	limit of detection	SPR	surface plasmon resonance
LSPR	localized surface plasmon resonance	TBATPB	tetrabutyl ammonium tetraphenylborate
LUMO	lowest unoccupied molecular orbital	TEM	transmission electron microscopy
MBA	4-mercaptobenzoic acid	TOM	tuneable optical metamaterials
MBE	molecular beam epitaxy	UV-Vis	ultraviolet-visible
MDDA	12-mercaptododecanoic acid		
NP	nanoparticle		

1. Background

1.1. Nanoparticles

Nanomaterials are commonly defined as materials that have at least one dimension sized between 1 to 100 nm, including nanoparticles (NPs, 3D), nanowires or nanotubes (2D), nanofilms (1D) and bulk materials comprised by the above mentioned nano-units.¹ Since the atoms are confined into a very limited space, NPs possess numerous unique optical²⁻⁴, electric⁵⁻⁸, catalytic^{9, 10} and biological¹¹⁻¹⁴ properties that are different from traditional bulk materials.¹⁵

NPs with different compositions are applied in various scenarios. For NPs based on semiconductors (commonly called quantum dots), the quantum confinement due to the small size of NPs split the continuous conduction and valence bands into quantized energy levels, which tunes the absorption and emission properties.¹⁶ The brightness, stability and high quantum efficiency provide these NPs with unrivalled advantages in display¹⁷ and imaging technologies^{18, 19}. Bearing outstanding biocompatibilities, NPs composed by organic materials such as liposomes, polymersomes, can incorporate into different kinds of biological systems, thus are found extremely handy in diagnostic and therapeutic applications.^{20, 21} Metallic NPs, as will be discuss later, possess unique plasmon resonance modes²² that are not available for bulk materials when stimulated by the incident light and thus are widely used in plasmonics²³, surface enhanced Raman spectroscopy (SERS)²⁴, surface enhanced fluorescence²⁵, and even cancer thermal therapy²⁶. Though the optical output of both metallic and semiconductor NPs are size sensitive, metallic NPs can achieve further tunability when their plasmon-polaritons couple with other collective excitations in nearby components.^{27, 28}

Noteworthy, the combination of different kinds of materials of NPs is sometimes obligatory and rewarding. For example, most inorganic and metallic NPs, due to attractive van der Waals forces²⁹, are prone to aggregation over long time periods, which cripples their applications in practice.³⁰ Organic ligands such as citrate³¹, thiolated alkane³², carboxylic acid³³, long chain polymers³⁴ and even DNA³⁵ have all been demonstrated to stabilise the NPs. In addition, as will be discussed, these ligands offer another dimension to tune the properties of NPs. Another good example of the synergic combination is the magnetic materials-polymer core-shell NPs. In biomedical applications, once injected into tissues or animal bodies, pure organic NPs usually drift randomly or follow passively the pathway of metabolism, which renders the diagnosis or treatment slow and inefficient.³⁶ Directed by magnetic fields, the embedded magnetic beads can guide the medicine carrier directly to the target tissues and also make the recollection of the NPs much easier.³⁷

1.2. Basics of nano-plasmonics

The Lycurgus cup displayed in the British Museum, London, is always a must-see for people interested in plasmonics. As shown in the **Figure 1.1**, the cup appears green in colour, if a white light source is outside the cup and the observer's eyes detect the light reflected from the cup. In contrast, if the cup is illuminated from inside, it appears red, in which case light transmitted through the cup reaches the observer's eyes. Only recently has it been shown that the unique optical properties of the cup are due to gold and silver NPs being embedded into the glass body, which selectively scatter the green light. This gives the cup a green tint under the reflection configuration.³⁸ Under the transmission configuration, the majority of the green light before reaching the eyes, will first be absorbed or scattered by the NPs within the cup. Therefore, the filtered transmitted light has the colour of red, which is the complementary colour of green. This interesting switching of colours is an excellent example of nano-plasmonics.



Figure 1.1 Lycurgus Cup illuminated from outside (left) and inside (right). The Trustees of the British Museum.

The large number of free electrons in metals gives it a unique way of interacting with any electromagnetic (EM) wave. The collective resonance of these electrons on the surface, often referred as surface plasmon resonance (SPR)³⁹, has enabled a vast variety of applications such as SERS⁴⁰⁻⁴², chemical or biological sensors^{43, 44}, light harvesting for photovoltaic cells⁴⁵ and catalysts⁴⁶, etc. One of the simplest and widely used models of understanding the interaction between metal and the incident light is the Drude model.⁴⁷ By ignoring the restoring force in the Lorentz model, the dielectric function of a metal can be defined as⁴⁷

$$\varepsilon(\omega) = \varepsilon_{\infty} \left(1 - \frac{\omega_p^2}{\omega^2 + i\gamma_0\omega} \right) \quad 1.1$$

where ω is the frequency, ε_{∞} the background permittivity at high frequency, ω_p the natural oscillation frequency of the free-electron-plasmon, γ_0 the collision rate of free electrons with the crystal or impurities.⁴⁷

For metals, γ_0 is normally smaller than ω . By separating the real and imaginary parts, it can be found that the condition $\text{Re}[\varepsilon(\omega)] = 0$ gives $\omega \approx \omega_p$. This could be used for calculating the plasmon frequency.

More importantly, only under the condition that $\text{Re}[\varepsilon(\omega)] < 0$ and $\text{Im}[\varepsilon(\omega)]$ is small, the plasmon resonances could happen. This can be explained by taking a NP as an example. The local electric field in the spherical NP follows such relationship⁴⁷:

$$E = \frac{3\varepsilon_M}{\varepsilon(\omega) + 2\varepsilon_M} E_0 \quad 1.2$$

where ε_M is the permittivity of the surrounding medium, E_0 is the incident field. When $\varepsilon(\omega) \approx -2\varepsilon_M$ and the absorption $[\text{Im}(\varepsilon(\omega))]$ is very small, the local electric field could be very large. This is a signature of the plasmon resonance. For metals, as shown in Eq 1.1, when the frequency is smaller than the plasmon frequency, their permittivity has the chance to be as negative as $-2\varepsilon_M$. This provides metals the possibility of producing a sharp peak/dip in the absorption/reflection spectra.

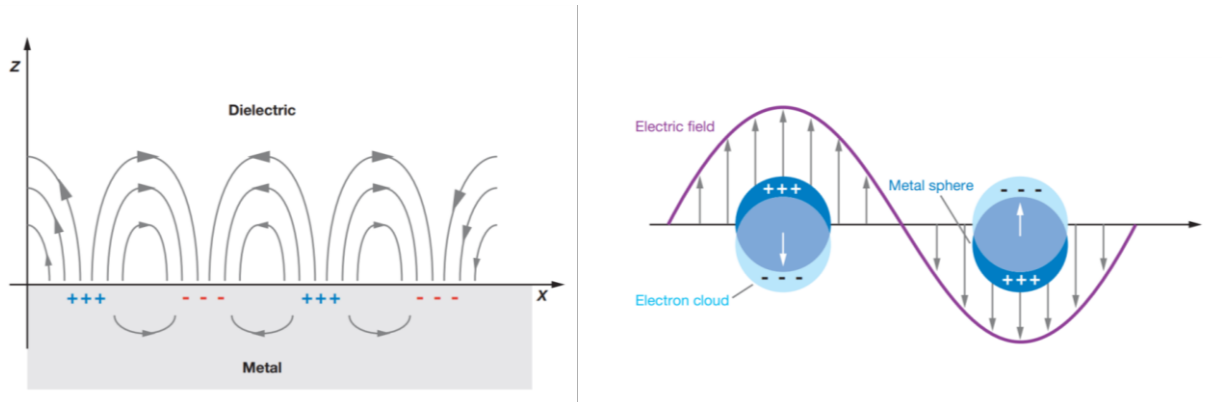


Figure 1.2 Schematic diagrams illustrating (left) a surface plasmon polariton (or propagating plasmon) of a metal plate and (right) a localized surface plasmon of NPs. Reprinted with permission from Ref.⁴⁸

Based on different configurations, two kinds of surface plasmon resonance are found: the propagating one in the planar metallic plate and the localized one in NPs (**Figure 1.2**).⁴⁸ In the case of propagating surface plasmon polaritons, the damping of the wave due to the absorption of the metal could be very small under the conditions that the $\text{Im}(\varepsilon(\omega))$ is small and the $|\text{Re}(\varepsilon(\omega))|$ is large. This propagating length along the x-y direction could be as long as many times of the wavelength especially for the low frequency range.⁴⁹ However, in the z direction, only evanescent wave could be stimulated whose decay length is limited to the nanoscale.⁵⁰ The resonance condition is very sensitive to the excitation wavelength, polarization, incident angle and materials' permittivity.⁴⁷ By combining a prism with a metal surface according to Otto or Kretschmann setup, people can employ this propagating mode for the measurement of refractive index and further applications such as monitoring biological binding at the interfaces.⁵¹

In the case of localized surface plasmon resonance (LSPR) in NPs, a quasi-static approximation is assumed when the wavelength of the incident light is much larger than the diameter of NPs. The electric field of the incident light stimulates an oscillation of electrons, which not only absorb light but also scatter light.⁴⁸ Moreover, apart from the influence of the permittivity and the incident wavelength, the absorption and scattering in LSPR is also sensitive to the material, shape, size and the coupling between NPs. This is the reason for the numerous applications that were mentioned previously.⁴⁷ One important effect needs to be highlighted here and will be referred later is the coupling among NPs. As shown in **Figure 1.3**, the electric field could be considerably intensive within the gaps in NP dimers. These gaps are named as ‘hot spots’ in the field of SERS because of large enhancement of localized electric field. Additionally, this coupling becomes increasingly stronger when the interparticle distance decreases, which also induces a noticeable redshift of the LSPR peaks.⁵² Based on this effect, all kinds of thrilling applications have been proposed such as nano-plasmonic rulers⁵³, ultra-sensitive sensors⁴³, tunable nano-antennas⁵⁴ and absorbers⁵⁵.

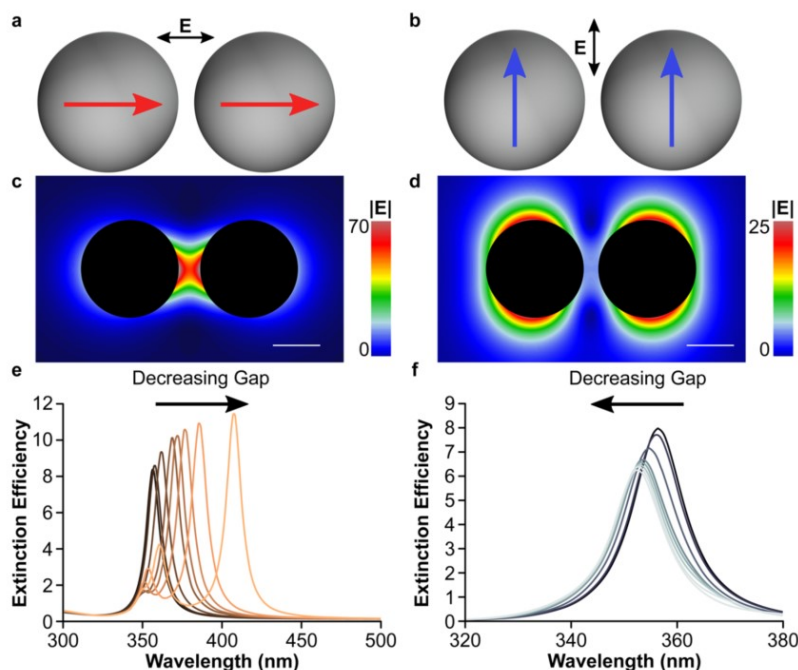


Figure 1.3 Plasmon coupling in spherical dimers with small gaps. (a) Constructive dipolar coupling in spheres with light polarized along the dimer axis. (b) Destructive interference between dipoles with light polarized across the dimer axis. Electric field intensity of constructively (c) and destructively (d) interfering 10 nm radius Ag spheres separated by a 5 nm gap. Extinction spectra of a 10 nm radius sphere Ag dimer with decreasing interparticle gaps with light polarized along (e) and across (f) the dimer axis. The interparticle gaps in (e) and (f) (from darkest to lightest trace) are 50, 40, 30, 20, 10, 5, 4, 3, 2, and 1 nm. The scale bar is 10 nm. Reprinted with permission from Ref.⁵²

1.3. Surface enhanced Raman scattering

The interactions between light and nanoscale matter could produce various interesting effects. For example, a molecule can be excited from its ground state v_0 to a vibrational state v_1 , when absorbs the incident

infrared light (**Figure 1.4**). If the energy of this incident photon is larger than the LUMO-HOMO gap of the molecule, the molecule will first jump onto the electron level $s1$, then returns to its ground level $s0$, releasing the energy as a photon. This is called fluorescence. The scattering of light, different from the IR absorption and fluorescence, does not require a specific excited energy state. A virtual energy level is facilitated to help with demonstrating different types of scattering in **Figure 1.4**. After the discovery of Raman effect in 1928 by C.V. Raman and K.S. Krishnan, and L. Mandelstam and G. Landsberg, the scattering of light was used to be classified as elastic scattering (Rayleigh scattering) and inelastic scattering. The later can be further categorized as Stokes and anti-Stokes lines with respect to the loss or gain of the energy of the scattered light. To be more specific, the dipole moment interacting with the photon can be expressed as follows⁴⁷:

$$P = [\alpha_0 E_0 \cos(2\pi\nu_i t)] + \frac{\delta\alpha}{\delta Q} \frac{Q_0 E_0}{2} [\cos[2\pi t(\nu_i - \nu_m)] + \cos[2\pi t(\nu_i + \nu_m)]] \quad 1.3$$

where α_0 is the polarizability at the equilibrium position, E_0 the incident electric field, t the time, α the molecular polarizability, Q the nuclear displacement, ν_m the vibrational energy of the molecule. The first term describes the elastic scattering while the second and third denote the Stokes ($\nu_i - \nu_m$) and anti-Stokes ($\nu_i + \nu_m$) scattering respectively.

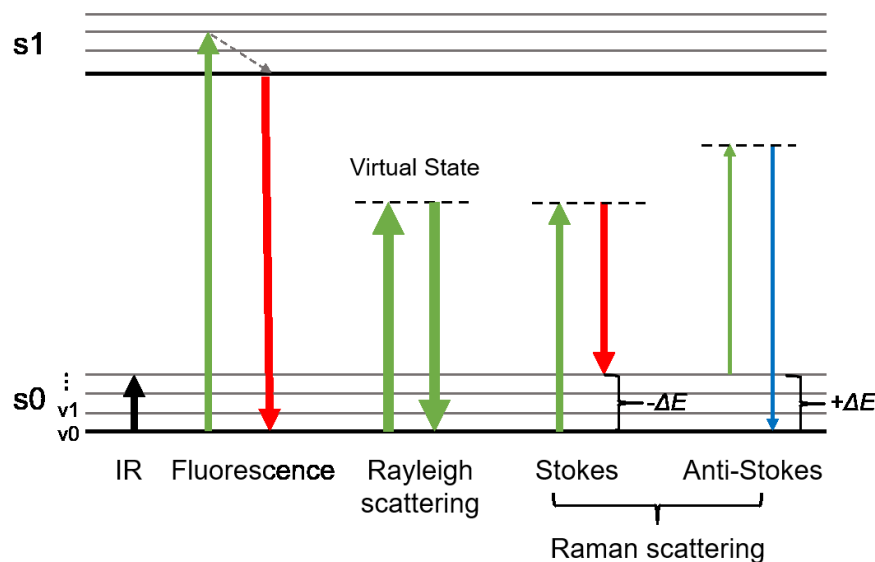


Figure 1.4 Jablonski diagram for the infrared (IR) absorption, fluorescence, Rayleigh scattering and Raman scattering. Within the electron energy ground level $s0$, two vibrational states (ν_0 and ν_1) are schematically depicted. $s1$ denoted one excited electron level.

It is inelastic scattering that forms the basis of Raman spectroscopy and SERS. Since the change in energy after the scattering is only related to the vibrational energy levels of the molecule, the spectra versus the

energy change or the more commonly used Raman shift ($\frac{1}{\lambda_i} - \frac{1}{\lambda_s}$) can be used as a fingerprint to identify chemicals. Due to the Boltzmann distribution of energy levels, the number of molecules at v_0 is much larger than v_1 , resulting in a higher intensity of Stokes lines rather than that of anti-Stokes lines. Nevertheless, the overall intensity of the inelastic scattering is extremely low (less than 10^{-7} of the elastic scattering)⁵⁶, which requires further enhancement for practical applications. Therefore, SERS was developed to be able to enhance the Raman signal more than 10^5 times.⁴⁷

In general, there are two mechanisms behind amplification of the SERS signal: chemical enhancement and electromagnetic enhancement. The latter is widely believed to be the main contribution and has a close relationship with the plasmonic resonance.⁴⁷ As discussed in Section 1.2, SPR can be excited in the vicinity of the metal surface, which gives rise to the local field enhancement and radiation enhancement of the Raman dipole. The overall enhancement factor (EF) can be expressed as⁴⁷:

$$EF \approx F_f F_r \approx \frac{|E_{loc}(\omega)|^4}{|E_i|^4} \quad 1.4$$

where F_f is the local field enhancement factor, F_r the radiation enhancement factor, E_{loc} the local electric field near the metal, E_i the electric field of incident light.⁴⁷ Considering E_{loc} could be hundreds of magnitudes larger than E_i ⁵⁶, the consequential EF could be spectacularly large, especially in the places called ‘hot spots’, such as tips and gaps of NPs and metal plates. The experimental EF can be calculated as:

$$EF = \frac{I_{SERS}}{N_{SERS}} \bigg/ \frac{I_{Raman}}{N_{Raman}} \quad 1.5$$

Where I_{SERS} and I_{Raman} are the intensity of SERS and Raman signals respectively, while the N_{SERS} and N_{Raman} are the numbers of molecules generating signal.

Another technique for enhancing Raman signal is resonance Raman spectroscopy. The excitation energy of the laser is optimised to overlap with the energy of the electronic transitions of the analytes. The resultant Raman signal is witnessed to have a boost up to 10^6 times, though fluorescence is also generated as a side-effect.⁵⁶

1.4. Tunable metamaterials

Metamaterials are materials that have periodically arranged sub-wavelength structures that can manipulate light-matter interactions.⁵⁷ Though chemically composed by ordinary base materials, metamaterials distinguish themselves by their micro- or nano-structures and many unique properties and applications such

as negative refractive index⁵⁸⁻⁶⁰, cloaking^{61, 62}, super lenses⁶³, artificial chirality^{64, 65} and all kinds of sensors^{51, 66}. Current research interests are focussed on tunable, switchable and nonlinear metamaterials that are adaptive to multiple functionalities and ambient stimuli.⁶⁷⁻⁶⁹ As mentioned previously, the optical output of metamaterials due to plasmonic resonance is largely dependent on the materials, size, shape and distributions of their nano-structures. Among all these parameters, the distributions of the nanostructures or the interparticle distance can be readily tuned *in situ*.⁷⁰ Before demonstrating our tunable metamaterials in later chapters, several typical tuning methods are introduced in this section.

1.4.1. Mechanical tuning

When talking about changing distances, mechanical strains and the resultant deformations are the most straightforward methods that come to mind. Mechanical tunability exploits the rearrangement of the nanostructures that are accommodated on elastic substrates such as polydimethylsiloxane (PDMS).⁷¹⁻⁷³

By anchoring ~ 250 nm diameter gold NP dimmers onto a stretchable substrate, Jeremy J. Baumberg group⁷⁴ examined the fundamental coupling effects of the dimer in response to the mechanical deformation. A clear shift of the SPR peaks can be witnessed with different stretching ratio of the substrate at two polarizing directions (**Figure 1.5**). Although didn't precisely measure the change of the interparticle distance, they qualitatively correlated the experimental scattering spectra under different stretching ratio to the theoretically generated spectra with designated separation, envisaging future applications in tunable SERS if this gap can be narrowed further.

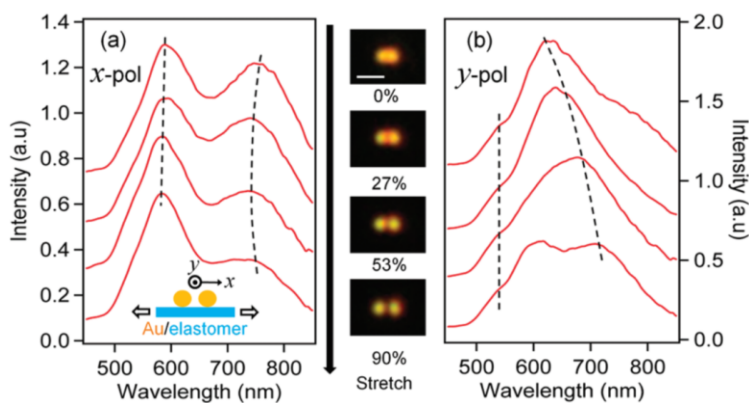


Figure 1.5 Measured dark-field scattering spectra of a single Au nanoparticle dimer deposited on stretchable elastomeric film. From top to bottom, the film is stretched by 0%, 27%, 53%, and 90%. Incident light is polarized along (a) the dimer axis (x direction, as in lower schematic) and (b) perpendicular to the dimer axis (y direction). (middle) Dark-field microscope images of the dimer at different stretching distances; scale bar is $1 \mu\text{m}$. Reprinted with permission from Ref.⁷⁴

In a more application-oriented research by R. Agarwal et al.⁷⁵, they proposed reconfigurable phase-only computer-generated metasurface holograms with up to three image planes operating in the visible regime. The device is based on arrays of gold nanorods anchored on a stretchable polydimethylsiloxane substrate.

Stretching the substrate rearranges the distribution of the nanorods array, enlarges the hologram images and changes the location of the image plane. Once fixing the observing distance, these devices can switch the displayed holographic image between multiple distinct images (**Figure 1.6**). This work provides the possibility for stretchable metasurface holograms for dynamically reconfigurable optical communication and display.

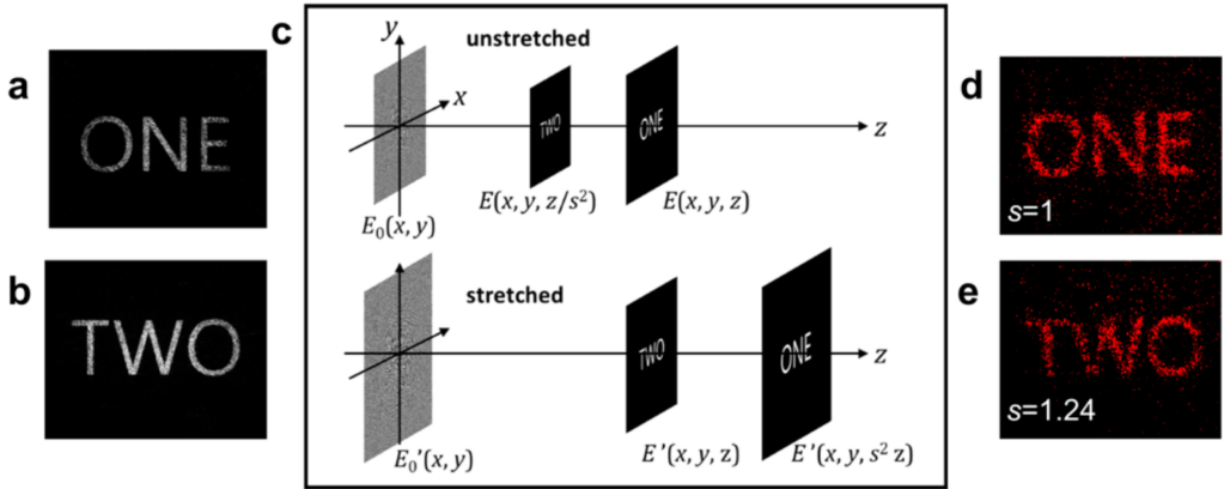


Figure 1.6 Design and performance of a two plane metasurface hologram on a stretchable PDMS substrate. (a-b) Computer reconstructions of computer-generated hologram image planes. (c) Schematic of two-plane hologram and mechanism for hologram image switching by stretching. (d-e) Experimentally measured hologram images at an image plane 200 μm from the metasurface for a device that is (d) not stretched and (e) stretched 124%. Reprinted with permission from Ref.⁷⁵

To further exploit the shifting of SPR frequency due to a change in interparticle distance, Naomi J. Halas et al.⁷⁶ reported a plasmonic device that can be tuned continuously across the entire visible spectrum, based on integrating a square array of aluminium nanostructures into an elastomeric substrate. By stretching the substrate in either of its two dimensions, the period and therefore the scattering colour can be red shifted or blue shifted subjected to the stretching directions, covering the entire visible spectrum (**Figure 1.7**). The unique two-dimensional design of this structure enables active mechanical colour tuning, under gentle elastic modulation with no more than 35% strain. This full-colour plasmonic device has a wide and diverse range of possible applications, such as highly sensitive surface stress or colorimetric sensors, and new types of real-time displays.

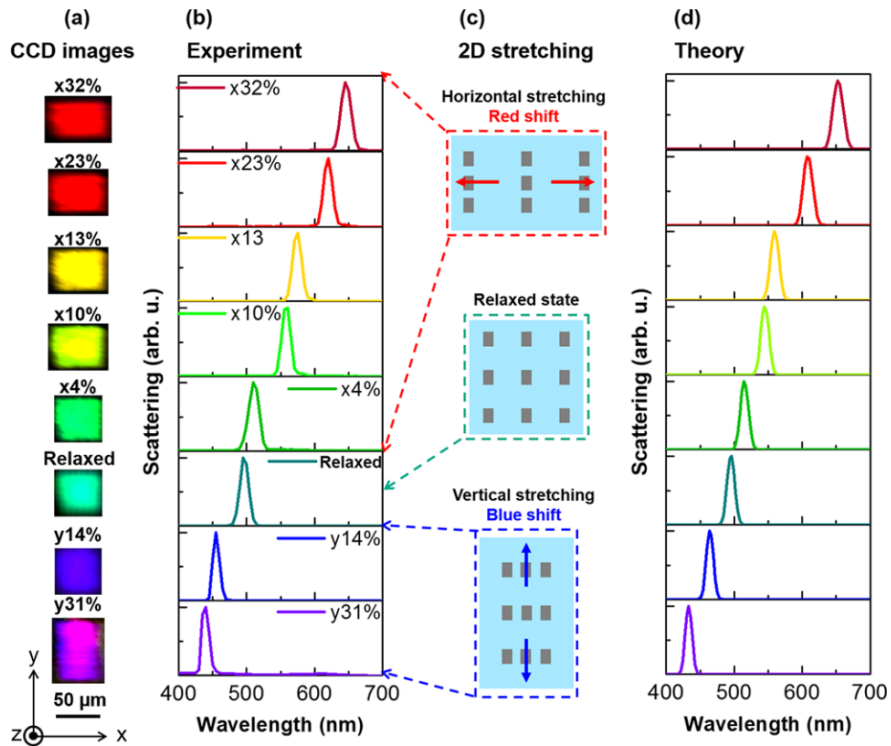


Figure 1.7 Full colour tuning on a single plasmonic device. (a) CCD images and (b) experimental spectra of the device at different stretching conditions. (c) Schematic of the two-dimensional stretching method for full-colour tuning. (d) The corresponding simulated scattering spectra. device, the colour of the scattering light is blue shifted. Reprinted with permission from Ref.⁷⁶

1.4.2. Thermal tuning

The change of temperature has ubiquitous influence upon the properties of materials such as the thermal expansion coefficients, although this effect is often too small to be noticeable at room temperature. Therefore, some non-linear effects that induce drastic changes over a small temperature range are required for practical applications. Most of the current thermo-responsive metamaterials are based on reactions or phase-transition effects of particular organic⁷⁷⁻⁸⁰ or inorganic⁸¹⁻⁸³ materials.

Vanadium dioxide (VO_2) is one of the most widely exploited inorganic building blocks for thermo-responsive meta-devices. At the critical temperature around 68°C , VO_2 experiences a phase transition between dielectric and metal states. The resultant changes in permittivity, especially the imaginary part became very handy for designing switchable absorbers.⁸⁴ Using ion irradiation through nanometer scale masks, Mikhail A. Kats et al.⁸⁵ selectively defect-engineered the insulator-metal transition of VO_2 , a prototypical correlated phase-transition material whose optical properties change dramatically depending on its state (**Figure 1.8**). After the intensive study on the influence of the Ar^+ injection upon the transition temperature, they demonstrated several optical metasurfaces, including tunable absorbers and polarizers based on thermally triggered dichroism.

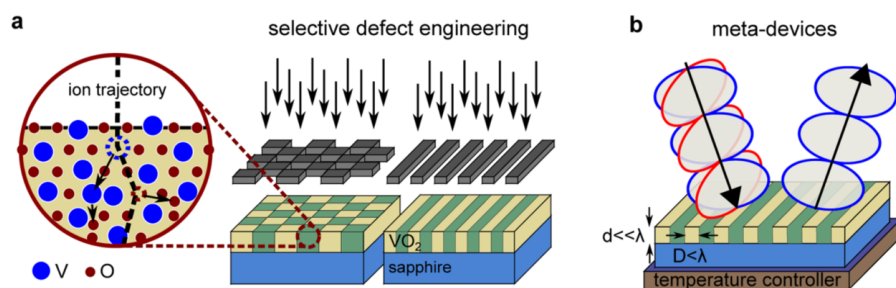


Figure 1.8 Optical meta-devices based on defect engineering of phase-transition materials. (a) The thermally driven insulator-to-metal phase transition of vanadium dioxide (VO_2) can be modified by deliberately introducing structural defects into the lattice (defect engineering). Spatially selective defect engineering is achieved by ion beam irradiation through a mask. The enlarged area shows the primary displacement of both vanadium and oxygen lattice atoms by an incoming energetic ion and the subsequent damage cascade. The complex refractive indices of the insulating and metallic states are similar for the intrinsic and irradiated VO_2 , but the phase transition of the irradiated regions occurs at a much lower temperature. (b) The irradiated features can be made much smaller than the wavelength of light, so the resulting film becomes a metasurface with effective optical properties. One example is a tunable polarizer comprising stripes of irradiated and intrinsic VO_2 , creating a metasurface with a variable degree of optical anisotropy. Reprinted with permission from Ref.⁸⁴

Not only interesting for biomedical applications such as drug-delivery, thermo-responsive polymers are particularly fascinating for real-time tuning of plasmonic active nanomaterials.⁸⁶⁻⁸⁸ Since the earliest report of the thermal phase transition behaviour of poly(N-isopropylacrylamide) (pNIPAM) in 1967 by Scarpa et al.,⁸⁹ temperature remains the most extensively exploited stimuli in the field of responsive polymers.⁸⁸ Below the lower critical solution temperature (LCST, $\sim 32^\circ\text{C}$), the hydrogen bonds between the water molecules and the C=O and N-H groups on pNIPAM dominate, rendering the chains of pNIPAM extended. Above the LCST, the hydrogen bonds break, and the interaction of hydrophobic methyl groups and the main-chain hydrocarbons with each other results in a more coiled conformation.⁹⁰ By functionalizing NPs or substrates with pNIPAM, a temperature dependent change in ligand length can be achieved resulting in an excellent means for auxetically tuning the structure and the resultant optical properties (**Figure 1.9**). Typical strategies involve utilizing this polymer to anchor plasmonic NPs randomly into another polymer matrix⁹¹, on micro-gel⁸⁶, in bulk solution⁹² or at a liquid-liquid interface.⁷⁸

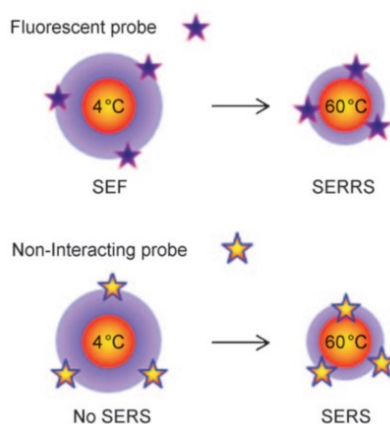


Figure 1.9 Schematic representation of the application of thermo-responsive $\text{Au}@p\text{NIPAM}$ microgels for surface enhanced fluorescence (SEF) and surface-enhanced resonance Raman scattering (SERRS) (top), and as molecular traps for surface-enhanced Raman scattering (SERS) of non-interacting molecular probes (bottom). Reprinted with permission from Ref.⁹²

1.4.3. Chemical tuning

For NPs dispersed in liquid, the ligands on the NPs and the chemicals in the bulk solution provide many convenient ways of tuning the NP assemblies. As mentioned previously, to improve the stability of NPs, charged ligands are indispensable to provide repelling electrostatic forces against the attracting van der Waals forces that induce aggregation. Therefore, the adjustment of this delicate balance will induce the rearrangement of NP arrays. Before going to extremes, the number of these charges on the NPs can be modulated by ligands⁹³, pH⁹⁴ and solvent⁹⁵. In addition, the concentration of electrolyte can also screen these charges and further tune the separation of NPs.^{23, 96} Dr. Leonora Velleman et al.⁹⁷, from our group, used a combination of X-ray diffraction and optical reflectance to determine the structural arrangement and plasmon coupling between gold NPs assembled at a water | 1,2-dichloroethane interface. The density of the NP array assembled at the interface can be controlled via the concentration of electrolytes within either the aqueous (NaCl) or organic phase (TBA TPB). At higher electrolyte concentration more nanoparticles can settle at the LLI resulting in a decrease in nanoparticle spacing as observed from X-ray diffraction experiments. As the NPs come closer, the increased plasmonic coupling produces a red-shift in the optical reflectance spectra (**Figure 1.10**), which demonstrated a simple way of chemically tuning the optical response of the NP array.

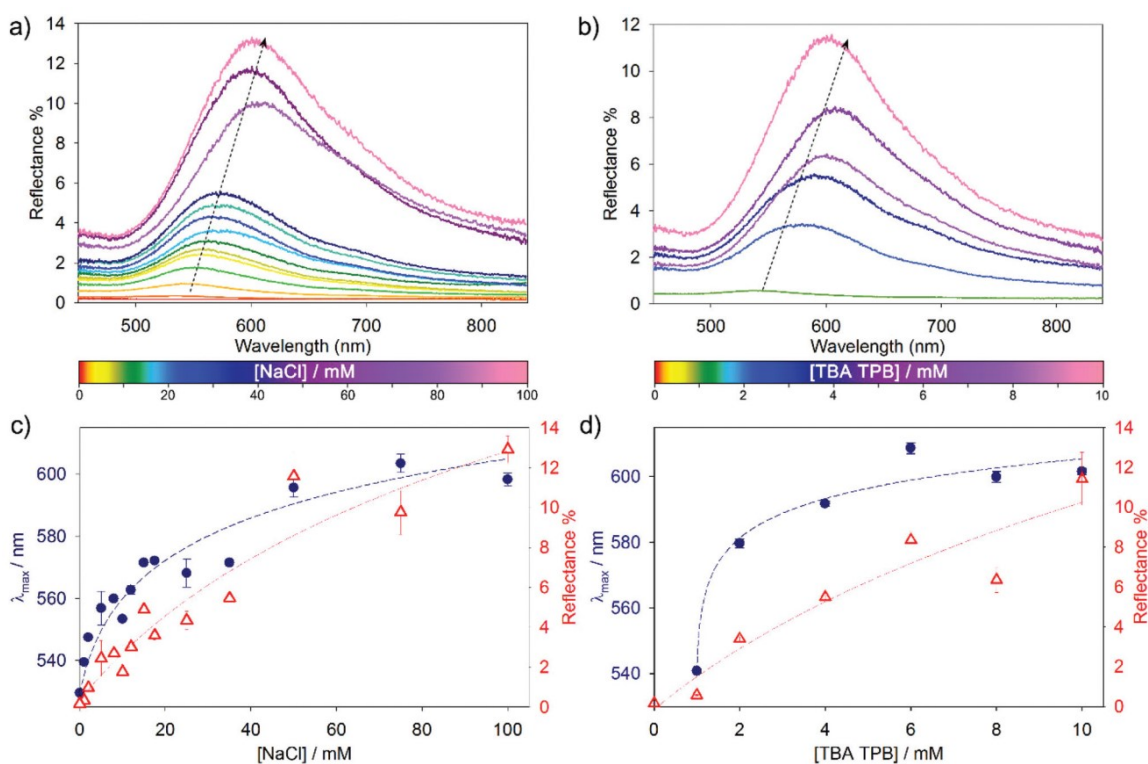


Figure 1.10 Reflectance spectra for NPs assembled at the water–DCE interface at varied electrolyte concentration, (a) NaCl in the aqueous phase, and (b) TBA TPB in the organic phase. Wavelength maxima positions (red triangles) and reflectance at maximum (black dots) of the NP films extracted from reflectance plots for varying NaCl (c) and TBA TPB (d). Note: reflectance spectra shown are the average of five reflectance spectra taken from different areas on each sample. Reprinted with permission from Ref.⁹⁷

Chemically controlling the specific binding between NPs is another widely used method.^{98, 99} DNA as a programmable linker is very versatile in changing the conformation of NP assembly.¹⁰⁰ The specific hybridization between complementary single strand DNA that anchored on different parts of nanomaterials facilitated numerous applications in sensors^{101, 102}, nanorobots¹⁰³ and biological delivery¹⁰⁴. Among them, Paul Alivisatos group¹⁰⁵, by combining lithographic techniques with DNA-based self-assembly methods, constructed responsive plasmonic metamaterials that exhibit the plasmonic analogue of an effect known as electromagnetically induced transparency (EIT), which can dramatically change their spectra upon motion of their constituent parts. The EIT-like effect in these assemblies can be tuned by precisely controlling the positioning of the plasmonic nanoparticles in these structures (**Figure 1.11**). For example, changing the ionic environment or dehydrating the sample will change the conformation of the DNA linkers and therefore the distance between the nanoparticles. Dark-field spectra of individual assemblies show peak shifts of up to many tens of nanometres. This dynamic metamaterial represents a steppingstone toward state-of-the-art plasmonic sensing platforms and next-generation dynamic metamaterials.¹⁰⁵

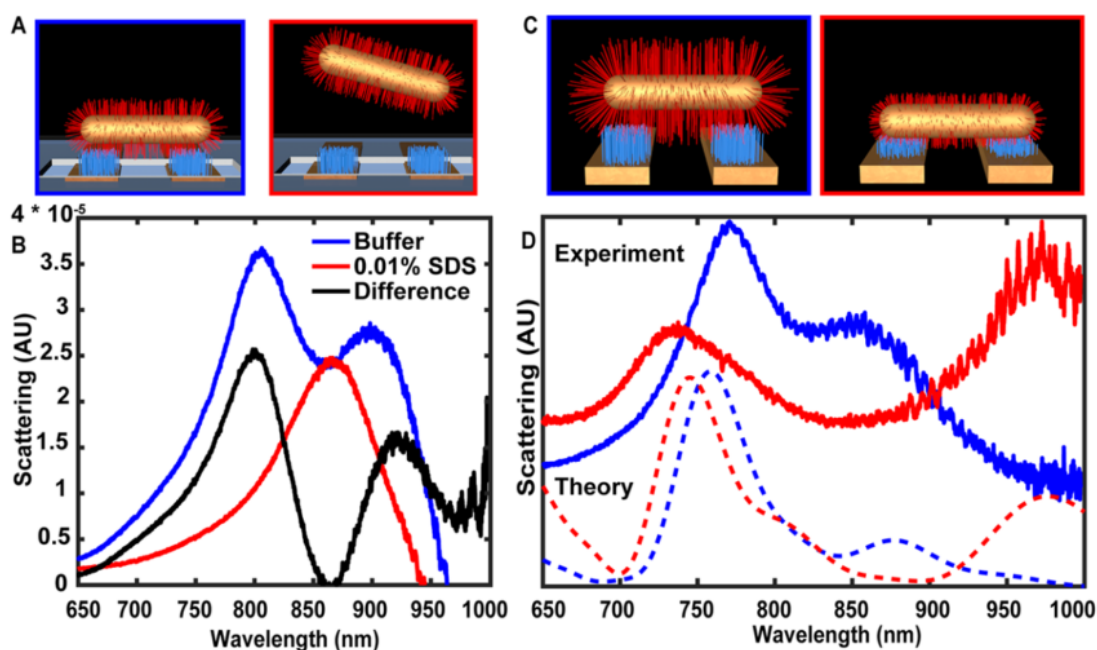


Figure 1.11 Dynamics of the hybrid inorganic–organic structure that exhibits an EIT-like effect. (a) Salt-based disassembly and destruction of EIT-like property due to changing ionic strength. The assembled structure in the blue box represents the structure in 0.5 M NaCl. The structure in the red box represents the disassembly in 0.01% SDS solution. (b) The blue trace is the measured dark-field EIT-like feature of an assembly taken in 0.5 M NaCl buffer. After flowing in water, a single peak of the same structure (red) is observed in dark-field imaging. This peak corresponds to the longitudinal resonance of the remaining parallel rods. The black trace is the difference of the two peaks and represents the true EIT-like effect of the assembled structure had the dipolar resonance of the parallel rods been completely suppressed. (c) Response to the hydration environment of the EIT-like assemblies. Side-on view of the hydrated state where the DNA is in its extended conformation (blue box). The DNA collapses upon removal of the solvent and dehydration (red box). (d) Dark-field spectra of the EIT-like assembly in its hydrated state (solid blue) and dry state (solid red). When the assembly is dehydrated, the rods come closer together, which will increase the magnitude of the EIT-like effect, broadening the transparency window. FDTD simulation of the hydrated state (dashed blue) and dry state (dashed red). Scattering intensity is normalized to make the shift in peak positions clear. The theory and experimental data are offset for clarity. Reprinted with permission from Ref.¹⁰⁵

1.4.4. Electric related tuning

Electric tuning covers a wide range of subordinate methods such as electromagnetic^{106, 107}, electrostatic¹⁰⁸, piezoelectric^{109, 110} and electrochemical^{111, 112} approaches. Mikhail Lapine et al.¹⁰⁶, first introduced the concept of magnetoelastic metamaterials, where multiple arrays of metallic rings were stacked in elastic polymer membranes (**Figure 1.12**). The electromagnetic tuning is achieved by utilizing the Ampere forces among different arrays of the metal rings and the elastic forces from the polymer. This enables the electromagnetically induced forces to change the metamaterial structure, dynamically tuning its effective properties.¹⁰⁶

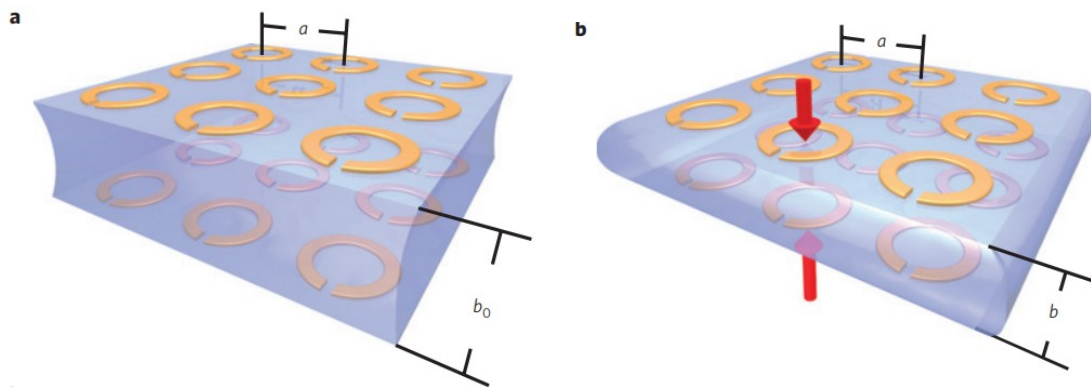


Figure 1.12 Two layers of the bulk sample are shown. (a) The metamaterial before the electromagnetic field is applied. (b) The metamaterial is compressed by the electromagnetic forces acting between the elements. Dimensionless lattice parameters a and b are normalized to the resonator radius r_0 . Reprinted with permission from Ref.¹⁰⁶

Nikolay Zheludev group¹⁰⁸, proposed a tunable metamaterial that is actuated by electrostatic forces arising from the application of only a few volts to its nanoscale building blocks. Supported by pairs of parallel strings cut from a flexible silicon nitride membrane of nanoscale thickness, those building blocks of picogram mass, can be driven synchronously to megahertz frequencies to electromechanically reconfigure the metamolecules and dramatically change the transmission and reflection spectra of the metamaterial (**Figure 1.13**). The metamaterial's colossal electro-optical response allows for either fast continuous tuning of its optical properties (up to 8% optical signal modulation at up to megahertz rates) or high-contrast irreversible switching in a device only 100 nm thick.¹⁰⁸

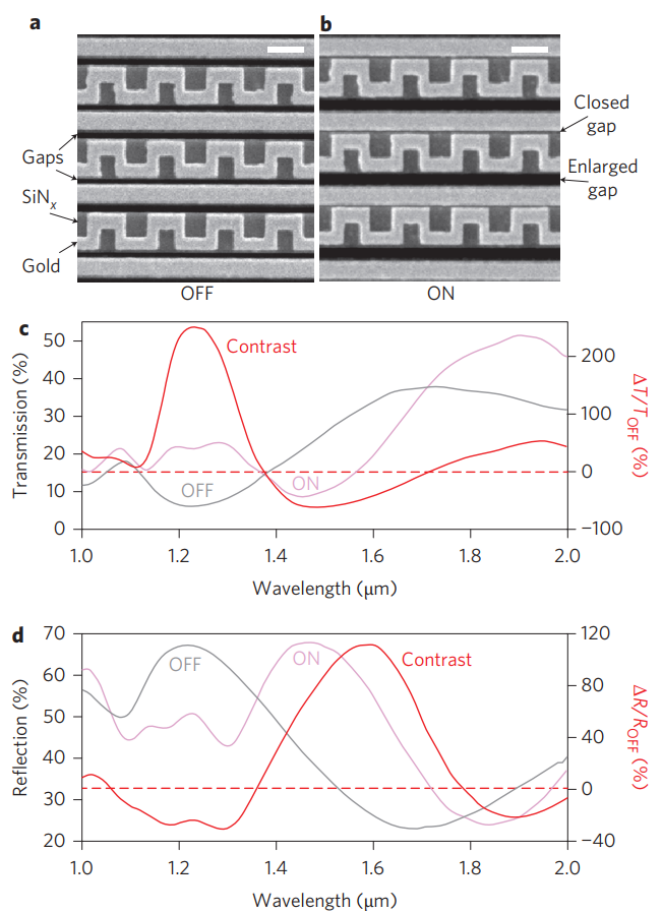


Figure 1.13 (a & b) SEM images of the metamaterial in its OFF (a) and ON (b) states. Scale bar, 500 nm. c–d, Transmission (c), reflection (d) spectra of the device in the OFF and ON states (left axis) and the corresponding switching contrast (right axis). Reprinted with permission from Ref.¹⁰⁸

Yu Hui et al.¹⁰⁹ proposed a thin piezoelectric plasmonic metasurface forming the resonant body of a nanomechanical resonator with simultaneously tailored optical and electromechanical properties. They experimentally demonstrate that it is possible to achieve high thermomechanical coupling between electromagnetic and mechanical resonances in a single ultrathin piezoelectric nanoplate. The combination of nanoplasmonic and piezoelectric resonances allows the proposed device to selectively detect long-wavelength infrared radiation with unprecedented electromechanical performance and thermal capabilities (**Figure 1.14**). These attributes lead to the demonstration of a fast, high-resolution, uncooled infrared detector with $\sim 80\%$ absorption for an optimized spectral bandwidth centred around 8.8 μm .¹⁰⁹

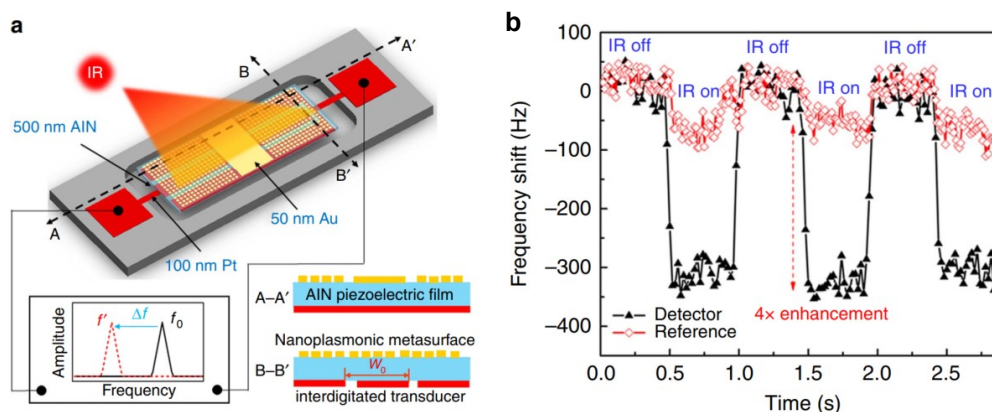


Figure 1.14 (a) Mock-up view: an aluminium nitride nanoplate is sandwiched between a bottom metallic interdigitated electrode and a top nanoplasmonic metasurface. The incident IR radiation is selectively absorbed by the plasmonic metasurface and heats up the resonator, shifting its resonance frequency from f_0 to f' due to the temperature dependence of its resonance frequency. (b) Measured response of the plasmonic piezoelectric resonator and a conventional AlN MEMS resonator to a modulated IR radiation emitted by a 1,500-K global (2–16 mm broadband spectral range). Reprinted with permission from Ref.¹⁰⁹

For electrochemical methods, one of the most challenging tasks is to maintain the stability and the reversibility at the same time.¹¹¹ An electrochemically bistable switchable mirror was achieved by changing the potential of the two thiol-modified indium tin oxide (ITO) electrodes in ionic liquids containing Ag^+ ions (**Figure 1.15**).¹¹¹ The on state (applying -2.5 V) not only reduced the Ag^+ ions onto the cathode, forming a reflective mirror, but also build up a viscous electrical double layer in the ionic liquid electrolyte. Under the voltage-off state, this double layer becomes a barrier protecting the metal thin film from dissolving by the bromide ions, maintaining the bistability for more than 2 hours.

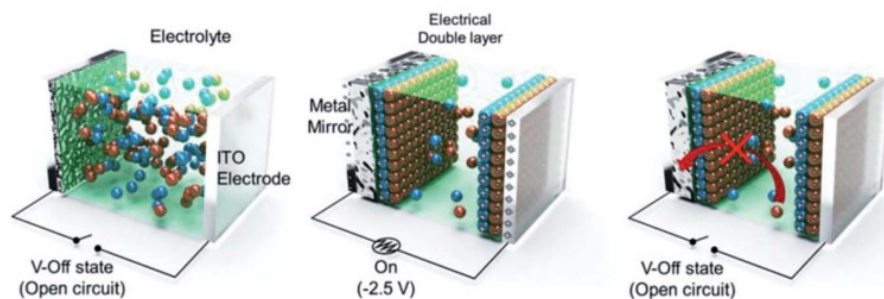


Figure 1.15 Schematic diagram of the ion distribution in the transparent state, reflective state, and V-off state. Reprinted with permission from Ref.¹¹¹

1.4.5. Optical tuning

Light-metamaterial interactions not only produce all kinds of interesting optical phenomena, but also could be employed as a way to tune the metamaterials themselves in return. Maiken Mikkelsen et al. constructed an optically tunable plasmonic nanoantenna based on the coupling of silver nano-cubes and the silver substrate. The UV light can transfer the spiropyran spacer between the cube and the substrate into

merocyanine, which induce a dramatic change in refractive index of the interlayer, and as a result change the extinction coefficient of the overall system (**Figure 1.16**).¹¹³

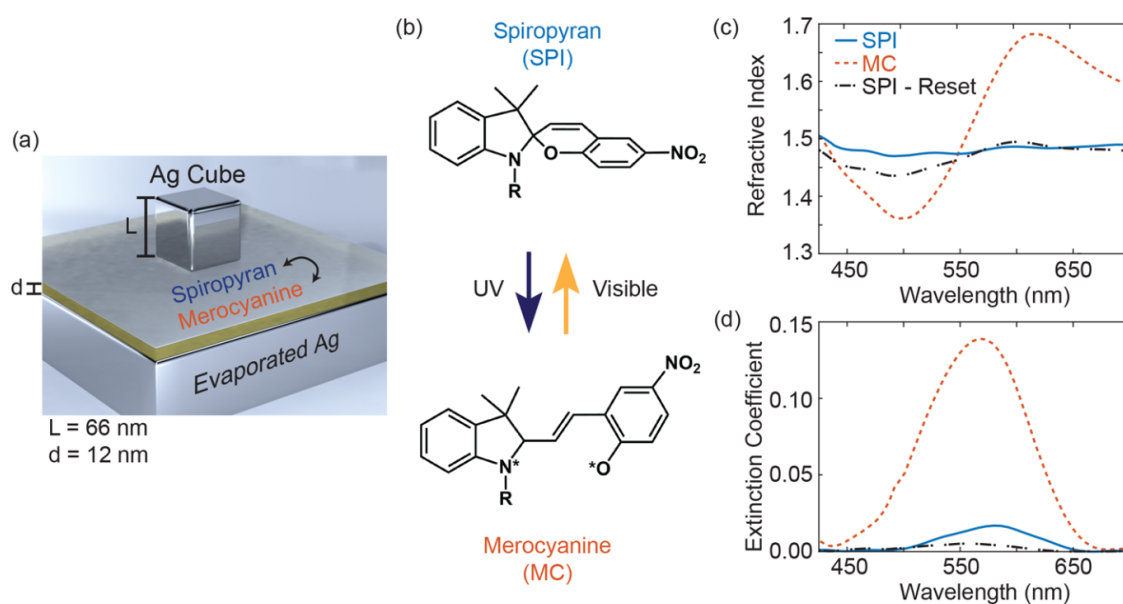


Figure 1.16 (a) Schematic of film coupled nanopatch antenna with 66 nm nanocube and 12 nm photochromic spacer layer over a 75 nm silver film. (b) Chemical structure diagram showing two isomers of SPI that can be alternated through either UV or visible light exposure. (c,d) Refractive index and extinction coefficient of a 12 nm layer of SPI/PMMA before (blue “SPI”) and after UV exposure (red “MC”) and after being thermally reset (yellow “SPI-Reset”). Reprinted with permission from Ref.¹¹³

The SPR of plasmonic metamaterials can induce thermal impact on local structures, enables another way of modulating light with light. Jun-Yu Ou et al. deposited gold NP patterns on silicon nitride substrate.¹¹⁴

The deformation of the substrate due to the optical heating effect of the gold NPs allows to tune the output signal at MHz frequency range with milliwatt power level. Another type of optically actuated single nano-oscillator was constructed by placing a pNIPAM wrapped gold NP on metallic substrate.¹¹⁵ The irradiation of laser stimulates the LSPR of NP on the substrate, generating heat that increases the local temperature beyond the LCST of pNIPAM. This reduces the distance between the NP and the substrate, tunes the scattering signal of this system.

1.5. Aims and objectives

The assembly of NPs at interfaces exhibits numerous interesting optical effects and has applications involving plasmonics and SERS. One of the most challenging tasks in this field is designing ‘smart’ devices that can re-adjust themselves to respond to environmental stimuli or to meet the demands of different applications: a sensor that has different responses to multiple analytes in the same solution; an optical filter that can adjust its density and wavelength within a wide range; a solar cell that can regulate light-harvest and heat-dissipation over all weather conditions, and a SERS substrate that can boost interesting Raman

peaks at selected wavenumbers. All these potential applications require in-situ tunability of the structures and properties of these systems which is not yet completely solved in the existing literature.

The projects described in this thesis share the same objective of tuning the structure and optical response of different plasmonic NP assemblies at interfaces. This objective can be further divided into two sub-objectives. Firstly, to assemble NPs at either the SLI or the LLI; and secondly, to adjust their structure and optical output through electrical, thermal and chemical approaches. This thesis is therefore organized according to the different tuning methods applied at different interfaces.

Chapter 1 gives an introduction to the state of the art and general overview of the field, including brief introductions of nanoparticles and applications, the basics of plasmonics and SERS, and the theoretical framework that supports all the later experiments. Chapter 2 details each of the experimental techniques and the experimental setups in the projects, such as NP synthesis, film deposition, SEM, UV-Vis, reflectance and Raman measurements, electrochemical cells and thermal control setups. Chapter 3 demonstrates a novel electric potential controlled switchable reflector at the SLI. By adjusting the potentials of the metallic substrate, a plasmonic array of 16 nm gold NPs can be reversibly assembled or disassembled, switching the system between ‘absorber’ and ‘reflector’. Chapter 4 further develops an electro-tunable nanoplasmonic surface for amplified SERS, by assembling relatively large NPs (40 nm) on the SLI. With the increase of interfacial potential, the narrowed interparticle gaps produce not only a substantial plasmonic coupling band in the reflectance spectra, but also numerous ‘hot spots’ boosting the SERS output. Also at the SLI, a thermo-responsive auxetic metasurface based on the coupling between a metallic NP array and substrate is demonstrated in Chapter 5. We show that such meta-surfaces can be tuned to exhibit substantial changes in the optical properties both in terms of wavelength and intensity, through the temperature-controlled variation of the interparticle distance within the nanoparticle monolayer as well as its separation from the substrate. Then, we migrate to an LLI system where label-free sensing of lead (Pb^{2+}) based on the self-assembly of NPs is presented in Chapter 6. The glutathione (GSH) functionalized NPs used here specifically bind to lead, leading to the formation of a reflective golden mirror. This technique allows the detection of lead with improved sensitivity and faster dynamics as compared with bulk aggregation methods. In Chapter 7, an electro-tunable nanoplasmonic liquid mirror is proposed that is based on the electrochemically assembled NP array at LLI. The optical outputs can be tailored by applying different electric potentials at the interface. Lastly, Chapter 8 describes future directions and developments.

1.6. References

(1) Singh, S. C., *Nanomaterials*. Chichester : Wiley-VCH ; Weinheim; John Wiley, 2012; pp 36-38.

- (2) Jain, P. K.; Huang, X. H.; El-Sayed, I. H.; El-Sayed, M. A. Noble Metals on the Nanoscale: Optical and Photothermal Properties and Some Applications in Imaging, Sensing, Biology, and Medicine. *Acc. Chem. Res.* **2008**, *41*, 1578-1586.
- (3) Moreau, A.; Ciraci, C.; Mock, J. J.; Hill, R. T.; Wang, Q.; Wiley, B. J.; Chilkoti, A.; Smith, D. R. Controlled-Reflectance Surfaces with Film-Coupled Colloidal Nanoantennas. *Nature* **2012**, *492*, 86-89.
- (4) Jain, P. K.; El-Sayed, M. A. Plasmonic Coupling in Noble Metal Nanostructures. *Chem. Phys. Lett.* **2010**, *487*, 153-164.
- (5) Brownson, D. A. C.; Kampouris, D. K.; Banks, C. E. Graphene Electrochemistry: Fundamental Concepts through to Prominent Applications. *Chem. Soc. Rev.* **2012**, *41*, 6944-6976.
- (6) Wei, W.; Yang, S.; Zhou, H.; Lieberwirth, I.; Feng, X.; Müllen, K. 3D Graphene Foams Cross-linked with Pre-encapsulated Fe₃O₄ Nanospheres for Enhanced Lithium Storage. *Adv. Mater.* **2013**, *25*, 2909-2914.
- (7) Ma, Y.; Zhao, M. G.; Cai, B.; Wang, W.; Ye, Z. Z.; Huang, J. Y. 3D Graphene Foams Decorated by CuO Nanoflowers for Ultrasensitive Ascorbic Acid Detection. *Biosens. Bioelectron.* **2014**, *59*, 384-388.
- (8) Heller, A.; Feldman, B. Electrochemical Glucose Sensors and Their Applications in Diabetes Management. *Chem. Rev.* **2008**, *108*, 2482-2505.
- (9) He, W. W.; Wu, X. C.; Liu, J. B.; Hu, X. N.; Zhang, K.; Hou, S. A.; Zhou, W. Y.; Xie, S. S. Design of AgM Bimetallic Alloy Nanostructures (M = Au, Pd, Pt) with Tunable Morphology and Peroxidase-Like Activity. *Chem. Mat.* **2010**, *22*, 2988-2994.
- (10) Ma, Y.; Zhao, M. G.; Cai, B.; Wang, W.; Ye, Z. Z.; Huang, J. Y. 3D Graphene Network@WO₃ Nanowire Composites: a Multifunctional Colorimetric and Electrochemical Biosensing Platform. *Chem. Commun.* **2014**, *50*, 11135-11138.
- (11) Wang, B.; He, X.; Zhang, Z.; Zhao, Y.; Feng, W. Metabolism of Nanomaterials in Vivo: Blood Circulation and Organ Clearance. *Acc. Chem. Res.* **2012**, *46*, 761-769.
- (12) Hu, X. G.; Zhou, Q. X. Health and Ecosystem Risks of Graphene. *Chem. Rev.* **2013**, *113*, 3815-3835.
- (13) Lim, E.-K.; Kim, T.; Paik, S.; Haam, S.; Huh, Y.-M.; Lee, K. Nanomaterials for Theranostics: Recent Advances and Future Challenges. *Chem. Rev.* **2014**, *115*, 327-394.
- (14) Shen, J.; Li, Y.; Gu, H.; Xia, F.; Zuo, X. Recent Development of Sandwich Assay Based on the Nanobiotechnologies for Proteins, Nucleic Acids, Small Molecules, and Ions. *Chem. Rev.* **2014**, *114*, 7631-7677.
- (15) Stewart, M. E.; Anderton, C. R.; Thompson, L. B.; Maria, J.; Gray, S. K.; Rogers, J. A.; Nuzzo, R. G. Nanostructured Plasmonic Sensors. *Chem. Rev.* **2008**, *108*, 494-521.
- (16) Michalet, X.; Pinaud, F. F.; Bentolila, L. A.; Tsay, J. M.; Doose, S.; Li, J. J.; Sundaresan, G.; Wu, A. M.; Gambhir, S. S.; Weiss, S. Quantum Dots for Live Cells, in Vivo Imaging, and Diagnostics. *Science* **2005**, *307*, 538-544.
- (17) Panfil, Y. E.; Oded, M.; Banin, U. Colloidal Quantum Nanostructures: Emerging Materials for Display Applications. *Angew. Chem.-Int. Edit.* **2018**, *57*, 4274-4295.
- (18) Shirasaki, Y.; Supran, G. J.; Bawendi, M. G.; Bulovic, V. Emergence of Colloidal Quantum-Dot Light-Emitting Technologies. *Nat. Photonics* **2013**, *7*, 13-23.
- (19) Biju, V.; Itoh, T.; Ishikawa, M. Delivering Quantum Dots to Cells: Bioconjugated Quantum Dots for Targeted and Nonspecific Extracellular and Intracellular Imaging. *Chem. Soc. Rev.* **2010**, *39*, 3031-3056.
- (20) Torchilin, V. P. Micellar Nanocarriers: Pharmaceutical Perspectives. *Pharm. Res.* **2007**, *24*, 1-16.
- (21) Allen, T. M.; Cullis, P. R. Liposomal Drug Delivery systems: From Concept to Clinical Applications. *Adv. Drug Deliv. Rev.* **2013**, *65*, 36-48.
- (22) Sau, T. K.; Rogach, A. L.; Jackel, F.; Klar, T. A.; Feldmann, J. Properties and Applications of Colloidal Nonspherical Noble Metal Nanoparticles. *Adv. Mater.* **2010**, *22*, 1805-1825.
- (23) Edel, J. B.; Kornyshev, A. A.; Kucernak, A. R.; Urbakh, M. Fundamentals and Applications of Self-Assembled Plasmonic Nanoparticles at Interfaces. *Chem. Soc. Rev.* **2016**, *45*, 1581-1596.
- (24) Lane, L. A.; Qian, X.; Nie, S. SERS Nanoparticles in Medicine: From Label-Free Detection to Spectroscopic Tagging. *Chem. Rev.* **2015**, *115*, 10489-10529.

- (25) Lakowicz, J. R. Radiative decay engineering 5: metal-enhanced fluorescence and plasmon emission. *Anal. Biochem.* **2005**, *337*, 171-194.
- (26) Hu, M.; Chen, J. Y.; Li, Z. Y.; Au, L.; Hartland, G. V.; Li, X. D.; Marquez, M.; Xia, Y. N. Gold Nanostructures: Engineering Their Plasmonic Properties for Biomedical Applications. *Chem. Soc. Rev.* **2006**, *35*, 1084-1094.
- (27) Halas, N. J.; Lal, S.; Chang, W. S.; Link, S.; Nordlander, P. Plasmons in Strongly Coupled Metallic Nanostructures. *Chem. Rev.* **2011**, *111*, 3913-3961.
- (28) Ghosh, S. K.; Pal, T. Interparticle Coupling Effect on the Surface Plasmon Resonance of Gold Nanoparticles: From Theory to Applications. *Chem. Rev.* **2007**, *107*, 4797-4862.
- (29) Parsegian, V. A., *Van der Waals Forces: A Handbook for Biologists, Chemists, Engineers, and Physicists*. Cambridge University Press: Cambridge, 2005; pp 41-61.
- (30) Lebovka, N. I., Aggregation of Charged Colloidal Particles. In *Polyelectrolyte Complexes in the Dispersed and Solid State I: Principles and Theory*, Muller, M., Ed. Springer-Verlag Berlin: Berlin, 2014; Vol. 255, pp 57-96.
- (31) Frens, G. Controlled Nucleation for the Regulation of the Particle Size in Monodisperse Gold Suspensions. *Nature* **1973**, *241*, 20-22.
- (32) Sellers, H.; Ulman, A.; Shnidman, Y.; Eilers, J. E. Structure and Binding of Alkanethiolates on Gold and Silver Surfaces: Implications for Self-assembled Monolayers. *J. Am. Chem. Soc.* **1993**, *115*, 9389-9401.
- (33) Turek, V. A.; Elliott, L. N.; Tyler, A. I. I.; Demetriadou, A.; Paget, J.; Cecchini, M. P.; Kucernak, A. R.; Kornyshev, A. A.; Ediel, J. B. Self-Assembly and Applications of Ultraconcentrated Nanoparticle Solutions. *ACS Nano* **2013**, *7*, 8753-8759.
- (34) Chen, J.; Guo, L.; Qiu, B.; Lin, Z.; Wang, T. Application of Ordered Nanoparticles Self-assemblies in Surface Enhanced Spectroscopy. *Mater. Chem. Front.* **2017**.
- (35) Mirkin, C. A.; Letsinger, R. L.; Mucic, R. C.; Storhoff, J. J. A DNA-Based Method for Rationally Assembling Nanoparticles into Macroscopic Materials. *Nature* **1996**, *382*, 607-609.
- (36) Harashima, H.; Kiwada, H. Liposomal Targeting and Drug Delivery: Kinetic Consideration. *Adv. Drug Deliv. Rev.* **1996**, *19*, 425-444.
- (37) Lu, A. H.; Salabas, E. L.; Schuth, F. Magnetic Nanoparticles: Synthesis, Protection, Functionalization, and Application. *Angew. Chem.-Int. Edit.* **2007**, *46*, 1222-1244.
- (38) Freestone, I.; Meeks, N.; Sax, M.; Higgitt, C. The Lycurgus Cup - A Roman Nanotechnology. *Gold Bull.* **2007**, *40*, 270-277.
- (39) Maier, S. A., *Plasmonics : Fundamentals and Applications*. Maier, S. A., Ed. Springer: New York, 2007; pp 65-88.
- (40) Booth, S. G.; Cowcher, D. P.; Goodacre, R.; Dryfe, R. A. W. Electrochemical modulation of SERS at the liquid/liquid interface. *Chem. Commun.* **2014**, *50*, 4482-4484.
- (41) Cialla, D.; Marz, A.; Bohme, R.; Theil, F.; Weber, K.; Schmitt, M.; Popp, J. Surface-enhanced Raman spectroscopy (SERS): progress and trends. *Anal. Bioanal. Chem.* **2012**, *403*, 27-54.
- (42) Sharma, B.; Frontiera, R. R.; Henry, A. I.; Ringe, E.; Van Duyne, R. P. SERS: Materials, Applications, and the Future. *Mater. Today* **2012**, *15*, 16-25.
- (43) Anker, J. N.; Hall, W. P.; Lyandres, O.; Shah, N. C.; Zhao, J.; Van Duyne, R. P. Biosensing with Plasmonic Nanosensors. *Nat. Mater.* **2008**, *7*, 442-453.
- (44) Shipway, A. N.; Katz, E.; Willner, I. Nanoparticle Arrays on Surfaces for Electronic, Optical, and Sensor Applications. *ChemPhysChem* **2000**, *1*, 18-52.
- (45) Mandal, P.; Sharma, S. Progress in Plasmonic Solar Cell Efficiency Improvement: A Status Review. *Renew. Sust. Energ. Rev.* **2016**, *65*, 537-552.
- (46) Tada, H.; Kiyonaga, T.; Naya, S. Rational Design and Applications of Highly Efficient Reaction Systems Photocatalyzed by Noble Metal Nanoparticle-Loaded Titanium(IV) Dioxide. *Chem. Soc. Rev.* **2009**, *38*, 1849-1858.
- (47) Le Ru, E. C.; Etchegoin, P. G., *Principles of Surface-Enhanced Raman Spectroscopy : and Related Plasmonic Effects*. Elsevier: Amsterdam; Heidelberg, 2011; pp 29-297.

- (48) Willets, K. A.; Duyn, R. P. V. Localized Surface Plasmon Resonance Spectroscopy and Sensing. *Annu. Rev. Phys. Chem.* **2007**, *58*, 267-297.
- (49) Brockman, J. M.; Nelson, B. P.; Corn, R. M. Surface Plasmon Resonance Imaging Measurements of Ultrathin Organic Films. *Annu. Rev. Phys. Chem.* **2000**, *51*, 41-63.
- (50) Knobloch, H.; Brunner, H.; Leitner, A.; Aussenegg, F.; Knoll, W. Probing the Evanescent Field of Propagating Plasmon Surface Polaritons by Fluorescence and Raman Spectroscopies. *J. Chem. Phys.* **1993**, *98*, 10093-10095.
- (51) Roh, S.; Chung, T.; Lee, B. Overview of the Characteristics of Micro- and Nano-Structured Surface Plasmon Resonance Sensors. *Sensors* **2011**, *11*, 1565-1588.
- (52) Ross, M. B.; Mirkin, C. A.; Schatz, G. C. Optical Properties of One-, Two-, and Three-Dimensional Arrays of Plasmonic Nanostructures. *J. Phys. Chem. C* **2016**, *120*, 816-830.
- (53) Turek, V. A.; Cecchini, M. P.; Paget, J.; Kucernak, A. R.; Kornyshev, A. A.; Edel, J. B. Plasmonic Ruler at the Liquid-Liquid Interface. *ACS Nano* **2012**, *6*, 7789-7799.
- (54) Giannini, V.; Fernandez-Dominguez, A. I.; Heck, S. C.; Maier, S. A. Plasmonic Nanoantennas: Fundamentals and Their Use in Controlling the Radiative Properties of Nanoemitters. *Chem. Rev.* **2011**, *111*, 3888-3912.
- (55) Ma, Y.; Zagar, C.; Klemme, D. J.; Sikdar, D.; Velleman, L.; Montelongo, Y.; Oh, S.-H.; Kucernak, A. R.; Edel, J. B.; Kornyshev, A. A. A Tunable Nanoplasmonic Mirror at an Electrochemical Interface. *ACS Photonics* **2018**, *5*, 4604-4616.
- (56) Schlücker, S., *Surface Enhanced Raman Spectroscopy Analytical, Biophysical and Life Science Applications*. Wiley-VCH: Weinheim; John Wiley, 2013; pp 241-252.
- (57) Cai, W.; Shalaev, V., *Optical Metamaterials : Fundamentals and Applications*. Cai, W.; Shalaev, V., Eds. Springer: New York, 2016; pp 1-10.
- (58) Pendry, J. B.; Schurig, D.; Smith, D. R. Controlling Electromagnetic Fields. *Science* **2006**, *312*, 1780-1782.
- (59) Pendry, J. B.; Luo, Y.; Zhao, R. K. Transforming the Optical Landscape. *Science* **2015**, *348*, 521-524.
- (60) Smith, D. R.; Pendry, J. B.; Wiltshire, M. C. K. Metamaterials and Negative Refractive Index. **2004**, *305*, 788-792.
- (61) Cai, W. S.; Chettiar, U. K.; Kildishev, A. V.; Shalaev, V. M. Optical Cloaking with Metamaterials. *Nat. Photonics* **2007**, *1*, 224-227.
- (62) Shin, D.; Urzhumov, Y.; Jung, Y.; Kang, G.; Baek, S.; Choi, M.; Park, H.; Kim, K.; Smith, D. R. Broadband Electromagnetic Cloaking with Smart Metamaterials. *Nat. Commun.* **2012**, *3*, 1213.
- (63) Lu, D. L.; Liu, Z. W. Hyperlenses and Metalenses for Far-Field Super-Resolution Imaging. *Nat. Commun.* **2012**, *3*, 9.
- (64) Wang, Z.-G.; Ding, B. Engineering DNA Self-Assemblies as Templates for Functional Nanostructures. *Acc. Chem. Res.* **2014**, *47*, 1654-1662.
- (65) Zhao, X.; Xu, L.; Sun, M.; Ma, W.; Wu, X.; Xu, C.; Kuang, H. Tuning the Interactions between Chiral Plasmonic Films and Living Cells. *Nat. Commun.* **2017**, *8*, 2007.
- (66) Pandey, P.; Datta, M.; Malhotra, B. D. Prospects of Nanomaterials in Biosensors. *Anal. Lett.* **2008**, *41*, 159-209.
- (67) Zheludev, N. I. The Road Ahead for Metamaterials. *Science* **2010**, *328*, 582-583.
- (68) Zheludev, N. I.; Kivshar, Y. S. From Metamaterials to Metadevices. *Nat. Mater.* **2012**, *11*, 917-924.
- (69) Ou, J. Y.; Plum, E.; Jiang, L.; Zheludev, N. I. Reconfigurable Photonic Metamaterials. *Nano Lett.* **2011**, *11*, 2142-2144.
- (70) Ciraci, C.; Chen, X.; Mock, J. J.; McGuire, F.; Liu, X.; Oh, S.-H.; Smith, D. R. Film-Coupled Nanoparticles by Atomic Layer Deposition: Comparison with Organic Spacing Layers. *Appl. Phys. Lett.* **2014**, *104*, 023109.
- (71) Hsueh, H. Y.; Yao, C. T.; Ho, R. M. Well-Ordered Nanohybrids and Nanoporous Materials from Gyroid Block Copolymer Templates. *Chem. Soc. Rev.* **2015**, *44*, 1974-2018.

- (72) Yu, X. L.; Zhou, J.; Liang, H. Y.; Jiang, Z. Y.; Wu, L. L. Mechanical Metamaterials Associated with Stiffness, Rigidity and Compressibility: A Brief Review. *Prog. Mater. Sci.* **2018**, *94*, 114-173.
- (73) Walia, S.; Shah, C. M.; Gutruf, P.; Nili, H.; Chowdhury, D. R.; Withayachumnankul, W.; Bhaskaran, M.; Sriram, S. Flexible Metasurfaces and Metamaterials: A Review of Materials and Fabrication Processes at Micro- and Nano-Scales. *Appl. Phys. Rev.* **2015**, *2*, 14.
- (74) Huang, F.; Baumberg, J. J. Actively Tuned Plasmons on Elastomerically Driven Au Nanoparticle Dimers. *Nano Lett.* **2010**, *10*, 1787-1792.
- (75) Malek, S. C.; Ee, H.-S.; Agarwal, R. Strain Multiplexed Metasurface Holograms on a Stretchable Substrate. *Nano Lett.* **2017**, *17*, 3641-3645.
- (76) Tseng, M. L.; Yang, J.; Semmlinger, M.; Zhang, C.; Nordlander, P.; Halas, N. J. Two-Dimensional Active Tuning of an Aluminum Plasmonic Array for Full-Spectrum Response. *Nano Lett.* **2017**, *17*, 6034-6039.
- (77) Balamurugan, S.; Mendez, S.; Balamurugan, S. S.; O'Brien, M. J.; López, G. P. Thermal Response of Poly(N-isopropylacrylamide) Brushes Probed by Surface Plasmon Resonance. *Langmuir* **2003**, *19*, 2545-2549.
- (78) Ding, T.; Rudrum, A. W.; Herrmann, L. O.; Turek, V.; Baumberg, J. J. Polymer-Assisted Self-Assembly of Gold Nanoparticle Monolayers and Their Dynamical Switching. *Nanoscale* **2016**, *8*, 15864-15869.
- (79) Gehan, H.; Fillaud, L.; Chehimi, M. M.; Aubard, J.; Hohenau, A.; Felidj, N.; Mangeney, C. Thermo-induced Electromagnetic Coupling in Gold/Polymer Hybrid Plasmonic Structures Probed by Surface-Enhanced Raman Scattering. *ACS Nano* **2010**, *4*, 6491-6500.
- (80) Han, F.; Vivekchand, S. R. C.; Soeriyadi, A. H.; Zheng, Y.; Gooding, J. J. Thermoresponsive Plasmonic Core-Satellite Nanostructures with Reversible, Temperature Sensitive Optical Properties. *Nanoscale* **2018**, *10*, 4284-4290.
- (81) Cao, T.; Zhang, X. Y.; Dong, W. L.; Lu, L.; Zhou, X. L.; Zhuang, X.; Deng, J. H.; Cheng, X.; Li, G. X.; Simpson, R. E. Tuneable Thermal Emission Using Chalcogenide Metasurface. *Adv. Opt. Mater.* **2018**, *6*, 8.
- (82) Qu, Y. R.; Li, Q.; Du, K. K.; Cai, L.; Lu, J.; Qiu, M. Dynamic Thermal Emission Control Based on Ultrathin Plasmonic Metamaterials Including Phase-Changing Material GST. *Laser Photon. Rev.* **2017**, *11*, 6.
- (83) Qu, Y. R.; Cai, L.; Luo, H.; Lu, J.; Qiu, M.; Li, Q. Tunable Dual-Band Thermal Emitter Consisting of Single-Sized Phase-Changing GST Nanodisks. *Opt. Express* **2018**, *26*, 4279-4287.
- (84) Kats, M. A.; Sharma, D.; Lin, J.; Genevet, P.; Blanchard, R.; Yang, Z.; Qazilbash, M. M.; Basov, D. N.; Ramanathan, S.; Capasso, F. Ultra-Thin Perfect Absorber Employing a Tunable Phase Change Material. *Appl. Phys. Lett.* **2012**, *101*, 221101.
- (85) Rensberg, J.; Zhang, S.; Zhou, Y.; McLeod, A. S.; Schwarz, C.; Goldflam, M.; Liu, M.; Kerbusch, J.; Nawrodt, R.; Ramanathan, S.; Basov, D. N.; Capasso, F.; Ronning, C.; Kats, M. A. Active Optical Metasurfaces Based on Defect-Engineered Phase-Transition Materials. *Nano Lett.* **2016**, *16*, 1050-1055.
- (86) Karg, M.; Pastoriza-Santos, I.; Perez-Juste, J.; Hellweg, T.; Liz-Marzan, L. M. Nanorod-Coated PNIPAM Microgels: Thermoresponsive Optical Properties. *Small* **2007**, *3*, 1222-1229.
- (87) Karg, M.; Hellweg, T. New "Smart" Poly(NIPAM) Microgels and Nanoparticle Microgel Hybrids: Properties and Advances in Characterisation. *Curr. Opin. Colloid Interface Sci.* **2009**, *14*, 438-450.
- (88) Roy, D.; Brooks, W. L. A.; Sumerlin, B. S. New Directions in Thermoresponsive Polymers. *Chem. Soc. Rev.* **2013**, *42*, 7214-7243.
- (89) Scarpa, J. S.; Mueller, D. D.; Klotz, I. M. Slow Hydrogen-deuterium Exchange in a Non- α -Helical Polyamide. *J. Am. Chem. Soc.* **1967**, *89*, 6024-6030.
- (90) Futscher, M. H.; Philipp, M.; Müller-Buschbaum, P.; Schulte, A. The Role of Backbone Hydration of Poly(N-isopropyl acrylamide) Across the Volume Phase Transition Compared to its Monomer. *Sci. Rep.* **2017**, *7*, 17012.
- (91) Wang, C.; Flynn, N. T.; Langer, R. Controlled Structure and Properties of Thermoresponsive Nanoparticle-Hydrogel Composites. *Adv. Mater.* **2004**, *16*, 1074-1079.

- (92) Xu, H.; Xu, J.; Jiang, X.; Zhu, Z.; Rao, J.; Yin, J.; Wu, T.; Liu, H.; Liu, S. Thermosensitive Unimolecular Micelles Surface-Decorated with Gold Nanoparticles of Tunable Spatial Distribution. *Chem. Mater.* **2007**, *19*, 2489-2494.
- (93) Velleman, L.; Scarabelli, L.; Sikdar, D.; Kornyshev, A. A.; Liz-Marzan, L. M.; Edel, J. B. Monitoring Plasmon Coupling and SERS Enhancement through in Situ Nanoparticle Spacing Modulation. *Faraday Discuss.* **2017**, *205*, 67-83.
- (94) Lim, I. I. S.; Ouyang, J.; Luo, J.; Wang, L. Y.; Zhou, S. Q.; Zhong, C. J. Multifunctional Fullerene-Mediated Assembly of Gold Nanoparticles. *Chem. Mat.* **2005**, *17*, 6528-6531.
- (95) Pengo, P.; Pasquato, L.; Scrimin, P. Gold Nanoparticles Protected with Triethyleneglycol-Functionalized Thiolates: Acid-Induced Clustering of the Aggregates and Solvent Dependent Optical Properties. *J. Supramol. Chem.* **2002**, *2*, 305-310.
- (96) Edel, J. B.; Kornyshev, A. A.; Urbakh, M. Self-Assembly of Nanoparticle Arrays for Use as Mirrors, Sensors, and Antennas. *ACS Nano* **2013**, *7*, 9526-9532.
- (97) Velleman, L.; Sikdar, D.; Turek, V. A.; Kucernak, A. R.; Roser, S. J.; Kornyshev, A. A.; Edel, J. B. Tuneable 2d Self-Assembly of Plasmonic Nanoparticles at Liquid|Liquid Interfaces. *Nanoscale* **2016**, *8*, 19229-19241.
- (98) Mayer, K. M.; Hafner, J. H. Localized Surface Plasmon Resonance Sensors. *Chem. Rev.* **2011**, *111*, 3828-3857.
- (99) Gopinath, S. C. B.; Lakshmi Priya, T.; Awazu, K. Colorimetric Detection of Controlled Assembly and Disassembly of Aptamers on Unmodified Gold Nanoparticles. *Biosens. Bioelectron.* **2014**, *51*, 115-123.
- (100) Veneziano, R.; Ratanalert, S.; Zhang, K.; Zhang, F.; Yan, H.; Chiu, W.; Bathe, M. Designer Nanoscale DNA Assemblies Programmed from the Top Down. *Science* **2016**, *352*, 1534-1534.
- (101) He, L.; Musick, M. D.; Nicewarner, S. R.; Salinas, F. G.; Benkovic, S. J.; Natan, M. J.; Keating, C. D. Colloidal Au-Enhanced Surface Plasmon Resonance for Ultrasensitive Detection of DNA Hybridization. *J. Am. Chem. Soc.* **2000**, *122*, 9071-9077.
- (102) Abbas, A.; Linman, M. J.; Cheng, Q. A. New Trends in Instrumental Design for Surface Plasmon Resonance-based Biosensors. *Biosens. Bioelectron.* **2011**, *26*, 1815-1824.
- (103) Shim, T. S.; Estephan, Z. G.; Qian, Z.; Prosser, J. H.; Lee, S. Y.; Chenoweth, D. M.; Lee, D.; Park, S.-J.; Crocker, J. C. Shape Changing Thin Films Powered by DNA Hybridization. *Nat. Nanotechnol.* **2016**, *12*, 41.
- (104) Chou, L. Y. T.; Zagorovsky, K.; Chan, W. C. W. DNA Assembly of Nanoparticle Superstructures for Controlled Biological Delivery and Elimination. *Nat. Nanotechnol.* **2014**, *9*, 148-155.
- (105) Litt, D. B.; Jones, M. R.; Hentschel, M.; Wang, Y.; Yang, S.; Ha, H. D.; Zhang, X.; Alivisatos, A. P. Hybrid Lithographic and DNA-Directed Assembly of a Configurable Plasmonic Metamaterial That Exhibits Electromagnetically Induced Transparency. *Nano Lett.* **2018**, *18*, 859-864.
- (106) Lapine, M.; Shadrivov, I. V.; Powell, D. A.; Kivshar, Y. S. Magnetoelastic Metamaterials. *Nat. Mater.* **2011**, *11*, 30.
- (107) Chen, H. T.; Taylor, A. J.; Yu, N. F. A Review of Metasurfaces: Physics and Applications. *Rep. Prog. Phys.* **2016**, *79*, 40.
- (108) Ou, J.-Y.; Plum, E.; Zhang, J.; Zheludev, N. I. An Electromechanically Reconfigurable Plasmonic Metamaterial Operating in the Near-Infrared. *Nat. Nanotechnol.* **2013**, *8*, 252.
- (109) Hui, Y.; Gomez-Diaz, J. S.; Qian, Z.; Alù, A.; Rinaldi, M. Plasmonic Piezoelectric Nanomechanical Resonator for Spectrally Selective Infrared Sensing. *Nat. Commun.* **2016**, *7*, 11249.
- (110) Hou, Z. L.; Assouar, B. M. Tunable Solid Acoustic Metamaterial with Negative Elastic Modulus. *Appl. Phys. Lett.* **2015**, *106*, 5.
- (111) Park, C.; Seo, S.; Shin, H.; Sarwade, B. D.; Na, J.; Kim, E. Switchable Silver Mirrors with Long Memory Effects. *Chem. Sci.* **2015**, *6*, 596-602.
- (112) Montelongo, Y.; Sikdar, D.; Ma, Y.; McIntosh, A. J. S.; Velleman, L.; Kucernak, Anthony R.; Edel, J. B.; Kornyshev, A. A. Electrotunable Nanoplasmonic Liquid Mirror. *Nat. Mater.* **2017**, *16*, 1127-1135.

- (113) Wilson, W. M.; Stewart, J. W.; Mikkelsen, M. H. Surpassing Single Line Width Active Tuning with Photochromic Molecules Coupled to Plasmonic Nanoantennas. *Nano Lett.* **2018**, *18*, 853-858.
- (114) Ou, J.-Y.; Plum, E.; Zhang, J.; Zheludev, N. I. Giant Nonlinearity of an Optically Reconfigurable Plasmonic Metamaterial. *Adv. Mater.* **2016**, *28*, 729-733.
- (115) Cormier, S.; Ding, T.; Turek, V.; Baumberg, J. J. Actuating Single Nano-Oscillators with Light. *Adv. Opt. Mater.* **2018**, *6*, 1701281.

2. Materials and methods

2.1. NP synthesis and functionalization

Generally speaking, fabrication of NPs, like other nanomaterials, fall into two categories: top-down and bottom-up methods. Lithography, either based on light or electron beam, is one of the most widely used top-down methods.¹ Through masking and etching processes, the unneeded parts of materials are removed from the bulk substrates, leaving well organized NP patterns. Electron beam lithography normally has better resolution than photolithography because the use of electron beam breaks the diffraction limit of light.² Within the resolution limit, the most attractive feature of lithography for fabricating NPs is that people can precisely control the shape, size, distance and distribution of NPs.^{3,4} This gives lithography an unrivalled advantage for constructing NP super lattices, though the cost is generally much higher than bottom-up methods.⁵

On the other hand, bottom-up methods aim to assemble materials into desired structures through physical or chemical approaches. Templating is one of the most ingenious physical methods: using for example array of polystyrene spheres⁶ or even butterfly wings⁷ as the templates, materials are deposited into the gaps and holes of the templates by physical methods such as atomic layer deposition (ALD)⁸ or electro-deposition⁹. Thus it is possible to obtain substrates with the inverse features from the templates.

Chemical reduction in liquid phase is one of the most versatile and low-cost methods of synthesizing noble metal NPs.^{5, 10} The choice of metal sources, reductants, solvents, time, temperature and capping ligands results in different sizes, and shapes of NPs.¹⁰ Brust–Schiffrin method¹¹ and Turkevitch-Frens method¹² are two popular methods for synthesizing nano-spheres. Though a bit delicate, Brust–Schiffrin method can produce very stable and uniform gold clusters with diameters smaller than 10 nm. With the aid of tetraoctylammonium bromide, AuCl_4^- is transferred to toluene from water, then reduced by NaBH_4 and stabilized by alkane-thiols. In Turkevitch-Frens method, sodium citrate is introduced into the boiling HAuCl_4 aqueous solution, acting as reductant and capping ligand. By changing the citrate-gold ratio, the diameter of resultant NPs ranges from 16 nm to 147 nm.¹² The two methods were further optimized and developed for synthesizing NPs with different sizes and shapes.^{13, 14} For example, some surfactants such as CTAB were found to be able to bind to specific crystallographic facets resulting in rod-like NPs with double SPR bands in UV-Vis spectra.^{15, 16}

In this thesis, Turkevitch-Frens method was employed for fabricating 16 nm gold NPs, because of its simplicity and narrow dispersion in sizes. Since the gold source is corrosive, polytetrafluoroethylene (PTFE) spatula and weighing boats were used to handle the powder. To avoid unwanted contamination and

nucleation during synthesis, all the glassware in contact with the solution was cleaned using aqua regia, sodium hydrogen carbonate solution and DI water. The typical fabrication protocol of 16 nm citrate capped gold NPs can be described as follows. A 500 mL 0.01 wt% HAuCl₄ solution was heated to boil on a hot plate with magnetic stirring. Then 10 mL of 1 wt% sodium citrate was quickly pipetted into the boiling solution which was kept for 30 min to allow the reaction to finish. It is within this period of time, the light yellowish HAuCl₄ solution turns into a burgundy red colour of 16 nm NP solution.

Though as a classical capping ligand, citrate sometimes cannot provide sufficient protection against aggregation especially under high electrolyte concentration¹⁷ or cannot provide some key functions for 'smart' optical applications. Luckily, citrate can be easily exchanged by other ligands after NP fabrication. In Chapter 3, to further stabilize NPs and to control the amount of negative charges on NPs, 12-mercaptododecanoic acid (MDDA) was used to displace the citrate. 500 mL 16 nm NP solution prepared through Turkevitch-Frens method was heated to 60 °C, after which 3 mg MDDA was added. After maintaining the temperature for 2 h, the NP solution was allowed to naturally cool to room temperature and stored in a fridge for further use.

In Chapter 4, we intend to explore the SERS responses of NP assemblies. Therefore, larger NPs with better SERS enhancement are desired. However, one problem of the Turkevitch-Frens method is that with the increase of NP diameter, the roundness and uniformity degrade. Therefore 40 nm NPs were fabricated using a seed mediated method proposed by Brown¹⁸. 540 mL water was mixed into 60 mL previously obtained 16 nm NP solution. Followed by the addition of 6 mL 0.2 M NH₂OH·HCl, 5 mL of 1 wt% HAuCl₄ was quickly injected with vigorous stirring. After the reaction finished, 612 µL 10 mM solution of 80% 4-Mercaptobenzoic acid (MBA), 20% MDDA was added into the solution and incubated for 12 hr. Centrifugation of the NPs were performed at 1500 rcf (relative centrifugal force) for 1 h and refilled with DI water.

In Chapter 5, the construction of the thermo-responsive auxetic metasurface requires the functionalization of pNIPAM onto the NPs. To be more specific, after naturally cooling down the 16 nm citrate NP solution, amine terminated pNIPAM (M_n = 2500) was added to achieve a final concentration of 0.01 wt% and was kept for 12 hours. Excess pNIPAM was removed by centrifugation at 6000 rcf for 30 min.

Finally, in Chapter 6, GSH, a ligand that can specifically bind to lead ions was functionalized onto 44 nm gold NPs. 30 mL as prepared citrate functionalized 16 nm gold NPs were mixed with 270 mL MilliQ water and 3 mL 0.2 M NH₂OH solution. Under vigorous magnetic stirring, 2.5 mL 1 % wt HAuCl₄ was added into the solution and allowed to react for 5 min. To functionalise the NPs with GSH, 600 µl 1 M NaOH was injected into 300 mL as prepared citrate functionalized 44 nm gold NPs to improve the stability prior to the

addition of 3 mL 1 mM GSH. GSH was incubated for 6 h to fully functionalise the NP surface. Then the pH of the solution was adjusted to 8 followed by 30 min centrifugation at 1500 rcf to remove the excess free GSH.

Table 2.1 summarises the NPs used in this thesis.

Table 2.1 the diameters and functioning ligands of NPs used in this thesis

Chapters	Diameters (nm)	Ligands
3	16	MDDA
4	40	MBA-MDDA
5	16	pNIPAM
6	44	GSH
7	16	MDDA

2.2. Film deposition

Flat and uniform metallic films are crucial for successful implementation of the SLI systems. TiN/Ag substrates used in Chapter 3 and 4 are fabricated by our collaborators Daniel J. Klemme and Prof. Sang-Hyun Oh from University of Minnesota, Minneapolis, US. There are several reasons for depositing a thin layer of TiN atop of Ag. First, TiN is a stable semiconductor with relatively good conductivity and transparency, which will not impose too much impact on the optical and electrochemical properties of the whole system. In addition, since silver is reactive in terms of chemistry and electrochemistry, TiN acts as a passive layer to isolate silver from the solution. At last, TiN also prevent the drifting negatively charged thiolated molecules from attaching to the silver substrate, making it easier for assembling negatively charged NPs on the substrates. As to the experimental procedure, silicon substrates were firstly stripped of their native oxide layer in a hydrofluoric acid bath. A 2 nm titanium adhesion layer was then evaporated onto the substrate, followed by a 125 nm Ag layer. The sample was then immediately placed in a plasma-enhanced atomic layer deposition (PEALD) system, where 5 or 10 nm of TiN was deposited at a temperature of 270°C. The sample was left to cool in the chamber before exposing it to atmosphere in order to avoid excessive oxidation. Before use, the TiN/Ag substrates were rinsed with acetone, ethanol and DI water.

Au substrates and octanethiol self-assembled monolayer (SAM) used in Chapter 5 was fabricated by us. A 125 nm thick Au film was deposited through sputter coating (Quorum Tech, Q150T) on a silicon wafer with a 10 nm titanium interlayer. The substrates were washed vigorously by acetone, ethanol and DI water before and after the deposition. The substrates were soaked into a 1 wt% octane thiol solution in ethanol

for 1 hour to form a self-assembled monolayer of octane thiol and washed by ethanol and DI water for later use. There are three main reasons for introducing an octane-thiol SAM on the Au substrate. 1. Preventing the NPs and substrate from touching each other. This SAM interlayer provides unique possibilities to study isolated plasmonic coupling between the NP array and the metallic substrates. 2. Gold is vulnerable to contaminants non-specifically absorbing on the surface. This is problematic especially as it is important to precisely control the distance between NP array and the substrate. Octane-thiol SAM passivates the gold substrate and improves overall stability. 3. The SAM prevents NP aggregation and hence helps to ensure the system is reversible. The hydrophobic interactions between the octane-thiol on the substrate and the pNIPAM on the NPs are very helpful to keep the NPs stable and resilient on the gold substrate.

2.3. UV-Vis

Ultraviolet-visible (UV-Vis) spectroscopy is a commonly used technique for qualitatively or quantitatively determining analytes that can absorb lights within ultraviolet to visible range. Provided that the extinction coefficient (ϵ) is known, the routine way of utilizing UV-Vis is to determine the concentration of analytes according to the Beer-Lambert law:

$$A = \lg \frac{I_0}{I} = \epsilon c L \quad 2.1$$

Where A is the absorption, I_0 the incident intensity of light, I the transmitted intensity of light, c the concentration of analyte, L the light path length. For common analytes, the extinction coefficient can be referred from literature or measured from home-made calibration curves. However, for NPs, the determination of concentration through UV-Vis is not straight forward. First, it is relatively hard to obtain a reference since the size and concentration of NP solution could vary from batch to batch. In addition, different size of NPs delivers different extinction coefficient, which makes it harder for building a reliable calibration curve with two variables.

Fortunately, the UV-Vis spectra can provide information about both the concentration and the size of NPs. As mentioned in Chapter 1, the SPR frequency of NPs is closely related to their sizes. By correlating the wavelength of SPR absorption peak to the transmission electron microscopy (TEM) measured NP diameters, W. Haiss et al.¹⁹ fitted an equation to determine the NP diameter by UV-Vis:

$$d = \frac{\ln \left(\frac{\lambda_{SPR} - 512}{6.53} \right)}{0.0216} \quad 2.2$$

After pinning down the size of NPs, the extinction coefficient can be further fitted. The equation for calculating the number density of NPs¹⁹ is:

$$N = \frac{A_{450} \times 10^{14}}{d^2 \left[-0.295 + 1.36 \exp \left(- \left(\frac{d - 96.8}{78.2} \right)^2 \right) \right]} \quad 2.3$$

Where A_{450} is the absorbance value at 450 nm.

Another good application of UV-Vis is the determination of NP aggregation. NPs are prone to agglomeration due to their high surface energy and thus require the functionalization of citrate, thiolated molecules or polymers.²⁰ Nevertheless, when the electrolyte concentration is too high, or the NP solution is too old, or other molecules (wanted or unwanted) bind to the surfaces of NPs, functionalized NPs can still aggregate. As can be seen from **Figure 2.1**, for high quality 16 nm gold NPs, the SPR absorption peak located around 520 nm under monodisperse state red shifts and broadens upon increasing the concentration of NaCl. This is typical for NP aggregation. When NPs aggregate into a larger cluster, the surface plasmon-polaritons of nearby NPs couple with each other as if forming a larger NP. Qualitatively, as shown in Eq. 2.2, when the diameter of the aggregated NP cluster is larger than the single NP, the absorption peak is red shifted.

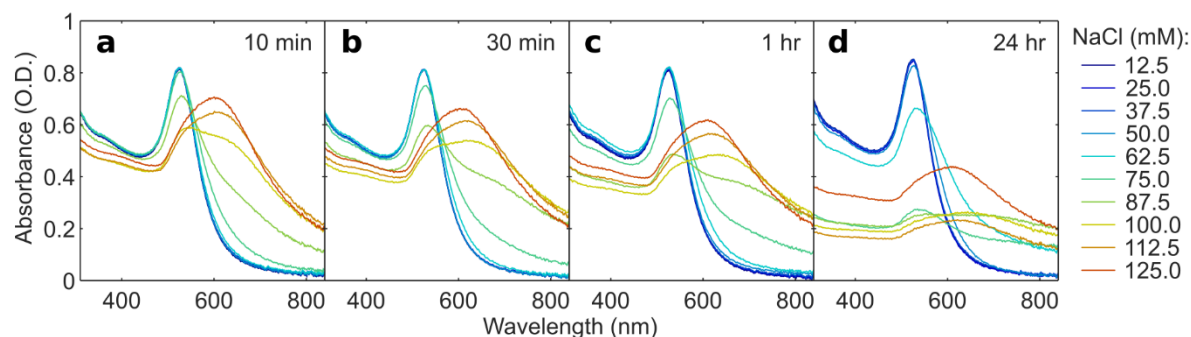


Figure 2.1 Time dependent UV-Vis spectroscopy of 16 nm Au-MDDA NPs at different concentrations of NaCl. Ten concentrations up to 125 mM of NaCl in steps of 12.5 mM were followed over 24 hours. The spectroscopy was performed at 10 min, 30 min, 1 hr and 24 h from (a) to (d) respectively. Reprinted with permission from Ref.¹⁷

2.4. Electron microscopy

As mentioned in the last section, though UV-Vis can estimate the diameters of NPs, its accuracy is reduced when the diameter is less than 35 nm.¹⁹ Therefore, the designated 16 nm NPs require a more direct approach to check their size, shape and distribution. Scanning electron microscopy (SEM) and transmission electron microscopy (TEM) are two powerful techniques for imaging nanomaterials. Instead of using light as the media, attenuated electron beams are emitted from the electron guns and directed to the samples by

electromagnetic lenses.²¹ For SEM, secondary and backscattered electrons are collected near the surface of the samples, while the TEM forms the images from the transmitted electron beams.²¹

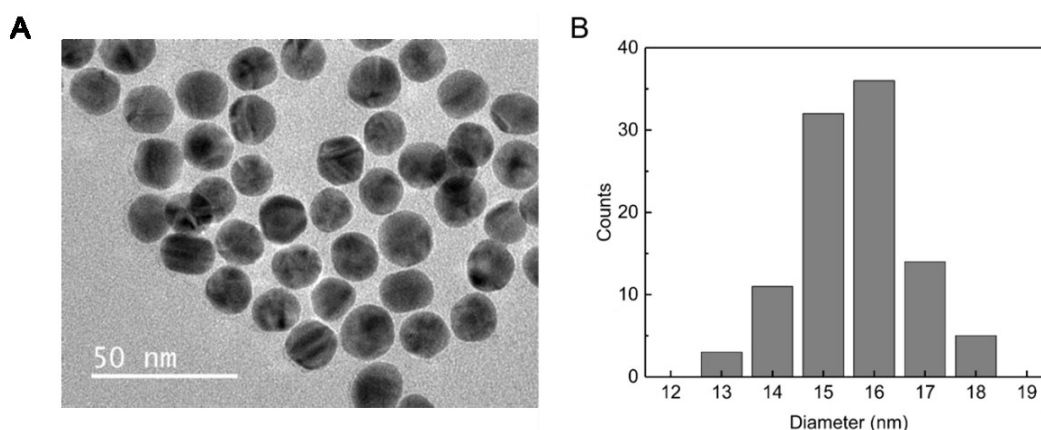


Figure 2.2 A. TEM image of as prepared 16 ± 1 nm NPs. B. Statistics of the measured diameters of NPs. Reprinted with permission from Ref.²²

In our particular scenario, TEM is used to measure the diameters of our 16 ± 1 nm (**Figure 2.2**) and 40 ± 3 nm (**Figure 2.3**) NPs. The statistics shown beside the TEM images illustrate that the 16 nm NPs have smaller standard deviation compared with the 40 nm NPs. For TEM sample preparation, 1 mL as-prepared NPs solution is first centrifuged to remove the ligands and electrolytes. After redispersion in water, 10 μ L NP solution was pipetted onto a copper mesh covered by a thin carbon membrane. The droplet on the mesh was allowed to evaporate naturally at room temperature for further measurements.

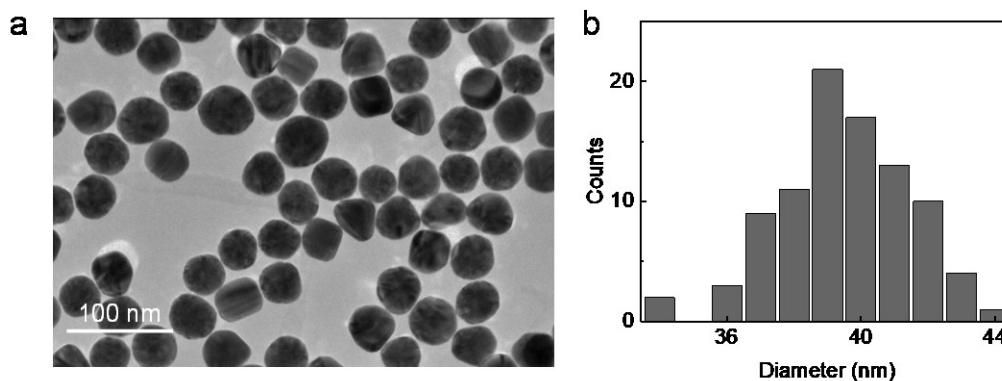


Figure 2.3 (a) Transmission electro-microscope (TEM) image of 40 ± 3 nm Au nanoparticles (NPs). (b) Statistics of NP diameter measured from TEM images.

To examine the NPs directly on the substrates used in this thesis, SEM had to be used as TEM is not easily applicable when our 125 nm thick metallic substrates can shield the transmitting electron beam.²¹ As to the SEM sample preparation, the NPs on substrate deposited overnight were carefully removed from the NP-solution and quickly dried by a nitrogen gas line. No further coating was applied before the SEM measurement, due to the inherent good conductivity of the samples.

However, one should keep in mind that the SEM images are performed on samples that are removed from solution and dried, and measured in high vacuum. When the samples are taken out from the solution, the functionalizing ligands lose their charges. Hence the repulsion between them is suppressed, and since the nanoparticles are not anchored at the interface, they move closer to each other and form islands. This opens up parts of the substrate surface free from nanoparticles. Therefore, this rearrangement and distribution of NPs renders the direct comparison between the wet optical signal and dried SEM image not meaningful. Nevertheless, the SEM images are still useful to qualitatively compare the density of NPs on substrates and to confirm no major 3D agglomeration formed.

2.5. Reflectance measurement

Reflectance is both convenient and informative measurement technique to determine the plasmonic coupling in our systems and was used in all aspects of this thesis. In different chapters, this versatile measurement is normally coupled with other measurement techniques, such as Raman, electrochemistry measurements or thermal regulation. The general experimental setup of reflectance measurement is shown in **Figure 2.4**.

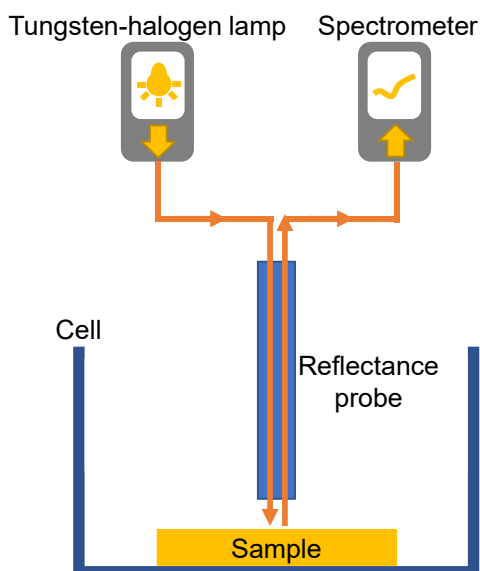


Figure 2.4 Experimental setup for reflectance measurement.

The white light emitted by a tungsten halogen lamp (Ocean Optics) was transmitted through a multimode fibre in a reflectance probe (Ocean Optics, focal length 2 mm), vertically hit the sample either at SLI or LLI. After the interaction between the incident light and the samples, the far-field reflected light was collected by the same probe and transmitted to an Andor 163 spectrograph fitted with an iDus charge-coupled device.

During the measurements, the dark background was firstly taken when the light source was off, and any stray light was shielded by a black curtain. Then, the light source was turned on with suitable intensity while a silver mirror (Thorlabs) was inserted under the probe as a positive reference. After focusing the light beam through aligning the probe in x-y-z direction, the acquisition time and averaging number was set in the software controlling the spectrometer. Then a positive reference of 100 % reflectance was taken. By placing the probe to the sample, and re-focus the beam, the reflectance spectra for designated samples can be obtained.

2.6. Effective medium theory

The assembly of NPs at interfaces of two different media has drawn interest both experimentally and theoretically. Though all kinds of experimental methods, either bottom-up or top-down, have been demonstrated, the theoretical study of the optical response of such assembly is still valuable for understanding the physical phenomena and for giving directions to future experimental optimisations. A light weight ‘effective medium theory (EMT)’ was developed to give fast and accurate calculations for the optical responses of the NP assembly at liquid-liquid interfaces (LLI) and solid-solid interfaces (SLI),^{23, 24} systematically tested against full-wave (COMSOL Multiphysics) simulations.

Over the following chapters, EMT will be used to help interpret and understand the experimental optical data. Here, as an example, the EMT is applied to a ‘five-layer’ SLI system to briefly introduce this versatile theoretical framework.²² For a given lateral structure of the NP-array, its contribution to the system optical response, in this theory, can be described as that of a pseudo-film. The frequency-dependent dielectric polarizability of that ‘film’ is expressed through the optical polarizability of individual NPs which is described by a dipolar approximation, and most importantly, with account for interactions of localized plasmons between NPs, with the substrate, and the surrounding medium.

In the current case (**Figure 2.5**), light interacts with the electrolyte solution (medium 1), nanoparticle array (medium 2), medium 3 located between the array and interface (can be also electrolyte or a layer of ligands, acting as ‘spacer’ layer), and the conductive film (medium 4) coating the semi-infinite electrode (medium 5). The detailed structure is sketched in **Figure 2.5**, where d , h_s and h_f are the thicknesses of the layer representing the NP array, the spacer, and the coating film, respectively; a is the centre-to-centre separation between NPs. For each layer, dielectric constants are labelled as $\epsilon_1, \epsilon_2, \epsilon_3 \equiv \epsilon_1, \epsilon_4$ and ϵ_5 . By doing so, the NP surrounding medium [layers 1 and 3] were considered to be frequency-independent ($\epsilon_1 \equiv \epsilon_3$). On the other hand, the Au NP layer (layer 2) and the substrate layers (layers 4 and 5) were characterised by frequency-dependent dielectric constants. Then the effective polarizability and permittivity of the pseudo-

film of the NP array are calculated, containing contributions from both the interactions with other NPs in the array and the images of the effective dipoles emerging due to excitation of localized plasmons. That completes the information needed for the subsequent application of the Fresnel's theory to the multi-layered system, to calculate the reflectance spectra.²⁵

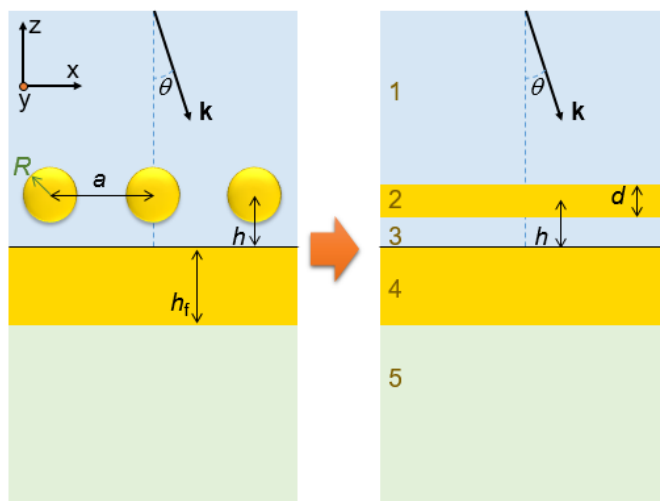


Figure 2.5 Schematic representation of a nanoparticle ‘mirror-on-mirror’ system and its corresponding 5-layer stack model, introduced in Ref.²²

To check the validity of the EMT in the NPs on metallic substrate system, the coverage calculated from EMT fittings of the optical spectra was compared with that calculated from SEM images of the dried samples.

Figure 2.6A shows the experimental (dried samples) and theoretically-fitted spectra of the changes in reflectance at different NaCl concentrations, during the assembly process (for details, please see **Chapter 3**). Currently we just need to know that the different NaCl concentration induce different density of NPs on the substrates. The coverage was calculated in the following way. In the theory²⁴, first, NP-layers were modelled as a 1-nm-thick fictitious continuous film, with permittivity calculated from EMT that considers the changes in interparticle spacings. Then, it is assumed that ‘ f ’ fraction of the whole surface is composed of this effective film, while the rest $1-f$ fraction denotes bare interface. By fitting experimental reflectance spectra, therefore, the values of these coverage fractions for the three concentrations (20, 40, 60 mM NaCl) were extracted as 7%, 29% and 44%, respectively.

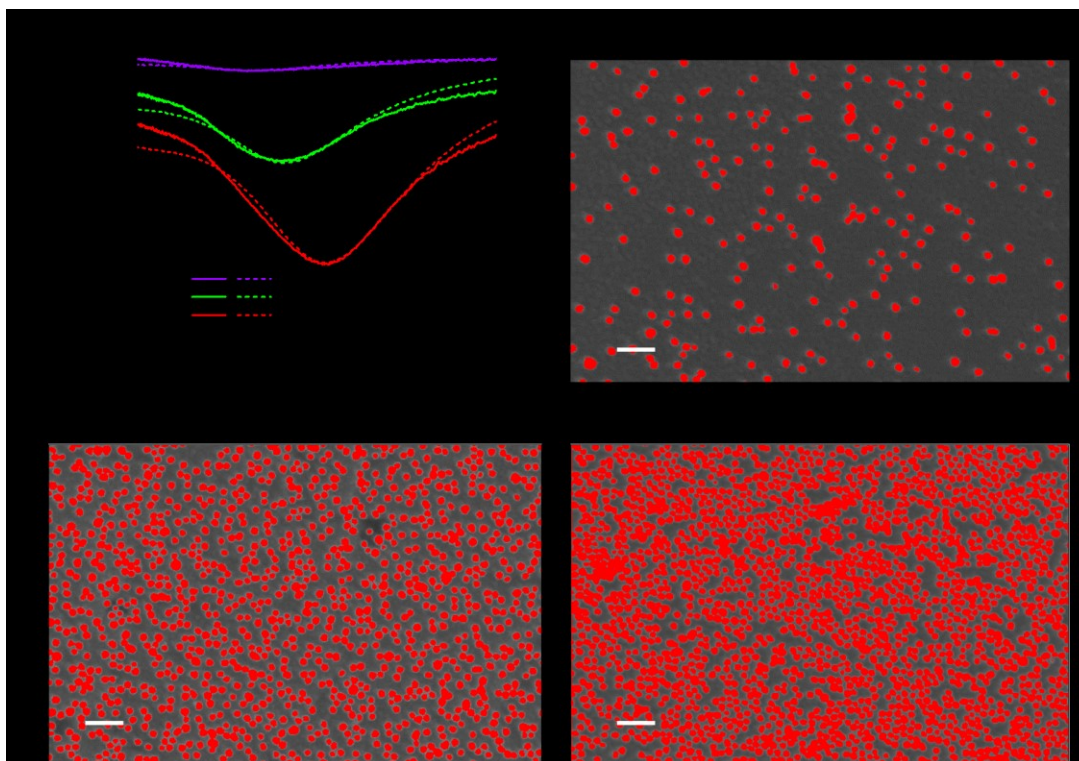


Figure 2.6 Comparing the NP coverages calculated from SEM and EMT. A. Experimental (solid) and theoretically fitted (dashed) curves of the change in reflectance of NPs/TiN/Ag for different NaCl concentrations after drying, with respect to the pristine TiN/Ag substrate. B, C and D are the SEM images for different dried NPs/TiN/Ag samples with red- pseudo-coloured NPs for calculating NP coverages, scale bar 100 nm.

The NP surface coverage values calculated from SEM images are shown in **Figures 2.6B, C and D**. The dots highlighted in red show the areas covered by NPs. By counting the number of pixels of all the red dots and dividing that by the total pixels of the whole images, the surface coverage was calculated to be 6%, 28% and 47% for 20, 40 and 60 mM dried samples respectively.

The excellent agreement between the surface coverage estimates made from SEM images and from analysing the reflection spectra gives additional support to the validity of the EMT in the treatment of our samples.

2.7. Raman spectroscopy and SERS EF calculation

2.7.1. SERS measurement

The basic setup of Raman microscope is shown in **Figure 2.7**. Briefly, the beam from a 632.8 nm HeNe laser (HRP170, Thorlabs, 21 mW) was directed by two silver mirror (Thorlabs) passing through a set of neutral density filters to control the final measured laser power from the stage as 0.81 mW. Two bandpass filters (Laser 2000, LL01-633-12.5) were used to clean up the laser beam. Then the beam was directed to an Olympus 20x, NA 0.45 objective (LCPLFLN-LCD) by A dichroic filter (LPD01-633RU-25x36x2.0,

Semrock) and finally reached the sample. The resultant Raman signal passed through the same objective and dichroic filter and filtered by a long pass Raman filter (LP02-633RU-25, Semrock) before the signal being collected by a spectrograph (Shamrock SR-303i, Andor) and an electron-multiplying charge-coupled device camera (EMCCD, Newton DU970BV, Andor).

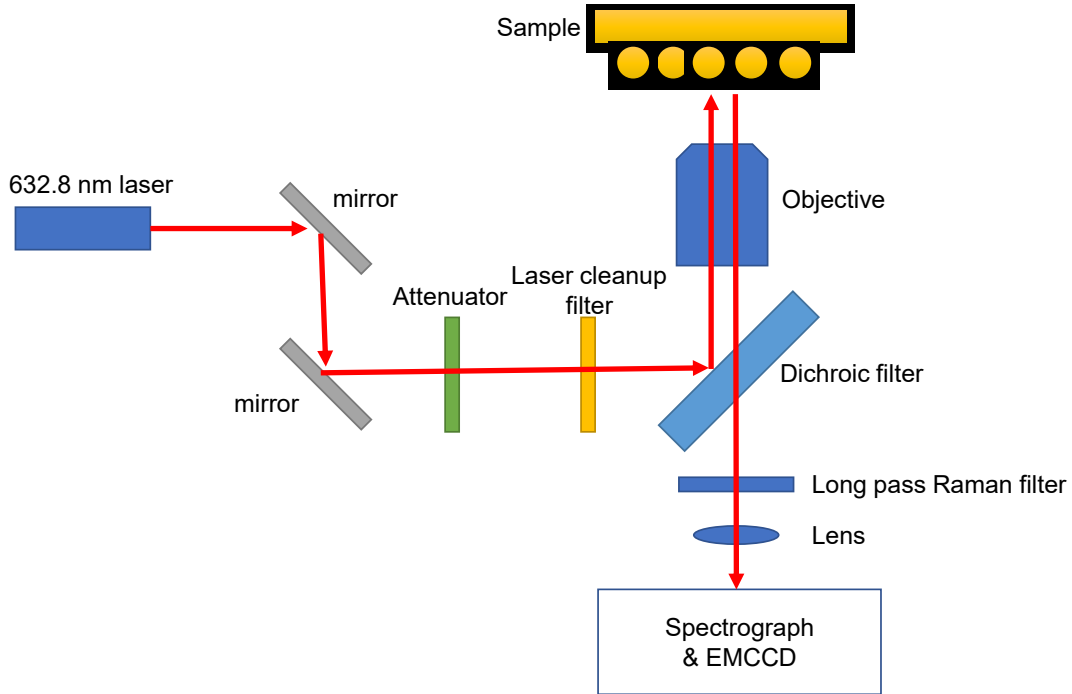


Figure 2.7 Scheme of the light path of the Raman microscope.

2.7.2. Calculation of experimental SERS EF

The experimental EF was calculated according to Eq. 1.5²⁶. The intensity of SERS and Raman signals were directly measured from experiments. The numbers of molecules generating SERS and Raman signals, noted as N_{SERS} and N_{RS} respectively, need further calculation. Since the surface area of the substrates is the same with either SERS or Raman and will be cancelled in EF equation, 1 cm^2 will be used for ease of calculation.

$N_{\text{RS}} = m \times N_A / M_{\text{MBA}}$, m is the mass of MBA solid on 1 cm^2 substrate, N_A the Avogadro constant, M_{MBA} the molecular weight of MBA.

$$N_{\text{SERS}} = N_{\text{NP}} \times S_{\text{NP}} \times \sigma_{\text{MBA-NP}}$$

N_{NP} is the number of NPs on 1 cm^2 : $N_{\text{NP}} = 1/S_{\text{NP-lattice}} = 1/(\sin 60^\circ \times a^2)$, $S_{\text{NP-lattice}}$ is the hexagonal NP array lattice area, a is the interparticle distance calculated from EMT theory.

S_{NP} is the surface area of single NP: $S_{\text{NP}} = 4\pi r^2$

$\sigma_{\text{MBA-NP}}$ is the MBA density on NP surface, which is taken from previous research²⁷.

2.7.3. Calculation of theoretical SERS EF

Numerical simulation of the near-field distribution patterns of the Au NP assembly on TiN/Ag substrate provided theoretical estimates of the SERS EFs, calculated as $\max(|\mathbf{E}/\mathbf{E}_0|^4)$, where \mathbf{E}/\mathbf{E}_0 is the local electric field enhancement factor at the wavelength of the reflectance dip. The full-wave simulations were conducted using the RF module of COMSOL Multiphysics[®], a commercially available finite-element-method software. In the simulation model, perfectly spherical Au nanospheres were arranged in a hexagonal lattice on top of a TiN/Ag-substrate film of the thicknesses specified in the experiments. A unit cell was designed, which extended in both lateral dimensions using periodic boundary conditions to emulate a NP monolayer assembled on the TiN/Ag substrate with large lateral dimensions. Frequency domain solver was deployed for the simulation studies with extremely small meshing, where the maximum and the minimum mesh element size was chosen to be $\lambda/10$ (where λ is the wavelength of light in that medium) and 1.5 nm, respectively. Such dense meshing incorporates fine structural details of the system in the numerical simulations and hence, allows to make a good estimation of the SERS EFs.

2.8. Electrochemical setup and measurement

2.8.1. Electrochemical cell

The electrochemical cell contains electrolyte solution, the samples and all the electrodes connected to the potentiostat, **Figure 2.8**. A substrate was inserted into a polytetrafluoroethylene (PTFE) holder which connected the substrate with a platinum wire leading to the working electrode. Two other holes on the holder were to accommodate Ag/AgCl reference electrode and platinum counter electrode, to constitute a three-electrode system connecting to the Gamry potentiostat.

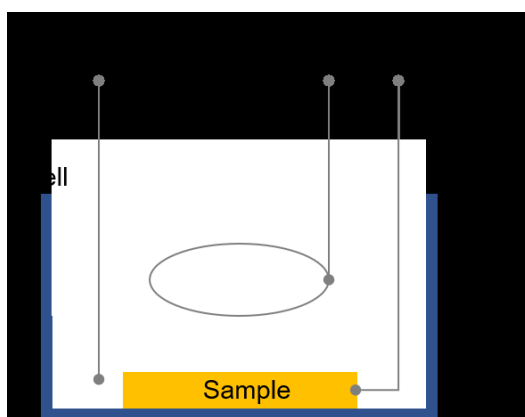


Figure 2.8 Scheme of the electrochemistry cell containing a three-electrode system.

2.8.2. Capacitance measurement

Before performing any electrochemical measurements, all the platinum wires were ultrasonically cleaned in a water bath and washed using acetone, ethanol, and DI water. The Ag/AgCl reference electrodes were

prepared by oxidizing the 0.25 mm diameter Ag wire in saturated KCl solution under 2.0 V bias for 60 s in a two-electrode system.

The capacitance as a function of potential bias was obtained by fitting the impedance data to the equivalent circuit of **Figure 2.9** for each value of the bias voltage. It consists of an interface capacitance C_I (the electrical double layer on the solution side and the space charge capacitance in the solid side) and a leakage resistance R_I (reflecting a possibility of ion transfer across the interface) in parallel, and a series resistance R_S (the ion transport bulk solution resistance).

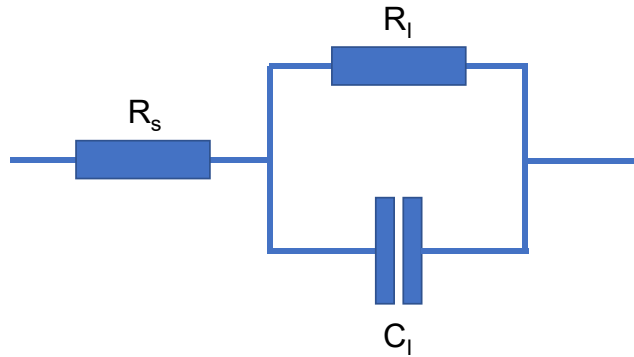


Figure 2.9 Equivalent circuit utilized in the analysis of impedances. The circuit consist of a connection in parallel – capacitance and a bypass ion transfer resistance at the interface, C_I and R_I , and in-series bulk ion transport resistance, R_S .

The complex impedance corresponding to the equivalent circuit in **Figure 2.9** is:

$$Z' + iZ'' = R_S + \frac{1}{i\omega C + 1/R_I} \quad 2.4$$

where ω is the angular frequency. Hence, the capacitance can be retrieved from the experimental data:

$$C = -\frac{Z''}{\omega[(Z' - R_S)^2 + Z''^2]} \quad 2.5$$

For our experimental configuration, it was found that R_S of the used solution was small compared to the contribution of R_I and C_I , and hence, set to zero for the calculation.

The measurement of capacitance was performed with a Gamry potentiostat with a three-electrode configuration as described in a previous section. The experiment involved polarisation of the interface at different applied potentials with an oscillation of 1 mV_{rms} at 1, 10, 100 Hz. The modulus and phase of the current response were converted to a complex impedance through Euler's formula, and R_I and C_I were extracted using Eq. 2.4 and 2.5.

2.9. References

- (1) Guo, Z.; Tan, L., *Fundamentals and Applications of Nanomaterials*. Artech House: Boston, 2009; pp 173-174.
- (2) Okazaki, S. High Resolution Optical Lithography or High Throughput Electron Beam Lithography: The Technical Struggle from the Micro to the Nano-fabrication Evolution. *Microelectron. Eng.* **2015**, *133*, 23-35.
- (3) Litt, D. B.; Jones, M. R.; Hentschel, M.; Wang, Y.; Yang, S.; Ha, H. D.; Zhang, X.; Alivisatos, A. P. Hybrid Lithographic and DNA-Directed Assembly of a Configurable Plasmonic Metamaterial That Exhibits Electromagnetically Induced Transparency. *Nano Lett.* **2018**, *18*, 859-864.
- (4) Donthu, S.; Pan, Z. X.; Myers, B.; Shekhawat, G.; Wu, N. G.; Dravid, V. Facile Scheme for Fabricating Solid-state Nanostructures Using E-beam Lithography and Solution Precursors. *Nano Lett.* **2005**, *5*, 1710-1715.
- (5) Fan, M. K.; Andrade, G. F. S.; Brolo, A. G. A review on the fabrication of substrates for surface enhanced Raman spectroscopy and their applications in analytical chemistry. *Anal. Chim. Acta* **2011**, *693*, 7-25.
- (6) Zhang, X. L.; Dai, Z. G.; Zhang, X. G.; Dong, S. L.; Wu, W.; Yang, S. K.; Xiao, X. H.; Jiang, C. Z. Recent Progress in the Fabrication of SERS Substrates Based on the Arrays of Polystyrene Nanospheres. *Sci. China-Phys. Mech. Astron.* **2016**, *59*, 126801.
- (7) Huang, J. Y.; Wang, X. D.; Wang, Z. L. Controlled Replication of Butterfly Wings for Achieving Tunable Photonic Properties. *Nano Lett.* **2006**, *6*, 2325-2331.
- (8) Liu, M. N.; Li, X. L.; Karuturi, S. K.; Tok, A. I. Y.; Fan, H. J. Atomic Layer Deposition for Nanofabrication and Interface Engineering. *Nanoscale* **2012**, *4*, 1522-1528.
- (9) Kempa, T. J.; Bediako, D. K.; Kim, S. K.; Park, H. G.; Nocera, D. G. High-Throughput Patterning of Photonic Structures with Tunable Periodicity. *Proc. Natl. Acad. Sci. U. S. A.* **2015**, *112*, 5309-5313.
- (10) Lu, X. M.; Rycenga, M.; Skrabalak, S. E.; Wiley, B.; Xia, Y. N., Chemical Synthesis of Novel Plasmonic Nanoparticles. In *Annual Review of Physical Chemistry*, Annual Reviews: Palo Alto, 2009; Vol. 60, pp 167-192.
- (11) Brust, M.; Walker, M.; Bethell, D.; Schiffrin, D. J.; Whyman, R. Synthesis of Thiol-Derivatised Gold Nanoparticles in a Two-Phase Liquid-Liquid System. *Chem. Commun.* **1994**, 801-802.
- (12) Frens, G. Controlled Nucleation for the Regulation of the Particle Size in Monodisperse Gold Suspensions. *Nature* **1973**, *241*, 20-22.
- (13) Daniel, M. C.; Astruc, D. Gold Nanoparticles: Assembly, Supramolecular Chemistry, Quantum-Size-Related Properties, and Applications Toward Biology, Catalysis, and Nanotechnology. *Chem. Rev.* **2004**, *104*, 293-346.
- (14) Murphy, C. J.; San, T. K.; Gole, A. M.; Orendorff, C. J.; Gao, J. X.; Gou, L.; Hunyadi, S. E.; Li, T. Anisotropic Metal Nanoparticles: Synthesis, Assembly, and Optical Applications. *J. Phys. Chem. B* **2005**, *109*, 13857-13870.
- (15) Chen, H. J.; Shao, L.; Li, Q.; Wang, J. F. Gold Nanorods and Their Plasmonic Properties. *Chem. Soc. Rev.* **2013**, *42*, 2679-2724.
- (16) Hu, M.; Chen, J. Y.; Li, Z. Y.; Au, L.; Hartland, G. V.; Li, X. D.; Marquez, M.; Xia, Y. N. Gold Nanostructures: Engineering Their Plasmonic Properties for Biomedical Applications. *Chem. Soc. Rev.* **2006**, *35*, 1084-1094.
- (17) Montelongo, Y.; Sikdar, D.; Ma, Y.; McIntosh, A. J. S.; Velleman, L.; Kucernak, Anthony R.; Ediel, J. B.; Kornyshev, A. A. Electrotunable Nanoplasmonic Liquid Mirror. *Nat. Mater.* **2017**, *16*, 1127-1135.
- (18) Brown, K. R.; Walter, D. G.; Natan, M. J. Seeding of Colloidal Au Nanoparticle Solutions. 2. Improved Control of Particle Size and Shape. *Chem. Mat.* **2000**, *12*, 306-313.
- (19) Haiss, W.; Thanh, N. T. K.; Aveyard, J.; Fernig, D. G. Determination of Size and Concentration of Gold Nanoparticles from UV-Vis Spectra. *Anal. Chem.* **2007**, *79*, 4215-4221.

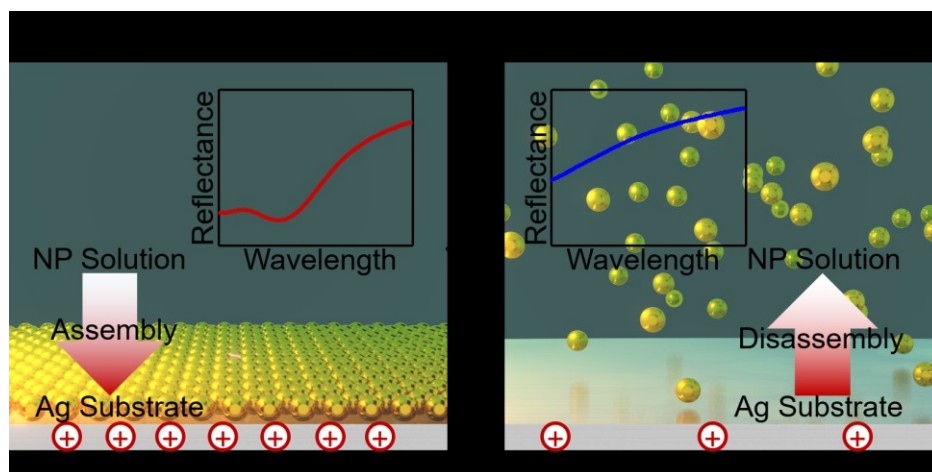
- (20) Saha, K.; Agasti, S. S.; Kim, C.; Li, X.; Rotello, V. M. Gold Nanoparticles in Chemical and Biological Sensing. *Chem. Rev.* **2012**, *112*, 2739-2779.
- (21) Egerton, R. F., *Physical Principles of Electron Microscopy : An Introduction to TEM, SEM, and AEM*. SPRINGER: New York, 2018; pp 9-19.
- (22) Ma, Y.; Zagar, C.; Klemme, D. J.; Sikdar, D.; Velleman, L.; Montelongo, Y.; Oh, S.-H.; Kucernak, A. R.; Edel, J. B.; Kornyshev, A. A. A Tunable Nanoplasmonic Mirror at an Electrochemical Interface. *ACS Photonics* **2018**, *5*, 4604-4616.
- (23) Kornyshev, A. A.; Marinescu, M.; Paget, J.; Urbakh, M. Reflection of Light by Metal Nanoparticles at Electrodes. *Phys. Chem. Chem. Phys.* **2012**, *14*, 1850-1859.
- (24) Sikdar, D.; Hasan, S. B.; Urbakh, M.; Edel, J. B.; Kornyshev, A. A. Unravelling the Optical Responses of Nanoplasmonic Mirror-on-Mirror Metamaterials. *Phys. Chem. Chem. Phys.* **2016**, *18*, 20486-20498.
- (25) Belloni, J.; Mostafavi, M.; Remita, H.; Marignier, J.-L.; Marie-Odile Delcourt, a. Radiation-induced Synthesis of Mono- and Multi-Metallic Clusters and Nanocolloids. *New J. Chem.* **1998**, *22*, 1239-1255.
- (26) Le Ru, E. C.; Etchegoin, P. G., *Principles of Surface-Enhanced Raman Spectroscopy : and Related Plasmonic Effects*. Elsevier: Amsterdam; Heidelberg, 2011; pp 29-297.
- (27) Velleman, L.; Scarabelli, L.; Sikdar, D.; Kornyshev, A. A.; Liz-Marzan, L. M.; Edel, J. B. Monitoring Plasmon Coupling and SERS Enhancement through in Situ Nanoparticle Spacing Modulation. *Faraday Discuss.* **2017**, *205*, 67-83.

3. Electric potential controlled switchable reflector at solid-liquid interface

3.1. Abstract

Designing tunable optical metamaterials is one of the great challenges in photonics. Strategies for reversible tuning of nano-engineered devices are currently being sought through electromagnetic or piezo effects. For example, bottom-up self-assembly of nanoparticles at solid | liquid or liquid | liquid interfaces can be used to tune optical responses by varying their structure either chemically or through applied voltage. In this chapter, we report on a fully reversible tunable-colour mirror based on a TiN-coated Ag substrate immersed in an aqueous solution of negatively charged Au NPs. Switching electrode polarization is shown to be able to fully control the assembly/disassembly of NPs at the electrode/electrolyte interface within a 0.6 V-wide electrochemical window. The plasmon coupling between the adsorbed NP array and the electrode at high positive potentials produces a dip in the optical reflectance spectrum, creating the ‘absorber’ state. Desorption of NPs at low potentials eliminates the dip, returning the system to the reflective ‘mirror’ state. The intensity and wavelength of the dip can be finely-tuned through electrode-potential and electrolyte concentration. The excellent match between the experimental data and the theory of optical response for such systems allows us to extract valuable information on equilibrium and kinetic properties of NP-assembly/disassembly. Together with modelling of the latter, this study promotes optimisation of such systems for building electrotunable reflector-devices.

Please note that the theoretical fittings for reflectance spectra and interparticle distances are contributed by Cristian Zagar and Debabrata Sikdar. The theoretical adsorption kinetics are contributed by Cristian Zagar. The major parts of this chapter were published in Ref.¹



3.2. Introduction

Metamaterials based on periodic subwavelength structures possess exceptional optical properties for manipulating light–matter interactions.²⁻⁶ For instance, invisibility cloaks^{7, 8}, super lenses⁹⁻¹¹, colour display^{12, 13} and nanoantenna for solar energy¹⁴⁻¹⁷ have demonstrated the “programmable” nature of metamaterials with numerous promising applications.¹⁸⁻²⁰ The most extensively studied ones have been the strongly coupled plasmonic systems exhibiting exotic dielectric and magnetic properties.²¹⁻²³

There is currently a strong demand for *in situ* tunability of the optical properties of such systems.^{20, 22, 24, 25} For normally static architectures built by conventional lithography², mechanical²⁵⁻²⁷ and thermal²⁸ effects that induce physical deformation of the materials are already widely used to tune the output without need for major reconstruction of the topology. Alternatively, bottom-up methods, based on self-assembly of nanoscale building blocks, can be used for *in situ* generation of structures and the tailoring of their optical signals.²⁹⁻³⁸

Systems composed of NPs deposited on metallic substrates (NPoMS), where NPs and substrates are electromagnetically coupled, have been shown to be tailorable by varying the component materials, shape and size of NPs and the spacing between NPs themselves and between NPs and the substrate.³⁹⁻⁴³ Such systems have been widely exploited in sensing^{44, 45}, optical nonlinearity⁴⁶, nanoantenna⁴⁷ and SERS⁴⁸. However, one of the most challenging tasks is to be able to reversibly change the structure and tailor the properties of these systems in real-time.^{24, 49, 50}

Several steps have been taken in this direction, including structures wherein an aluminium substrate was coupled with gold NPs.⁵¹ Aluminium being naturally reactive, the light scattering signal from such an interface was continuously tuned through the oxidation of aluminium. An alternative is to tether NPs on metallic substrates in a liquid environment. For tethered cuboid NPs on transparent electrodes, theory has estimated that the reflection spectrum can be visibly affected by the orientation of the cuboids when a voltage is applied to the electrode.⁵² Earlier, the Smith group had successfully anchored gold NPs onto a gold substrates through the linkage of a charged polymer interlayer.⁵³ By applying different electrode potentials on the gold substrates, reversible tuning of local plasmonic coupling was achieved. Furthermore, Di Martino *et al.* have shown a continuous adjustment of SERS signals upon variation of potential using a gold electrode coated with a SAM of thiolated molecules onto which gold NPs were placed.⁵⁴ However, since the NPs are attached to the substrate, the flexibility of the rearrangement of these structures is somewhat restrained, which limits the extent of optical tunability.

Recently, our group reported on the creation of an electro-tunable nanoplasmonic liquid mirror based on NP assembly at an interface of two immiscible electrolytic solutions (ITIES).⁵⁵ Within the potential window at which ions do not cross the interface, oppositely charged electrical double layers form on both sides of the LLI. When the aqueous phase is polarized negatively relative to the organic phase, the energy well for negatively charged NPs at the interface deepens, facilitating the formation of a dense array of NPs at the interface. This array provides substantial reflection of the incident light. On the other hand, polarizing the aqueous phase positively destroys the well, pushing NPs back to the aqueous bulk, switching off the nanoplasmonic liquid mirror. That work has proved that NPs can be reversibly attracted to or repelled from a polarized interface.

This chapter shows that voltage-controlled assembly/disassembly of NP arrays can be achieved also at a ‘classical’ electrochemical electrode | electrolyte interface. But the effect of this manipulation is entirely different. In the NPoMS system under study, by changing electrode polarization, the outputs between ‘absorber’ and ‘mirror’ states can be reversibly tuned.

The coupling between dissipating localised plasmons of adsorbed gold NPs and surface plasmons on the metallic electrode contributes to absorption of incident light.⁵⁶ The absorption intensity, the wavelength at its maximum, and, to a lesser extent, the breadth of absorption band – all depend on the size of NPs and the density of NP arrays. For a given size of NP, this absorption causes a dip in the reflectance spectrum. It deepens with densification of the NP array, and the wavelength of the reflection minimum moves towards the red. The state with the quenched reflection will hereafter be called the ‘absorber’ state, as compared to the ‘mirror’ state of the bare substrate.

Specifically, the switchable device presented below is based on a silver electrode covered by thin protective TiN film, accommodated in an electrochemical cell composed of aqueous NaCl electrolyte and dispersed gold NPs. Due to a large negative charge on the NPs, an energy well trapping NPs at the interface is formed when the TiN/Ag substrate is positively polarized. With careful control of the NaCl concentration in the NP solution, which provides screening of electrostatic interactions, the average distance between the neighbouring NPs and thereby the overall density of the array of NPs on the TiN/Ag surface can be tailored. To switch the device from the ‘absorber’ back to its ‘mirror’ state, the positive polarization of the TiN/Ag electrode needs to be reduced. This will make the energy well for NPs at SLI shallower or even completely eliminated, thus facilitating desorption of NPs. This process is fully reversible within a 0.6 V wide electrochemical window.

Noteworthy, the coverage of NPs on the electrode can be estimated through comparing the variation of experimentally measured reflectance spectra with theoretical ones, in which the main input parameter is the average distance between the assembled NPs.⁵⁷

As compared with previous systems where dried or tethered NPs on metallic substrates were used, ours has numerous advantages: (i) it is based on controlled self-assembly of NPs; (ii) real-time tailoring of interparticle distances can tune the reflectance spectrum, including the reversible turning on-and-off of the ‘absorber’/‘mirror’ states; (iii) the homogeneous distribution of electric field on the planar electrode substrate provides a convenient up-scaling route for macroscale applications.

3.3. Experimental system and theoretical framework

3.3.1. Electrochemical-optical cell.

The substrate for the solid | liquid interface was made from 10.0 ± 0.2 nm thick TiN deposited via atomic layer deposition on 125 nm thick Ag, **Figure 3.1a**. Ag surfaces are ideal reflectors of visible light, widely used in a variety of optical applications. However, when in contact with aqueous solutions, Ag is vulnerable to oxidation. A thin film of TiN was therefore deposited on top of the Ag surface to minimize corrosion. Importantly, this TiN film is thin enough to provide good transparency and electronic conduction.⁵⁸⁻⁶⁰ The TiN/Ag substrate with the PTFE holder was interfaced into an electrochemical cell with aqueous electrolyte and used as the working electrode, **Figure 3.1b**. The cell also accommodated a reference and a counter electrode, along with a vertically aligned fibre coupled optical probe for focusing and collecting light.

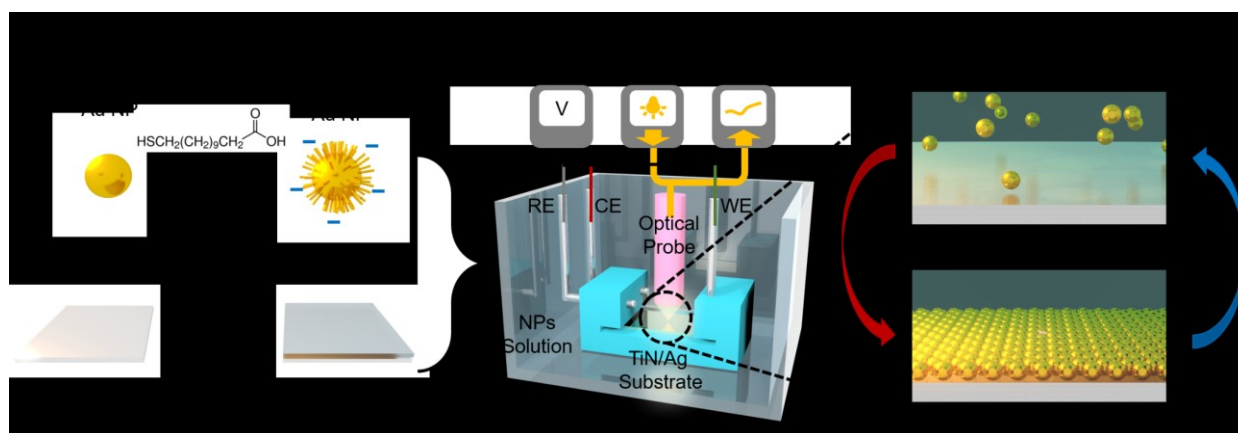


Figure 3.1 Principles of electro-switchable ‘mirror’/‘absorber’. (a) Functionalization of Au NPs and coating of the silver substrate. (b) Three-electrode electrochemical-optical cell, including TiN/Ag substrate (in a PTFE holder) as the working electrode, Ag/AgCl and Pt serving as reference and counter electrodes, respectively, and the optical probe focused vertically on the substrate to collect the reflectance signal at normal incidence. (c) Switching between ‘absorber’ and ‘mirror’ states via assembling or disassembling NPs on TiN/Ag.

By biasing the working electrode, it was possible to reversibly control assembly and disassembly of 16 ± 1 nm gold NPs, introduced in the aqueous phase, to and from the TiN/Ag substrate. This has the net effect of switching the device between ‘absorber’ and ‘mirror’ states, **Figure 3.1c**. The Au NPs were capped with MDDA. The as-made citrate capped NPs are prone to aggregation at high ionic strengths.⁶¹ Hence, to minimize aggregation, the ligand was exchanged with MDDA which has been shown to stabilize NPs in a wide range of salt concentrations. Since the NPs are covered by negatively charged carboxylic ligands, the pH and salt concentration directly influence the surface charge density on NPs and the electrolyte screening of these charges, respectively, which both determine the stability of the NP solution.

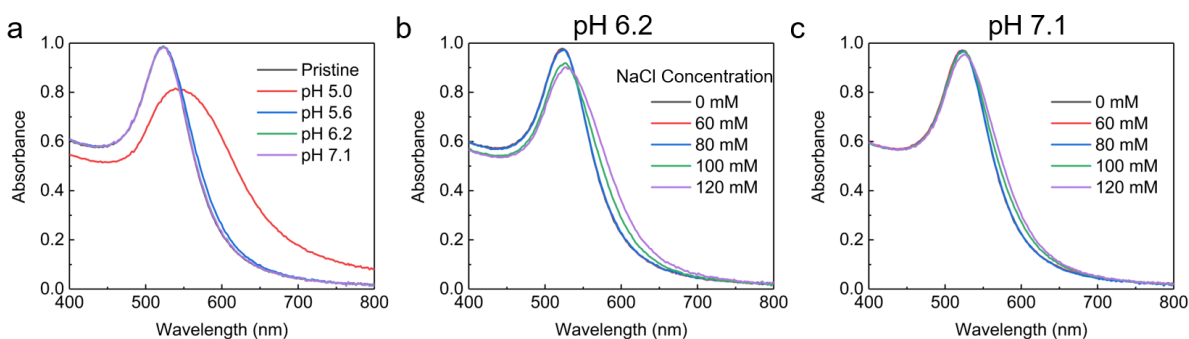


Figure 3.2 Stability of NP solution. (a). UV-vis spectra of NP solution with 60 mM NaCl at different pH and pristine as-prepared NP solution as the reference. (b). UV-vis spectra of NP solution at pH 6.2 with different concentration of NaCl. (c). UV-vis spectra of NP solution at pH 7.1 with different concentration of NaCl.

Agglomeration of NPs has a signature in bulk light-absorption spectra, in the form of the appearance of a shoulder in the orange/red part of the spectrum. As shown in the **Figure 3.2a**, with increasing pH, the typical shoulders for aggregation of NPs at around 600 nm disappear, indicating that higher pH does increase the stability of NPs. Above pH 6.2, NPs were found to be able to tolerate electrolyte concentration as high as 60 mM NaCl.

To better understand why this pH can stabilize NPs, the surface charge on NPs is estimated. For a NP of 16 nm diameter, the surface area is 804 nm^2 . Given the number of MDDA molecules during the synthesis is excess to that needed for the full coverage of NP surface, and the packing density of the MDDA is 1.333 per nm^2 , one can estimate the number of MDDA on the single NP as about 1100 molecules.⁵⁵ Assuming the adsorbed and the drifting MDDA to have the same pK_a , the following equations can be obtained:

$$pK_a = -\log_{10} \left(\frac{[MDD^-][H^+]}{[MDDA]_{\text{initial}} - [MDD^-]} \right) = pH + \log_{10} \left(\frac{[MDDA]_{\text{initial}}}{[MDD^-]} - 1 \right) \quad 3.1$$

$$\frac{1}{10^{(pK_a - pH)} + 1} = \frac{[MDD^-]}{[MDDA]_{\text{initial}}} \quad 3.2$$

where $MDDA_{\text{initial}}$ is the total amount of MDDA present in all forms and MDD^- is the disassociated form which carries one negative charge on each molecule. Since the pK_a of MDDA is about 4.8 and the pH our systems are operating with is 6.2, the disassociation ratio would be 0.96. Thus, the total negative charges on single NP is about 1050.

Considering the high disassociation ratio at pH 6.2, further increase of pH would not make much difference regarding the stability of NPs. This was experimentally confirmed by comparing the stability of NP-dispersions with respect to salt concentration at pH 6.2 and pH 7.1: both can tolerate 80 mM solution, as an upper limit for electrolyte concentration (**Figures 3.2b and c**). Therefore, pH 6.2 is used in all experiments. Such well stabilized NP solution can tolerate a wide range of NaCl concentrations and gives us more freedom for the voltage-control of the assembly and disassembly process.

3.3.2. Potential of zero charge and electrochemical window

To understand and control the assembly and disassembly of NPs by changing electrode polarization, it is important to delineate the electrode potential with respect to the potential of zero charge (PZC). Measurements of interfacial capacitance may help to evaluate the latter. The capacitance of the TiN/Ag substrates was measured using 60 mM NaCl at frequencies of 1, 10, and 100 Hz, as shown in **Figure 3.3a**. For its interpretation, the following considerations should be kept in mind.

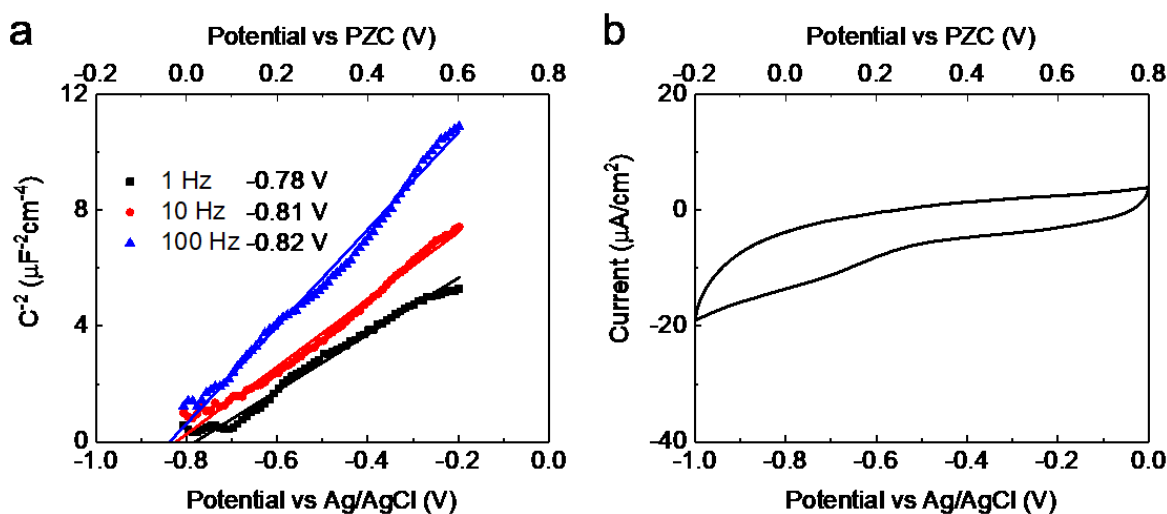


Figure 3.3 (a) Mott-Schottky plot for the capacitance of TiN/Ag electrode in 60 mM NaCl aqueous solution, determining PZC under 1, 10, 100 Hz impedance measurements. (b) Cyclic voltammogram of TiN/Ag in 60 mM NaCl with 20 mV/s scanning rate.

Without a significant electrical current across the electrode/electrolyte interface, TiN is believed to behave like an n-type semiconductor⁶² capable to form a space-charge⁶³ at the SLI alongside the counter-charge of the ionic double layer. This adds space charge capacitance, C_{sc} , in series to the double layer capacitance,

C_{dl} , *i.e.* the total capacitance of the interface is $C = (C_{sc}^{-1} + C_{dl}^{-1})^{-1}$. The smaller of the two capacitances will therefore dominate it and in our case, is the space-charge one.

The double layer capacitance in aqueous electrolytes of such concentration even close to PZC is about 15-18 $\mu\text{F}/\text{cm}^2$, whereas the values of C observed are close to 1 $\mu\text{F}/\text{cm}^2$.⁶⁴ Furthermore, the voltage dependence of C^{-2} shown in **Figure 3.3a** increases but not decreases with electrode potential as it would have been for the case of the double layer Gouy-Chapman capacitance.⁶⁴ The measured capacitance rather obeys the Mott-Schottky law⁶⁵ for a semiconductor, $C_{sc}^{-2} \propto E - E_{PZC} - k_B T/e$, where E is the applied potential, E_{PZC} the potential of zero charge, k_B Boltzmann constant and T the absolute temperature, ($k_B T/e$ is the so called thermal voltage, at room temperature = 0.0256 V). **Figure 3.3a** displays a linear-like relationship between the potential and C^{-2} , which suggests that the space charge capacitance dominates the overall interfacial capacitance. This agrees with literature for similar systems^{62, 66, 67}. For all three frequencies the plots consistently returned the same intercept at -0.8 V vs Ag/AgCl, which acts as a good estimate for the PZC. This value of PZC will be taken as the prime reference when potentials applied to the substrates are discussed.

Cyclic voltammetry with NPs present was performed to determine the electrochemical window of the system (**Figure 3.3b**) to ensure no unwanted electrochemical reactions take place. The potential window was therefore determined to be 0.1 to 0.7 V vs PZC (-0.7 to -0.1 V vs Ag/AgCl). In this range the maximum current density does not exceed 15 $\mu\text{A}/\text{cm}^2$ at a scan rate of 20 mV/s. The amount of charge during one assembly and one disassembly processes are 1.2 mC cm^{-2} (*i.e.* an average current of 0.2 $\mu\text{A cm}^{-2}$), and -11 mC cm^{-2} (an average current of -1.8 $\mu\text{A cm}^{-2}$). This asymmetrical charge transfer is attributed to the low operation potential (-0.7 V vs. Ag/AgCl) during the disassembly process leading to the occurrence of oxygen reduction. For future compact devices, a sealed cell from the atmosphere would possibly lower this current. The low average current and relatively high electrolyte concentration suggest that any static potential is $\ll 1$ mV, therefore electrophoretic effects may be ignored. Although a more positive electrode bias would favour NP assembly, potentials above 0.7 V vs PZC were not used, as it would lead to oxidation of the silver substrate even through the TiN coating.

3.3.3. Optical reflectivity.

As mentioned in Chapter 2, A ‘five-layer’ EMT was used to interpret the optical reflectance spectra, the foundations of which were presented in Ref.⁵⁶ To be more specific, the Au NP layer (layer 2) and the substrate layers (layers 4 and 5) were characterised by frequency-dependent dielectric constants, which were modelled by a Drude-Lorentz (DL) formula with parameters listed in Table 3.1:

Table 3.1 Drude-Lorentz (DL) fitting parameters for bulk Au, TiN, and Ag

	ϵ_∞	ω_p/eV	γ_p/eV	f_1	ω_1/eV	γ_1/eV	f_2	ω_2/eV	γ_2/eV
Au	5.0896	9.0271	0.0760	1.4288	2.9530	0.9541	1.8465	4.0616	1.5639
TiN	1.1667	4.9652	3.0574	2.4881	12.877	22.407	4.8438	5.8305	5.2834
Ag	3.7180	9.2093	0.0200	0.4242	4.2840	0.3430	–	–	–

Thus calculated reflection spectra can be fitted to the experimental reflectivity spectra, giving the array density. Firstly, this procedure will be applied to the equilibrium data obtained at different applied voltages, then to study the kinetics of adsorption-desorption, by monitoring the dynamics of change of reflection spectra, after abrupt change of the electrode potential. This will give us full information about the voltage-controlled assembly-disassembly of NP arrays. The comparison of the measured and thus calculated reflectance spectra will let us test the validity of the overall picture, and identify the key effects that govern the assembly process.

3.3.4. Adsorption equilibria.

Assembly of NPs at an SLI requires the balancing of forces, between NPs and the interface, and between NPs themselves. The main forces acting between NPs, both in the bulk and on the surface, are van der Waals attraction and electrostatic repulsion. Electrostatic forces need to be strong enough to stop NPs from coming too close to each other, otherwise van der Waals interactions may force the NPs to aggregate. As described in the previous sections, these forces are carefully adjusted by the pH and electrolyte concentration, thereby tuning, respectively, the average charge of NPs and the screening of electrostatic interactions, thus making the solution stable. The influence of electrolyte concentration not only affects NP stability in the bulk solution, but also affects the inter-particle forces at the interface.⁶⁸

The interaction of NPs with the substrate include image interactions of charged NPs with the interface, image-modified pair interaction between NPs at the interface, and the corresponding van der Waals interactions.

The electrostatic interactions of this kind are complicated by the strong nonlinear response of electrolyte to charged NPs. Nevertheless, calculations are performed within the linear response approximation, to get a flavour of the balance of forces that allows particles to adsorb at high positive electrode potentials, and desorb at low ones, respectively.

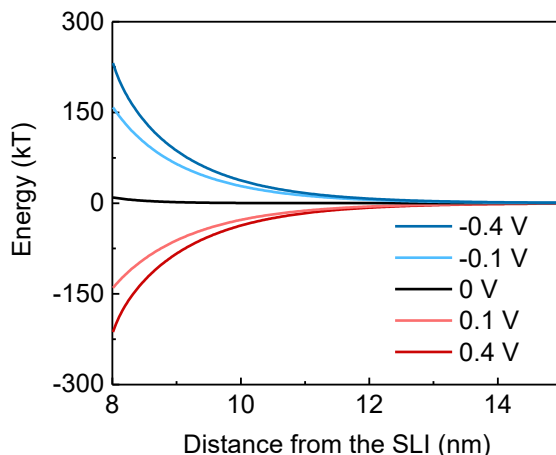


Figure 3.4 Typical model calculation of the electrostatic self-energy profiles of individual NPs as a function of distance to the working electrode at different applied potentials (vs. PZC) for such solution: it demonstrates a crossover from attraction to repulsion at large enough negative potentials of the electrode.⁶⁹

Careful analysis has shown that van der Waals forces for the system are less important than electrostatic interactions. Therefore, our conclusions of the feasibility of the voltage-controlled adsorption-desorption are predominantly rested on electrostatic calculations. **Figure 3.4** shows typical results of such calculations for the described system: the computed, interaction energy of one NP with the electrodes as a function of a distance from its surface. One can clearly see that this interaction can be easily switched between attractive and repulsive modes, indicating the possibility of tuning the system by varying the electrode potential.

3.3.5. Adsorption kinetics

To describe the kinetics of NP adsorption-desorption, monitored through fitting the measured and calculated reflectance data, a phenomenological theory developed in colloid and interface science is adopted.⁷⁰ The kinetics of assembly of particles at the interface is generally determined by three rates, of – adsorption, desorption and diffusion. The account of all three contributions to this process, following Miura and Seki⁷⁰ leads to integro-differential equation on fractional coverage, θ :

$$\frac{d\theta}{d\tau} = \left[r - \int_0^\tau \frac{1}{\sqrt{\pi(\tau - \tau_1)}} \frac{d\theta}{d\tau_1} d\tau_1 \right] (1 - \theta) - \kappa_d \theta \quad 3.3$$

The above equation establishes the coverage dependence on dimensionless time, τ , and parameters r and κ_d . All these dimensionless quantities can be expressed, in terms of adsorption and desorption constants (k_a, k_d), diffusion coefficient (D), maximum coverage (Γ_m), bulk concentration (c_0) and time (t), as follows:

$$\tau = \frac{k_a^2 \Gamma_m^2}{D} t, r = \frac{D c_0}{k_a \Gamma_m^2}, \kappa_d = \frac{D}{k_a^2 \Gamma_m^2} k_d \quad 3.4$$

Note that this equation does not take into account interactions between the adsorbed particles. Nevertheless, it is applicable here because at the values of inter-particle separations that reflectance experiments established (≈ 10 nm NP surface-to surface separation) interactions between particles are heavily screened by electrolyte (Debye length, $L_D = 1.24$ nm). The solution to this equation, when all three rates are comparable, can only be obtained numerically. But there are two limiting cases, when analytical solutions are possible.

The first one is the adsorption-desorption-controlled regime, when diffusion limitations are insignificant. Under such conditions, the integral in Eq. 3.3 becomes small compared to parameters r and κ_d and can, therefore, be neglected. This simplification allows for an easy separation of variables, followed by integration, giving:

$$\theta = \frac{r}{r + \kappa_d} [1 - e^{-(r+\kappa_d)\tau}] \quad 3.5$$

The main assumption behind this limiting case is valid whenever particles have to overcome a high free energy barrier (both into and out of the adsorption well), as adsorption and desorption will become very slow compared to diffusion. The second case occurs when diffusion is rate determining, and is modelled by the following equation, which partially takes saturation into account:

$$\theta = 1 - e^{-2 \frac{c_0}{\Gamma_m} \sqrt{\frac{Dt}{\pi}}} \quad 3.6$$

Fitting the adsorption kinetics data to either Eq. 3.5 or 3.6 does not show good match, and hence the full Eq. 3.3 needs to be implemented.

3.4. Results and discussions

3.4.1. Assembly of NPs – the ‘absorber’ state

As discussed above (**Figure 3.4**), at 0.7 V vs PZC, NPs are expected to be trapped within the energy well at the SLI to form a two-dimensional plasmonic array. Although we do not have direct *in situ* structural information about such NP arrays,³⁶ an average distance between NPs from the measured reflection spectra can be extracted, by comparing them with theory.

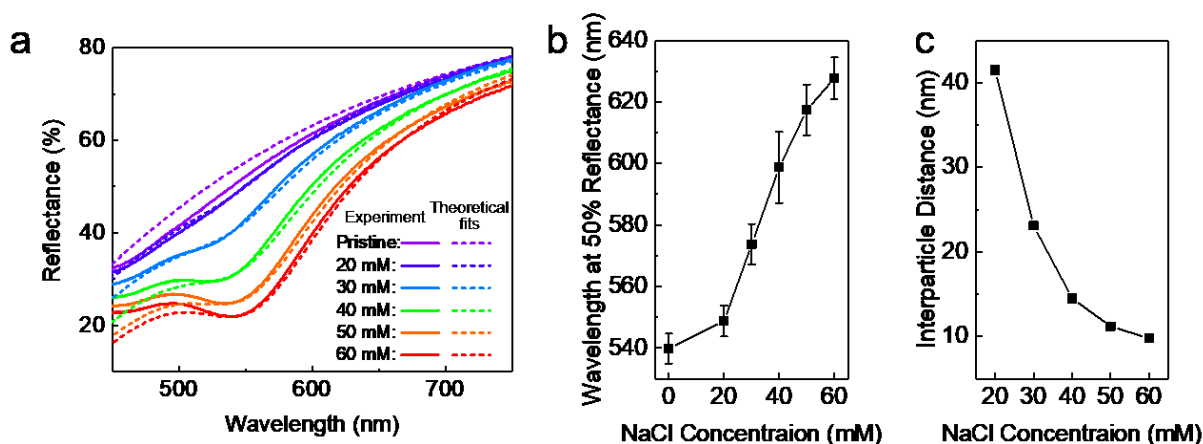


Figure 3.5 Controlling the assembly of NPs on TiN/Ag by varying NaCl concentrations at an applied potential of 0.7 V vs. PZC. (a). Experimental (solid) and theoretically fitted (dashed) reflectance curves of NPs assembly on TiN/Ag at different concentrations of NaCl after 12 h deposition of NPs at 0.7 V vs PZC. The wavelengths at 50% reflectance (b) and the evaluated interparticle distances (c) for NPs assembled on TiN/Ag at different concentrations of NaCl.

As seen in the static reflectance spectra (**Figure 3.5a**), the concentration of NaCl plays a vital role during the assembly process. The violet curve in **Figure 3.5a** shows the reflectance spectrum at normal incidence to the pristine TiN/Ag substrate when the device is in its ‘mirror’ state. To assemble NPs on the substrate, *i.e.* to switch the device to its ‘absorber’ state, the substrate is polarised at 0.7 V vs PZC for 12 hours to ensure equilibrium has been reached as after 3-4 hours the optical signal remains almost constant. When the concentration of NaCl in the solution is less than 20 mM, the optical signal remains predominantly unchanged due to the sparsely distributed NPs on the substrate. With the increase of the NaCl concentration, a concavity (dip) in reflectance spectra evolves within the visible range and the whole spectrum shifts to the red, **Figure 3.5a**. Specifically, the wavelength corresponding to 50% reflectance shifts from 540 nm to 628 nm when the concentration of NaCl increases to 60 mM, **Figure 3.5b**. This is caused by an increase in the number of adsorbed NPs at the interface as can clearly be seen via comparison with EMT. Fitting the theory to experimental data shows excellent match between the two sets of curves and could therefore be used to determine the only fitting parameter – inter-particle distance, **Figure 3.5c**. This absorption-induced concavity in the reflectance spectra evolving with assembly of NPs can be even better seen if the reflectance spectrum of the pristine substrate is subtracted from the spectra with adsorbed NPs (**Figure 3.6a**): Both the wavelength and the intensity of this dip increase with increasing NaCl concentration from zero up to 60 mM, giving rise to a wavelength shift from 525 nm to 557 nm and a maximal 30% drop in reflectance, versus pristine silver mirror, **Figure 3.6b**.

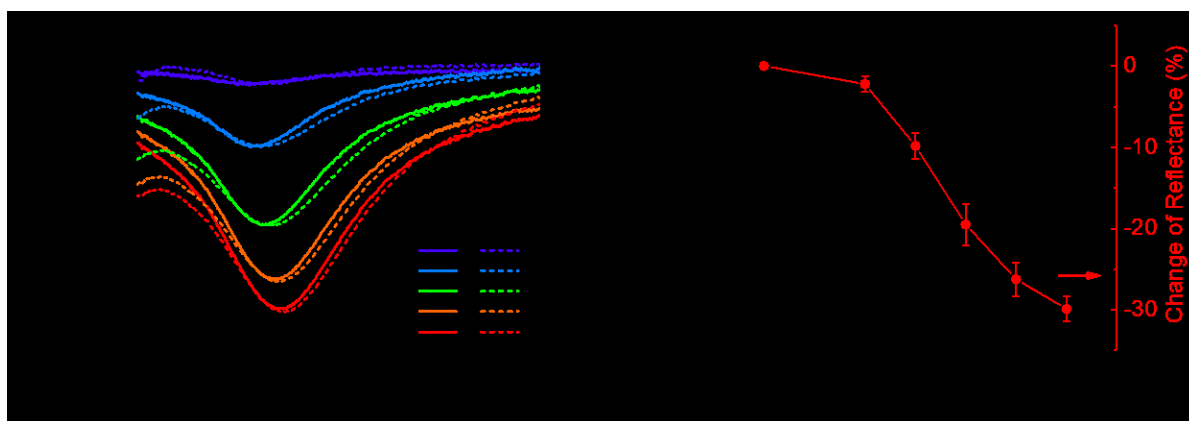


Figure 3.6 (a) Experimental (solid) and theoretically fitted (dashed) curves of the change in reflectance of NPs/TiN/Ag for different NaCl concentrations, with respect to the pristine TiN/Ag substrate, which shows the broad reflectance dip evolving with densification of the adsorbed NP array. (b) Derived from Panel a, the wavelength (black squares) and the change of reflectance (red dots) of the dip.

Ex situ SEM is a powerful tool to directly visualize the arrays formed at interfaces, albeit after drying. SEM images of rapidly dried samples shown in **Figure 3.7** give a glimpse of the effect of electrolyte concentration on NP density. Although array rearrangement during and after drying is likely, these images show similar trends in coverage to that discussed above. Namely, higher concentrations of NaCl in the original solution induce higher population of NPs. The excellent agreement between the surface coverage estimates made from SEM images and EMT reinforces close correlation between the experiments and our theoretical analyses, **Figure 2.6**.

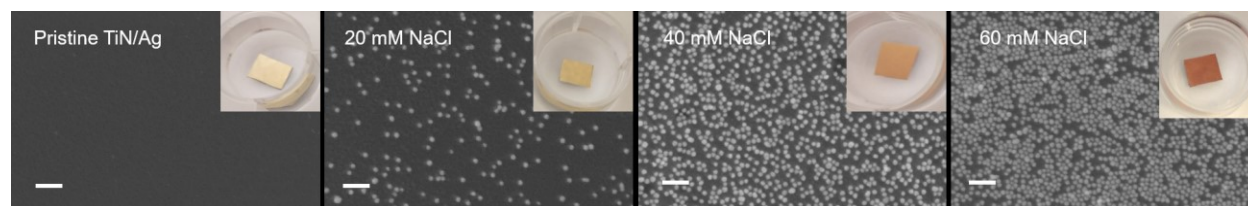


Figure 3.7 SEM of dried samples after NP assembling under indicated electrolyte conditions; scale bar 100 nm; the white dots represent the adsorbed NPs, shown at the dark background of bare TiN/Ag substrate. Digital camera photos (insets) of wet samples after NP assembling on TiN/Ag under indicated electrolyte conditions.

The inset optical images show the macroscale appearance of wet samples with NPs assembled on the substrates. By naked eye, no nonuniformity is observed in any of these samples. The pristine substrate is the most reflective sample and appears golden due to the TiN-coating. The colours change from yellow to orange and then to red as the NP density is increased. These colour changes are also consistent with our reflectance spectra: since the coupled substrate-NP system exhibit the reflectance dip centred around the green region.

The essential role of NaCl can be understood from theoretical modelling of the NP-NP pair interaction. The magnitudes of these interaction energies are plotted (**Figure 3.8**) against NP separations, for multiple electrolyte concentrations. Electrostatic screening of repulsive interparticle forces can, therefore, be tuned

by controlling the NaCl concentration, weakening repulsion to such a degree that NPs can assemble into a relatively dense array, giving rise to a strong change in reflectance. For details of the calculation of pair interactions see Ref.⁶⁹.

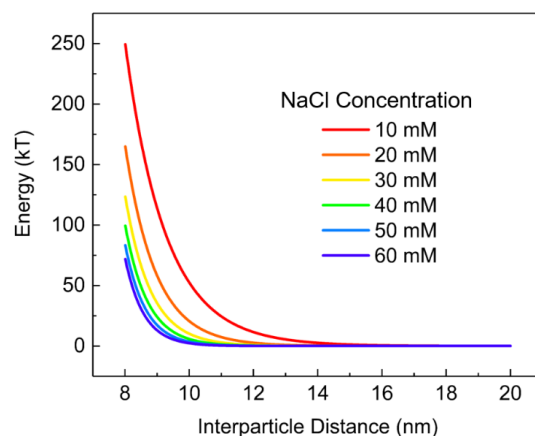


Figure 3.8 Energy profiles of NP pair in different concentration of NaCl.⁶⁹

To understand the dynamics of the assembly process, the reflectance over the course of the whole process was monitored. **Figures 3.9a** and **b** demonstrate the evolution of the experimental and theoretically fitted reflectance spectra for an immersed pristine TiN/Ag substrate in 60 mM NaCl NP solution at 0.7 V vs PZC. Fitting the theoretical reflectance spectra to the experimental ones, aiming at the perfect match in the region of the dip, we thus extracted the inter-particle distance or the related quantity of the surface coverage at different times. Interpretation of results implies that the rearrangement of the lattice of adsorbed NPs is significantly faster than their diffusion towards the surface.

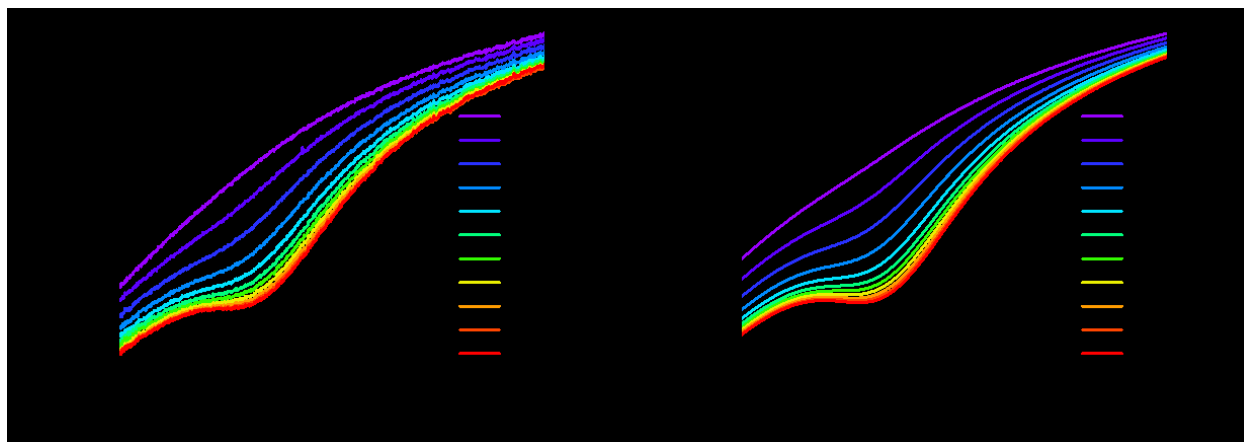


Figure 3.9 The kinetics of the NP assembly triggered by electrode polarisation. Experimental (a) and theoretically fitted (b) time-dependent reflectance curves of NPs assembled on TiN/Ag in a solution of $2.2 \times 10^{12} \text{ cm}^{-3}$ NPs and 60 mM NaCl under 0.7 V vs PZC, starting from pristine TiN/Ag.

The depth of the reflection dip initially keeps deepening, asymptotically approaching a plateau around -30% (Figure 3.10a). At the same time, the wavelength of the dip red-shifts from 525 nm to 555 nm, which is consistent with our static data.

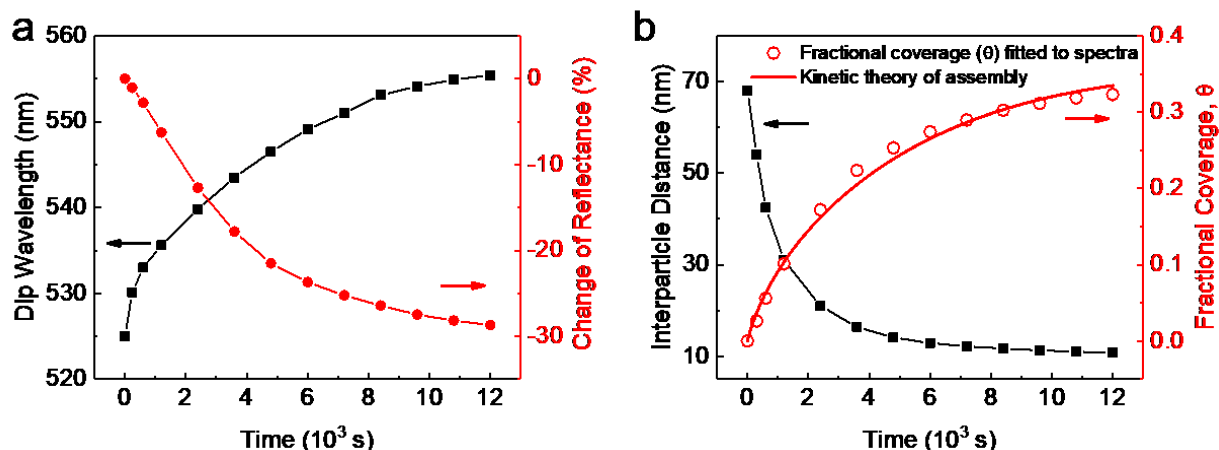


Figure 3.10 (a) The corresponding experimental time-dependent wavelengths (black squares) and the change of reflectance (red dots) at the reflection dip (obtained by subtracting the reflectance data for pristine TiN/Ag from Figure 3.9a). (b) The time-dependent interparticle distances (black squares); the fractional coverage $\theta(t)$ (red empty circles), as extracted from fitting the theory to reflectance data; and the numerical results from the kinetic adsorption theory (red line), as described in the text.

Interparticle distance/surface coverage (Figure 3.10b), calculated from fitting the reflectance data to the EMT theory (Figure 3.9b), helps to understand the dynamics of NP assembly at the SLI. By definition, surface coverage refers to the number of nanoparticles per unit area, while fractional coverage stands for the fraction of maximum coverage, Γ_m . Figure 3.10b shows how interparticle distance decreases and fractional coverage, θ , increases, after jump-wise imposing 0.7 V vs PZC. Coverage data are further found to have a good match with a kinetic model⁷⁰ (red line) which takes into account the contributions from adsorption, desorption and diffusion.

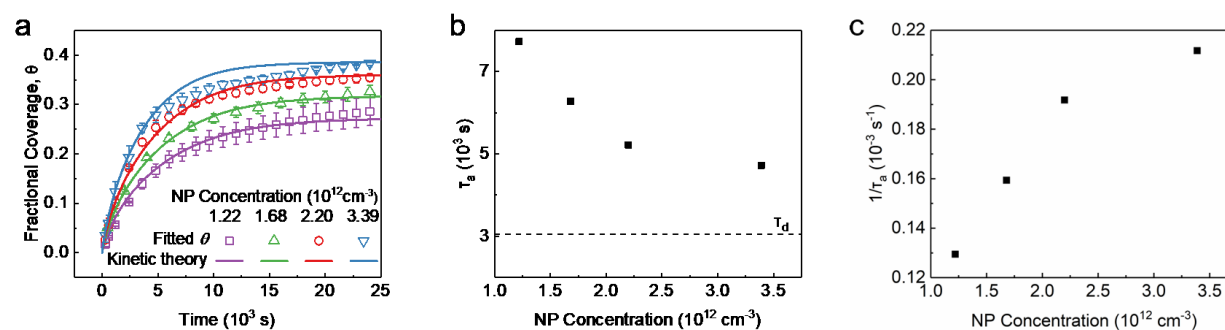


Figure 3.11 (a) The extracted fractional coverage $\theta(t)$ (empty symbols) and the results of kinetic adsorption theory (lines) corresponding to the indicated concentrations of NPs. (b) The fitted characteristic ‘adsorption time’ (τ_a) and ‘desorption time’ (τ_d) involved in the kinetic adsorption theory (see the text), for different concentrations of NPs. (c) The fitted inverse characteristic ‘adsorption time’ (τ_a) involved in the kinetic adsorption theory, for different concentrations of NPs.

The time evolution of the coverage obtained for four different concentrations of NPs is shown in **Figure 3.11a**. Fitting of the kinetic model allows to evaluate characteristic adsorption and desorption times, τ_a and τ_d – the parameters of the kinetic adsorption isotherm, as described in Section 3.3.5. The results are shown in **Figure 3.11b**, with τ_a as expected decreasing with the concentration of NPs. But their dependence is nontrivial. Generally, the rate constants, k_a and k_d of the elementary acts of adsorption and desorption, are related to these times as: $\tau_a^{-1} = k_a c_a$, where c_a is the concentration of NPs at the surface just before the adsorption barrier, and $\tau_d^{-1} = k_d$. Increase of the bulk concentration of NPs could increase, proportionally, c_a at low concentrations, but such proportionality may no longer hold at higher concentrations, **Figure 3.11c**. It might be, however, premature to speculate about this deviation because of the lower accuracy of the reflection signal at high NP concentration due to increased optical absorbance in the bulk, a potential reason of the less good fit for the blue curve in **Figure 3.11a**.

3.4.2. Disassembly of NPs – the ‘mirror’ state

Upon assembly, in the ‘absorber’ state, NPs are trapped in the energy wells at the SLI. To drive them away from the substrate and switch back to a ‘mirror’, one must lower the electrode potential, making it less positive with respect to the PZC, which is expected to weaken the adsorption well and, correspondingly, diminish the barrier that hinders the escape of NPs from the well. This is confirmed from the trend seen when the potential of NPs/TiN/Ag electrode from the ‘absorber’ state is lowered. **Figure 3.12a** shows the static reflectance spectra at different electrode potentials. Maintaining the assembled samples at high potentials (0.5 – 0.7 V) will not release the NPs from the SLI back into the bulk solution, and data from EMT fitting indicates that the interparticle distance remains almost unchanged, **Figure 3.12b**. This suggests that the energy well at the SLI is still substantial. By further lowering the potential, a dramatic weakening of the optical signal is witnessed which is also accompanied by a substantial blue shift of the wavelength of 50% reflectance, from 628 nm back to 541 nm, **Figure 3.12c**. The fitted interparticle distance also dramatically increases from the close-packed 10 nm to sparsely distributed 45 nm, meaning the majority of the NPs have left the SLI.

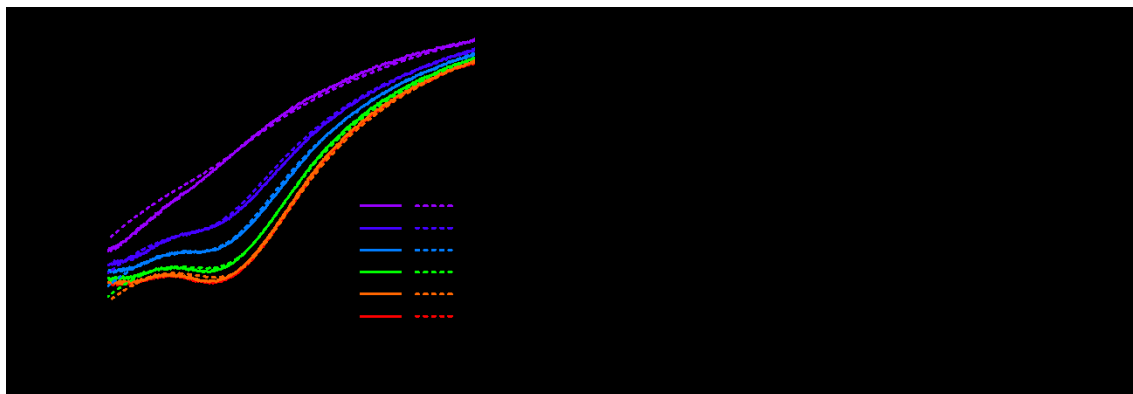


Figure 3.12 The disassembly of NPs on TiN/Ag, controlled by reducing the potential from the assembly potential (0.7 V vs PZC). (a) Experimental (solid) and theoretically fitted (dashed) reflectance curves of disassembling NPs on TiN/Ag in 60 mM NaCl under 0.1 – 0.7 V vs PZC. The experiments start from fully assembled NPs/TiN/Ag at 0.7 V vs PZC, with gradual disassembly by stepwise reducing the potential to 0.1 V vs PZC. The wavelength at 50% reflectance (b) and the fitted interparticle distances (c) for NPs assembled on TiN/Ag at different potentials (as derived from data in Panel a).

By subtracting the reflectance of pristine TiN/Ag, **Figure 3.13a** shows how the dip diminishes when the electrode potential drops down and the system gets back to the ‘mirror’ state. A more quantitative look at the dip position shows the reverse trend compared with the assembly process: the loss of reflectance recovers from -30% to almost zero and the dip wavelength also shifts from 556 nm back to 528 nm, **Figure 3.13b**.

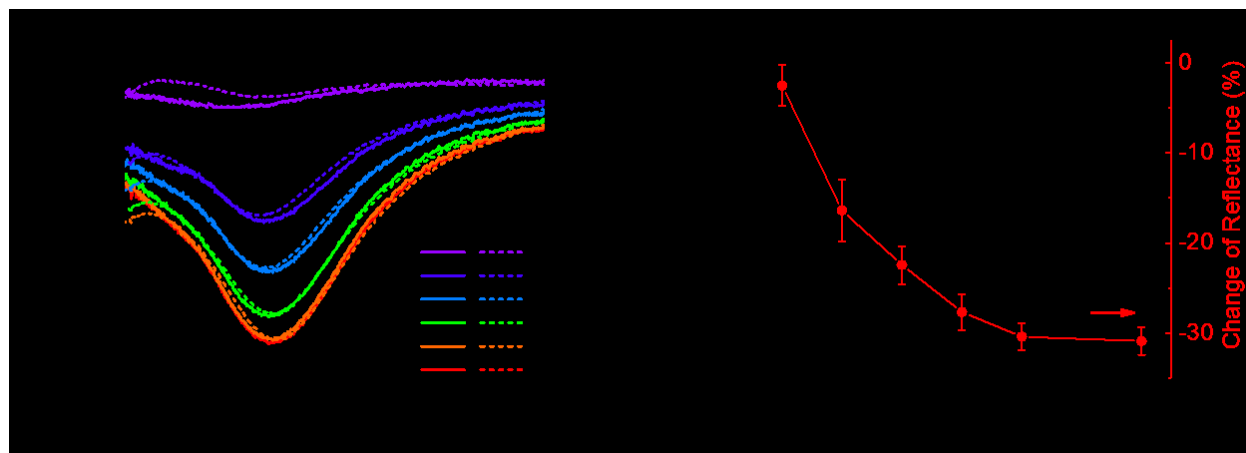


Figure 3.13 (a) Experimental (solid) and theoretically fitted (dashed) curves of the change of reflectance of NP/TiN/Ag with respect to the pristine TiN/Ag substrate under different indicated potentials. (b) The wavelengths (black squares) and the change of reflectance (red dots) at the reflection dip, as derived from the data of Panel a.

Similar to the assembly process, the dynamics of the disassembly process was monitored by implementing a jump-wise change in the electrode potential from 0.7 V to 0.1 V vs PZC. The closely matched experimental data and theoretical fits depict how the densely packed NP array on the substrate becomes more reflective and can revert back to its ‘mirror’ state, **Figures 3.14a** and **b**. This is quantified in **Figure 3.14c**, where the wavelength of the dip blue-shifts back from 555 nm to 528 nm and the depth of the dip decreases from -30% to almost 0. Values of the coverage θ , estimated by EMT-fitting, give us a picture of

the kinetics of disassembly. The time dependence of the coverage during disassembly follows a simple model. One can assume that very low, negative potentials make the energy barrier much lower for desorption, compared to adsorption. This allows us to neglect the adsorption rate in the kinetic Langmuir adsorption isotherm resulting in a trivial, exponential decay of the coverage. Confirmation of such law is shown in **Figure 3.14d**.

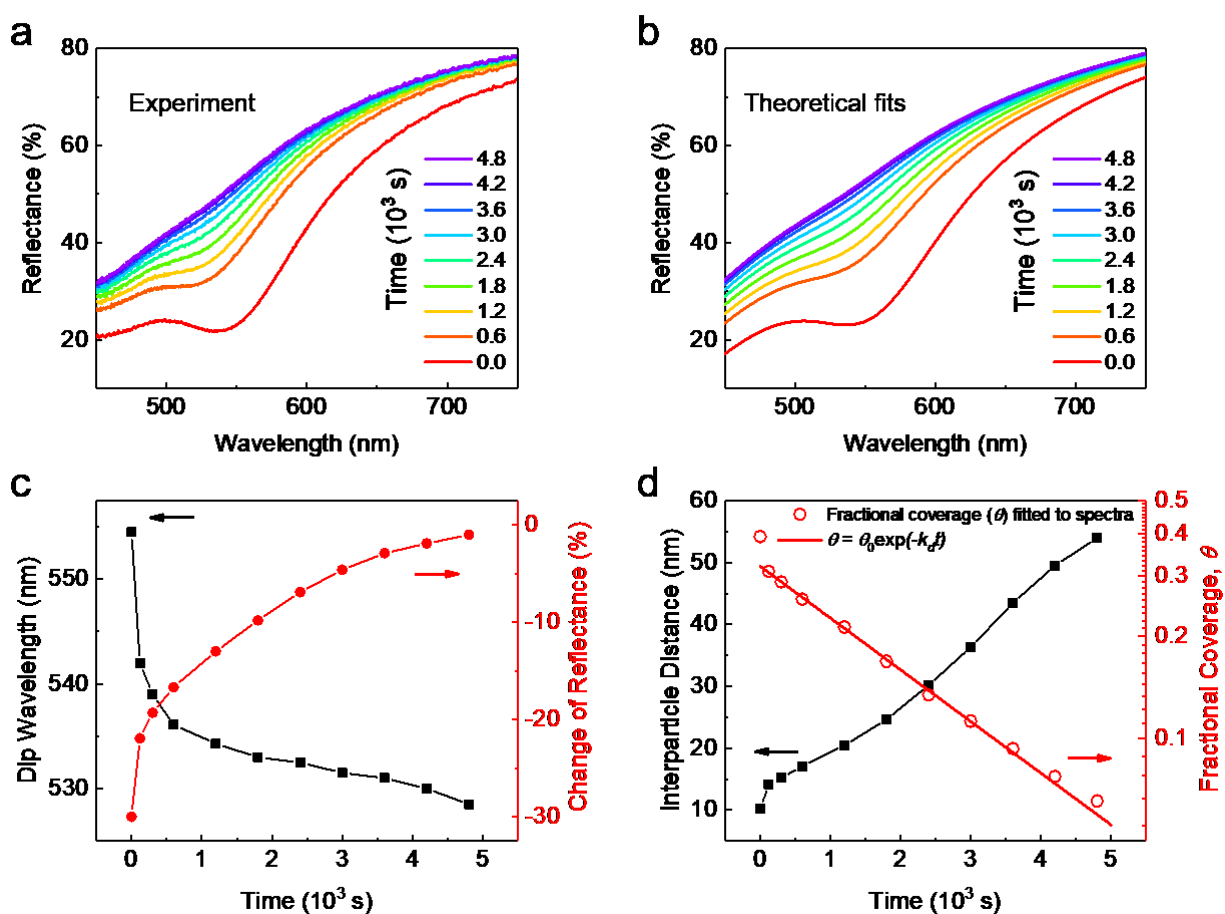


Figure 3.14 The desorption-limited kinetics of NP disassembly at 0.1 V vs PZC. **Experimental.** (a) and theoretically fitted (b) time-dependent reflectance curves of NPs disassembling from TiN/Ag in a solution of $2.20 \times 10^{12} \text{ cm}^{-3}$ NP and 60 mM NaCl after an electrode potential jump from 0.7 V to 0.1 V vs PZC, starting from fully assembled NPs/TiN/Ag. (c) The time-dependency of the wavelength (black squares) and of the change of reflectance (red dots) at the reflection dip obtained by subtracting the reflectance of pristine TiN/Ag. (d) The calculated time-dependent interparticle distances (black squares), fractional coverage $\theta(t)$ extracted from Panel b (red empty circles), and the exponential desorption isotherm $[\theta = \theta_0 \exp(-k_d t)]$, (red straight line).

3.4.3. Reversibility

Having demonstrated the ‘mirror’ state (after the NPs leave the interface) and an ‘absorber’ state (after the NPs assemble at the interface), we check reversibility of this process in the same system. **Figure 3.15a** shows the interchange between these two states in multiple cycles. Initially, the electrode is polarised at 0.7 V vs PZC. While such value is maintained (‘red-labelled’ regions), the reflectance slowly drops down,

meaning that NPs are assembling onto the substrate. Switching the potential to 0.1 V ('blue' regions), leads to the increase in reflectance, meaning NPs are leaving the SLI, bringing the system back to the 'mirror' state. The spectra of 'mirror' and 'absorber' states in these cycles are shown in **Figure 3.15b** alongside with the dip wavelength and interparticle distance (**Figure 3.15c**), demonstrating the system can be switched on and off for multiple times. No NP aggregation is witnessed in the bulk solution after the reversibility experiments (**Figure 3.16**).

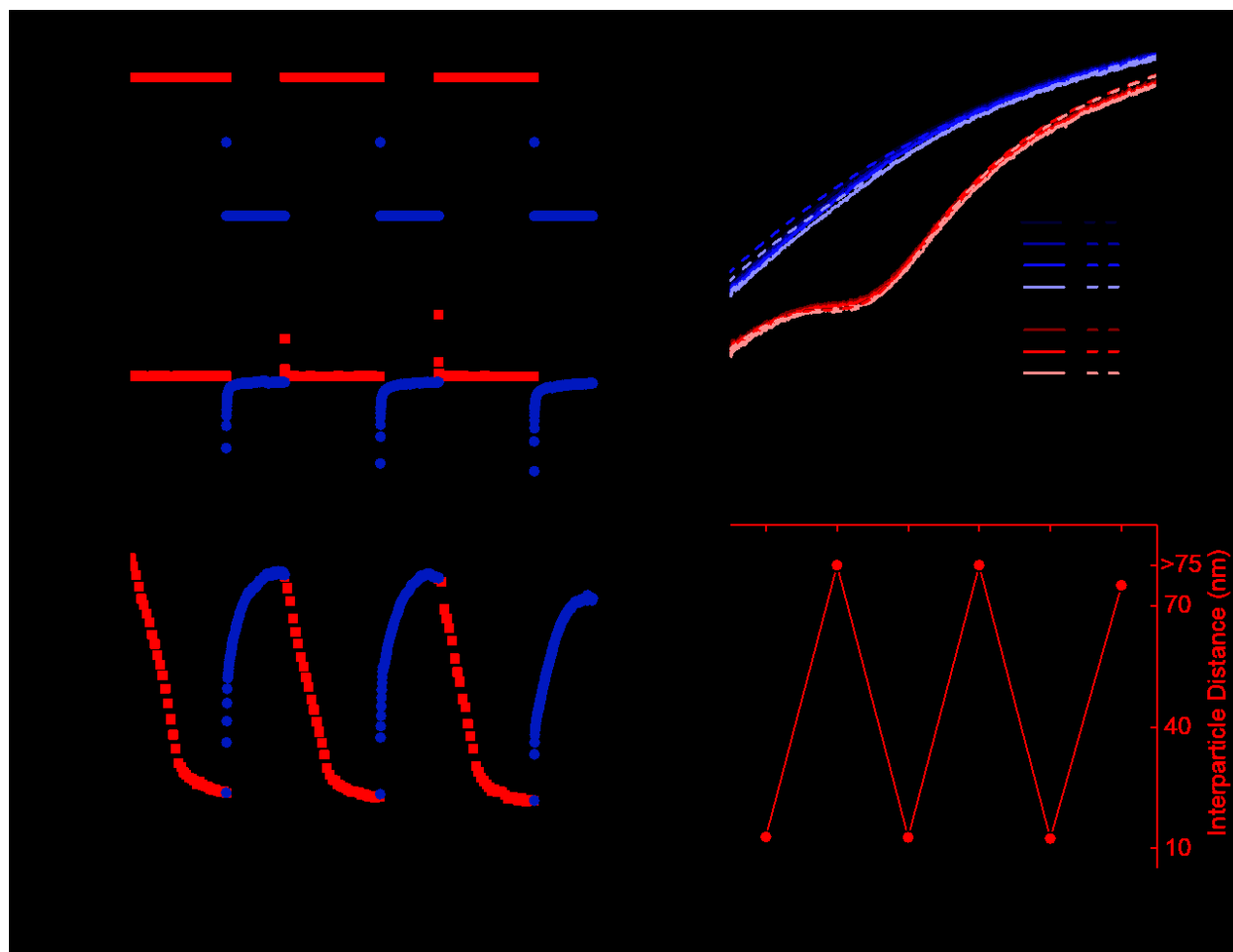


Figure 3.15 Reversible switching of the system between the 'mirror' state (0.1 V vs PZC) and the 'absorber' state (0.7 V vs PZC). (a) The electrode potential over time (top), the corresponding electrochemical current (middle) and the change of reflection dip (bottom). (b) The 'mirror' and 'absorber' spectra at different cycles. (c) The dip wavelength and interparticle distance for the 'absorber' (Abs.) and 'mirror' (Mir.) states at different cycles

A closer examination on the reversibility spectra reveals a tiny dip for the mirror state after multiple cycles. The theoretical fitting also gives the last cycle a 75 nm interparticle distance. This means that after the disassembly process, a small number of NPs are still "stuck" on the SLI. As has been mentioned previously, there is an energy barrier for adsorption in the vicinity of the SLI, and the potential well behind it (presumably a metastable one). If the negative potential is not large enough for totally removing this barrier, some NPs would be very hard to remove. Also considering that the lowest negative potential applied is 0.1

V vs PZC (still positive to PZC), it's also reasonable to see some NPs are still trapped. To totally remove those NPs for fully recovery, a substantial negative potential is needed. However, limited by the current electrochemical window of the electrodes and electrolytes, this still awaits further exploration. The improvement will be reached by using nonaqueous solutions that will allow higher electrode polarisations.

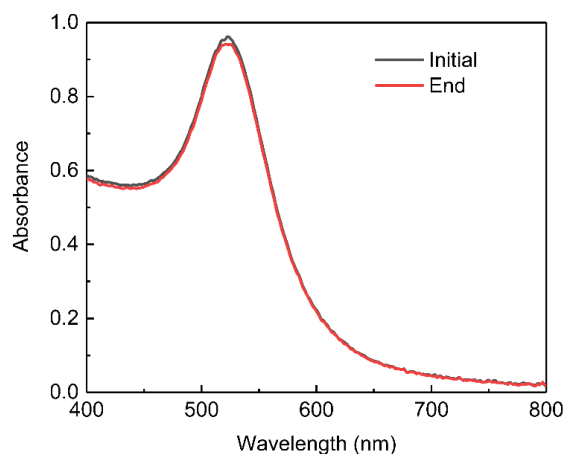


Figure 3.16 UV-vis spectra of NP solution before and after the reversibility experiment.

3.5. Conclusions

In this chapter we have demonstrated an effect of electrotunable reflection of light from a solid electrode in electrolytic solutions, the spectra of which get modified by voltage-controlled physisorption of plasmonic NPs.

A positively polarized planar TiN/Ag-electrode attracts negatively charged 16 nm AuNPs leading to formation of adsorbed two-dimensional arrays of NPs. Making polarization more negative repels NPs from the electrodes, disassembling the array. For this system, the coupling of surface plasmon modes in the electrode with localized coupled plasmon resonances in the adsorbed NPs leads to the suppressed reflection in green, making the substrates red coloured. But after NPs leave the interface, its optical response returns to the one of the bare TiN/Ag -electrode. The switching between these two states is reversible.

By adjusting the electric potential of the Ag substrate or the NaCl concentration of NP solution, the interparticle distance of this NP array at the SLI could be finely tuned, allowing control of both the wavelength and intensity of the reflectance dip.

The EMT theory of the optical response of this system relates the optical properties of the interface with adsorbed NPs to optical polarizability of NPs and the structure of the adsorbed NP arrays. Fitting the theory

to the reflectivity data allows to extract the average distance between NPs in the arrays, both – at equilibrium and during the assembly/disassembly.

Extracting the time-dependent coverage of the electrode by NPs from the evolution of reflectance spectrum, and subsequent treatment of the results with the kinetic theory of adsorption-desorption, suggest that: (i) both the adsorption and desorption stages have to overcome energy barriers that are affected by electrode potential; (ii) the account of all three stages – diffusion, adsorption, and desorption – is important for interpreting the data, except for disassembly at low potentials which follows a much simpler law.

The observed rates of assembly/disassembly in the convection-free system are too slow for practical applications where fast-switching is required. Had those kinetics been exclusively diffusion limited, the natural solution to the problem would have been miniaturization of the cell⁷¹ to shorten the diffusion path. However, that could help only partially.

Indeed, the seemingly present free energy barriers for adsorption and desorption point at the necessity of creating a system with a larger electrochemical window, so that higher electrode potentials (greater than 1 volt) could be applied to lower or fully eliminate those barriers. Miniaturization of the cell would also enable speeding-up the response time.

Independently of any potential applications and developments, the present work presents the proof of concept for a new type of electrovariable plasmonic reflector. Making it a practical, tunable optical device will be the subject of future investigations, along the ways paved in this work.

3.6. References

- (1) Ma, Y.; Zagar, C.; Klemme, D. J.; Sikdar, D.; Velleman, L.; Montelongo, Y.; Oh, S.-H.; Kucernak, A. R.; Edel, J. B.; Kornyshev, A. A. A Tunable Nanoplasmonic Mirror at an Electrochemical Interface. *ACS Photonics* **2018**, *5*, 4604-4616.
- (2) Zheludev, N. I.; Kivshar, Y. S. From Metamaterials to Metadevices. *Nat. Mater.* **2012**, *11*, 917-924.
- (3) Cai, W.; Shalaev, V., *Optical Metamaterials : Fundamentals and Applications*. Cai, W.; Shalaev, V., Eds. Springer: New York, 2016; pp 1-10.
- (4) Schuller, J. A.; Barnard, E. S.; Cai, W.; Jun, Y. C.; White, J. S.; Brongersma, M. L. Plasmonics for Extreme Light Concentration and Manipulation. *Nat. Mater.* **2010**, *9*, 193.
- (5) Lal, S.; Link, S.; Halas, N. J. Nano-Optics from Sensing to Waveguiding. *Nat. Photonics* **2007**, *1*, 641.
- (6) Wang, W.; Ramezani, M.; Väkeväinen, A. I.; Törmä, P.; Rivas, J. G.; Odom, T. W. The Rich Photonic World of Plasmonic Nanoparticle Arrays. *Mater. Today* **2018**, *21*, 303-314.
- (7) Chen, H. S.; Zheng, B.; Shen, L.; Wang, H. P.; Zhang, X. M.; Zheludev, N. I.; Zhang, B. L. Ray-Optics Cloaking Devices for Large Objects in Incoherent Natural Light. *Nat. Commun.* **2013**, *4*, 6.
- (8) Pendry, J. B.; Schurig, D.; Smith, D. R. Controlling Electromagnetic Fields. *Science* **2006**, *312*, 1780-1782.
- (9) Lu, D. L.; Liu, Z. W. Hyperlenses and Metalenses for Far-Field Super-Resolution Imaging. *Nat. Commun.* **2012**, *3*, 9.

- (10) Wang, Q.; Rogers, E. T. F.; Gholipour, B.; Wang, C. M.; Yuan, G. H.; Teng, J. H.; Zheludev, N. I. Optically Reconfigurable Metasurfaces and Photonic Devices Based on Phase Change Materials. *Nat. Photonics* **2016**, *10*, 60-75.
- (11) Pendry, J. B.; Luo, Y.; Zhao, R. K. Transforming the Optical Landscape. *Science* **2015**, *348*, 521-524.
- (12) Xiong, K.; Tordera, D.; Emilsson, G.; Olsson, O.; Linderhed, U.; Jonsson, M. P.; Dahlin, A. B. Switchable Plasmonic Metasurfaces with High Chromaticity Containing Only Abundant Metals. *Nano Lett.* **2017**, *17*, 7033-7039.
- (13) Kunli, X.; Gustav, E.; Ali, M.; Xinxin, Y.; Lei, S.; H., J. E. W.; B., D. A. Plasmonic Metasurfaces with Conjugated Polymers for Flexible Electronic Paper in Color. *Adv. Mater.* **2016**, *28*, 9956-9960.
- (14) Li, W.; Valentine, J. Metamaterial Perfect Absorber Based Hot Electron Photodetection. *Nano Lett.* **2014**, *14*, 3510-3514.
- (15) Atwater, H. A.; Polman, A. Plasmonics for Improved Photovoltaic Devices. *Nat. Mater.* **2010**, *9*, 205.
- (16) Tordera, D.; Zhao, D.; Volkov, A. V.; Crispin, X.; Jonsson, M. P. Thermoplasmonic Semitransparent Nanohole Electrodes. *Nano Lett.* **2017**, *17*, 3145-3151.
- (17) Jonsson, G.; Tordera, D.; Pakizeh, T.; Jaysankar, M.; Miljkovic, V.; Tong, L. M.; Jonsson, M. P.; Dmitriev, A. Solar Transparent Radiators by Optical Nanoantennas. *Nano Lett.* **2017**, *17*, 6766-6772.
- (18) Zheludev, N. I. The Road Ahead for Metamaterials. *Science* **2010**, *328*, 582-583.
- (19) Fan, Z.; Govorov, A. O. Plasmonic Circular Dichroism of Chiral Metal Nanoparticle Assemblies. *Nano Lett.* **2010**, *10*, 2580-2587.
- (20) Yang, A.; Hryn, A. J.; Bourgeois, M. R.; Lee, W.-K.; Hu, J.; Schatz, G. C.; Odom, T. W. Programmable and Reversible Plasmon Mode Engineering. *Proc. Natl. Acad. Sci. U. S. A.* **2016**, *113*, 14201-14206.
- (21) Maier, S. A., Plasmonics : Fundamentals and Applications. Maier, S. A., Ed. Springer: New York, 2007; pp 65-88.
- (22) Halas, N. J.; Lal, S.; Chang, W. S.; Link, S.; Nordlander, P. Plasmons in Strongly Coupled Metallic Nanostructures. *Chem. Rev.* **2011**, *111*, 3913-3961.
- (23) Wang, D.; Yang, A.; Hryn, A. J.; Schatz, G. C.; Odom, T. W. Superlattice Plasmons in Hierarchical Au Nanoparticle Arrays. *ACS Photonics* **2015**, *2*, 1789-1794.
- (24) Litt, D. B.; Jones, M. R.; Hentschel, M.; Wang, Y.; Yang, S.; Ha, H. D.; Zhang, X.; Alivisatos, A. P. Hybrid Lithographic and DNA-Directed Assembly of a Configurable Plasmonic Metamaterial That Exhibits Electromagnetically Induced Transparency. *Nano Lett.* **2018**, *18*, 859-864.
- (25) Ou, J. Y.; Plum, E.; Zhang, J. F.; Zheludev, N. I. An Electromechanically Reconfigurable Plasmonic Metamaterial Operating in the Near-Infrared. *Nat. Nanotechnol.* **2013**, *8*, 252-255.
- (26) Shin, D.; Urzhumov, Y.; Jung, Y.; Kang, G.; Baek, S.; Choi, M.; Park, H.; Kim, K.; Smith, D. R. Broadband Electromagnetic Cloaking with Smart Metamaterials. *Nat. Commun.* **2012**, *3*, 1213.
- (27) Si, K. J.; Sikdar, D.; Chen, Y.; Eftekhari, F.; Xu, Z.; Tang, Y.; Xiong, W.; Guo, P.; Zhang, S.; Lu, Y.; Bao, Q.; Zhu, W.; Premaratne, M.; Cheng, W. Giant Plasmene Nanosheets, Nanoribbons, and Origami. *ACS Nano* **2014**, *8*, 11086-11093.
- (28) Ou, J. Y.; Plum, E.; Jiang, L.; Zheludev, N. I. Reconfigurable Photonic Metamaterials. *Nano Lett.* **2011**, *11*, 2142-2144.
- (29) Shevchenko, E. V.; Talapin, D. V.; Kotov, N. A.; O'Brien, S.; Murray, C. B. Structural Diversity in Binary Nanoparticle Superlattices. *Nature* **2006**, *439*, 55-59.
- (30) Edel, J. B.; Kornyshev, A. A.; Kucernak, A. R.; Urbakh, M. Fundamentals and Applications of Self-Assembled Plasmonic Nanoparticles at Interfaces. *Chem. Soc. Rev.* **2016**, *45*, 1581-1596.
- (31) Scanlon, M. D.; Smirnov, E.; Stockmann, T. J.; Peljo, P. Gold Nanofilms at Liquid-Liquid Interfaces: An Emerging Platform for Redox Electrocatalysis, Nanoplasmonic Sensors, and Electrovariable Optics. *Chem. Rev.* **2018**.
- (32) Bera, M. K.; Chan, H.; Moyano, D. F.; Yu, H.; Tatur, S.; Amoanu, D.; Bu, W.; Rotello, V. M.; Meron, M.; Král, P.; Lin, B.; Schlossman, M. L. Interfacial Localization and Voltage-Tunable Arrays of Charged Nanoparticles. *Nano Lett.* **2014**, *14*, 6816-6822.

- (33) Edel, J. B.; Kornyshev, A. A.; Urbakh, M. Self-Assembly of Nanoparticle Arrays for Use as Mirrors, Sensors, and Antennas. *ACS Nano* **2013**, *7*, 9526-9532.
- (34) Booth, S. G.; Dryfe, R. A. W. Assembly of Nanoscale Objects at the Liquid/Liquid Interface. *J. Phys. Chem. C* **2015**, *119*, 23295-23309.
- (35) Su, B.; Abid, J.-P.; Fermín, D. J.; Girault, H. H.; Hoffmannová, H.; Krtil, P.; Samec, Z. Reversible Voltage-Induced Assembly of Au Nanoparticles at Liquid|Liquid Interfaces. *J. Am. Chem. Soc.* **2004**, *126*, 915-919.
- (36) Velleman, L.; Sikdar, D.; Turek, V. A.; Kucernak, A. R.; Roser, S. J.; Kornyshev, A. A.; Edel, J. B. Tuneable 2d Self-Assembly of Plasmonic Nanoparticles at Liquid|Liquid Interfaces. *Nanoscale* **2016**, *8*, 19229-19241.
- (37) Kiely, C. J.; Fink, J.; Brust, M.; Bethell, D.; Schiffrin, D. J. Spontaneous Ordering of Bimodal Ensembles of Nanoscopic Gold Clusters. *Nature* **1998**, *396*, 444.
- (38) Smirnov, E.; Peljo, P.; Scanlon, M. D.; Gumy, F.; Girault, H. H. Self-Healing Gold Mirrors and Filters at Liquid-Liquid Interfaces. *Nanoscale* **2016**, *8*, 7723-7737.
- (39) Hentschel, M.; Saliba, M.; Vogelgesang, R.; Giessen, H.; Alivisatos, A. P.; Liu, N. Transition from Isolated to Collective Modes in Plasmonic Oligomers. *Nano Lett.* **2010**, *10*, 2721-2726.
- (40) Kim, J.-W.; Kovalenko, O.; Liu, Y.; Bigot, J.-Y. Exploring the Angstrom Excursion of Au Nanoparticles Excited away from a Metal Surface by an Impulsive Acoustic Perturbation. *ACS Nano* **2016**.
- (41) Lalander, C. H.; Zheng, Y.; Dhuey, S.; Cabrini, S.; Bach, U. DNA-Directed Self-Assembly of Gold Nanoparticles onto Nanopatterned Surfaces: Controlled Placement of Individual Nanoparticles into Regular Arrays. *ACS Nano* **2010**, *4*, 6153-6161.
- (42) Lassiter, J. B.; McGuire, F.; Mock, J. J.; Ciraci, C.; Hill, R. T.; Wiley, B. J.; Chilkoti, A.; Smith, D. R. Plasmonic Waveguide Modes of Film-Coupled Metallic Nanocubes. *Nano Lett.* **2013**, *13*, 5866-5872.
- (43) Ciraci, C.; Chen, X.; Mock, J. J.; McGuire, F.; Liu, X.; Oh, S.-H.; Smith, D. R. Film-Coupled Nanoparticles by Atomic Layer Deposition: Comparison with Organic Spacing Layers. *Appl. Phys. Lett.* **2014**, *104*, 023109.
- (44) Cao, S.-H.; Cai, W.-P.; Liu, Q.; Xie, K.-X.; Weng, Y.-H.; Huo, S.-X.; Tian, Z.-Q.; Li, Y.-Q. Label-Free Aptasensor Based on Ultrathin-Linker-Mediated Hot-Spot Assembly To Induce Strong Directional Fluorescence. *J. Am. Chem. Soc.* **2014**, *136*, 6802-6805.
- (45) Yavas, O.; Svedendahl, M.; Dobosz, P.; Sanz, V.; Quidant, R. On-a-chip Biosensing Based on All-Dielectric Nanoresonators. *Nano Lett.* **2017**, *17*, 4421-4426.
- (46) Hu, M.; Ghoshal, A.; Marquez, M.; Kik, P. G. Single Particle Spectroscopy Study of Metal-Film-Induced Tuning of Silver Nanoparticle Plasmon Resonances. *J. Phys. Chem. C* **2010**, *114*, 7509-7514.
- (47) Li, C.-Y.; Gao, J.-H.; Yi, J.; Zhang, X.-G.; Cao, X.-D.; Meng, M.; Wang, C.; Huang, Y.-P.; Zhang, S.-J.; Wu, D.-Y.; Wu, C.-L.; Xu, J.-H.; Tian, Z.-Q.; Li, J.-F. Plasmon-Enhanced Ultrasensitive Surface Analysis Using Ag Nanoantenna. *Anal. Chem.* **2018**, *90*, 2018-2022.
- (48) Lacharaise, P. D.; Le Ru, E. C.; Etchegoin, P. G. Guiding Molecules with Electrostatic Forces in Surface Enhanced Raman Spectroscopy. *ACS Nano* **2009**, *3*, 66-72.
- (49) Lumdee, C.; Toroghi, S.; Kik, P. G. Post-fabrication Voltage Controlled Resonance Tuning of Nanoscale Plasmonic Antennas. *ACS Nano* **2012**, *6*, 6301-6307.
- (50) Park, C.; Seo, S.; Shin, H.; Sarwade, B. D.; Na, J.; Kim, E. Switchable Silver Mirrors with Long Memory Effects. *Chem. Sci.* **2015**, *6*, 596-602.
- (51) Ding, T.; Sigle, D.; Zhang, L.; Mertens, J.; de Nijs, B.; Baumberg, J. Controllable Tuning Plasmonic Coupling with Nanoscale Oxidation. *ACS Nano* **2015**, *9*, 6110-6118.
- (52) Sikdar, D.; Bucher, A.; Zagar, C.; Kornyshev, A. A. Electrochemical Plasmonic Metamaterials: Towards Fast Electro-Tuneable Reflecting Nanoshutters. *Faraday Discuss.* **2017**, *199*, 585-602.
- (53) Mock, J. J.; Hill, R. T.; Tsai, Y.-J.; Chilkoti, A.; Smith, D. R. Probing Dynamically Tunable Localized Surface Plasmon Resonances of Film-Coupled Nanoparticles by Evanescent Wave Excitation. *Nano Lett.* **2012**, *12*, 1757-1764.

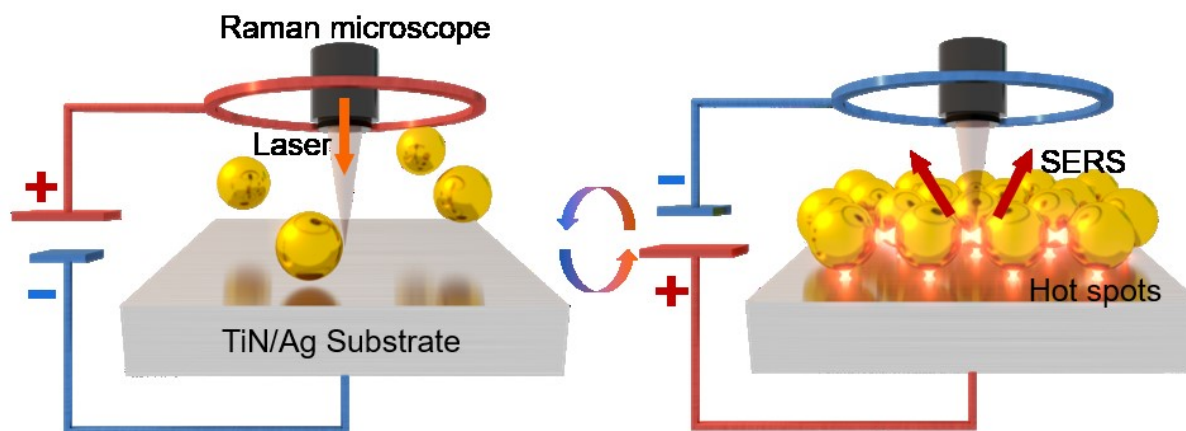
- (54) Di Martino, G.; Turek, V. A.; Lombardi, A.; Szabó, I.; de Nijs, B.; Kuhn, A.; Rosta, E.; Baumberg, J. J. Tracking Nanoelectrochemistry Using Individual Plasmonic Nanocavities. *Nano Lett.* **2017**, *17*, 4840-4845.
- (55) Montelongo, Y.; Sikdar, D.; Ma, Y.; McIntosh, A. J. S.; Velleman, L.; Kucernak, Anthony R.; Edel, J. B.; Kornyshev, A. A. Electrotunable Nanoplasmonic Liquid Mirror. *Nat. Mater.* **2017**, *16*, 1127-1135.
- (56) Sikdar, D.; Hasan, S. B.; Urbakh, M.; Edel, J. B.; Kornyshev, A. A. Unravelling the Optical Responses of Nanoplasmonic Mirror-on-Mirror Metamaterials. *Phys. Chem. Chem. Phys.* **2016**, *18*, 20486-20498.
- (57) Sikdar, D.; Kornyshev, A. A. Theory of Tailorable Optical Response of Two-Dimensional Arrays of Plasmonic Nanoparticles at Dielectric Interfaces. *Sci. Rep.* **2016**, *6*, 16.
- (58) Solovan, M. N.; Brus, V. V.; Maistruk, E. V.; Maryanchuk, P. D. Electrical and Optical Properties of Tin Thin Films. *Inorg. Mater.* **2014**, *50*, 40-45.
- (59) Dimitriadis, C. A.; Logothetidis, S.; Alexandrou, I. Schottky-Barrier Contacts of Titanium Nitride on N-Type Silicon. *Appl. Phys. Lett.* **1995**, *66*, 502-504.
- (60) V., N. G.; M., S. V.; Alexandra, B. Alternative Plasmonic Materials: Beyond Gold and Silver. *Adv. Mater.* **2013**, *25*, 3264-3294.
- (61) He, D.; Bligh, M. W.; Waite, T. D. Effects of Aggregate Structure on the Dissolution Kinetics of Citrate-Stabilized Silver Nanoparticles. *Environ. Sci. Technol.* **2013**, *47*, 9148-9156.
- (62) Massiani, Y.; Medjahed, A.; Picq, G. Photoelectrochemical Characterization of Oxidized Films of Titanium Nitride and Titanium Obtained by Reaction Sputtering. *Thin Solid Films* **1992**, *207*, 109-116.
- (63) Gelderman, K.; Lee, L.; Donne, S. W. Flat-Band Potential of a Semiconductor: Using the Mott-Schottky Equation. *J. Chem. Educ.* **2007**, *84*, 685.
- (64) Grahame, D. C. The Electrical Double Layer and the Theory of Electrocapillarity. *Chem. Rev.* **1947**, *41*, 441-501.
- (65) Morrison, S. R., *Electrochemistry at Semiconductor and Oxidized Metal Electrodes*. Morrison, S. R., Ed. Springer: New York, 2011; pp 119-149.
- (66) Li, C.-T.; Li, S.-R.; Chang, L.-Y.; Lee, C.-P.; Chen, P.-Y.; Sun, S.-S.; Lin, J.-J.; Vittal, R.; Ho, K.-C. Efficient Titanium Nitride/Titanium Oxide Composite Photoanodes for Dye-Sensitized Solar Cells and Water Splitting. *J. Mater. Chem. A* **2015**, *3*, 4695-4705.
- (67) McShane, C. M.; Choi, K.-S. Photocurrent Enhancement of n-Type Cu₂O Electrodes Achieved by Controlling Dendritic Branching Growth. *J. Am. Chem. Soc.* **2009**, *131*, 2561-2569.
- (68) Turek, V. A.; Cecchini, M. P.; Paget, J.; Kucernak, A. R.; Kornyshev, A. A.; Edel, J. B. Plasmonic Ruler at the Liquid-Liquid Interface. *ACS Nano* **2012**, *6*, 7789-7799.
- (69) Zagar, Z.; Rhys-Griffiths, R.; Podgornik, R.; Kornyshev, A. A. On the Voltage-Controlled Assembly of NP Arrays at Electrochemical Solid/Liquid Interfaces. **2018**, *arXiv:1810.05019*, arXiv.org e-Print archive.
- (70) Miura, T.; Seki, K. Diffusion Influenced Adsorption Kinetics. *J. Phys. Chem. B* **2015**, *119*, 10954-10961.
- (71) Kang, S.; Mathwig, K.; Lemay, S. G. Response Time of Nanofluidic Electrochemical Sensors. *Lab Chip* **2012**, *12*, 1262-1267.

4. Electro-variable surface enhanced Raman spectroscopy at solid-liquid interface

4.1. Abstract

Tuning the properties of optical metamaterials in real time is one of the grand challenges of photonics. Being able to do so will enable a new class of photonic materials for use in applications such as surface enhanced Raman spectroscopy and reflectors/absorbers. One strategy to achieving this goal is based on the electrovariable self-assembly and disassembly of two-dimensional nanoparticle arrays at a metal-liquid interface. As expected the structure results in plasmonic coupling between NPs in the array but perhaps as importantly between the array and the metal surface. In such a system the density of the nanoparticle array can be controlled by the variation of electrode potential. Due to the additive effect, less than 1 V variation of electrode potential can give rise to a dramatic simultaneous change in optical reflectivity from $\sim 93\%$ to $\sim 1\%$ and the amplification of the SERS signal by up to 5 orders of magnitude. The process allows for reversible tunability. These concepts are demonstrated in this chapter, using a platform based on the voltage-controlled assembly of 40 nm Au-nanoparticle arrays at a TiN/Ag electrode in contact with aqueous electrolyte. We show that all the physics underpinning the behaviour of this platform works precisely as suggested by the proposed theory, setting the electrochemical nanoplasmonics as a promising new direction in photonics research.

Please note that the theoretical fittings of reflectance spectra and theoretical SERS enhancement factors are contributed by Debabrata Sikdar. The major parts of this chapter were submitted for publication and are with referees as “Ye Ma, Debabrata Sikdar, Aleksandra Fedosyuk, Leonora Velleman, Daniel J. Klemme, Sang-Hyun Oh, Anthony R. Kucernak, Alexei A. Kornyshev, Joshua B. Edle, Electrotunable Nanoplasmonics for Amplified SERS Sensing”.



4.2. Introduction

The plasmonic coupling among metallic nanostructures under the excitation of incident light has not only drawn substantial theoretical interest¹⁻³, but also looks promising for applications in optical sensing⁴, solar energy⁵, biomedical therapy⁶ and especially SERS⁷⁻¹¹. The vibrational Raman fingerprints of target molecules can be enhanced several orders of magnitude, due to the synergic coupling of LSPR of NPs¹², surface modified planar substrates¹³ or a combination of both³. Previous reports based on deposited NPs¹⁴ or lithographic features^{7, 15} on dry substrates have beautifully demonstrated that the surrounding media¹⁶, metal species⁸, size¹⁷, shape¹⁸, interparticle distance^{16, 19} and the gap between the substrate and NPs³ are crucial for the resonance strength, frequency and the resultant SERS signals. The latter is caused by the local near-field enhancement ('hot spots') inside or around these nanostructures.

Some of those structures may be fixed/nanofabricated, others – self assembled. One of the challenging tasks, is, therefore, to adjust those structures in situ, to be able to rationally tune the intensity of hot spots for maximizing SERS signals.²⁰ Among many methods such as mechanically²¹ or thermally²²⁻²⁴ induced deformation of the nanostructures, or in the case of wet systems – changing pH²⁵ or chemical concentrations²⁶ of solution can reconfigure the NP assemblies. Particularly interesting is voltage-controlled tuning of the structure of adsorbed NP arrays at electrochemical interfaces. This causes minimal disturbance to the system, when tuning the plasmonic coupling. By applying different static²⁷ or dynamic²⁸ potentials on the substrate electrodes, researchers can either control the adsorption of ions^{28, 29} or, for potentials outside of the electrochemical windows of such systems, the electron exchange²⁷ between NP and the electrodes. Both can affect SERS signals. Our group has previously demonstrated voltage controlled self-assembly of arrays of moderate-size (16 nm) NPs at both liquid-liquid³⁰ and solid-liquid³¹ interfaces.

In this chapter, relatively large NPs (40 nm) onto an Ag electrode-substrate were successfully assembled within an optical-electrochemical cell. By controlling the electrode potential, both the reflectance and SERS signal can be optically tuned in real-time. With the help of optical reflectance theory, these spectra can be reproduced allowing us to reveal information about the structure of the NP array *in situ*. The variation of the structure was correlated with variation in the SERS. Thus the results presented below demonstrate fine tuning of interparticle gaps and the significant amplification of SERS signal. Compared with previously demonstrated SERS active substrates, our electrovariable SERS system allows for real-time tailorable nanostructures that can be reused.

4.3. Results and discussions

4.3.1. Working principle and experimental setup

As shown in **Figure 4.1**, to achieve the electro-tunability of the SERS signal, a planar 125 nm thick Ag substrate with 5 nm TiN coating is connected to the working electrode of a potentiostat. A Pt ring and an Ag/AgCl wire comprise the counter and reference electrode respectively in a three-electrode system. The setup was immersed into an electrochemical cell containing 4-Mercaptobenzoic acid (4-MBA) functionalized 40 ± 3 nm NP solution with 20 mM PBS and 20 mM LiCl. A Raman microscope was used to focus 0.81 mW 633 nm He-Ne laser onto the solid-liquid interfaces and to collect the Raman signal simultaneously. By replacing the Raman microscope with a fibre coupled reflectivity probe, the reflectance spectra of the interface can be additionally acquired. These reflectance spectra not only quantitatively demonstrate the dramatic colour changes during the electro-variable process which will be showed later, but provide vital structural information about the nanoscale rearrangement of NPs on the substrates once ‘decoded’ by our EMT³².

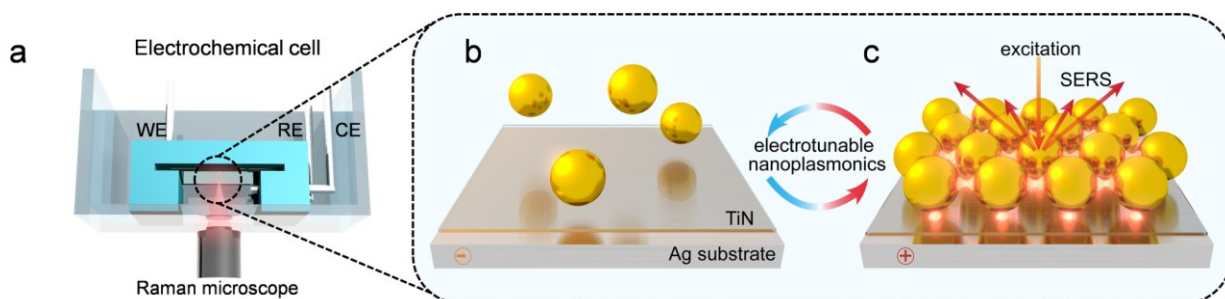


Figure 4.1 Scheme of the experimental setup of the optical-electrochemical cell (a) and the switchable assembly of 40 nm NPs, functionalized by negatively charged 4-MBA ligands, on TiN/Ag substrate under low (b) and high (c) applied voltage. The working electrode of the potentiostat is connected to the substrate, and a Raman microscope is focusing through an optically transparent electrochemical cell. When the applied positive potential of the substrate is low, few NPs are assembled, inducing weak Raman signal (left). Higher positive potential at the interface electrosorbs a monolayer array of NPs which generates Raman hot spots and delivers stronger SERS signals (right), the denser is the NP monolayer.

The potential of zero charge of the TiN/Ag substrate is an essential reference point during the whole electro-variable experiments.^{30, 31} By measuring the capacitance of the TiN/Ag under different frequencies, we found all the results (**Figure 4.2a**) following the Mott–Schottky law: $C_{SC}^{-2} \propto E - E_{PZC} - k_B T/e$, where C_{SC} is the capacitance of the space charge in TiN, E is the applied potential, E_{PZC} is the potential of zero charge, k_B is the Boltzmann constant, and T the absolute temperature. This linear relationship indicates that the space charge capacitance of the TiN layer dominates the overall capacitance. The PZC can be extracted as -0.8 V vs Ag/AgCl from the intercepts of these fitted lines. This PZC will be the prime reference during later discussions of potentials. The cyclic voltammetry was measured to ensure the maximum current would not exceed $10 \mu\text{A cm}^{-2}$ over the potential range where NPs were assembled (**Figure 4.2b**).

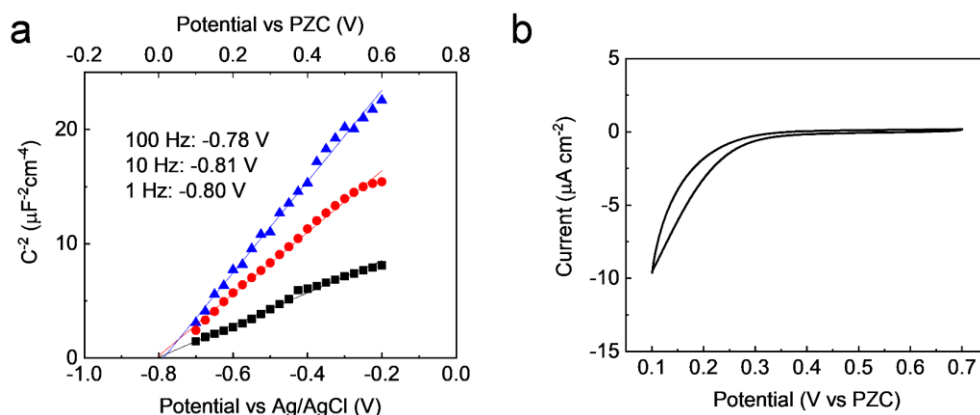


Figure 4.2 (a) Mott–Schottky plot for the capacitance of TiN/Ag electrode in 20 mM PBS, 20 mM LiCl aqueous solution, determining PZC as -0.8 V vs Ag/AgCl, under 1, 10, and 100 Hz impedance measurements. All the linear fittings ($C^{-2} \propto E - E_{PZC} - k_B T/e$) give a similar intercept. (b) Cyclic voltammogram of TiN/Ag in 20 mM PBS, 20 mM LiCl aqueous solution with 10 mV/s scanning rate.

When the potential applied on the substrate is low, an electrostatic energy barrier exists at the solid-liquid interface, repelling NPs away (**Figure 4.1b**). Lacking the plasmonic coupling between the substrate and NPs and among the NP array, the corresponding reflectance spectra have no difference from the pristine TiN/Ag (**Figure 4.3a-ii**, black and yellow curves). In addition, no MBA signal could be observed from the Raman spectra (**Figure 4.3b-ii**, yellow curve), since there is almost no MBA in the laser detecting volume and low enhancement of the Raman signal from the analyte molecules at planar TiN/Ag substrates.

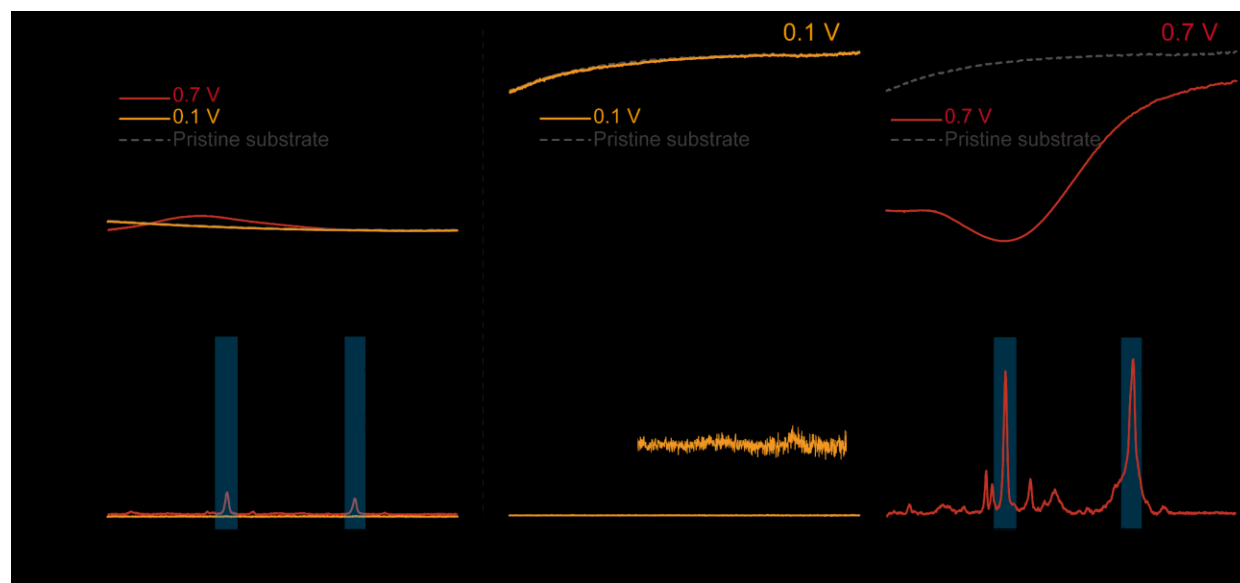


Figure 4.3 The experimental reflectance spectra (a) and SERS spectra (b) of NPs on TiN/glass at 0.1 and 0.7 V (i), NPs on TiN/Ag at 0.1 V (ii) and NPs on TiN/Ag at 0.7 V (iii). The inset of panel b-ii shows the 50× its original intensity. Comparison of these curves highlights the effect of complex plasmonic coupling between the nanoparticles and the substrate metal, which evolves with the increase of positive electrode potential that enhances the electroadsorption of NPs and give rise to denser NP array. The significantly enhanced characteristic peaks of 4-MBA at 1078 cm^{-1} and 1589 cm^{-1} indicates the effect of Raman hot spots in the system.

By switching the substrate to higher potential, for instance 0.7 V vs PZC, the attractive electrostatic forces between the positively charged substrate and the negatively charged NPs construct an energy well in the vicinity of the solid-liquid interfaces, assemble the NPs into a two-dimensional array on the substrate (**Figure 4.1c**). This structure affords two kinds of plasmonic coupling: 1) the coupling among the NP array and 2) between the substrate and NP array.

Characteristic reflectance and SERS signals arise from the formation of such structures. First, the plasmonic active NP array on the substrate almost totally quenched the reflectance at ~ 580 nm shown in **Figure 4.3a-iii**, red curve. Compared with previous studies using smaller, 16 nm NPs³¹, the reflectance dip here can be redshifted to 580 nm and deepened to -90 %. More importantly, SERS “hot spots” are formed not only among the NP array but also between the substrate and the array, where the Raman signals of 4-MBA are significantly enhanced. As shown in **Figure 4.3b-iii**, the red curve, when 0.7 V potential is applied the two characteristic Raman peaks for 4-MBA at 1078 cm^{-1} and 1589 cm^{-1} shoot up, corresponding to the ν_{12} and ν_{8a} aromatic ring vibrations from the adsorbed 4-MBA.³³

The plasmonic coupling between metallic NPs has been studied extensively, but the coupling between a metallic substrate and an electro-variable 2D NP array is still relatively new and intriguing from both experimental and theoretical viewpoints. Reflectance and SERS comparisons are made between the Au NP array on TiN/glass substrate [Panels (i) in **Figure 4.3**] and on TiN/Ag [Panels (ii) and (iii) in **Figure 4.3**]. It is easy to see a peak in the reflectance spectra of the NPs/TiN/glass at 0.7 V_{PZC} (**Figure 4.3a-i**), which is very much like that of an array of NPs at the liquid | liquid interface^{30, 34} showing the enhancement of reflectance for the wavelengths of the plasmon resonance in the array of gold NPs. The NP array on the Ag substrate under 0.7 V, however, quenches the reflectivity of the Ag substrate to such an extent that the reflectance around 580 nm is even lower than the lone NP array. Both effects are in accordance with our previous studies³⁰⁻³².

This exotic phenomenon of quenching of reflection on the NPs/TiN/Ag sample demonstrates the strong coupling between this large, 40-nm-NP array and the metallic substrate, which also gives rise to the enhancement of Raman signal. When the array of 4-MBA functionalized NPs is assembled on the TiN/glass substrate under 0.7 V, the sample gives a distinguishable Raman signal (~ 3000 counts at 1078 cm^{-1}) due to the coupling among the NPs (**Figure 4.3b-i**, red curve). By comparison, once those 4-MBA functionalized NPs are assembled onto the TiN/Ag substrate under 0.7 V, the intensity of the Raman peak increases by ~ 8.3 folds as compared with NPs on TiN/glass (**Figure 4.3b-iii**), highlighting the synergistic effect between the NP array and the Ag substrate.

4.3.2. Potential dependant reflectance and SERS

The detailed electro-tunable behaviours of this system were examined through reflectance and SERS when different potentials applied to the substrates. Though the drying process during the SEM sampling, at some extent, disturbs the arrangement of the wet NPs on the substrates, a qualitative view of the influence of the potential can still be pictured in **Figure 4.4**: with the increase of the potential, a surge of the NP population is clearly witnessed. This increased population and its resultant enhanced plasmonic coupling can be visualized by the dramatic changes in the macroscale colours of the wet samples shown in digital camera photos (inset of **Figure 4.4**). Starting from the original silver colour of the pristine substrate, higher potential delivers redder and darker appearance and ultimately a purplish black colour for the 0.7 V sample.

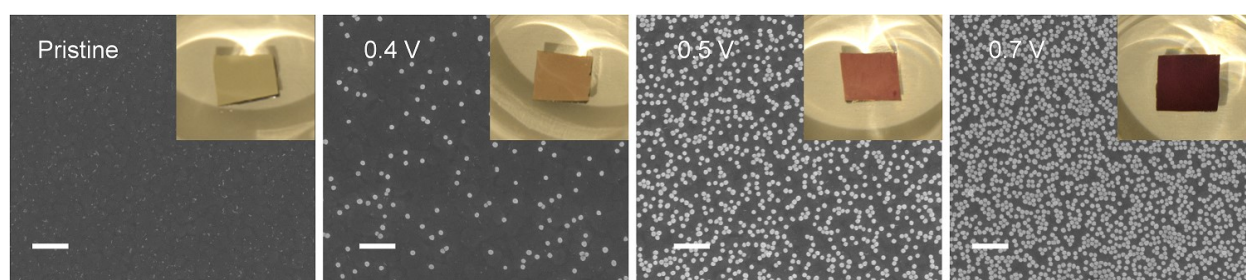


Figure 4.4 SEM of dried samples after NP assembling under indicated potentials; scale bar 200 nm; the white dots represent the adsorbed NPs, shown at the dark background of bare TiN/Ag substrate. Digital camera photos (insets) of wet samples after NP assembling on TiN/Ag under indicated potentials.

Reflectance measurements and theoretical calculations provide more quantitative insight for this electro-variable phenomenon. With the increase of the substrate potential, a distinctive reflectance dip gets deeper and red-shifted, as can be seen from excellently matched experimental and theoretical fitted spectra (**Figure 4.5a** and **b**). Within the lower potential region (<0.4 V), both the dip depth and dip wavelength (**Figure 4.5c**) change slowly. EMT is also employed in fitting the experimental curves. The parameters of Drude-Lorentz model in the system is listed in **Table 4.1**. Theoretical calculation (**Figure 4.6**) indicates that the interparticle distances in these cases are too large to generate effective plasmonic coupling.

Table 4.1 Parameters of the Drude-Lorentz model for Au, TiN, and Ag:

Material	ϵ_{∞}	$\omega_{p,D}$ (eV)	γ_D (eV)	δ_1	$\omega_{p1,L}$ (eV)	$\gamma_{1,L}$ (eV)	S_2	$\omega_{p2,L}$ (eV)	$\gamma_{2,L}$ (eV)
Au	5.9752	8.8667	0.03799	1.76	3.6	1.3	0.952	2.8	0.737
TiN [#]	2.667	10.707	0.195	0.195	2.264	0.722	5.312	4.894	3.875
Ag	3.718	9.2093	0.02	0.4242	4.284	0.737	-	-	-

[#]The parameters for TiN coating are slightly different to that of the bulk TiN, as these are fitted to match the measured optical reflectance from a bare 5 nm TiN coating on top of an Ag substrate.

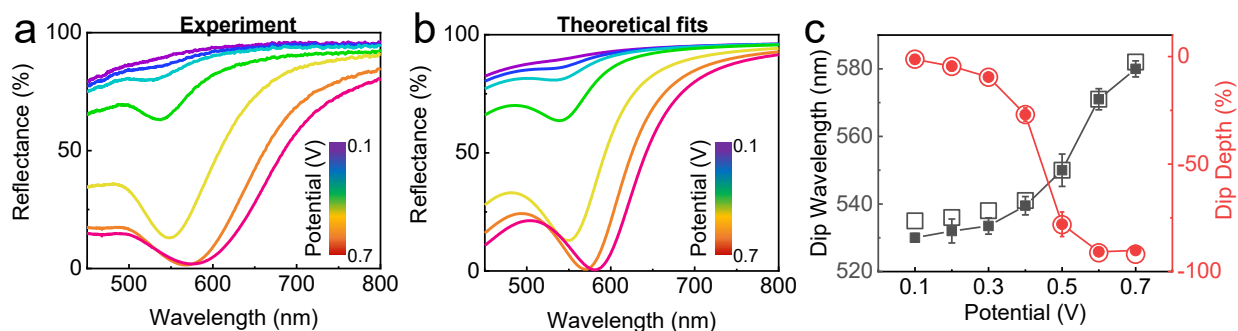


Figure 4.5 (a) Experimental reflectance spectra of assembling NPs on TiN/Ag under 0.1 – 0.7 V vs PZC. (b) Theoretically fitted reflectance spectra of assembling NPs on TiN/Ag under 0.1 – 0.7 V vs PZC. (c) The experimental (solid) and theoretically fitted (empty) dip wavelength (black squares) and dip depth (red dots) under 0.1 – 0.7 V vs PZC.

Further increase in potential induces dramatic optical changes: the dip wavelength red-shifts from 530 nm to 580 nm while the dip depth from almost zero to -92 %. This can be explained by the strong plasmonic coupling when NPs are getting closer with each other. The reason why they are getting closer was described by us already in Ref³¹. At positive electrode potentials, negatively charged NPs get electroadsorbed at the electrode, but as they electrostatically repel each other, they prefer not to come close to each other. With further increase of the positive potential, the driving force for each NPs to be adsorbed at the interface gets stronger, and more NPs adsorb at the electrode, tolerating interparticle repulsion, and hence the NP-array gets denser.³⁵ Theoretical calculation (**Figure 4.6**) indicates that the interparticle distance, starting from several hundreds of nm at 0.1 V, quickly reduces to 20 nm at 0.7 V.

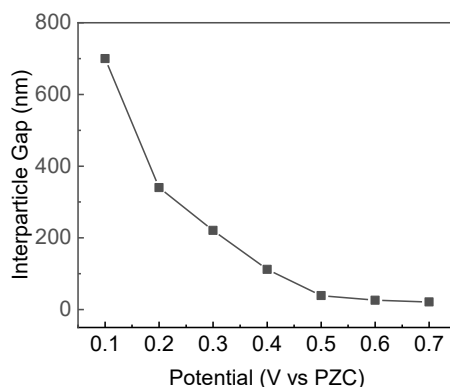


Figure 4.6 Theoretically calculated interparticle gap (red dots) under 0.1 – 0.7 V vs PZC

Based on the electromagnetic mechanism of SERS, the variation of the plasmonic coupling due to the change of the interfacial potential also offers a brand-new way to enhance the Raman signals. When the potential is low, the two characteristic peaks at 1078 cm^{-1} and 1589 cm^{-1} are almost indistinguishable from the base lines (**Figure 4.7a**). The intensity of these peaks climb gradually (in an almost linear fashion) when the potential is less than 0.4 V, but more instructive is the linear dependence on the density of the NP array, which is inversely proportional to the square of interparticle separation, shown in the inset in **Figure 4.7b**.

Such linear dependence shows that the increase in the SERS intensity here is just due to the increase of the population of NPs at the interface: each individual electroadsorbed NP delivers a hot spot between it and the substrate metal, but the hottest ones emerge only at closer approach of NPs due to the coupling of the localised plasmon excitations between the NPs, presumably amplified by the proximity to the metallic substrate. No manifestation of intensification of the SERS-signal beyond the one coming out from the mere increase of NPs for low electrode potentials means the absence of any noticeable interparticle coupling at the corresponding interparticle distances, in perfect correlation with the reflectivity data.

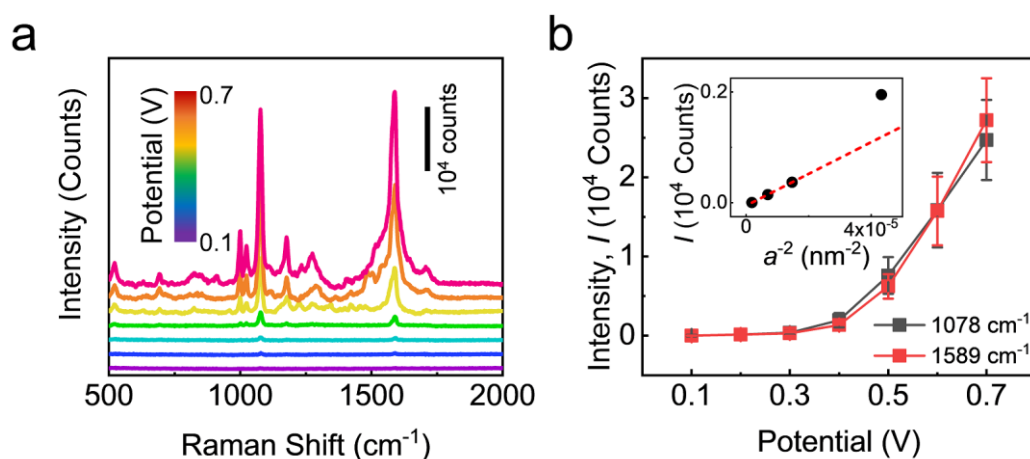


Figure 4.7 (a) Experimental Raman spectra of MBA from the NP array on TiN/Ag under 0.1 – 0.7 V vs PZC. (b) The intensity of characteristic Raman peaks of MBA at 1078 cm^{-1} (black) and 1589 cm^{-1} (red) under 0.1 – 0.7 V vs PZC. Inset shows the Raman peak intensity (I) vs the inverse of the square of the interparticle distance (a^{-2}), extracted from fitting the reflectance data to the theory (c.f. Figure 4.6), in the interval of 0.1 V between 0.1 - 0.4 V. A good linear fit from 0.1 to 0.3 V indicates very weak interparticle coupling under low potentials, because the increase in the signal (hardly noticeable in the main graph) is just due to increase of the number of particles on the surface delivering hot spots that form between individual NPs and the substrate metal.

All in all, the SERS signal should obviously increase with the increasing number of NPs on the substrate, due to increased electrostatic energy trap, thereby increasing the net number of associated 4-MBA Raman-reporters within the detection volume. However, as the interparticle gap is large within this potential range (**Figure 4.6**), the coupling between NPs is negligible and so does the increase of the corresponding experimental enhancement factor (**Figure 4.8**), $EF = \frac{I_{\text{SERS}}/N_{\text{SERS}}}{I_{\text{RS}}/N_{\text{RS}}}$ [where I_{SERS} and I_{RS} denote the intensity of SERS and Raman signals, N_{SERS} and N_{RS} are the numbers of molecules generating SERS and Raman signals, respectively]. As the potential increases beyond 0.4 V, the intensities of the peaks rocket to ~ 25000 counts at 0.7 V; both the experimental and theoretical EFs surge quickly to reach beyond 10^5 level at 0.7 V. This means that the amplification of the SERS signal benefits majorly not only from the increased number of NPs and 4-MBA molecules, but from the ever-growing plasmonic coupling with gradual red-shift of LSPR towards the excitation laser wavelength.³⁶

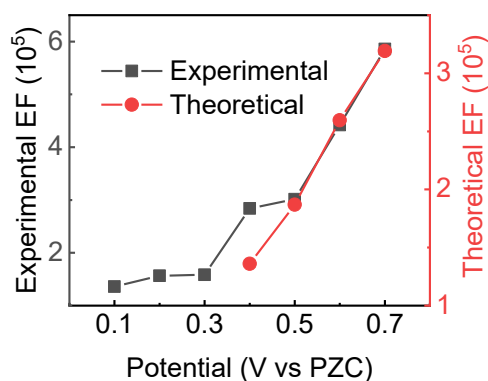


Figure 4.8 Experimental (black squares) and theoretically calculated (red dots) SERS enhancement factor (EF) under 0.1 – 0.7 V vs PZC. The theoretical EF is not calculated below 0.3 V because the gaps are too large to return converging results.

It can be noticed that the experimental EFs are slightly larger than the theoretical ones, where perfectly spherical NPs in a uniform hexagonal lattice is considered for modelling. Considering the existence of edges/spikes on our fabricated NPs and the fact that interparticle gaps may have some dispersion and spatial non-uniformity, a small population of NPs with narrow local interparticle gaps could generate much stronger SERS signals that would contribute to larger experimental values of EF.^{18, 26}

4.3.3. Dynamics of the electro-variable SERS

The time evolution of the optical response and SERS signals were also monitored during the potential controlled assembly of NPs on the substrates. **Figure 4.9a** and **b** demonstrate the experimental and theoretically fitted reflectance spectra over 10 h when both the dip wavelength and dip depth first experience a fast evolution stage before reaching the equilibrium plateau at the 580 nm wavelength and -92 % dropped-down intensity (**Figure 4.9c**). A similar trend in plateauing can be found in the theoretically calculated interparticle gaps (**Figure 4.10**). Compared to similar systems with smaller NPs, the time of reaching the equilibrium for our 40 nm NPs is longer, due to their larger diameter and correspondingly smaller diffusion coefficient (usually following the Stokes–Einstein equation³⁷). Nevertheless, higher NP concentrations and shorter diffusion lengths in miniaturized setups could accelerate this process for practical applications.

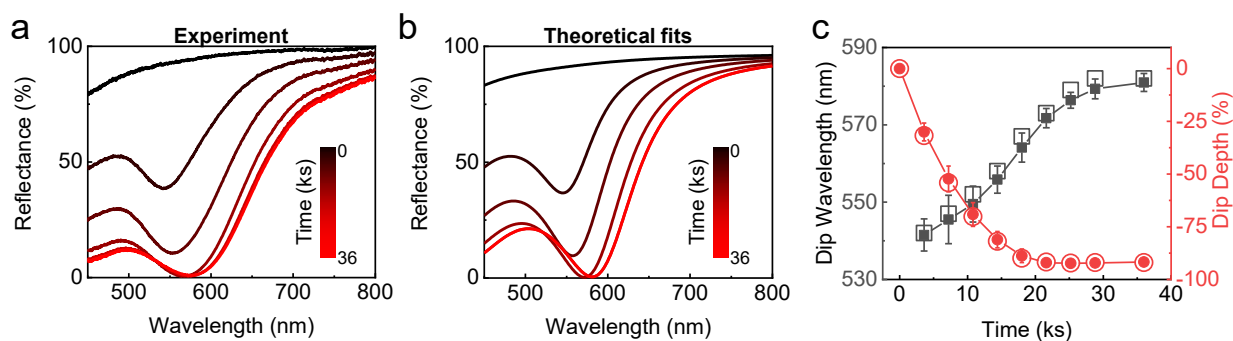


Figure 4.9 Kinetics of the NP assembly triggered by applying 0.7 V vs PZC and the time-evolution of resultant optical signals. (a) The time-dependent reflectance spectra of NPs electrosorbed on TiN/Ag in 20 mM PBS, 20 mM LiCl NP solution, under 0.7 V vs

PZC, starting from pristine TiN/Ag. (b) The theoretically fitted time-dependent reflectance spectra of NPs assembling on TiN/Ag. (c) The time-dependent experimental (solid), theoretically fitted (empty) dip wavelength (black squares) and dip depth (red dots).

It should be emphasized again, that as we have seen first in **Figures 4.3a, 4.5a and 4.9a** demonstrate the counter-intuitive effect of complete quenching of reflection from an array of large NPs on metallic substrates at the wavelength of the coupled plasmon resonance, the signatures of which have been predicted earlier theoretically.^{32, 38, 39}

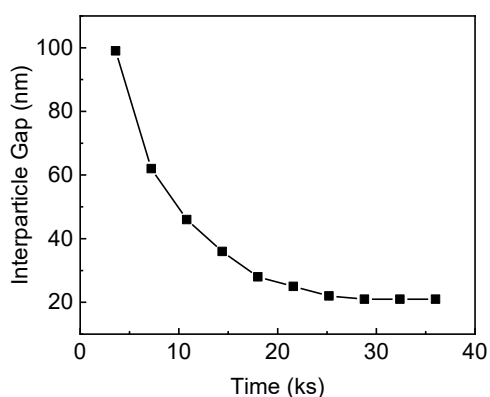


Figure 4.10 Theoretically calculated interparticle gap during the NP assembly process.

Back to the signal evolution, the change of the SERS signals follows a slightly different pattern after the abrupt application of the positive bias (**Figure 4.11a**). Unlike the fast quenching process of the reflectivity in the initial stage, the intensities of the Raman peaks grow relatively slow (**Figure 4.11b**). Generally speaking, the plasmonic coupling and the resultant Raman enhancement prevail only when the gaps between NPs are below the NP diameter.⁴⁰ Considering the interparticle gaps in the first 14 ks is still larger than this value (**Figure 4.10**), the Raman hot spots in these gaps are still too weak to generate a noticeable enhanced Raman signals than the individual NPs. However, this hot spot effect becomes more dominant after 14 ks when the gap falls below 40 nm. The calculated experimental and theoretical EFs in **Figure 4.11c** support this observation.

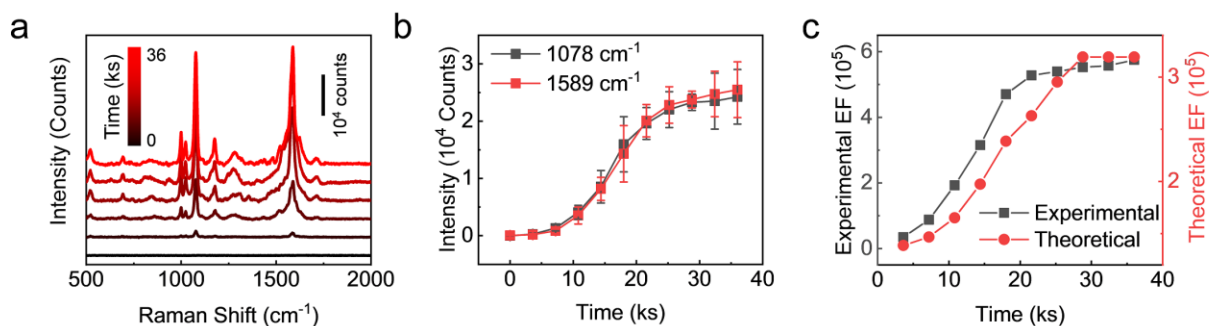


Figure 4.11 (a) The time-dependent SERS spectra of 4-MBA attached to NPs assembling on TiN/Ag in 20 mM PBS 20 mM LiCl NP solution under 0.7 V vs PZC, starting from pristine TiN/Ag. (b) The corresponding experimental time-dependent intensity of characteristic SERS peaks of 4-MBA at 1078 cm^{-1} (black) and 1589 cm^{-1} (red). (c) The time-dependent experimental (black squares) and theoretically calculated (red dots) SERS enhancement factors (EF) under 0.7 V vs PZC.

4.3.4. Reversibility

The electro-tunability and reversibility of SERS signal is always desirable for reusable sensors, for lasers with different working frequencies or sensing different analytes. Though larger NPs provide stronger SERS amplifications, it is harder to achieve reversibility with larger NPs as compared to smaller ones, due to the slow diffusion speed of the former.⁴¹ Here by alternatively applying ± 0.7 V vs PZC to the substrate, the turning on and off of the system for multiple times was partially achieved. As shown in **Figure 4.12a**, under the ‘off state’ at -0.7 V, the plain substrate has a pink tint and the red letter ‘IC’ (standing for Imperial College) above the substrate is reflected distinctively. In contrast to that, the substrate becomes almost black and the ‘IC’ is overwhelmed by the dark background under the ‘on state’ at 0.7 V.

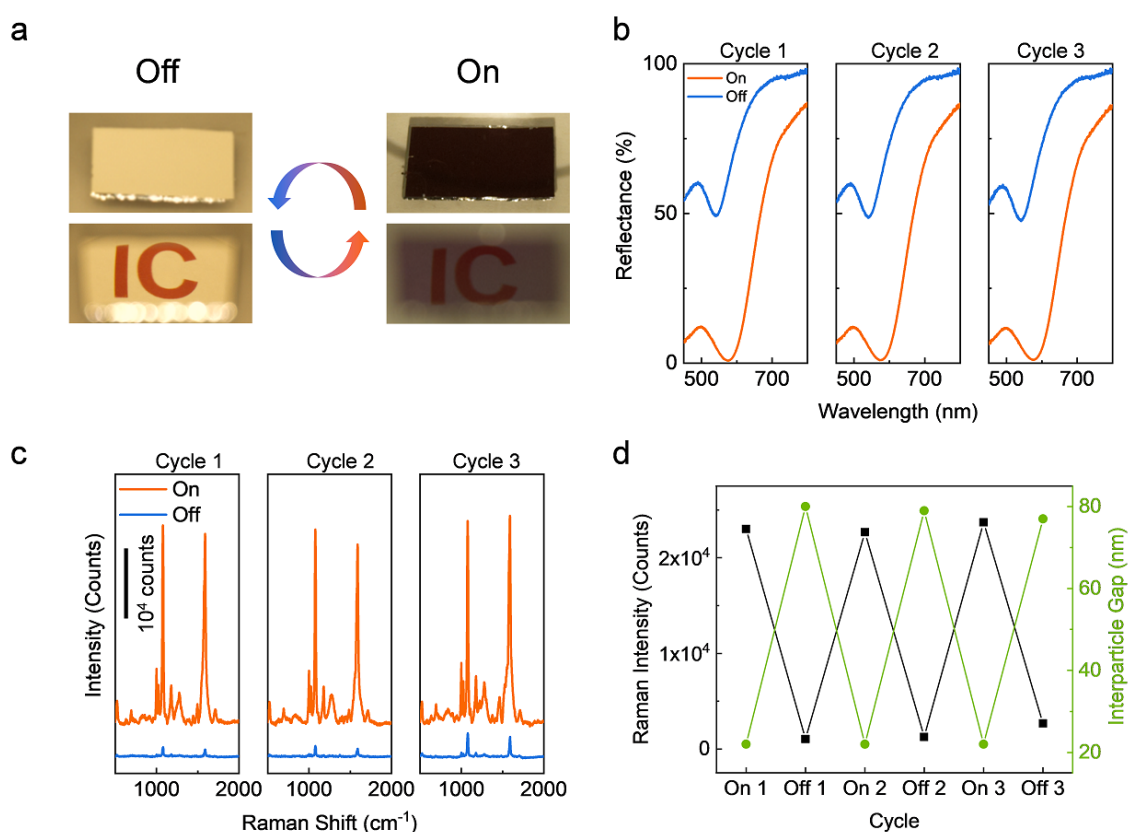


Figure 4.12 Reversible switching of the NP/TiN/Ag system. To switch off the system, a low potential (-0.7 V vs PZC) is applied to the substrate and maintained for 5 min. (a) The digital camera photos of the ‘off’ and ‘on’ states of the system in solution with plain (upper), and “IC” reflected (lower) images. The letters are drawn on A4 paper in red and are illuminated by white light. (b) Reflectance spectra of NP array on TiN/Ag substrate during multiple on/off cycles. (c) Raman spectra of 4-MBA from NP array on TiN/Ag substrate during multiple on/off cycles. (d) The Raman intensity and the calculated interparticle gaps for multiple on/off cycles.

The reflectance spectra within three cycles in **Figure 4.12b** demonstrate that the ‘on’ state is always reversible while we encountered some difficulties with completely repelling the NPs away at ‘off state’. Indeed, a small reflectance dip is persistent on all the three cycles, meaning a small number of NPs are permanently stuck on the solid-liquid interface under the present conditions, which may result from the

strong Van der Waals forces between the NPs and the substrate. [Note that, in Ref³¹ for smaller NPs, signatures of the activation barrier for NPs to leave the TiN/Ag surface in kinetic desorption isotherms was noticed. These barriers may be even higher for larger NPs]. Raman signals, on the contrary, in Figure 4.12c show almost complete reversibility. Theoretical calculation provides further evidence in Figure 4.12d that the ‘off state’ returns to an 80 nm interparticle gap, meaning the majority of NPs indeed has left the interface, but still leaving some behind.

4.4. Conclusions

The optical responses of the electrically assembled array of Au NPs on TiN/Ag electrode under different electrode potentials was investigated. Increasing positive polarization of the electrode stimulates adsorption of negatively charged nanoparticles, decreasing interparticle separations in the array. The narrowing the interparticle gaps strengthens the plasmonic coupling between NPs. As a consequence, it produces three related effects: 1. The emergence of the dip in reflection spectrum, which gets deeper and its wavelength shifts to the red with densification of the NP array (for dense NP arrays, at the dip minimum, the reflection is gone). 2. Emergence and further intensification of ‘hot spots’ (for electric field of electromagnetic radiation) between NPs, in addition to the hot spots between individual NPs and the substrate. 3. The red-shifting of the coupled plasmon resonance of the thus assembled NPs towards the wavelength of Raman excitation laser further amplifies SERS signal from analytes attached to NPs.

The theory of the optical reflection signal from such systems allows to quantify the values of interparticle gaps at any applied potential and use this information to estimate the SERS enhancement factor. The SERS data appears to be in full harmony with the reflectivity data.

The experimental results show for the first time the earlier theoretically predicted counter-intuitive phenomenon — complete quenching of reflection from an array of large NPs on metallic substrates at the wavelength of the coupled plasmon resonance.

Thanks to the strength of the observed effects, the convenience of the used electrochemical method, and the reversibility of the switching — this electrovariable plasmonic system provides a prototype for future versatile and sensitive re-configurable SERS sensors and switchable mirror-absorber platforms.

4.5. References

(1) Sikdar, D.; Kornyshev, A. A. Theory of Tailorable Optical Response of Two-Dimensional Arrays of Plasmonic Nanoparticles at Dielectric Interfaces. *Sci. Rep.* **2016**, *6*, 33712.

- (2) Solís, D. M.; Taboada, J. M.; Obelleiro, F.; Liz-Marzán, L. M.; García de Abajo, F. J. Optimization of Nanoparticle-Based SERS Substrates through Large-Scale Realistic Simulations. *ACS Photonics* **2017**, *4*, 329-337.
- (3) Nayak, D. R.; Bhat, N.; Venkatapathi, M.; Umapathy, S. Signal Enhancement from Tunable SERS Substrates: Design and Demonstration of Multiple Regimes of Enhancement. *J. Phys. Chem. C* **2018**, *122*, 9134-9140.
- (4) Stewart, M. E.; Anderton, C. R.; Thompson, L. B.; Maria, J.; Gray, S. K.; Rogers, J. A.; Nuzzo, R. G. Nanostructured Plasmonic Sensors. *Chem. Rev.* **2008**, *108*, 494-521.
- (5) Giannini, V.; Fernandez-Dominguez, A. I.; Heck, S. C.; Maier, S. A. Plasmonic Nanoantennas: Fundamentals and Their Use in Controlling the Radiative Properties of Nanoemitters. *Chem. Rev.* **2011**, *111*, 3888-3912.
- (6) Jain, P. K.; Huang, X. H.; El-Sayed, I. H.; El-Sayed, M. A. Noble Metals on the Nanoscale: Optical and Photothermal Properties and Some Applications in Imaging, Sensing, Biology, and Medicine. *Acc. Chem. Res.* **2008**, *41*, 1578-1586.
- (7) Liu, B.; Yao, X.; Chen, S.; Lin, H.; Yang, Z.; Liu, S.; Ren, B. Large-Area Hybrid Plasmonic Optical Cavity (HPOC) Substrates for Surface-Enhanced Raman Spectroscopy. *Adv. Funct. Mater.* **2018**, *28*, 1802263.
- (8) Wang, X. T.; Ma, G. S.; Li, A. R.; Yu, J.; Yang, Z.; Lin, J.; Li, A.; Han, X. D.; Guo, L. Composition-Adjustable Ag-Au Substitutional Alloy Microcages Enabling Tunable Plasmon Resonance for Ultrasensitive SERS. *Chem. Sci.* **2018**, *9*, 4009-4015.
- (9) Xu, Y.; Konrad, M. P.; Lee, W. W. Y.; Ye, Z.; Bell, S. E. J. A Method for Promoting Assembly of Metallic and Nonmetallic Nanoparticles into Interfacial Monolayer Films. *Nano Lett.* **2016**, *16*, 5255-5260.
- (10) Su, D.; Jiang, S. L.; Yu, M. N.; Zhang, G. Z.; Liu, H.; Li, M. Y. Facile Fabrication of Configuration Controllable Self-Assembled Al Nanostructures as UV SERS Substrates. *Nanoscale* **2018**, *10*, 22737-22744.
- (11) Tian, L.; Su, M.; Yu, F.; Xu, Y.; Li, X.; Li, L.; Liu, H.; Tan, W. Liquid-State Quantitative SERS Analyzer on Self-Ordered Metal Liquid-Like Plasmonic Arrays. *Nat. Commun.* **2018**, *9*, 3642.
- (12) Su, M.; Li, X.; Zhang, S.; Yu, F.; Tian, L.; Jiang, Y.; Liu, H. Self-Healing Plasmonic Metal Liquid as a Quantitative Surface-Enhanced Raman Scattering Analyzer in Two-Liquid-Phase Systems. *Anal. Chem.* **2019**, *91*, 2288-2295.
- (13) Srituravanich, W.; Fang, N.; Sun, C.; Luo, Q.; Zhang, X. Plasmonic Nanolithography. *Nano Lett.* **2004**, *4*, 1085-1088.
- (14) Ding, L.; Gao, Y.; Di, J. A Sensitive Plasmonic Copper(II) Sensor Based on Gold Nanoparticles Deposited on ITO Glass Substrate. *Biosens. Bioelectron.* **2016**, *83*, 9-14.
- (15) Yan, B.; Thubagere, A.; Premasiri, W. R.; Ziegler, L. D.; Dal Negro, L.; Reinhard, B. M. Engineered SERS Substrates with Multiscale Signal Enhancement: Nanoparticle Cluster Arrays. *ACS Nano* **2009**, *3*, 1190-1202.
- (16) Kim, I. H.; Kim, J. H.; Choi, J. Y.; Shin, C. H.; Kim, J. H.; Bae, G. T.; Shin, K. S. Tuning the Interparticle Distances in Self-Assembled Gold Nanoparticle Films With Their Plasmonic Responses. *Chem. Phys. Lett.* **2019**, *715*, 91-99.
- (17) Ashley, M. J.; Bourgeois, M. R.; Murthy, R. R.; Laramy, C. R.; Ross, M. B.; Naik, R. R.; Schatz, G. C.; Mirkin, C. A. Shape and Size Control of Substrate-Grown Gold Nanoparticles for Surface-Enhanced Raman Spectroscopy Detection of Chemical Analytes. *J. Phys. Chem. C* **2018**, *122*, 2307-2314.
- (18) Huang, Z. L.; Meng, G. W.; Hu, X. Y.; Pan, Q. J.; Huo, D. X.; Zhou, H. J.; Ke, Y.; Wu, N. Q. Plasmon-tunable Au@Ag Core-Shell Spiky Nanoparticles for Surface-Enhanced Raman Scattering. *Nano Res.* **2019**, *12*, 449-455.
- (19) Du, Y. X.; Wei, W.; Zhang, X. W.; Li, Y. B. Tuning Metamaterials Nanostructure of Janus Gold Nanoparticle Film for Surface-Enhanced Raman Scattering. *J. Phys. Chem. C* **2018**, *122*, 7997-8002.
- (20) Edel, J. B.; Kornyshev, A. A.; Kucernak, A. R.; Urbakh, M. Fundamentals and Applications of Self-Assembled Plasmonic Nanoparticles at Interfaces. *Chem. Soc. Rev.* **2016**, *45*, 1581-1596.

- (21) Laible, F.; Gollmer, D. A.; Dickreuter, S.; Kern, D. P.; Fleischer, M. Continuous Reversible Tuning of the Gap Size and Plasmonic Coupling of Bow Tie Nanoantennas on Flexible Substrates. *Nanoscale* **2018**, *10*, 14915-14922.
- (22) Lu, X. F.; Huang, Y. J.; Liu, B. Q.; Zhang, L.; Song, L. P.; Zhang, J. W.; Zhang, A. F.; Chen, T. Light-Controlled Shrinkage of Large-Area Gold Nanoparticle Monolayer Film for Tunable SERS Activity. *Chem. Mat.* **2018**, *30*, 1989-1997.
- (23) Han, F.; Vivekchand, S. R. C.; Soeriyadi, A. H.; Zheng, Y.; Gooding, J. J. Thermoresponsive Plasmonic Core-Satellite Nanostructures with Reversible, Temperature Sensitive Optical Properties. *Nanoscale* **2018**, *10*, 4284-4290.
- (24) Ma, Y.; Sikdar, D.; Fedosyuk, A.; Velleman, L.; Zhao, M.; Tang, L.; Kornyshev, A. A.; Edel, J. B. An Auxetic Thermo-Responsive Nanoplasmonic Optical Switch. *ACS Appl. Mater. Interfaces* **2019**, *11*, 22754-22760.
- (25) Curtis, T.; Taylor, A. K.; Alden, S. E.; Swanson, C.; Lo, J.; Knight, L.; Silva, A.; Gates, B. D.; Emory, S. R.; Rider, D. A. Synthesis and Characterization of Tunable, pH-Responsive Nanoparticle-Microgel Composites for Surface-Enhanced Raman Scattering Detection. *ACS Omega* **2018**, *3*, 10572-10588.
- (26) Velleman, L.; Scarabelli, L.; Sikdar, D.; Kornyshev, A. A.; Liz-Marzan, L. M.; Edel, J. B. Monitoring Plasmon Coupling and SERS Enhancement through in Situ Nanoparticle Spacing Modulation. *Faraday Discuss.* **2017**, *205*, 67-83.
- (27) Di Martino, G.; Turek, V. A.; Lombardi, A.; Szabó, I.; de Nijs, B.; Kuhn, A.; Rosta, E.; Baumberg, J. J. Tracking Nanoelectrochemistry Using Individual Plasmonic Nanocavities. *Nano Lett.* **2017**, *17*, 4840-4845.
- (28) Byers, C. P.; Hoener, B. S.; Chang, W.-S.; Link, S.; Landes, C. F. Single-Particle Plasmon Voltammetry (spPV) for Detecting Anion Adsorption. *Nano Lett.* **2016**, *16*, 2314-2321.
- (29) Zdaniauskienė, A.; Charkova, T.; Matulaitienė, I.; Eicher-Lorka, O.; Matijoška, A.; Skapas, M.; Selskis, A.; Niaura, G. Electrochemical Shell-Isolated Nanoparticle-Enhanced Raman Spectroscopy: Bonding, Structure, and Ion-Pairing of the Positive Charge Bearing Pyridinium Ring Terminated Monolayer at Smooth Gold Electrode. *J. Phys. Chem. C* **2018**, *122*, 1234-1242.
- (30) Montelongo, Y.; Sikdar, D.; Ma, Y.; McIntosh, A. J. S.; Velleman, L.; Kucernak, Anthony R.; Edel, J. B.; Kornyshev, A. A. Electrotunable Nanoplasmonic Liquid Mirror. *Nat. Mater.* **2017**, *16*, 1127-1135.
- (31) Ma, Y.; Zagar, C.; Klemme, D. J.; Sikdar, D.; Velleman, L.; Montelongo, Y.; Oh, S.-H.; Kucernak, A. R.; Edel, J. B.; Kornyshev, A. A. A Tunable Nanoplasmonic Mirror at an Electrochemical Interface. *ACS Photonics* **2018**, *5*, 4604-4616.
- (32) Sikdar, D.; Hasan, S. B.; Urbakh, M.; Edel, J. B.; Kornyshev, A. A. Unravelling the Optical Responses of Nanoplasmonic Mirror-on-Mirror Metamaterials. *Phys. Chem. Chem. Phys.* **2016**, *18*, 20486-20498.
- (33) Orendorff, C. J.; Gole, A.; Sau, T. K.; Murphy, C. J. Surface-Enhanced Raman Spectroscopy of Self-Assembled Monolayers: Sandwich Architecture and Nanoparticle Shape Dependence. *Anal. Chem.* **2005**, *77*, 3261-3266.
- (34) Velleman, L.; Sikdar, D.; Turek, V. A.; Kucernak, A. R.; Roser, S. J.; Kornyshev, A. A.; Edel, J. B. Tuneable 2d Self-Assembly of Plasmonic Nanoparticles at Liquid|Liquid Interfaces. *Nanoscale* **2016**, *8*, 19229-19241.
- (35) Zagar, Z.; Rhys-Griffiths, R.; Podgornik, R.; Kornyshev, A. A. On the Voltage-Controlled Assembly of NP Arrays at Electrochemical Solid/Liquid Interfaces. **2018**, *arXiv:1810.05019*, arXiv.org e-Print archive.
- (36) Willets, K. A.; Duynes, R. P. V. Localized Surface Plasmon Resonance Spectroscopy and Sensing. *Annu. Rev. Phys. Chem.* **2007**, *58*, 267-297.
- (37) Kalathi, J. T.; Yamamoto, U.; Schweizer, K. S.; Grest, G. S.; Kumar, S. K. Nanoparticle Diffusion in Polymer Nanocomposites. *Phys. Rev. Lett.* **2014**, *112*, 108301.
- (38) Kornyshev, A. A.; Marinescu, M.; Paget, J.; Urbakh, M. Reflection of Light by Metal Nanoparticles at Electrodes. *Phys. Chem. Chem. Phys.* **2012**, *14*, 1850-1859.

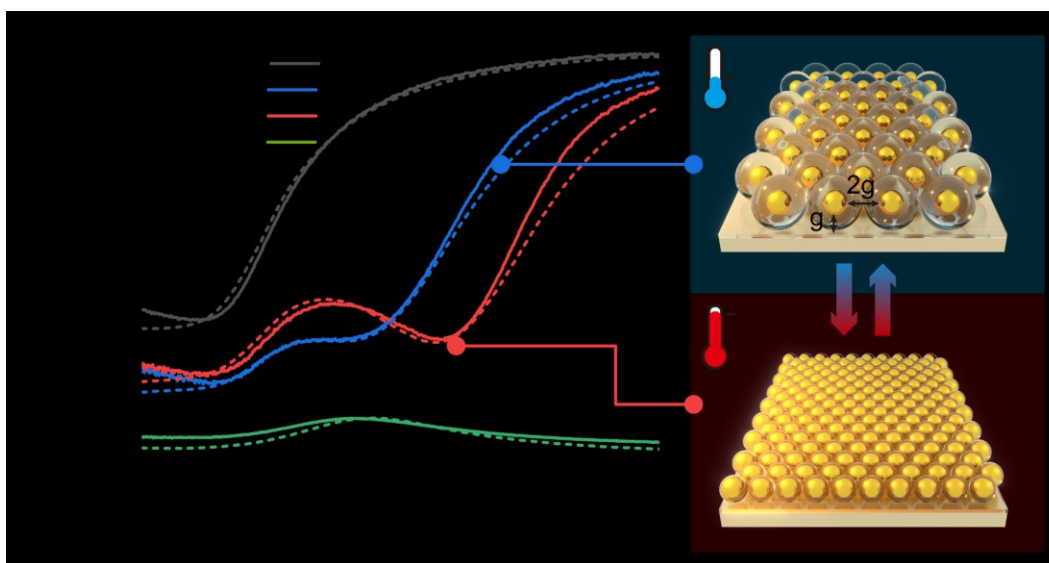
- (39) Truong, V. V.; de Dormale, B. Optical Absorption in Overcoats of Nanoparticle Arrays on a Metallic Substrate. *Plasmonics* **2011**, *6*, 195-200.
- (40) Ru, E. C. L.; Etchegoin, P. G. Single-Molecule Surface-Enhanced Raman Spectroscopy. *Annu. Rev. Phys. Chem.* **2012**, *63*, 65-87.
- (41) Booth, S. G.; Dryfe, R. A. W. Assembly of Nanoscale Objects at the Liquid/Liquid Interface. *J. Phys. Chem. C* **2015**, *119*, 23295-23309.

5. Thermo-responsive metasurface based on the coupling among metallic nanoparticle array and substrate

5.1. Abstract

Development and use of metamaterials have been gaining prominence in large part due to the possibility of creating platforms with ‘disruptive’ and unique optical properties. However, to date the majority of such systems produced using micro or nanotechnology, are static and can only perform certain target functions. Next-generation multifunctional smart optical metamaterials are expected to have tuneable elements with the possibility of controlling the optical properties in real time via variation in parameters such as pressure, mechanical stress, voltage, or through non-linear optical effects. Here, we address this challenge by developing a *thermally controlled optical switch*, based on the self-assembly of poly(N-isopropylacrylamide)-functionalised gold nanoparticles on a planar macroscale gold substrate. This chapter shows that such meta-surfaces can be tuned to exhibit substantial changes in the optical properties both in terms of wavelength and intensity, through the temperature-controlled variation of the interparticle distance within the nanoparticle monolayer as well as its separation from the substrate. This change is based on temperature induced auxetic expansion and contraction of the functional ligands. Such a system has potential for numerous applications, ranging from thermal sensors to regulated light harnessing.

Please note that the theoretical fittings of the reflectance spectra and calculated interparticle distances are contributed by Debabrata Sikdar. The major parts of this chapter were previously published in Ref.¹



5.2. Introduction

Tunable metamaterials are at the forefront of the expanding area of photonics.²⁻⁵ Their programmable and responsive nature has resulted in the fabrication of exceptionally versatile platforms with applications in sensors⁶⁻⁸, displays⁹, and cloaking¹⁰ amongst others. NPs on metallic substrates (NPoMS), holds promise for achieving tunability. The coupling between dissipating localized plasmons of NPs and surface plasmons on the metallic substrate can be tuned statically by the size, shape and materials of the two components.¹¹ However, as important but often neglected is the significance of the substrate-to-NP array distance which contributes heavily to their spectral properties. Furthermore, if such parameters can be controlled dynamically, it becomes possible to tune the optical response in real-time.^{12, 13} For example, it has been shown that tuning optical properties can be achieved via piezo actuation¹⁴ or mechanical stretching/shrinking of elastic quasi-2d-films.^{15, 16} Another example is the voltage controlled assembly and disassembly of NP arrays at electrochemical liquid/liquid or solid/liquid interfaces.^{17, 18} It was shown that one can reversibly assemble and disassemble NP arrays when the potential of the substrate is switched. This could also be used to tune the interparticle distance and as a result the reflectance spectra.¹⁸ Similarly, assembly/disassembly of NPs at an electrochemical interface of two immiscible electrolytic solutions, can be used to build an electro-switchable mirror /window metasurface.¹⁷ Alternatively by oxidizing or charging the spacer between NPs and substrate, researchers also confirmed that the gap width can induce intriguing changes in the scattering¹² and Raman¹⁹ signals. Theoretical calculation have estimated that these plasmonic effects could be further enhanced by tuning both the interparticle distance within a NP array and the gap width between the NP array and the substrate, at the same time.²⁰ However, *fast* real-time control of these optical ‘switches’ remains a challenge.

Alternative plasmonic switches, providing similar function, are based on a nontrivial, thermo-auxetic mechanism, which has relatively fast response times. Its key component is Poly(N-isopropylacrylamide) (pNIPAM), which is a water-soluble thermo-responsive polymer that had been widely used for various sensors and actuators, due to its desired operating temperature and sharp transition (within ~ 5 °C) and good reversibility around its lower critical solution temperature (LCST).^{21, 22} Below the LCST (~ 32 °C), the hydrogen bonds between the water molecules and the C=O and N-H groups on pNIPAM dominate, rendering the chains of pNIPAM extended (**Figure 5.1a**).²³ Above the LCST, the hydrogen bonds break, and the interaction of hydrophobic methyl groups and the main-chain hydrocarbons with each other results in a more coiled conformation.²³ By functionalizing NPs or substrates with pNIPAM, a temperature dependent change in ligand length can be achieved resulting in an excellent means for auxetically tuning the structure and the resultant optical properties. Typical strategies involve utilizing this polymer to anchor plasmonic NPs randomly into another polymer matrix²⁴, on micro-gel²⁵ or in bulk solutions²⁶. The optical

signal can be manipulated when a three-dimensional change of thermo-responsive polymer reduces/increases the interparticle distance, though the relatively rough control over the coupling between NPs could induce peak broadening or restricting tunability.^{24, 27-30} Another more versatile approach is to coat the NPs with pNIPAM^{21, 31} and even use them at a liquid-liquid interface.³² To date there have been no works reported where both the interparticle and gap-to-substrate distance within a monolayer array of thermally responsive NPs has been used to tune to the optical properties.

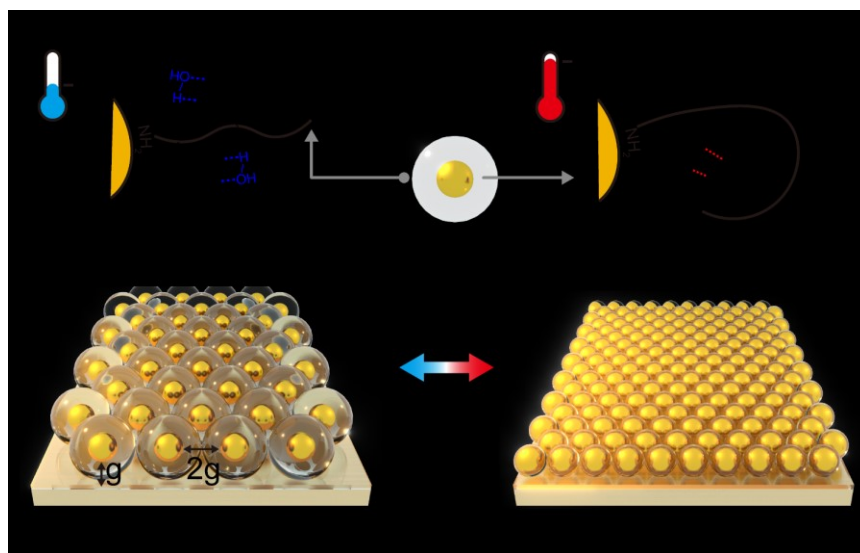


Figure 5.1 Molecular scale (a) and nanoscale (b & c) scheme of the swelling (left, cold)/shrinking (right, hot) of pNIPAM-NP array on gold substrate. The pNIPAM shell around the gold NPs gives the gap width between NP array and substrate as g and interparticle distance as $2g$ (b).

Below we propose and explore the properties of such a switch that relies on the coupling between NPs within the array as well as between NP's and the substrate. As a result, an exceptional optical phenomenon is obtained that is not achievable by linearly adding the optical signals from the two cases individually. A monolayer of pNIPAM-Au NPs is allowed to self-assemble on a planar Au substrate, with the temperature controlled by a Peltier heating/cooling element. Its thermo-responsive behaviour is demonstrated that the optical properties of such metasurfaces can be continuously tuned, producing a shift in the dip of the plasmon resonance between 562-596 nm. Comparing these experimental spectra with effective medium theory (EMT)²⁰ and simulations shows that it is possible to control the average distance between NPs and substrate by shrinking/expanding the NIPAM shell within the range of 1.8 – 4.0 nm.

5.3. Results and discussions

5.3.1. Experimental setup and working principle

Initially 16 ± 1 nm citrate stabilized Au NPs were synthesized and further functionalized by incubating with amine terminated pNIPAM. The NPs were then made to self-assemble at a water | 1,2-dichloroethane

interface followed by transferring onto octane-thiol functionalized 125 nm thick Au substrates. Initially, 10 mL as prepared pNIPAM Au NPs solution was mixed with 4 mL 1,2-dichloroethane in a PTFE jar. After 60 s vigorous shaking on a vortex machine, NPs spontaneously assembled at the LLI due to the capillary force and the hydrophobicity of pNIPAM. Allowing the top DCE layer to evaporate, a shining golden mirror of pNIPAM-NP could be seen atop of the water phase. Then a dried Au substrate with octane thiol SAM was carefully stamped onto this NP array and quickly removed from the solution. Before immersing the NP assembly on substrate into the temperature-controlled cell, the excessive NP solution on the surface of the substrates was washed away with water. The substrate was immersed in pure water and the temperature modulated between 20 and 50 °C using a closed loop PID controller and a Peltier heating/cooling element. A fibre coupled optical reflection probe was used to collect the spectra (**Figure 5.2**).

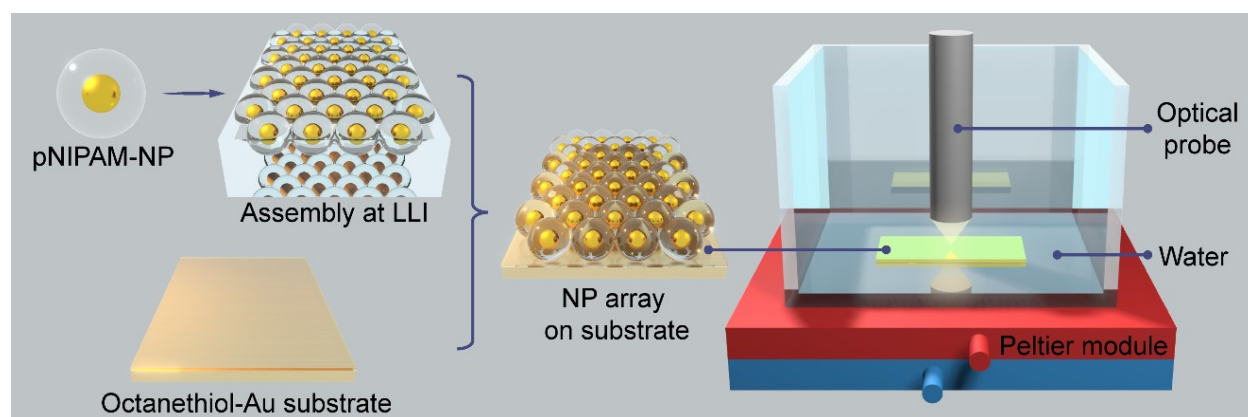


Figure 5.2 Fabrication and experimental setup: 16 nm Citrate capped Au NPs were coated by pNIPAM shell and assembled as a 2D array on water | 1,2-dichloroethane interface followed by transferring onto an octane-thiol functionalized 125 nm thick Au substrates. The pNIPAM-NP/Au substrate is immersed into a water-containing cell where a fibre coupled optical probe that is vertically focused onto the sample to shed light and collect the optical signal. The temperature is controlled by a PID (proportional–integral–derivative) controller coupled with a thermal probe and a Peltier module.

First, the optical properties of the pNIPAM-NP array on the gold substrate were examined prior to thermal experiments. Compared to pristine gold, it is not hard to notice the emergence of a reflectance dip in the green-yellow region at both 20 and 50 °C (**Figure 5.3a**) for the NP array on substrate. However, the 16 nm Au NP array alone without a substrate (such as at a liquid-liquid interface) produces a reflectance peak.^{17, 20} This non-linear effect is directly due to the proximity between NPs and distance between NP array and substrate. Our group have previously studied this theoretically using EMT and have explained that the dip originates from coupling of plasmon excitations between individual NPs with each other in the array, and between the substrate and the array (dashed lines in **Figure 5.3a**).²⁰ Optical images clearly show direct evidence of this effect, **Figure 5.3b**. This is also the reason that the wavelength of the dip for the array-on-substrate sample is significantly red-shifted when compared to the peak absorbance maxima in the bulk NP solution (**Figure 5.4a**).

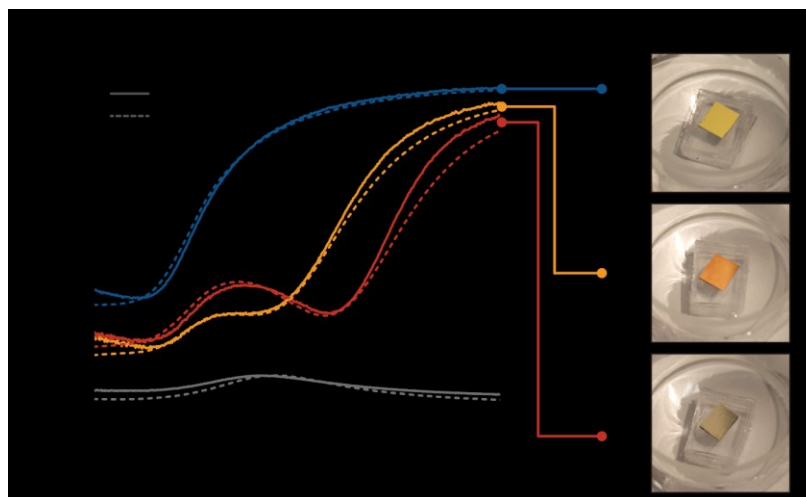


Figure 5.3 (a) Experimental (solid) and theoretical fitted (dashed) reflectance spectra of pristine gold substrate, pNIPAM NP array on gold substrates at low/high temperature and pNIPAM NP array on a liquid-liquid interface (LLI). (b) Digital camera photos of pristine Au substrate, pNIPAM-NP arrays on Au substrates at low/high temperature.

The thickness or length of the ligand is denoted by g , therefore, the gap distance between NP and substrate can be denoted as $g + 1/nm$ (with 1 nm being the approximate thickness for a monolayer of octanethiol), whilst the interparticle spacing within the array can be defined as $2g$, **Figure 5.1b**. At low temperature (20 °C, **Figure 5.1a** left), g is large and corresponds to the ‘swollen’ state of pNIPAM which is manifested in the bluer reflectance dip (~ 562 nm, **Figure 5.3a**). Whereas at higher temperature (50 °C, **Figure 5.1a** right) the pNIPAM shell decreases in g , resulting in a decrease in interparticle distance and the array-substrate gap, and hence a red-shift in the reflectance dip (~ 596 nm, **Figure 5.3a**). This spectral change can be directly observed from the macroscale photos of the samples (**Figure 5.3b**). Although scanning electron microscopy (SEM) imaging requires dehydration of the sample and cannot be used to calculate g , such images are helpful to confirm the successful assembly of NP array on substrate and to visualize whether a monolayer or alternatively multilayer is obtained, **Figure 5.4b**.

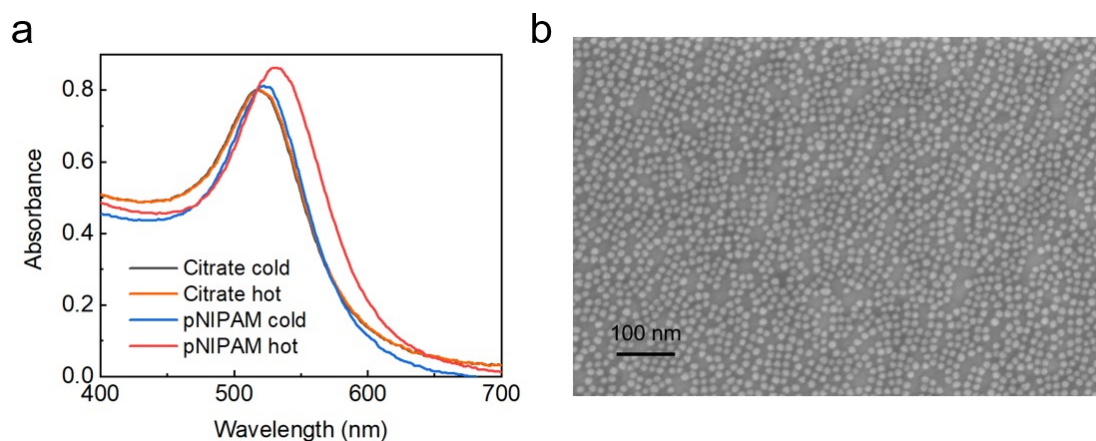


Figure 5.4 (a) UV-vis spectra of bulk solution of $9.8 \times 10^{11} \text{ cm}^{-2}$ citrate functionalized NPs and pNIPAM functionalized NPs under cold (20 °C) and hot (50 °C) conditions. (b) SEM image of pNIPAM NP array on gold substrate in dried condition, scale bar 100 nm.

Many reports have demonstrated that a superlattice of NP clusters could generate very interesting optical signals.^{33, 34} The long range plasmonic coupling of ordered NP clusters could induce secondary optical peaks apart from the main peaks. However, our intention here is to construct a continuous NP array on a metallic substrate, not the discontinuous ordered NP clusters as in the above-mentioned literatures, thus, no secondary peaks could be and were observed in our case. Our theory shows that in the case of substantial dispersion of the gap distance between NPs, the dip in reflectivity will be substantially broader and less deep, with the maximum position not located where it is currently seen, rather shifted to red.^{18, 20} Here, a different picture is observed, where the measurements correspond to close to ideally structured hexagonal NP arrays.

5.3.2. Temperature dependence of reflectivity

To better understand the thermal response of this system, reflectance spectra at varying temperatures were examined. Although the visible response of the metasurface to temperature change takes minutes, each designated temperature was first maintained for 30 min to ensure that the system fully reaches equilibrium. As shown in **Figure 5.5a**, the spectra red shifts with increasing temperature. This can be clearly seen in **Figure 5.5b** where the wavelength at 50% reflectance is plotted as well as the reflectivity at 600 nm. Impressively a shift of up to 36 nm could be obtained and was most pronounced around the LCST where the drastic change of the conformation of pNIPAM molecules induces the most significant swelling/shrinking rates ; for free pNIPAM in solution this takes place at 32 °C.²¹

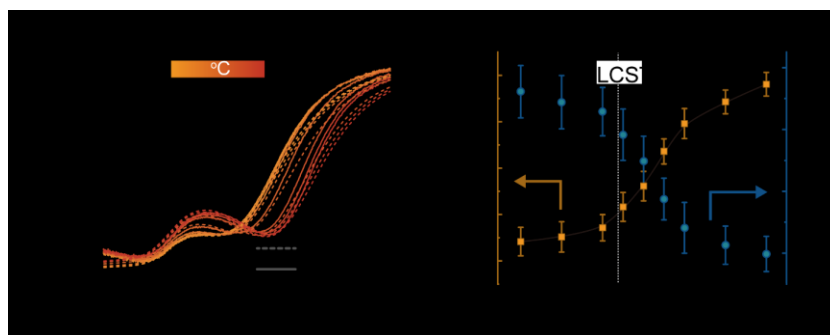


Figure 5.5 Static temperature dependent responses of pNIPAM NP array on gold substrate. (a) Static experimental (solid) reflectance spectra and theoretical fits (dashed lines) at different temperatures. (b) Wavelength at 50% reflectance and the reflectance at 600 nm [both from panel (a)] at different temperatures

By subtracting the reflectance signal from that of the pristine gold substrate, the change of reflectance is shown in **Figure 5.6a**. Plotting the data in this format enables a better understanding of the change in optical properties due to the swelling/shrinking of pNIPAM. Importantly, there is an excellent match between the theoretical simulations (based on the effective medium theory of Ref.^{18, 20} using only one fitting parameter g to the wavelength of the dip in the first iteration, followed by fitting the fraction of NP array on the substrate surface (*coverage fraction*) in the second iteration to reproduce the depth of the dip; all other

parameters are ‘known’). Due to excellent agreement with experimental data, these fits could be used to unambiguously determine g . For example, at 20 °C, g was determined to be ~ 4 nm (**Figure 5.6b**) and hence the NPs had an interparticle spacing of 8 nm and array-substrate gap of 5 nm. Increasing the temperature to 50 °C resulted in a g of ~ 1.8 nm and hence interparticle spacing of 3.6 nm (corresponding to 55% change between the two temperature states) and array-substrate gap of 2.8 nm. This shrinking ratio is similar to what has been reported by other researches utilizing core/shell structure of Au NPs/pNIPAM.^{25, 31, 32}

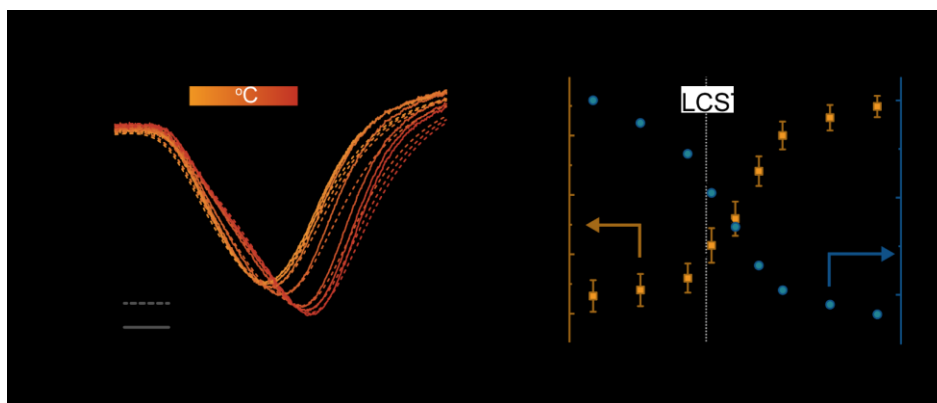


Figure 5.6 (a) Static spectra of experimental change of reflectance (Δ Reflectance, solid) and theoretical fits (dashed) at different temperatures vs pristine Au substrate. (b) Dip wavelength extracted from panel (a) and pNIPAM thickness, g , calculated from theory.

By subtracting the spectrum of 20 °C sample, the change of reflectance shown in **Figure 5.7** gives another view about how the temperature influence the reflectance output. When the temperature increases, due to the redshift of the plasmonic coupling dip shown in **Figure 5.6a**, the reflectance around 550 nm slightly recovers, while a major damping effect at ~ 618 nm can be witnessed. Note that the shift in dip wavelength caused by thermo-auxetic response can be as large as 34 nm (**Figure 5.6b**) which is larger than previous systems, e.g. shift of absorption peak $\Delta\lambda = 9$ -28 nm in nanorods coated pNIPAM microgel²⁵; $\Delta\lambda = 10$ nm in thermoresponsive cross-linked nanocapsules³⁵ and $\Delta\lambda = 20$ nm in dense Ag NP aggregates²⁸.

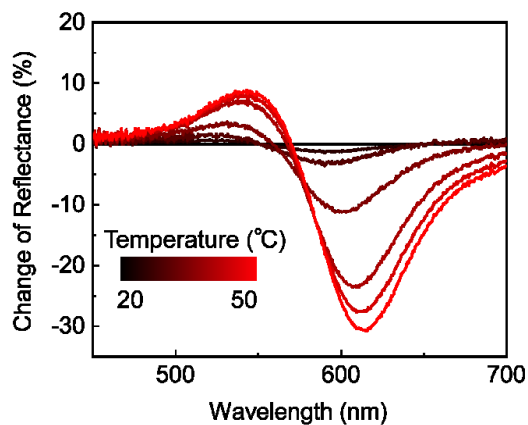


Figure 5.7 Static spectra of experimental change of reflectance (solid) at different temperatures vs 20 °C sample.

Accompanied by the drop in interparticle distance, the temperature change has another important influence on the surface coverage of the NP array on the substrate as the number of NPs on the substrate are fixed throughout the whole experiments. Thus, the shrinkage of the NP array during the heating is expected to induce the increase of open spaces (bare Au substrate). This nanoscale change can be seen in the optical reflectance spectra shown in **Figure 5.6a**: Although the interparticle distance and gap width was reduced by more than half, the change of reflectance only decreased by 10 %, indicating the more reflective bare Au substrate fraction contributed to this higher value of the reflectance, **Figure 5.8**. Starting from 0.88 at 20 °C, the fraction decreases in a similar fashion to g as temperature increases and finally settles at 0.56 at 50 °C.

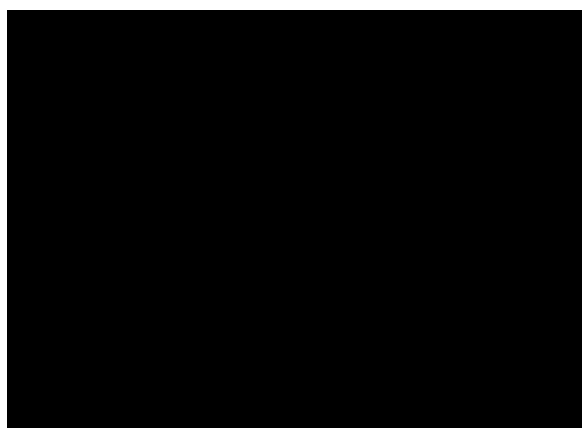


Figure 5.8 The calculated NP array coverages on the Au substrates at different static temperatures.

5.3.3. Kinetic response to thermal stimuli

To assess the kinetic response, the substrate was heated from 20 °C to 50 °C in 3 min, **Figure 5.9**. This was the fastest rate possible within our current configuration and its speed was limited by the volume of the water and the heating power which in turn governs the uniformity of the temperature within the bath. **Figure 5.9a** shows the typical kinetic evolution of the reflectance spectra during the heating. Trends in both the reflectance and dip wavelength were analogous to the static set of curves. At the end of the heating process, the dip wavelength reaches 596 nm, a value that is consistent with the static data (**Figure 5.9b**). By fitting these time dependent reflectance curves, thickness g can be calculated at different times, as shown in **Figure 5.9c**, indicating the interparticle distances within the array and the gap width between the array and the substrate are reducing accordingly.

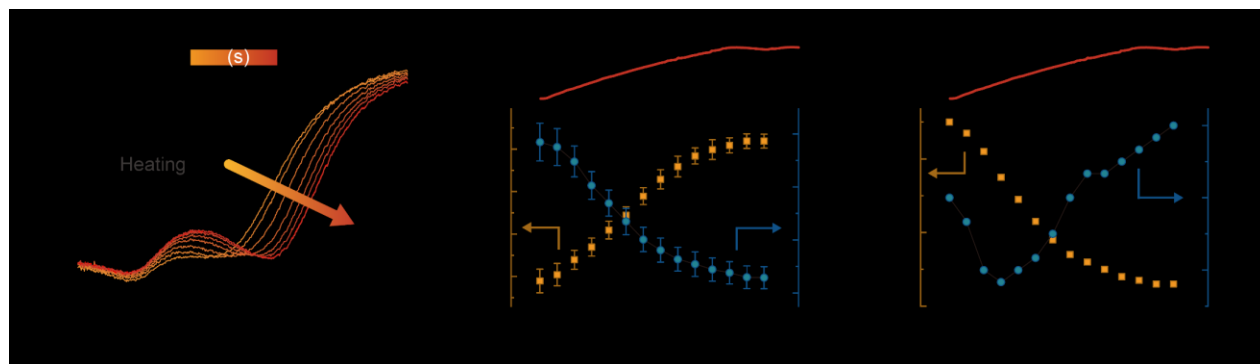


Figure 5.9 Kinetic responses of pNIPAM NP array on gold substrate during the heating process from 20 °C to 50 °C. (a) the time dependent reflectance spectra; (b) temperature profiles (top) and the corresponding dip wavelength and reflectance at 600 nm (bottom), extracted from panels (a). (c) The calculated values of g and its time derivative $g' = dg/dt$.

In the plot of the rate of change of g , an interesting phenomenon is observed: the rate, g' initially increases to a peak value (at ~ 50 s) then decreases to almost zero. After correlating the time to the local temperature (Figure 5.8c), it was found that the maximum rate lies at approximately 32 °C, the LCST of pNIPAM where the polymer experiences the phase transition. The changing rates of the dip wavelength follow the similar trend (Figure 5.10a).

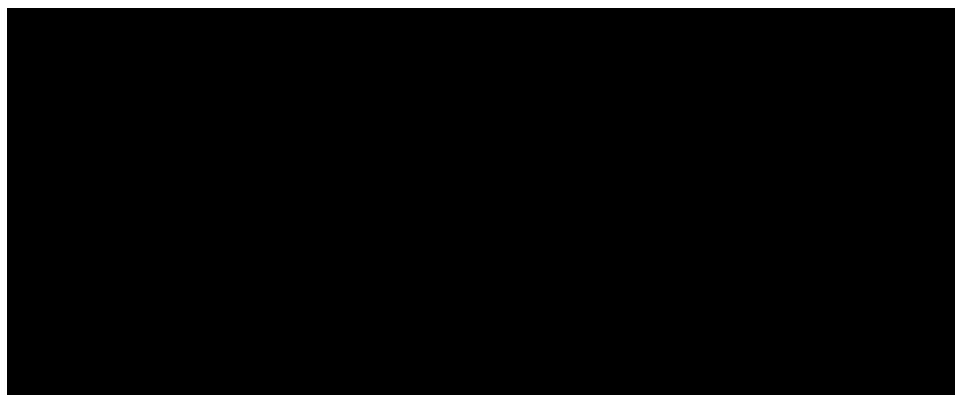


Figure 5.10 Changing rate of the dip wavelength (the first order derivative of λ , i.e., $d\lambda/dt$) during heating (a) and cooling (b) process.

In Figure 5.9 about the kinetic response to the thermal stimuli, the heating rate was intentionally reserved to maintain a stable temperature field in the cell. However, to examine the fastest response time of our system, the optical output was monitored during an instant injection of 50 °C water. Shown in Figure 5.11, a major jump within ~ 2 s is witnessed in both the dip wavelength and the reflectance at 600 nm. This suggests that the structural rearrangement of the polymer is not the rate limiting step in the current temperature controlling setup. This also implies that the system could in principle be further optimized for even more rapid switching.

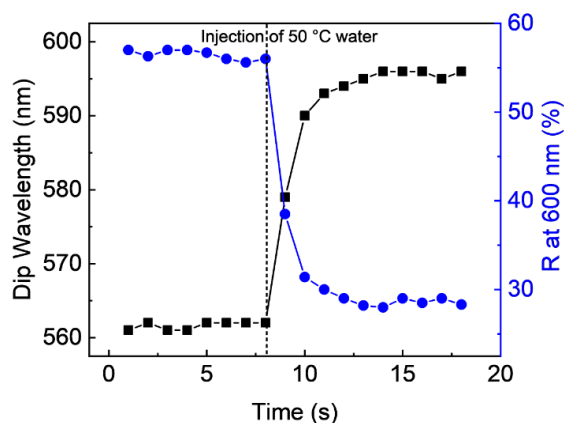


Figure 5.11 The dip wavelength and reflectance (R) at 600 nm before and after the injection of 50 °C water into the cell. Injected right after 8 s.

To access the cooling process, the temperature was decreased from 50 °C to 20 °C in 3 min followed by maintaining a 20 °C temperature for 20 min (**Figure 5.12b** top). Although the spectra gradually converged to that expected case (**Figure 5.12a**), it took over 8 times longer when compared to the heating cycle. A closer look at the change of reflectance at 600 nm and dip wavelength (**Figure 5.12b**) reveals a different pattern compared with the heating kinetics. A quick change of the optical signal is witnessed during the first 200 s. This can be easily understood since it is within this time that the temperature drops to 20 °C. However, there is a 17 nm red-shift in the dip wavelength when compared to the static case for the same temperature. Similar thermal hysteresis effects have been previously observed.³⁰ It took a further 20 min at 20 °C to bring the dip back to the expected value. Hence, a latency is observed during the swelling of pNIPAM and the expansion of the NP array. g , g' and λ' further imply that the swelling of pNIPAM is much slower than its shrinking process (**Figure 5.12c**, **Figure 5.10b**). A likely explanation is that above the phase transition coiled hydrophobic junctions ($-\text{CH}(\text{CH}_3)_2$) among pNIPAM molecules could inhibit the reformation of hydrogen bonds between pNIPAM ($-\text{CO}-\text{NH}-$) and water.

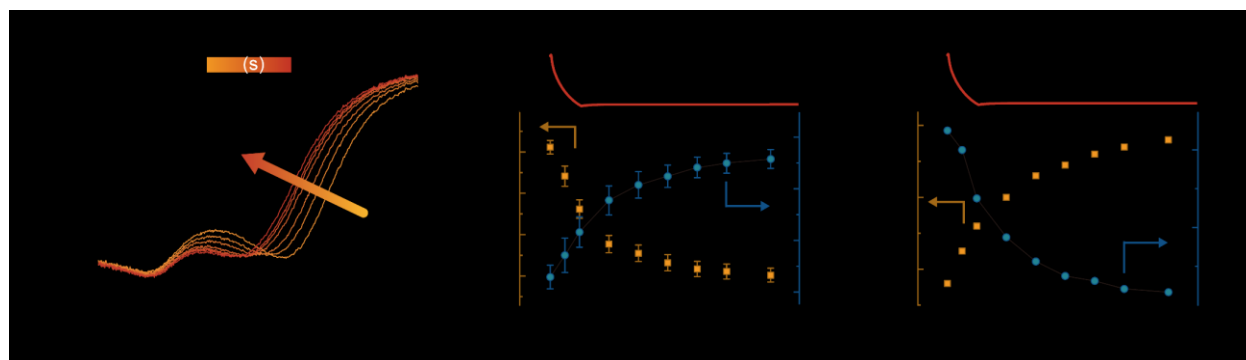


Figure 5.12 Kinetic responses of pNIPAM NP array on gold substrate during the cooling process from 50 °C to 20 °C. (a) the time dependent reflectance spectra; (b) temperature profiles (top) and the corresponding dip wavelength and reflectance at 600 nm (bottom), extracted from panels (a). (c) The calculated values of g and its time derivative $g' = dg/dt$.

5.3.4. Reversible optical switching

Reversibility is critical for any future applications. To examine this, the heating (3 min) and cooling (30 min) were cycled between 20 °C and 50 °C. Shown in **Figure 5.13a**, due to the auxetic behaviour of the optical switch, the red letters “IC” (stands for Imperial College) reflected from the metasurface exhibit noticeable changes between the cold and hot states. The reflectance spectra at low/high temperature (**Figure 5.13b**) can recover their shapes without much noticeable change after multiple cycles, indicating pNIPAM NP arrays on gold substrates acts as a robust platform. A slight red-shift of the spectra and reduction of the g at low temperature can be observed after four cycles (**Figure 5.13c**). As discussed previously, this is mainly due to the latency of the recovery of g and coverage at nanoscale due to the hysteresis of pNIPAM polymer.

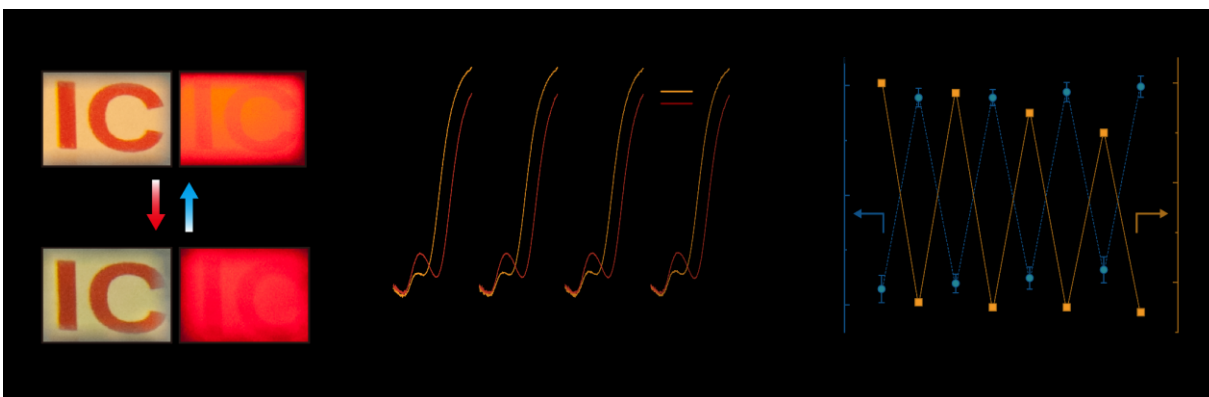


Figure 5.13 Thermal reversibility of the pNIPAM NP array on gold substrate. (a) The digital camera photos of the cold and hot states of reflected image of “IC” (abbreviation of “Imperial College”); the letters are drawn on A4 paper in red and are illuminated by white light (left) and 618 nm laser (right). The difference in the color and intensity of the letters under cold/hot conditions corresponds to the obtained red-shift of the dip in reflection. (b) Reflectance spectra of multiple cycles at cold (20 °C) and hot (50 °C) conditions; (c) The wavelength at 50% reflectance value and g for multiple cycles at cold (20 °C) and hot (50 °C) conditions.

5.4. Conclusions

A novel thermal responsive meta-surface based on a nanoplasmonic NPs on metallic substrate system was constructed. By heating or cooling the system, the thermally responsive pNIPAM shell surrounding each NP shrink or expand accordingly. The resultant structural changes both the interparticle distance among NPs in the array and the distance between NPs and metallic substrate, which directly influences the intensity and wavelength of its reflectance spectra. This is also confirmed by the excellent match between experiment and theoretical calculation. The kinetic experiments demonstrated that the optical response during the cooling process is slower than that during the heating, which implies a thermal hysteresis that may be due to the hydrophobic interactions among the pNIPAM molecules or between the pNIPAM and the substrate. Future applications of this system could be for nanoplasmonic rulers, thermal sensors, and self-regulated light harvesting and thermal dissipations in solar cells.

5.5. References

- (1) Ma, Y.; Sikdar, D.; Fedosyuk, A.; Velleman, L.; Zhao, M.; Tang, L.; Kornyshev, A. A.; Edel, J. B. Auxetic Thermoresponsive Nanoplasmonic Optical Switch. *ACS Appl. Mater. Interfaces* **2019**, *11*, 22754-22760.
- (2) Zheludev, N. I. The Road Ahead for Metamaterials. *Science* **2010**, *328*, 582-583.
- (3) Edel, J. B.; Kornyshev, A. A.; Kucernak, A. R.; Urbakh, M. Fundamentals and Applications of Self-Assembled Plasmonic Nanoparticles at Interfaces. *Chem. Soc. Rev.* **2016**, *45*, 1581-1596.
- (4) Scanlon, M. D.; Smirnov, E.; Stockmann, T. J.; Peljo, P. Gold Nanofilms at Liquid–Liquid Interfaces: An Emerging Platform for Redox Electrocatalysis, Nanoplasmonic Sensors, and Electrovariable Optics. *Chem. Rev.* **2018**, *118*, 3722-3751.
- (5) Zhao, Y.; Sun, M.; Ma, W.; Kuang, H.; Xu, C. Biological Molecules-Governed Plasmonic Nanoparticle Dimers with Tailored Optical Behaviors. *J. Phys. Chem. Lett.* **2017**, *8*, 5633-5642.
- (6) Abbas, A.; Linman, M. J.; Cheng, Q. A. New Trends in Instrumental Design for Surface Plasmon Resonance-based Biosensors. *Biosens. Bioelectron.* **2011**, *26*, 1815-1824.
- (7) Xu, L.; Sun, M.; Cheng, P.; Gao, R.; Wang, H.; Ma, W.; Shi, X.; Xu, C.; Kuang, H. 2D Chiroptical Nanostructures for High-Performance Photooxidants. *Adv. Funct. Mater.* **2018**, *28*, 1707237.
- (8) Zhao, X.; Xu, L.; Sun, M.; Ma, W.; Wu, X.; Xu, C.; Kuang, H. Tuning the Interactions between Chiral Plasmonic Films and Living Cells. *Nat. Commun.* **2017**, *8*, 2007.
- (9) Xiong, K.; Emilsson, G.; Maziz, A.; Yang, X.; Shao, L.; Jager, E. W. H.; Dahlin, A. B. Plasmonic Metasurfaces with Conjugated Polymers for Flexible Electronic Paper in Color. *Adv. Mater.* **2016**, *28*, 9956-9960.
- (10) Cai, W. S.; Chettiar, U. K.; Kildishev, A. V.; Shalaev, V. M. Optical Cloaking with Metamaterials. *Nat. Photonics* **2007**, *1*, 224-227.
- (11) Ciraci, C.; Hill, R. T.; Mock, J. J.; Urzhumov, Y.; Fernández-Domínguez, A. I.; Maier, S. A.; Pendry, J. B.; Chilkoti, A.; Smith, D. R. Probing the Ultimate Limits of Plasmonic Enhancement. *Science* **2012**, *337*, 1072-1074.
- (12) Mock, J. J.; Hill, R. T.; Tsai, Y.-J.; Chilkoti, A.; Smith, D. R. Probing Dynamically Tunable Localized Surface Plasmon Resonances of Film-Coupled Nanoparticles by Evanescent Wave Excitation. *Nano Lett.* **2012**, *12*, 1757-1764.
- (13) Yu, Y.; Yu, D.; Orme, C. A. Reversible, Tunable, Electric-Field Driven Assembly of Silver Nanocrystal Superlattices. *Nano Lett.* **2017**, *17*, 3862-3869.
- (14) Hui, Y.; Gomez-Diaz, J. S.; Qian, Z.; Alù, A.; Rinaldi, M. Plasmonic Piezoelectric Nanomechanical Resonator for Spectrally Selective Infrared Sensing. *Nat. Commun.* **2016**, *7*, 11249.
- (15) Si, K. J.; Sikdar, D.; Chen, Y.; Eftekhari, F.; Xu, Z.; Tang, Y.; Xiong, W.; Guo, P.; Zhang, S.; Lu, Y.; Bao, Q.; Zhu, W.; Premaratne, M.; Cheng, W. Giant Plasmene Nanosheets, Nanoribbons, and Origami. *ACS Nano* **2014**, *8*, 11086-11093.
- (16) Guo, P.; Sikdar, D.; Huang, X.; Si, K. J.; Su, B.; Chen, Y.; Xiong, W.; Yap, L. W.; Premaratne, M.; Cheng, W. Large-Scale Self-Assembly and Stretch-Induced Plasmonic Properties of Core–Shell Metal Nanoparticle Superlattice Sheets. *J. Phys. Chem. C* **2014**, *118*, 26816-26824.
- (17) Montelongo, Y.; Sikdar, D.; Ma, Y.; McIntosh, A. J. S.; Velleman, L.; Kucernak, Anthony R.; Edel, J. B.; Kornyshev, A. A. Electrotunable Nanoplasmonic Liquid Mirror. *Nat. Mater.* **2017**, *16*, 1127-1135.
- (18) Ma, Y.; Zagar, C.; Klemme, D. J.; Sikdar, D.; Velleman, L.; Montelongo, Y.; Oh, S.-H.; Kucernak, A. R.; Edel, J. B.; Kornyshev, A. A. A Tunable Nanoplasmonic Mirror at an Electrochemical Interface. *ACS Photonics* **2018**, *5*, 4604-4616.
- (19) Di Martino, G.; Turek, V. A.; Lombardi, A.; Szabó, I.; de Nijs, B.; Kuhn, A.; Rosta, E.; Baumberg, J. J. Tracking Nanoelectrochemistry Using Individual Plasmonic Nanocavities. *Nano Lett.* **2017**, *17*, 4840-4845.

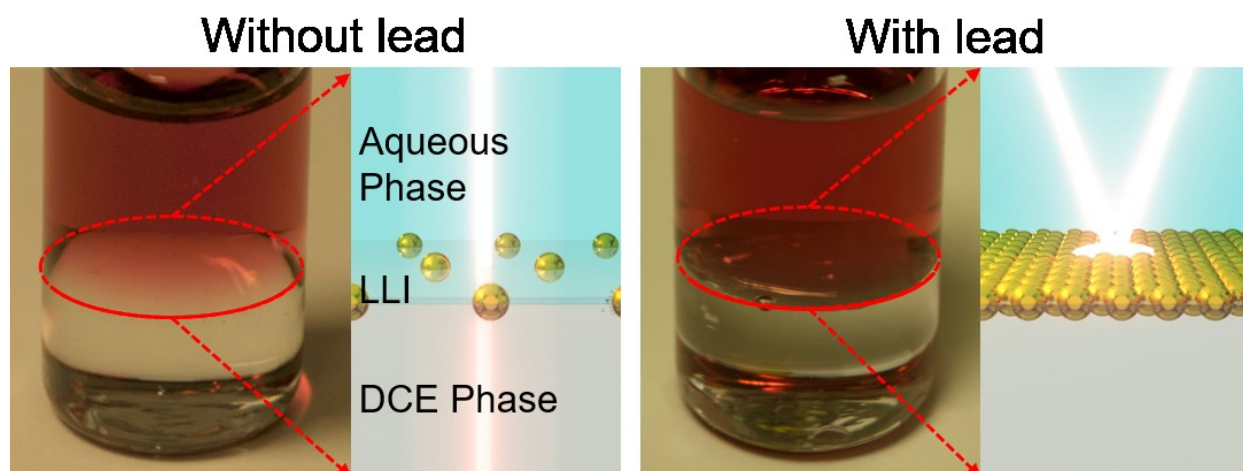
- (20) Sikdar, D.; Hasan, S. B.; Urbakh, M.; Edel, J. B.; Kornyshev, A. A. Unravelling the Optical Responses of Nanoplasmonic Mirror-on-Mirror Metamaterials. *Phys. Chem. Chem. Phys.* **2016**, *18*, 20486-20498.
- (21) Roy, D.; Brooks, W. L. A.; Sumerlin, B. S. New Directions in Thermoresponsive Polymers. *Chem. Soc. Rev.* **2013**, *42*, 7214-7243.
- (22) Karg, M.; Hellweg, T. New “Smart” Poly(NIPAM) Microgels and Nanoparticle Microgel Hybrids: Properties and Advances in Characterisation. *Curr. Opin. Colloid Interface Sci.* **2009**, *14*, 438-450.
- (23) Futscher, M. H.; Philipp, M.; Müller-Buschbaum, P.; Schulte, A. The Role of Backbone Hydration of Poly(N-isopropyl acrylamide) Across the Volume Phase Transition Compared to its Monomer. *Sci. Rep.* **2017**, *7*, 17012.
- (24) Wang, C.; Flynn, N. T.; Langer, R. Controlled Structure and Properties of Thermoresponsive Nanoparticle-Hydrogel Composites. *Adv. Mater.* **2004**, *16*, 1074-1079.
- (25) Karg, M.; Pastoriza-Santos, I.; Perez-Juste, J.; Hellweg, T.; Liz-Marzan, L. M. Nanorod-Coated PNIPAM Microgels: Thermoresponsive Optical Properties. *Small* **2007**, *3*, 1222-1229.
- (26) Xu, H.; Xu, J.; Jiang, X.; Zhu, Z.; Rao, J.; Yin, J.; Wu, T.; Liu, H.; Liu, S. Thermosensitive Unimolecular Micelles Surface-Decorated with Gold Nanoparticles of Tunable Spatial Distribution. *Chem. Mater.* **2007**, *19*, 2489-2494.
- (27) Samai, S.; Qian, Z.; Ling, J.; Guye, K. N.; Ginger, D. S. Optical Properties of Reconfigurable Polymer/Silver Nanoprism Hybrids: Tunable Color and Infrared Scattering Contrast. *ACS Appl. Mater. Interfaces* **2018**, *10*, 8976-8984.
- (28) Lewandowski, W.; Fruhnert, M.; Mieczkowski, J.; Rockstuhl, C.; Górecka, E. Dynamically Self-assembled Silver Nanoparticles as a Thermally Tunable Metamaterial. *Nat. Commun.* **2015**, *6*, 6590.
- (29) Fernández-López, C.; Polavarapu, L.; Solís, D. M.; Taboada, J. M.; Obelleiro, F.; Contreras-Cáceres, R.; Pastoriza-Santos, I.; Pérez-Juste, J. Gold Nanorod-pNIPAM Hybrids with Reversible Plasmon Coupling: Synthesis, Modeling, and SERS Properties. **2015**, *7*, 12530-12538.
- (30) Kim, D.; Kim, H.; Lee, E.; Jin, K. S.; Yoon, J. Programmable Volume Phase Transition of Hydrogels Achieved by Large Thermal Hysteresis for Static-Motion Bilayer Actuators. *Chem. Mater.* **2016**, *28*, 8807-8814.
- (31) Alvarez-Puebla, R. A.; Contreras-Caceres, R.; Pastoriza-Santos, I.; Perez-Juste, J.; Liz-Marzan, L. M. Au@pNIPAM Colloids as Molecular Traps for Surface-Enhanced, Spectroscopic, Ultra-Sensitive Analysis. *Angew. Chem.-Int. Edit.* **2009**, *48*, 138-143.
- (32) Ding, T.; Rudrum, A. W.; Herrmann, L. O.; Turek, V.; Baumberg, J. J. Polymer-Assisted Self-Assembly of Gold Nanoparticle Monolayers and Their Dynamical Switching. *Nanoscale* **2016**, *8*, 15864-15869.
- (33) Yan, B.; Thubagere, A.; Premasiri, W. R.; Ziegler, L. D.; Dal Negro, L.; Reinhard, B. M. Engineered SERS Substrates with Multiscale Signal Enhancement: Nanoparticle Cluster Arrays. *ACS Nano* **2009**, *3*, 1190-1202.
- (34) Hentschel, M.; Saliba, M.; Vogelgesang, R.; Giessen, H.; Alivisatos, A. P.; Liu, N. Transition from Isolated to Collective Modes in Plasmonic Oligomers. *Nano Lett.* **2010**, *10*, 2721-2726.
- (35) Wu, T.; Ge, Z.; Liu, S. Fabrication of Thermoresponsive Cross-Linked Poly(N-isopropylacrylamide) Nanocapsules and Silver Nanoparticle-Embedded Hybrid Capsules with Controlled Shell Thickness. *Chem. Mater.* **2011**, *23*, 2370-2380.

6. Label-free detection of lead employing nanoparticle self-assembly at liquid-liquid interface

6.1. Abstract

In this chapter, a novel lead sensor, based on the lead mediated assembly of glutathione (GSH) functionalized gold nanoparticles at a liquid-liquid interface (LLI), is proposed. The capillary forces trap NPs at the LLI, where a dense 2D array of NPs forms through the specific binding between the Pb (II) ions in the aqueous phase and the GSH ligands on the NPs. When lead is present, the resultant assembly of plasmonic NPs generates substantial reflectance signal, which provides a label-free approach for the detection of lead. Peak intensity and wavelength of the reflectance spectra combined with theoretical calculations facilitate this method to be used as a quantitative tool. Due to the condensing effect and self-healing nature of the NP array at the LLI, this sensor provides increased sensitivity when compared with other sensors based on NP aggregation.

Please note that the theoretical fittings of the reflectance spectra and calculated interparticle distances are contributed by Debabrata Sikdar. The material of this chapter is prepared for submission for publication as “Ye Ma, Debabrata Sikdar, Alexei A. Kornyshev, Joshua B. Edel, Label-free detection of lead employing nanoparticle self-assembly on liquid-liquid interface”



6.1. Introduction

It has been seemingly established that Ludwig van Beethoven had suffered and died of lead (Pb) poisoning.¹ At that time people were not aware of the toxic nature of this element. Now it is known that among various heavy metals, lead is one of the most harmful and ubiquitous toxins that is widely present in paints, batteries, combustion engine wastes, etc.² Due to its nondegradable and accumulative nature³, the reliable and convenient detection of lead in air, food and drinking water is critical for human health and environmental protection. Though the modern physical methods like inductively coupled plasma mass spectrometry (ICPMS) and atomic absorption spectrometry (AAS) can detect all kinds of heavy metals, sophisticated constructions and sample preparation limit their application in point-of-care and on-site detection.⁴

Gold NPs, thanks to their relatively large surface area for targeting analytes and unique optical and electrical properties, provide newly developed sensors with unprecedented sensitivity and versatility.⁵⁻⁷ By using a lead-dependent RNA-cleaving DNAzyme, Juewen Liu and Yi Lu⁸ demonstrated the control of the disassembly of gold NP aggregates in response to Pb²⁺, achieving the detection limit as 21 ppb in water. Exploiting the strong interaction between the lead ions in the solution and the crown ether on the surface on gold NPs, a fast colorimetric lead sensor with 52 ppb detection limit was proposed based on the lead mediated re-dispersion of NP aggregates.⁹ Using lead as the linker to GSH functionalized NPs, Wendy Chu et al.¹⁰, assembled NP into core-satellite structures, which showed improved colorimetric sensitivity (9.9 ppb) than the monodispersed NP solution.¹⁰ These approaches, which largely depend on the formation of agglomeration among NPs mediated by the analytes, can be conveniently read out by spectroscopies or even naked eye.¹¹ However, considering the large size of NPs, a relatively slow kinetics is inherited from their relatively low mobility and long diffusion length.^{12, 13} Thus, consistent and quick measurements employing NP aggregation in the bulk solution are still challenging.

Liquid-liquid interfaces (LLI) of two immiscible phases are an emerging versatile platform for assembling NPs as a two-dimensional optical active array.¹⁴ Due to the capillary forces to reduce the total interface energy, NPs that diffuse to the interface get trapped when piercing the LLI, thus forming a quasi-2d NP arrays.¹⁵ Such arrays are self-healing and non-degrading¹⁶, but if the NPs have been protected by charged ligands against their fusion in the bulk, they will not form dense arrays. Their densification can be controlled and hastened by introducing electrolytes¹⁵ that screen electrostatic repulsion, ambient electric¹⁷, magnetic fields¹⁸ or even by simply shaking.¹⁹ In the case of plasmonic NPs, the coupling between localized plasma excitations between them, makes the resultant optical properties of the array and the corresponding signals very sensitive to the density of such NP array. For the arrays at LLI, this property¹⁵, has been already widely used in photocatalysis²⁰, plasmonic nano-rulers²¹, switchable and conductive mirrors and filters²² and

especially SERS sensors²³⁻²⁷ that utilize hot spots for electromagnetic radiation in the narrow gaps between NPs.²⁸

In particular, based on SERS, Cecchini et al.²⁴ demonstrated that the assembly of gold NPs at LLI can detect trace organic analytes in either aqueous or oil phase when they capture and locate the Raman active molecules in the hotspots. Later, they found that the Raman signal oriented from π -stacking interaction between the mercury (II) and naphthalene-based polyaromatic ligands (PALs) can be greatly enhanced by the NP array at the LLI, which can be utilized for mercury detection.²³ However, since heavy metals are normally silent to most spectroscopic methods like Raman or fluorescence, signal reporters are often indispensable, making these techniques though ingenious, high cost and time consuming. In addition, SERS enhancement normally exists within the hotspots which are located in 1-5 nm gaps between the NPs.²⁹ Therefore, tuning the interparticle distance is essential to maximise enhancement.

Similar to SERS, the change of optical reflectance from LLI with adsorbed NP array is due to the coupled localised plasmon resonances in NPs.¹⁵ The reflectance intensity at maximum is substantial (between 20-60% at normal incidence, depending on the size of NPs, 16-40 nm in diameter), when the NPs in the array are separated by less than their diameter.^{30, 31} This opens up a wider range of NP gaps, as compared against narrow gaps of 1-5 nm for SERS, over which optical detection is possible. Moreover, unlike Raman or other second order nonlinear optical effects, the simple linear reflectance signal is stronger, requires no signal reporters, and overall needs less sophisticated facilities. Our previous studies has quantified the correlation between the reflection spectra, in particular peak intensity and wavelength, and the inter-NP distance in the arrays at the LLI.¹⁵ This effect provides new opportunities for sensing heavy metals with NPs functionalized by GSH ligands. When lead is present in solution in trace amounts, it can mediate bonding between closest GSH of neighbouring NPs on LLI. This will make the array denser, and the resultant change of reflectance is expected to have positive correspondence with the amount of lead in the solution.

In this chapter we demonstrate this effect and prove that a conceptually new lead sensor based on the reflectance change of the LLI could be designed. Moreover, a simple shaking process breaks the diffusion limit and delivers quick kinetics to reach the equilibrium and in a minute is ready to give a signal.

6.2. Results and discussions

6.2.1. The working principle and experimental setup

The scheme of the experimental principles is shown in **Figure 6.1**. When 1,2-dichloroethane (DCE) and 44 ± 3 nm GSH-NPs aqueous solution are injected into a vial, the two immiscible liquids form a well-defined

interface (**Figure 6.1a**). The samples have three distinctive parts: the aqueous phase containing NPs in bulk solution on the top, the DCE phase at the bottom and the interface in between where assembled NPs reside. Without lead, the transparent LLI (**Figure 6.1a-i**) and the low density of the NPs in the corresponding SEM image (**Figure 6.1a-iii**) indicate very few GSH NPs assembled at LLI.

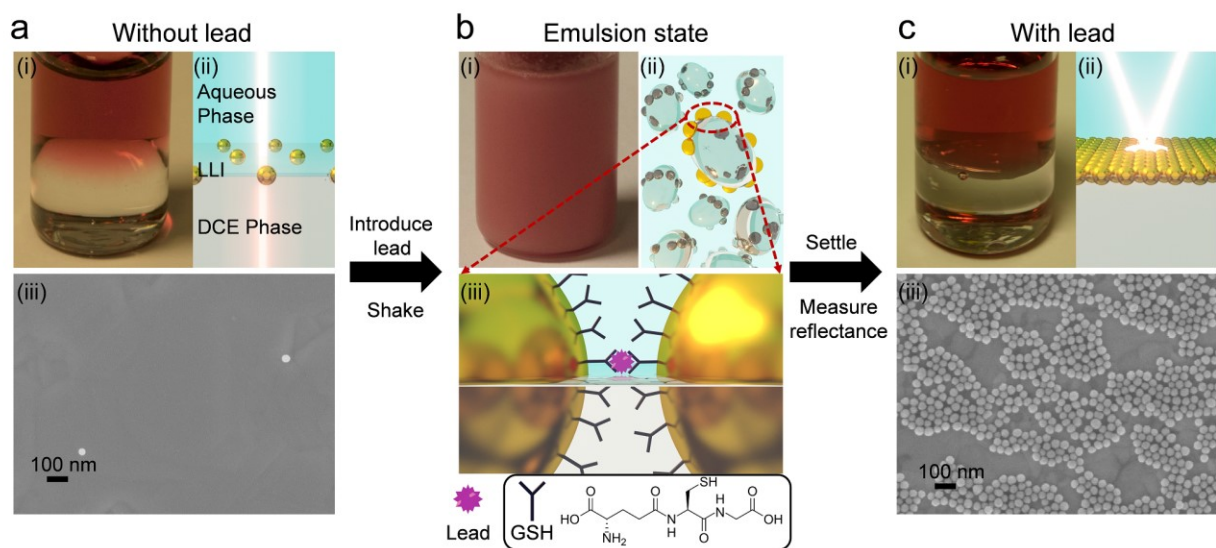


Figure 6.1 Scheme of GSH NP assembly at LLI for detection of lead - the operation principle. (a) Without lead, the immiscible GSH functionalized NP aqueous phase and DCE phase have a low-reflective planar interface with sparse number of NPs residing on it. (i) Digital camera photo of LLI: the red liquid on the top is the aqueous GSH NP phase; the colourless liquid at the bottom is the DCE phase; (ii) the scheme of the LLI; (iii) SEM images of the transferred NPs at LLI on Au substrates. (b) With the presence of (400 ppb) lead, shaking creates an emulsion state of the two phases. GSH NPs are driven by the capillary forces to the LLI of the droplets where lead ions link the neighbouring NPs together. (i) Digital camera photon of the emulsion state; (ii) the scheme of the emulsion state of the two phases; (iii) the schematic linkage between neighbouring NPs through the Pb-GSH bindings. (c) After settling down, the droplets merge back to the well-defined planar interface where the assembled GSH NP array reflect light. (i) Digital camera photo of LLI after NP assembling; (ii) the scheme of the LLI; (iii) SEM images of the transferred NPs at LLI on Au substrates.

With the presence of controlled amount of lead (400 ppb in the figure) followed by vigorous shaking in 60 s, an emulsion of the two phases is formed (**Figure 6.1b**). In this status, the capillary forces drive the NPs within the small droplets to the LLI, forming a loosely packed assembly layer.¹⁶ When trapped at the LLI, the DCE side of GSH NPs lose parts of their negative charge, thus have larger chance to come closer with each other. Namely, the LLI acts as a NP condenser that limits NPs on a 2D plane. The shaking process also shortens the diffusion length²⁴, helping the drifting Pb(II) ions to selectively chelate with the carboxyl groups of GSH on the surface of NPs³², which can link nearby NPs together on LLI (**Figure 6.1b**). This linkage greatly reduces the interparticle distance, thus strengthens the optical coupling within the assembly and the reflection signal. The trapping energy of nanoscale NPs at LLI has a positive relationship with their sizes³³⁻³⁵, but for a linked GSH NP array the energy to detach it from the LLI will scaled with a number of linked particles, thus the array will have even less chances to leave the LLI than a single NP.

After allowing the emulsion to settle down for one minute, those coupled NP assemblies previously on the droplets will merge together to form a well-defined planar reflective layer at LLI (**Figure 6.1c**). Compared with **Figure 6.1a-iii**, the populated SEM image further confirms that a more densely packed NP array was assembled at LLI when lead is introduced (**Figure 6.1c-iii**). Although the structures of the transferred NP arrays are expected to be different from how it may look at LLI *in situ*, the SEM images speak in favour of the importance of lead. This NP array greatly enhances their plasmonic resonance, thus boost the reflectance of LLI. By measuring the intensities of reflectance from the NP assembly at LLI, those values can be correlated to the concentrations of lead, which is expected to give better sensitivity than the bulk aggregation methods.

6.2.2. NPs functionalization and characterization in the bulk of aqueous solution

A careful study of GSH NP behaviour in the bulk is crucial for understanding how this NP system will function in any further applications. It has been found that GSH NPs in aqueous solution are vulnerable to self-agglomeration even without the mediation of lead ions in various situations: the formation of intermolecular bonds between -COOH groups at low pH³⁶, the head-to-head zwitterion-type electrostatic interactions around neutral pH³⁷, high concentration of GSH during synthesis and high speed of centrifugation. To secure the stability of GSH-NP solution, the pH of all the samples is kept above 6, GSH concentration as 10 μM and centrifugation speed at 1500 rcf (relative centrifugal force). Since citrate and lead cannot form strong chelate complex as GSH and lead do³⁸, citrate functionalized NPs is used as a control to prove the success of GSH functionalization and validate the detection method for lead in the bulk solution. In addition, the hydrated diameters of citrate or GSH functionalized NPs before/after adding lead were measured through dynamic light scattering (DLS). Revealed in **Figure 6.2**, the diameters of both citrate and GSH functionalized NPs are around 50 nm in the absence of lead. As expected, by adding 2 ppm lead, the output for citrate NPs stays unchanged while the GSH NPs give larger averaged diameter (100 nm) and broader distribution, confirming the formation of NP clusters mediated by lead.

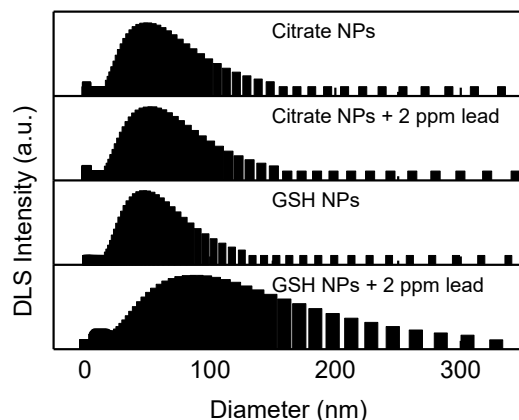


Figure 6.2 DLS measurements of the responses of citrate or GSH functionalized NPs to 2 ppm lead: only GSH NPs aggregate when lead exists. From top to bottom: Citrate NPs without lead, citrate NPs with 2 ppm lead, GSH NPs without lead, GSH NPs with 2 ppm lead.

It is well known that the agglomeration of gold NPs increases their frequency of plasmonic resonance. This induces a characteristic peak in the red region in the UV-vis spectra of the bulk, which is another handy indicator for assessing the degree of initial aggregation of GSH NPs in the bulk. The comparison of UV-vis spectra between the citrate and GSH functionalized NPs before/after adding lead (**Figure 6.3**) confirms the conclusions from the DLS: only GSH functionalized NPs aggregate in the presence of lead.

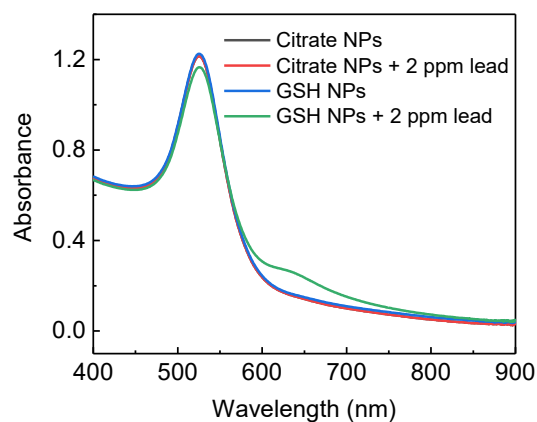


Figure 6.3 UV-vis spectra of Citrate- or GSH-functionalized Au NPs with 2 ppm lead ions in the bulk solution and without any presence of lead.

In addition, by adding controlled concentrations of lead into the GSH-NP solution, an obvious trend of the evolution of localised plasmon resonance peaks is revealed in **Figure 6.4**. Though there is no observable difference in the UV-Vis spectra between 0 and 0.5 ppm samples, with the further increase of the lead concentration, the peak at 525 nm from single particle mode gradually decreases while the peak originating from the agglomeration coupling mode substantially increases and red shifts from 628 nm to 770 nm. This confirms that under the designated protocol, the GSH molecules are successfully attached on the surface of 44 nm NPs, and the controlled amount of lead can induce the aggregation of these GSH NPs in the bulk solution.

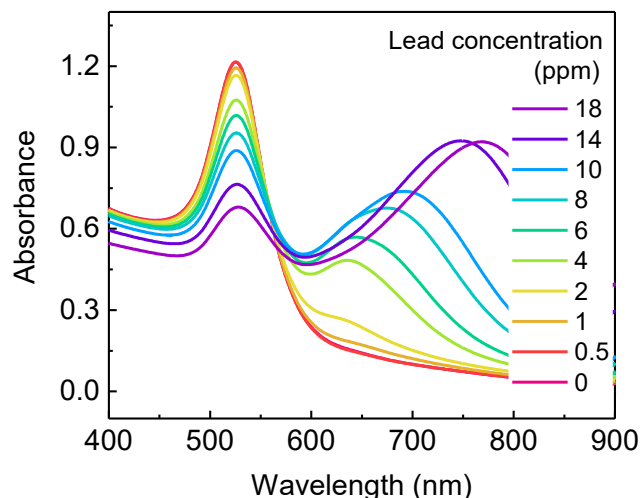


Figure 6.4 UV-vis spectra of GSH NPs bulk solution with different concentrations of lead (0, 0.5, 1, 2, 4, 6, 8, 10, 14, 18 ppm).

6.2.3. LLI

Compared with the bulk experiments in **Figure 6.4**, though 0.5 ppm (500 ppb) lead is too diluted to stimulate aggregation reaction in the bulk, 400 ppb in **Figure 6.1c**, however, is sufficient to induce NP assembly at LLI. This contrast highlights the vital role of the LLI ‘platform’ for the formation of the lead mediated NP assembly. Thermodynamically, the capillary energy, as the main driving force, has the tendency of entrapping and condensing NPs at the LLI. In addition, since DCE is a much less polar solvent than water, the degree of dissociation of the terminal groups of GSH that delivers the negative charge on them on the DCE side of NPs is substantially reduced. Therefore, the overall the electrostatic repelling forces among NPs are weakened and NPs have more chances to come close to each other. Alongside with the shaking process that breaks the diffusion limit, the dwindled repelling forces and shortened interparticle distance among NPs give lead ions higher chances to link neighbouring GSH NPs together. This is statistically more probable within a quasi-2D interfacial layer of NPs, which seemingly yields a higher sensitivity, as compared to bulk aggregation.

Increasing the ionic strength of aqueous phase has been proven to help the assembly of NPs at the LLI.^{15, 17, 39} To check that the reflectivity change and the NP assembly at the LLI in our case did not result from the increase of ionic strength, but due to the lead mediated assembly of GSH NPs, the responses of citrate functionalized NPs and GSH NPs were compared when adding 300 ppb lead or NaCl (**Figure 6.5**). The two curves of citrate NPs with and without lead show flat reflectance spectra and overlay with each other perfectly, indicating that lead cannot induce assembling of citrate NPs at LLI. For GSH NPs however, 300 ppb of lead significantly boosts the reflectance at 800 nm, confirming the lead – GSH bonding mechanism at the LLI. The GSH NP sample with 300 ppb NaCl remains the same with pristine GSH NPs, excluding any significant impact of the increase of ionic strength on the GSH NP assembly or direct optical effect.

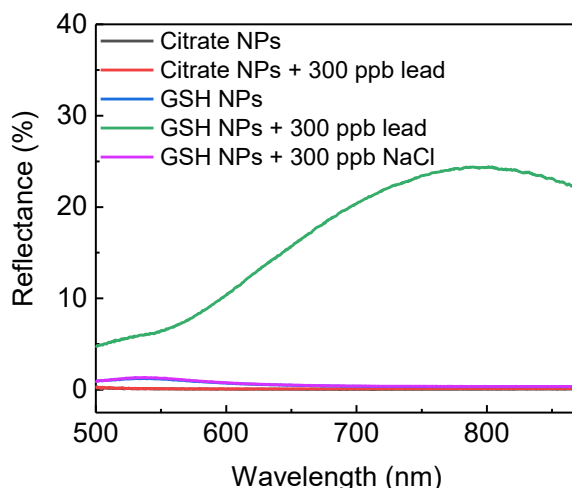


Figure 6.5 The response of reflectance spectra of citrate- or GSH-functionalized NPs arrays to 300 ppm lead: only GSH NPs form reflective LLI. Addition of 300 ppb NaCl does not cause any noticeable differences in reflectivity as compared to that of the pristine GSH NPs

It is not hard to notice that a small reflectance bump around 550 nm that can be seen when the pristine GSH NPs are compared with citrate NPs. Judging from the peak wavelength, I attribute this to single NP scattering at the LLI where very small number of NPs locate on the LLI (as depicted in **Figure 6.1a-iii**). Since in this case the average interparticle distance is extremely large, the coupling between these NPs thus is too small to produce observable reflectance. The five curves in **Figure 6.5** all prove that it is lead that assemble GSH NPs into a dense array and boosts the reflectance signal.

6.2.4. The effect of pH

Since the NPs are covered by GSH molecules, the degree of dissociation of these ligands will determine the surface charge of NPs, the electrostatic forces between NPs and the assembly density, as a result. Assuming the disassociating nature of GSH on NPs is similar to that of the free GSH, the pKa of $-\text{COOH}$ is 3.6 and $-\text{NH}_3^+$ 8.8. When pH is below 5, significant number of protonated $-\text{COOH}$ still present on the surface of NPs. This not only limits the total number of negative charges on NPs, but also raises the tendency of forming inter-particle hydrogen bonds between $-\text{COOH}$.³⁶ Moreover, under relatively low pH, GSH NPs are also vulnerable to self-aggregation derived from the head-to-head zwitterion-type electrostatic interactions between $-\text{COO}^-$ and $-\text{NH}_3^+$.³⁶ Our aggregation test on pH (**Figure 6.6**) also confirmed that, for our samples $\text{pH} < 6$, centrifugation and functionalization of GSH NPs are detrimental for the stability of NPs solutions even without the presence of lead. Therefore, to secure a robust monodisperse GSH NPs solution, the LLI measurements are only operated above pH 6.

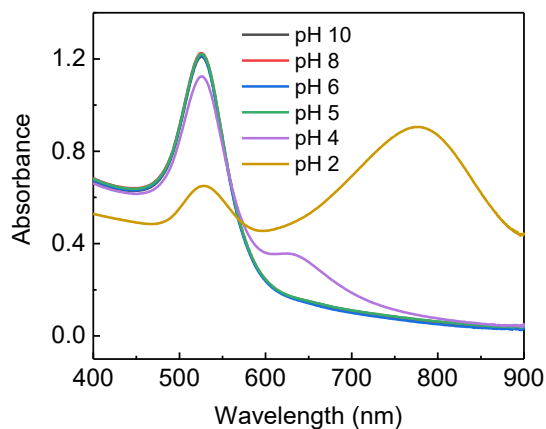


Figure 6.6 UV-vis spectra of the bulk solution of GSH Au NPs at different pH.

Based on the discussion above, higher pH is beneficial for the stability of GSH NPs. But too high pH has some side-effects on the sensitivity of lead detection. As shown in **Figure 6.7**, 250 ppb lead under pH 6 and 8 produce more than 20% reflectance at the LLI. However, further increase of pH will half, quarter or even eliminate the reflectance at LLI. Considering the pKa of $-\text{COOH}$ and $-\text{NH}_3^+$, above pH 6, more than 99% of $-\text{COOH}$ has been disassociated. Therefore, by adjusting the pH here, we are tuning the disassociate rate of $-\text{NH}_3^+$. When the pH is 11, nearly all the $-\text{NH}_3^+$ are in the deprotonated state rendering the GSH NPs too negative to come close with each other or forming assembly mediated by lead. By slowly decreasing the pH value, the number of $-\text{NH}_3^+$ increases which counteracts parts of the negative charges of $-\text{COO}^-$; this decreases the averaged interparticle distances, thus encouraging the assembly of NPs at LLI. A closer look at the pH 6 and 8 curves reveals an interesting fact: though the two cases show relatively similar intensity of reflectance, the peak wavelength for pH 8 is bluer than that of pH 6. This is attributed to the larger number of net negative charge on NPs for pH 8, which induces larger interparticle distance and shorter coupled plasmonic resonance frequency. To maintain the system both stable and sensitive as much as possible, our typical working condition is set at pH 8 for all the later experiments.

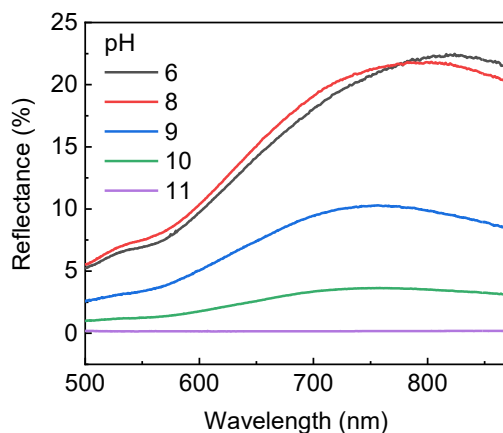


Figure 6.7 pH influence on the formation of GSH NP assembly (pH 6, 8, 9, 10, 11).

6.2.5. Sensing specificity

A good preclusion against interferences from other metal ions are indispensable for practical use. Here the response of the system to 200 ppb Pb(II), Fe(II), Ni(II), Hg(II), Ca(II), Cu(II), Co(II) and Cr(III) were tested.

Figure 6.8 shows that compared with the 16% maximum reflectance from lead, other metal ions have minor influence. This can be attributed to the good specific bonding between GSH and lead at pH 8 when -NH_3^+ cannot form chelation complex with other metal ions.^{40, 41}

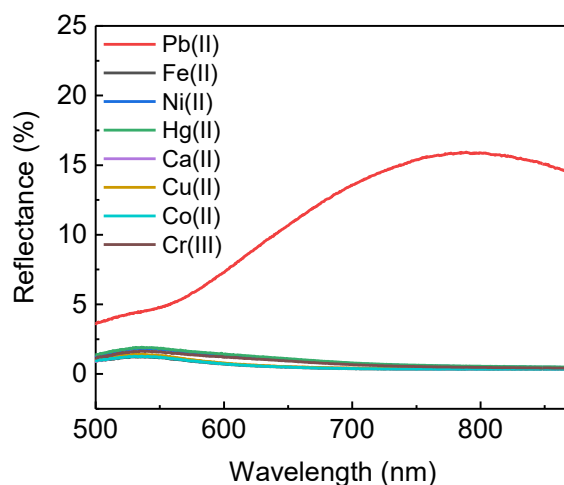


Figure 6.8 Specificity: Reflectance spectra at LLI of adding 200 ppb Pb(II), Fe(II), Ni(II), Hg(II), Ca(II), Cu(II), Co(II) and Cr(III).

6.2.6. Sensing dynamics

One of the current problems in detecting ions of heavy metals through NP agglomeration in the bulk is strong time-dependence of the signal.⁴² **Figure 6.9** shows the real-time UV-vis measurement of the bulk solution of GSH NPs with 0, 1, 4, 16 ppm lead. Within 45 mins, the absorbance at 525 nm decreases rapidly and continuously. In addition, different concentrations of lead give rise to divergent kinetic patterns. Therefore, unstable dynamics in the bulk could limit the consistency of such experiments.

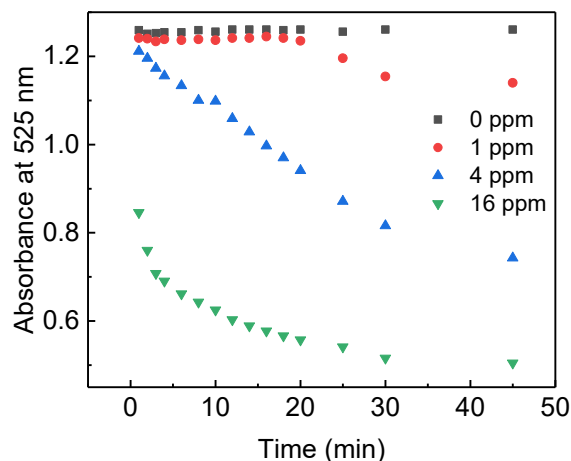


Figure 6.9 The time dependent absorbance of bulk GSH NPs at 525 nm with the presence of 0, 1, 4, 16 ppm lead in the bulk solution.

Luckily, at the LLI the situation is different. To examine the kinetics of the NP assembly at the LLI, the reflectance of the LLI with the presence of 0, 100, 200, 400 ppb lead was monitored. In **Figure 6.10**, the reflectance for different samples keeps nearly constant over 150 min. This impressive stability is attributed to the forces keeping NPs on the LLI and the shaking process which breaks the diffusion limit in the bulk. Before being trapped in the capillary energy well by the at the LLI, NPs need to first diffuse in the vicinity of the LLI. Unless the thickness of the aqueous phase is not miniaturized, this diffusion limited process for a still system can take hours even with the assistance of applying a voltage.¹⁷ The shaking step however, greatly shortens the diffusion time for the NPs to the LLI, so the LLI on droplets of DCE in water are quickly populated with NPs which are readily linked by lead ions. Therefore, only after settling for 1 min, the system can reach equilibrium between the LLI and the bulk solution.

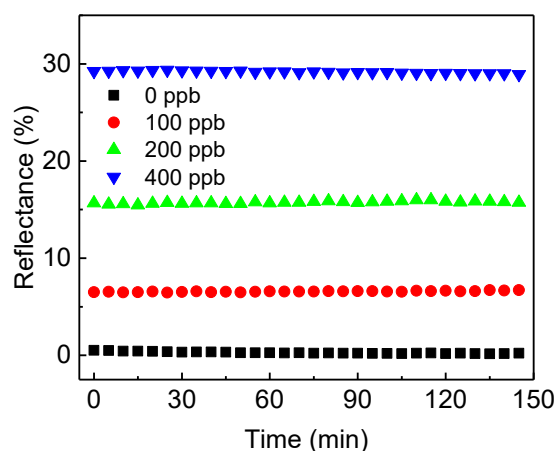


Figure 6.10 Time dependent measurements of reflectance at the maximum after 700 nm in the presence of 0, 100, 200, 400 ppb lead.

6.2.7. Quantitative estimates and signal calibration

Creating correlation between the reflectance of GSH NP array at the LLI and the lead concentration is indispensable for building quantitative lead sensors. **Figure 6.11a** shows the reflectance spectra at the LLI for different controlled amounts of lead in the aqueous phase. Without the presence of lead, the distances between NPs are too large to form a noticeable reflection signal. Still, it displays a signature of a mild maximum near 550 nm (the wave-length of the localised plasmon resonance in the individual NPs of that size), which the effective medium theory of reflectance would predict for sparse NP arrays.³¹ By increasing the concentration of lead, a reflectance peak emerges above 700 nm. As discussed below, this peak derives from the coupling of plasmon resonances between GSH NPs in a denser assembly. Alongside with the intensification of reflectance from 0 % (0 ppb) to almost 30 % (400 ppb), the peak wavelength also red shifts from 550 nm to 816 nm. Obviously, when more lead exists in the solution, more GSH NPs at LLI can be bonded together to form denser plasmonic array, which will red shift the maximum and increase the reflection intensity.

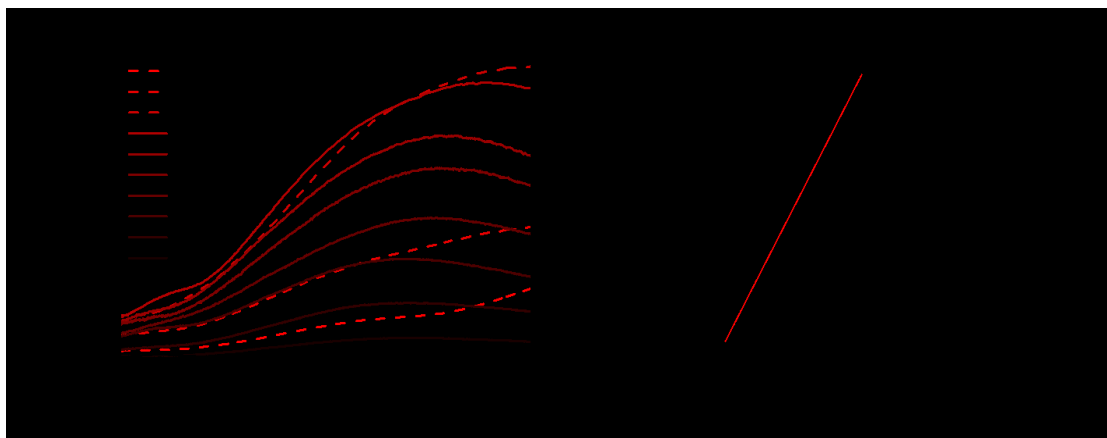


Figure 6.11 Quantification of detecting lead ions through their effect on reflectivity of the arrays of functionalized Au NPs at LLI. (a) The reflectance spectra of NP assembly at LLI with 0, 50, 100, 150, 200, 250, 300, 400, 500, 750, 1000 ppb lead. (b) Calibration curve: correlation between the height of reflectance maximum and the concentration of the lead.

Interestingly, when the lead concentration increases beyond 400 ppb, the reflectance has the tendency of decreasing (**Figure 6.11**). To interpret this counter-intuitive behaviour, the inset in **Figure 6.12** displays the photo of the sample with 1000 ppb lead. Aside from the distinctive blue colour of the bulk solution, there are visible clusters of aggregation on the wall of the container. Further detailed UV-vis measurements of the aqueous supernatant (**Figure 6.12**) reveal that concentrations below 400 ppb, GSH NPs are still in a monodisperse state, but more lead in solution can stimulate aggregation. So, the change of colours of the supernatant and the observation of the invers “V”-shape curve in **Figure 6.11b** tell us that the lead concentration has passed the 400 ppb.

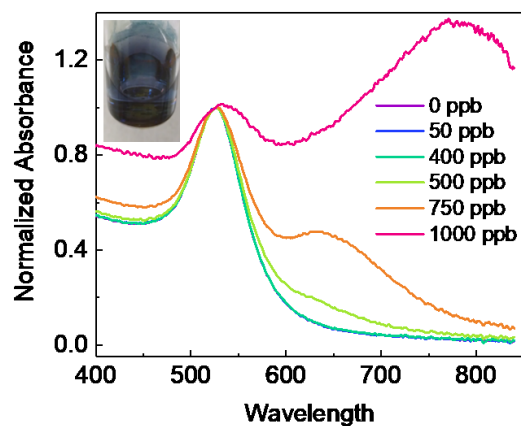


Figure 6.12 Normalized UV-vis absorbance spectra of GSH NP supernatant in LLI system with 0, 50, 400, 500, 750, 1000 ppb lead; inset, a typical photo of aggregated GSH NPs in LLI system with 1000 ppb lead.

Moreover, it is important to understand all subtleties of this effect. Comparing with the bulk UV-vis measurements in **Figure 6.4**, there is no indication of aggregation in the 500 ppb bulk-only sample, while in the LLI system the same concentration can induce obvious colour change in the aqueous supernatant. This difference can be rationalised by taking the influence of LLI into the account. As just mentioned, due

to its condensing effect for NPs, LLI can provide lower detection limit than the conventional bulk aggregation methods. Moreover, in the emulsion state, the LLI surface area of micro-droplets is much larger than that of the planar state. When the system is resettled back to the planar state, the reduced interfacial area can no longer accommodate all the bonded GSH NPs at higher lead concentrations. As a result, the excessive NP clusters will be released back into the supernatant. This explains why in the bulk solution, 500 ppb lead fails inducing aggregation while the same amount of lead in the LLI system can. In other words, the aggregation in the aqueous supernatant is derived from the migration of the assembled excessive GSH NPs from the LLI to the supernatant, not from the reaction happening uniformly in the bulk.

Based on the reflectance maximum due to the coupling of NP array at the LLI, a calibration curve correlating the reflectance to the concentration of lead is created (**Figure 6.11b**). A good linear relationship can be achieved with the range from 0 to 400 ppb. The calculated limit of detection (LOD, $S/N=3$) is 14 ppb. Since above 500 ppb the system is less stable, no fitting was attempted at higher concentrations. It should be noted that although the measured maximum reflectance can be correlated to two values of concentrations when taking the higher concentration range (500 ppb to 1000 ppb) into the account, one can easily distinguish them (for example between 200 ppb and 750 ppb, which have similar reflectance), by the wavelength of the reflectance peak, UV-vis measurement or the eye-observed colour of the supernatant.

Importantly, **Figure 6.13** depicts theoretically fitted reflectance spectra at different Pb concentrations. A four-layer stack model, based on our effective medium theory and multi-layer Fresnel scheme³¹, was utilized to better understand the mechanism behind the reflectance change from different assemblies of NPs at LLI. This model has been testified against full-wave finite element method (FEM) simulations and experiments in our previous works^{17,43}. It is known that interparticle distance is the only critical parameter that determines the reflectance peak wavelength for an array NPs (of a given size, shape, and composition) with designated parameters of media and the incident light.

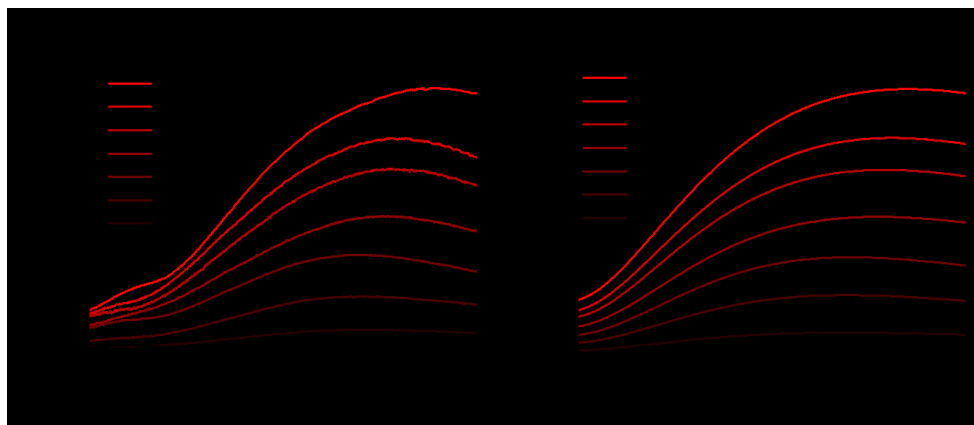


Figure 6.13 The experimental (a) and theoretically fitted (b) reflectance spectra of NP assembly at LLI with 0, 50, 100, 150, 200, 250, 300, 400 ppb lead.

The theoretical spectra were calculated in two steps. First, we assumed a uniform hexagonal array of 44 nm diameter gold nanospheres at LLI. The interparticle distance in the NP array was fitted to match the peak reflectance wavelength, extracted from **Figure 6.13a** for each lead concentration. But these calculated reflectance spectra provided much higher reflectance values than observed. This indicated that the LLI is not fully covered by NP array and hence, there is a need to adjust the model with account for the surface fraction being filled with closely packed NP arrays. We see evidence of this argument in our experiments, where islands and cracks on NP films are found in **Figure 6.1c-iii**. Therefore, as the second step in our theoretical calculation, we introduced in the theory the fraction of the surface covered by such islands and fitted this parameter to match the reflectance values. The final set of fitted reflectance spectra were obtained from weighted average from surface fractions covered by NPs and bare interface.

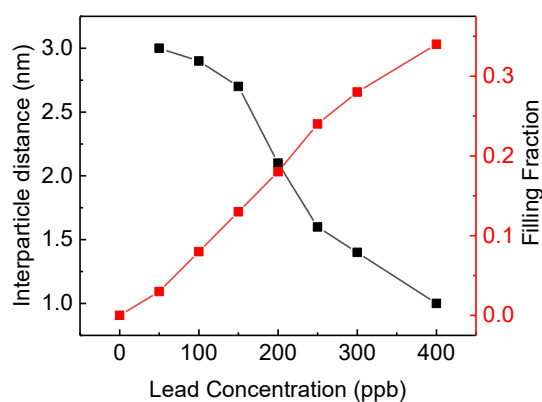


Figure 6.14 The calculated interparticle distance and filling fraction verses lead concentration.

The fitted values of interparticle gap (black) and portion of the surface covered by islands (red) are plotted as function of lead concentration in **Figure 6.14**. When no lead exists in the system, the interparticle distance is much larger than the diameter of NPs, which gives very blue peak wavelength and low reflectance. But once 50 ppb lead was introduced, the peak wavelength jumped from 550 nm to 755 nm, corresponding to 3 nm gap between neighbouring NPs. This distance decreases slowly and continuously to 1 nm when the concentration of lead increased to 400 ppb. Due to the bulk aggregation, theory calculation was not performed on samples above 400 ppb. Different from the free absorbed NPs at LLI¹⁵, the lead mediated assembly, revealed in **Figure 6.14**, have very restricted range of interparticle distance. This is attributed to the irreversible bonding between GSH NPs mediated by lead ions. Considering the length of GSH molecules as ~ 1.5 nm, the maximum interparticle distance would be ~ 3 nm if the two NPs are bonded by lead. This distance can be reduced by the rotation of GSH bonds and multiple lead conjugations between two NPs. Namely, with more lead available, more junctions between the opposing GSH ligands form, and to make it possible the closest ‘apex’ ligands must get compressed and the separation between NPs will get smaller. So, this simple physics and chemistry perfectly work, with the calculated 1 - 3 nm interparticle

distances making perfect sense. The estimation of NP portion of the surface covered by islands in **Figure 6.14** shows a linear like pattern with the increase of lead concentration which is also quite reasonable.

6.3. Conclusions

A label free method of detecting lead employing the self-assembly of GSH functionalized gold NPs at LLI has been demonstrated in this chapter. The capillary forces at LLI trap and condense NPs, thus increase the opportunity of forming specific coordinate bonds between NPs with the mediation of lead ions if the latter are present in the solution. With the increase of the concentration of lead, the reflectance signal is boosted due to the coupling of the increased number of NPs and shortened interparticle distance at LLI. A quicker equilibrium and higher sensitivity are witnessed when compared with bulk aggregation counterparts. This label-free approach by measuring reflectivity provides a simple and robust alternative to SERS or fluorescence where reporters and delicate microscopes are normally needed.

6.4. References

- (1) Stevens, M. H.; Jacobsen, T.; Crofts, A. K. Lead and the deafness of Ludwig van Beethoven. *Laryngoscope* **2013**, *123*, 2854-2858.
- (2) Mohan, D.; Pittman, C. U.; Bricka, M.; Smith, F.; Yancey, B.; Mohammad, J.; Steele, P. H.; Alexandre-Franco, M. F.; Gómez-Serrano, V.; Gong, H. Sorption of Arsenic, Cadmium, and Lead by Chars Produced from Fast Pyrolysis of Wood and Bark During Bio-oil Production. *J. Colloid Interface Sci.* **2007**, *310*, 57-73.
- (3) Deng, H.; Ye, Z. H.; Wong, M. H. Accumulation of Lead, Zinc, Copper and Cadmium by 12 Wetland Plant Species Thriving in Metal-Contaminated Sites in China. *Environ. Pollut.* **2004**, *132*, 29-40.
- (4) Park, J.; Kim, Y. A colorimetric probe for the selective naked-eye detection of Pb(II) ions in aqueous media. *Analyst* **2012**, *137*, 3246-3248.
- (5) Jain, P. K.; Huang, X. H.; El-Sayed, I. H.; El-Sayed, M. A. Noble Metals on the Nanoscale: Optical and Photothermal Properties and Some Applications in Imaging, Sensing, Biology, and Medicine. *Acc. Chem. Res.* **2008**, *41*, 1578-1586.
- (6) Saha, K.; Agasti, S. S.; Kim, C.; Li, X. N.; Rotello, V. M. Gold Nanoparticles in Chemical and Biological Sensing. *Chem. Rev.* **2012**, *112*, 2739-2779.
- (7) Cao, Y. W. C.; Jin, R. C.; Mirkin, C. A. Nanoparticles with Raman Spectroscopic Fingerprints for DNA and RNA Detection. *Science* **2002**, *297*, 1536-1540.
- (8) Liu, J.; Lu, Y. Stimuli-Responsive Disassembly of Nanoparticle Aggregates for Light-Up Colorimetric Sensing. *J. Am. Chem. Soc.* **2005**, *127*, 12677-12683.
- (9) Lin, S.-Y.; Wu, S.-H.; Chen, C.-h. A Simple Strategy for Prompt Visual Sensing by Gold Nanoparticles: General Applications of Interparticle Hydrogen Bonds. *Angew. Chem.-Int. Edit.* **2006**, *45*, 4948-4951.
- (10) Chu, W.; Zhang, Y.; Li, D.; Barrow, C. J.; Wang, H.; Yang, W. A Biomimetic Sensor for the Detection of Lead in Water. *Biosens. Bioelectron.* **2015**, *67*, 621-624.
- (11) Kim, H. N.; Ren, W. X.; Kim, J. S.; Yoon, J. Fluorescent and Colorimetric Sensors for Detection of Lead, Cadmium, and Mercury ions. *Chem. Soc. Rev.* **2012**, *41*, 3210-3244.
- (12) Schweizerhof, S.; Demco, D. E.; Mourran, A.; Fechete, R.; Möller, M. Diffusion of Gold Nanorods Functionalized with Thermoresponsive Polymer Brushes. *Langmuir* **2018**, *34*, 8031-8041.
- (13) Lim, I. I. S.; Ip, W.; Crew, E.; Njoki, P. N.; Mott, D.; Zhong, C.-J.; Pan, Y.; Zhou, S. Homocysteine-Mediated Reactivity and Assembly of Gold Nanoparticles. *Langmuir* **2007**, *23*, 826-833.

- (14) Edel, J. B.; Kornyshev, A. A.; Urbakh, M. Self-Assembly of Nanoparticle Arrays for Use as Mirrors, Sensors, and Antennas. *ACS Nano* **2013**, *7*, 9526-9532.
- (15) Velleman, L.; Sikdar, D.; Turek, V. A.; Kucernak, A. R.; Roser, S. J.; Kornyshev, A. A.; Edel, J. B. Tuneable 2d Self-Assembly of Plasmonic Nanoparticles at Liquid|Liquid Interfaces. *Nanoscale* **2016**, *8*, 19229-19241.
- (16) Edel, J. B.; Kornyshev, A. A.; Kucernak, A. R.; Urbakh, M. Fundamentals and Applications of Self-Assembled Plasmonic Nanoparticles at Interfaces. *Chem. Soc. Rev.* **2016**, *45*, 1581-1596.
- (17) Montelongo, Y.; Sikdar, D.; Ma, Y.; McIntosh, A. J. S.; Velleman, L.; Kucernak, Anthony R.; Edel, J. B.; Kornyshev, A. A. Electrotunable Nanoplasmonic Liquid Mirror. *Nat. Mater.* **2017**, *16*, 1127-1135.
- (18) Nie, Z.; Petukhova, A.; Kumacheva, E. Properties and Emerging Applications of Self-Assembled Structures Made from Inorganic Nanoparticles. *Nat. Nanotechnol.* **2009**, *5*, 15.
- (19) Scanlon, M. D.; Smirnov, E.; Stockmann, T. J.; Peljo, P. Gold Nanofilms at Liquid-Liquid Interfaces: An Emerging Platform for Redox Electrocatalysis, Nanoplasmonic Sensors, and Electrovariable Optics. *Chem. Rev.* **2018**, *118*, 3722-3751.
- (20) Gschwend, G. C.; Smirnov, E.; Peljo, P.; Girault, H. H. Electrovariable Gold Nanoparticle Films at Liquid-Liquid Interfaces: from Redox Electrocatalysis to Marangoni-Shutters. *Faraday Discuss.* **2017**, *199*, 565-583.
- (21) Turek, V. A.; Cecchini, M. P.; Paget, J.; Kucernak, A. R.; Kornyshev, A. A.; Edel, J. B. Plasmonic Ruler at the Liquid-Liquid Interface. *ACS Nano* **2012**, *6*, 7789-7799.
- (22) Smirnov, E.; Peljo, P.; Scanlon, M. D.; Gumy, F.; Girault, H. H. Self-Healing Gold Mirrors and Filters at Liquid-Liquid Interfaces. *Nanoscale* **2016**, *8*, 7723-7737.
- (23) Cecchini, M. P.; Turek, V. A.; Demetriadou, A.; Britovsek, G.; Welton, T.; Kornyshev, A. A.; Wilton-Ely, J. D. E. T.; Edel, J. B. Heavy Metal Sensing Using Self-Assembled Nanoparticles at a Liquid-Liquid Interface. *Adv. Opt. Mater.* **2014**, *2*, 966-977.
- (24) Cecchini, M. P.; Turek, V. A.; Paget, J.; Kornyshev, A. A.; Edel, J. B. Self-assembled Nanoparticle Arrays for Multiphase Trace Analyte Detection. *Nat. Mater.* **2013**, *12*, 165-171.
- (25) Booth, S. G.; Cowcher, D. P.; Goodacre, R.; Dryfe, R. A. W. Electrochemical modulation of SERS at the liquid/liquid interface. *Chem. Commun.* **2014**, *50*, 4482-4484.
- (26) Ma, Y.; Liu, H.; Mao, M.; Meng, J.; Yang, L.; Liu, J. Surface-Enhanced Raman Spectroscopy on Liquid Interfacial Nanoparticle Arrays for Multiplex Detecting Drugs in Urine. *Anal. Chem.* **2016**, *88*, 8145-8151.
- (27) Velleman, L.; Scarabelli, L.; Sikdar, D.; Kornyshev, A. A.; Liz-Marzan, L. M.; Edel, J. B. Monitoring Plasmon Coupling and SERS Enhancement through in Situ Nanoparticle Spacing Modulation. *Faraday Discuss.* **2017**, *205*, 67-83.
- (28) Maier, S. A., Plasmonics : Fundamentals and Applications. Maier, S. A., Ed. Springer: New York, 2007; pp 65-88.
- (29) Ding, S.-Y.; You, E.-M.; Tian, Z.-Q.; Moskovits, M. Electromagnetic Theories of Surface-Enhanced Raman Spectroscopy. *Chem. Soc. Rev.* **2017**, *46*, 4042-4076.
- (30) Jain, P. K.; El-Sayed, M. A. Plasmonic Coupling in Noble Metal Nanostructures. *Chem. Phys. Lett.* **2010**, *487*, 153-164.
- (31) Sikdar, D.; Kornyshev, A. A. Theory of Tailorable Optical Response of Two-Dimensional Arrays of Plasmonic Nanoparticles at Dielectric Interfaces. *Sci. Rep.* **2016**, *6*, 33712.
- (32) Feng, B. B.; Zhu, R.; Xu, S. M.; Chen, Y.; Di, J. W. A Sensitive LSPR Sensor Based on Glutathione-Functionalized Gold Nanoparticles on a Substrate for the Detection of Pb²⁺ Ions. *RSC Adv.* **2018**, *8*, 4049-4056.
- (33) Cappelli, S.; de Jong, A. M.; Baudry, J.; Prins, M. W. J. Interparticle Capillary Forces at a Fluid-Fluid Interface with Strong Polymer-Induced Aging. *Langmuir* **2017**, *33*, 696-705.
- (34) Flatté, M. E.; Kornyshev, A. A.; Urbakh, M. Understanding Voltage-induced Localization of Nanoparticles at a Liquid-Liquid Interface. *J. Phys.: Condens. Matter* **2008**, *20*, 073102.
- (35) Flatté, M. E.; Kornyshev, A. A.; Urbakh, M. Electrovariable Nanoplasmonics and Self-Assembling Smart Mirrors. *J. Phys. Chem. C* **2010**, *114*, 1735-1747.

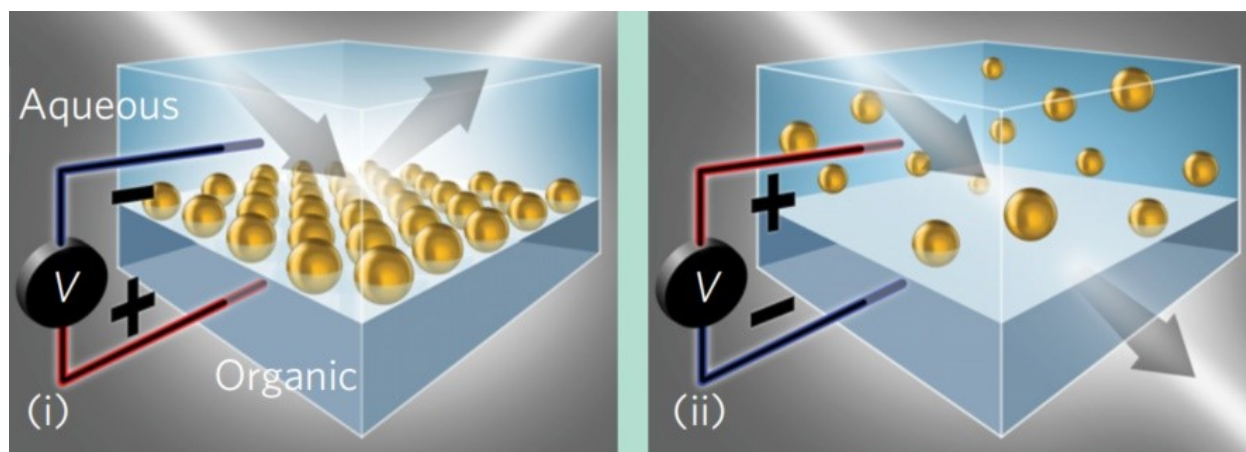
- (36) Lim, I. I. S.; Mott, D.; Ip, W.; Njoki, P. N.; Pan, Y.; Zhou, S.; Zhong, C.-J. Interparticle Interactions in Glutathione Mediated Assembly of Gold Nanoparticles. *Langmuir* **2008**, *24*, 8857-8863.
- (37) Liang, G.; Jin, X.; Qin, H.; Xing, D. Glutathione-capped, Renal-clearable CuS Nanodots for Photoacoustic Imaging and Photothermal Therapy. *J. Mater. Chem. B* **2017**, *5*, 6366-6375.
- (38) Panich, S.; Wilson, K. A.; Nuttall, P.; Wood, C. K.; Albrecht, T.; Edel, J. B. Label-Free Pb(II) Whispering Gallery Mode Sensing Using Self-Assembled Glutathione-Modified Gold Nanoparticles on an Optical Microcavity. *Anal. Chem.* **2014**, *86*, 6299-6306.
- (39) D'Souza Mathew, M.; Manga, M. S.; Hunter, T. N.; Cayre, O. J.; Biggs, S. Behavior of pH-Sensitive Core Shell Particles at the Air–water Interface. *Langmuir* **2012**, *28*, 5085-5092.
- (40) Beqa, L.; Singh, A. K.; Khan, S. A.; Senapati, D.; Arumugam, S. R.; Ray, P. C. Gold Nanoparticle-Based Simple Colorimetric and Ultrasensitive Dynamic Light Scattering Assay for the Selective Detection of Pb(II) from Paints, Plastics, and Water Samples. *ACS Appl. Mater. Interfaces* **2011**, *3*, 668-673.
- (41) Bala, T.; Prasad, B. L. V.; Sastry, M.; Kahaly, M. U.; Waghmare, U. V. Interaction of Different Metal Ions with Carboxylic Acid Group: A Quantitative Study. *J. Phys. Chem. A* **2007**, *111*, 6183-6190.
- (42) Chai, F.; Wang, C.; Wang, T.; Li, L.; Su, Z. Colorimetric Detection of Pb²⁺ Using Glutathione Functionalized Gold Nanoparticles. *ACS Appl. Mater. Interfaces* **2010**, *2*, 1466-1470.
- (43) Weir, H.; Edel, J. B.; Kornyshev, A. A.; Sikdar, D. Towards Electrotuneable Nanoplasmonic Fabry–Perot Interferometer. *Sci. Rep.* **2018**, *8*, 565.

7. Electrotunable nanoplasmonic liquid mirror

7.1. Abstract

This chapter reports on the first realization of a reversible electrotunable liquid mirror based on voltage-controlled self-assembly/disassembly of 16 nm diameter surfactant stabilized plasmonic nanoparticles at the interface of two immiscible electrolytic solutions. We show how the optical properties such as reflectance intensity and spectral position can be varied *in-situ* within a mere 0.5 V range of variation of applied voltage. This observed effect is in excellent agreement with the theoretical calculation of the optical response of such arrays, relating the corresponding variation of the average interparticle spacing to the voltage-driven nanoparticle assembly/disassembly process. We demonstrate that this novel electrochemical fully tunable nanoplasmonic platform can be switched from highly reflective ‘mirror’ to transmissive ‘window’ mode and back again. This study opens a route towards realization of such platforms in future micro/nanoscale electrochemical cells, enabling creation of tunable plasmonic metamaterials for application in optical switching and SERS-based sensing.

Please note that, in this chapter, the majority of the experimental measurements of reflectance and electrochemistry were performed by Dr. Yunuen Montelongo. I contributed the NP synthesis, characterization and a set of auxiliary experiments. The major parts of this chapter were published in Ref.¹



7.2. Introduction

The development of metamaterials has garnered interest ever since their initial introduction in the 19th century, leading to exploration and creation of artificial media for manipulation of electromagnetic waves. Recently, there has been a strong drive to build such media based on nanoscale bottom-up building blocks.²⁻⁴ These have been employed to create objects with unique electromagnetic properties for applications such as antennas, absorbers in solar cells, superlenses, cloaking, sensors, etc..⁵⁻¹² Although substantial advances have been made, tuning/modulating optical properties in real-time has remained elusive. If successful, such metamaterials would introduce dramatic change in their implications, and are expected to offer numerous new applications. For instance, energy efficient switchable windows can be designed where both the spectral range and the reflectivity can be fine-tuned. Such tuneable optical metamaterials (TOMs) can also be used to circumvent limitations in trace analyte sensing, ensuring capture and detection of analytes *via* real-time tuning of the TOM.

Here we report on a step towards realizing this goal by creating an electro-tuneable quasi-2-dimensional plasmonic platform: an electrically-switchable liquid mirror–window. It is based on voltage-controlled self-assembly/disassembly of negative-charge functionalized gold nanoparticles (NPs) at the interface of two immiscible electrolytic solutions (ITIES).^{13, 14} The principle underlying its operations is as follows. At this interface NPs can be made to adsorb spontaneously, driven by capillary forces. A dense monolayer of sufficiently large gold NPs reflects light due to coupled plasmon resonance.¹⁵⁻²⁰ However, charged NPs repel each other and may not settle close enough at the interface to form a dense layer resulting in a modest reflectivity unless they are driven to aggregation and formation of a multilayer. However, these systems cannot be made to spontaneously disassemble back into the liquid phase. In order to accomplish this latter aspect, the particles need to be trapped at the interface at sufficient density to form a plasmonically coupled monolayer, but not so close that they aggregate, (**Figure 7.1a-i** and **iii**). This is achieved by formation of a ‘potential energy well’ at the interface (**Figure 7.1a-v**) trapping any NP, however, electrostatic repulsion between the NPs diminishes the depth of the trapping well. Screening by electrolyte weakens the repulsion which effectively deepens the well, enabling the formation of highly reflective denser NP-arrays (**Figure 7.1a-ii, iv** and **vi**, also Ref.²¹⁻²³). However, such ‘chemical’ means of tailoring of inter-NP spacing and optical reflectivity^{24, 25} is restricted by an upper-limit of electrolyte concentration that ensures NPs do not agglomerate in the bulk or at the interface due to Van der Waals attraction.

A ‘physical’, *in-situ* means of control would be possible in an electrochemical liquid | liquid cell (c.f. **Figure 7.1b**). Here, negative polarisation of the aqueous phase relative to organic phase would push the NPs towards the interface forcing NPs to tolerate the proximity of each other, increasing the density, reflectivity,

while shifting the reflectance maximum towards the red end of the spectrum. Polarizing the aqueous phase positively will push NPs back into the bulk, diminishing their population at the interface, and thereby, decreasing the peak reflectivity and ‘blue-shifting’ it.

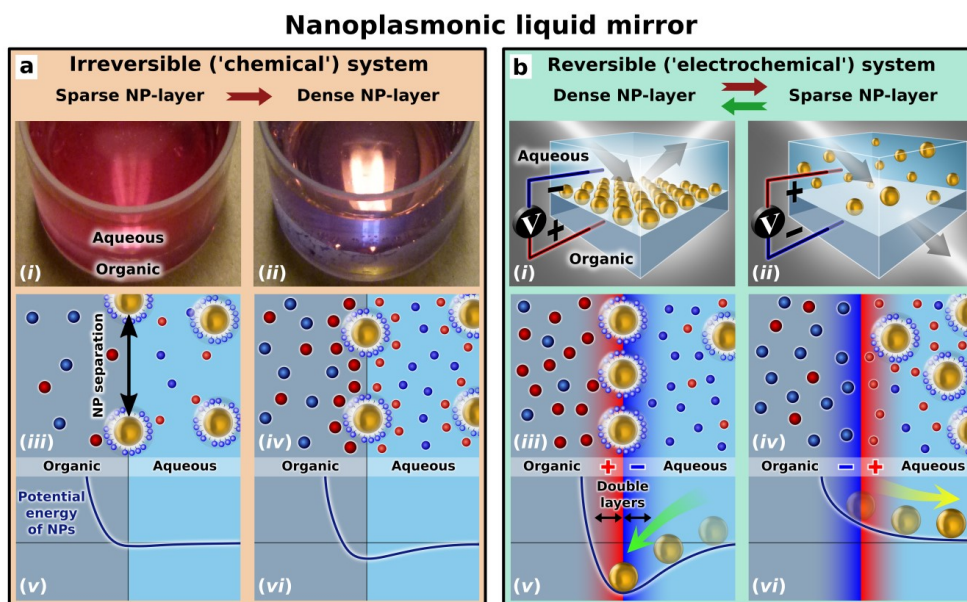


Figure 7.1 Nanoplasmonic liquid mirror strategies. (a) Spontaneous adsorption of NPs at the interface between aqueous and organic phases can be controlled by the concentration of electrolytes in either phases to transform a sparse NP layer into a dense layer, making it more reflective, as seen in photographs (i) and (ii). Increased concentration of electrolytes reduces electrostatic repulsion between NPs, functionalized by negatively charged ligands, allowing formation of denser layers, as shown in the cartoon (iii) to (iv). Cations, anions, and NPs, are depicted here as red, blue, and gold spheres, respectively (all sizes are not in scale, but in proper order). (v) to (vi) depict the change in the potential energy well for NPs at the interface, which gets deeper when the electrostatic repulsion between the NPs is reduced with the increase of electrolyte concentration. (b) Placing the system in an electrochemical cell would allow to reversibly control the assembly (adsorption) to and disassembly (desorption) of NPs from the interface by changing the polarity of the applied potential drop across the interface. This way the NP layer can be made even denser than that formed by the spontaneous assembly in the same system, or can be completely removed from the interface, as shown in schematics (i) to (ii), and (iii) to (iv). Two back-to-back electrical double layers form at the polarized interface, making the potential well for NPs deeper (v) or shallower (vi), subjected to the sign of the applied voltage. Such electro-tunable nanoplasmonic liquid mirror can thus be reversibly turned ‘on’ and ‘off’.

As mentioned, the density of the NP array at the interface can be statically controlled by the electrolyte concentration in the aqueous and organic phases and pH of the aqueous phase.^{25, 26} To introduce dynamic control over assembly/disassembly we need to vary the potential distribution at the ITIES. This is achieved by applying a potential difference between the electrodes in the aqueous (A) and organic (O) phases (**Figure 7.1b**), $\Delta\Phi_{AO} = \Phi_A - \Phi_O$. Under such potential bias of any polarity, two back-to-back electrical double layers will be formed on either side of the interface (**Figures 7.1b-iii** and **iv**). If one considers the total energy, U_{tot} , felt by a NP moving across the interface²⁷,

$$U_{tot} = U_{solv} + U_{cap} + U_{line} + U_{ext} \quad 7.1$$

comprising the free energy of transfer of a NP from aqueous to organic phase, U_{solv} (dominated by the Born solvation energy); a capillary term including interface tensions, U_{cap} ; line tension when the NP pierces the interface, U_{line} ; and the electrostatic energy of the NP in the polarized electrical double layer across the interface, U_{ext} . The potential well can be made deeper by applying $\Delta\Phi_{\text{AO}} < 0$ (**Figure 7.1b-v**). Reversing the sign of $\Delta\Phi_{\text{AO}}$ makes the well shallower or can totally eliminate it, or even create a repulsive energy profile to release the NPs into the aqueous phase (**Figure 7.1b-vi**).

The principles of such electro-tuneable optical platform and its main features have been proposed and theoretically investigated^{28, 29}, however, experimentally they have not been realized. Pioneering work by Girault's group³⁰ first demonstrated that populations of very small NPs (<2 nm) at the ITIES can be controlled reversibly by the applied voltage. Assembly-disassembly of such NPs are relatively easy to control, but as their polarizabilities are proportional to their volume, they do not exhibit a sufficiently strong optical response required to make a mirror. However, later Girault's and Brevet's group received indications of the reversible adsorption of larger core-shell gold-silver nanoparticles at the polarized ITIES using the nonlinear optical technique of surface second-harmonic generation (SHG).³¹ The SHG signals showed a reversible nature and an intensity controlled by the externally applied potential. But as mentioned by the authors, the observed experimental SHG intensity is "not straightforward to extract and relate to the particle surface density since the potential dependence of the adsorption isotherm is not precisely known". A recent study by Schlossman's group³², involving small size NPs, explored NP-arrays modulated by voltage variation for implications in SERS; however, the NP size was too small to generate profound enhancement of the Raman signals, sufficient for practical use, and the nanoparticle array can not be entirely "disassembled"²⁹. Dryfe's group³³ observed electro-tuneable SERS with large NPs, however, continuous tuning of the interparticle spacing and the resultant optical response of the NP-layer was not performed, nor was assembly/disassembly of the array.

In agreement with theoretical expectations^{21, 29}, a dense interfacial assembly of large NPs, of 50-60 nm in diameter, have been shown to provide up to ~40%-50% of maximum reflectivity (even at normal incidence)³⁴ and huge Raman signal enhancements³⁵. The connectivity of the assembly of 60 nm NPs, assessed through lateral conductivity measurements, has, as expected, positively affected the reflectivity. However, for such systems agglomeration at the interface is almost certainly present. Furthermore for larger NPs, already not negligibly smaller than the wavelength of incident light, the corrugation of the interface becomes noticeable, contributing to light scattering. Most importantly, achieving voltage-control over the density of the layer of large NPs, from a dense monolayer to sparse submonolayer, is more challenging due to a deeper capillary well trapping such NPs at the interface, and a propensity of the nanoparticles to agglomerate.

In this chapter, using functionalized gold NPs of moderate size (~16 nm in diameter), we get a strong optical response as well as its electro-tuneability. We present the first demonstration of an electrovariable liquid mirror based on monolayer NP arrays where the optical reflectivity of the interface can be electrically fine-tuned via the voltage-controlled arrays' assembly/disassembly. These observations are directly correlated with the theoretical gap-dependent plasmonic response of such systems. The demonstrated harmony between the theory and experiments signifies again that "physics works!", something that one can never become disenthralled about.

7.3. Gold nanoparticles and electrochemical liquid-liquid cell

Figure 7.2a shows a schematic of the experimental setup consisting of an electrochemical ITIES cell with an optical reflectivity probe and a four-electrode configuration. The ITIES comprises aqueous and organic [1,2-dichloroethane (1,2-DCE)] phases with 10 mM NaCl and 10 mM TBATPB (tetrabutyl ammonium tetraphenylborate), respectively. In our experiments we utilized MDDA (12-Mercaptododecanoic acid) stabilized gold NPs with a functionalized NP size of 16.1 ± 1.1 nm. We have previously shown that 16 nm NPs functionalized with MDDA can be used to control the average interparticle spacing at the interface over the range 6–35 nm²⁶. In this work we show that by incorporating electrovariability, we can bring interparticle distances even closer together by a factor of two (see below) making the optical effect event more dramatic.

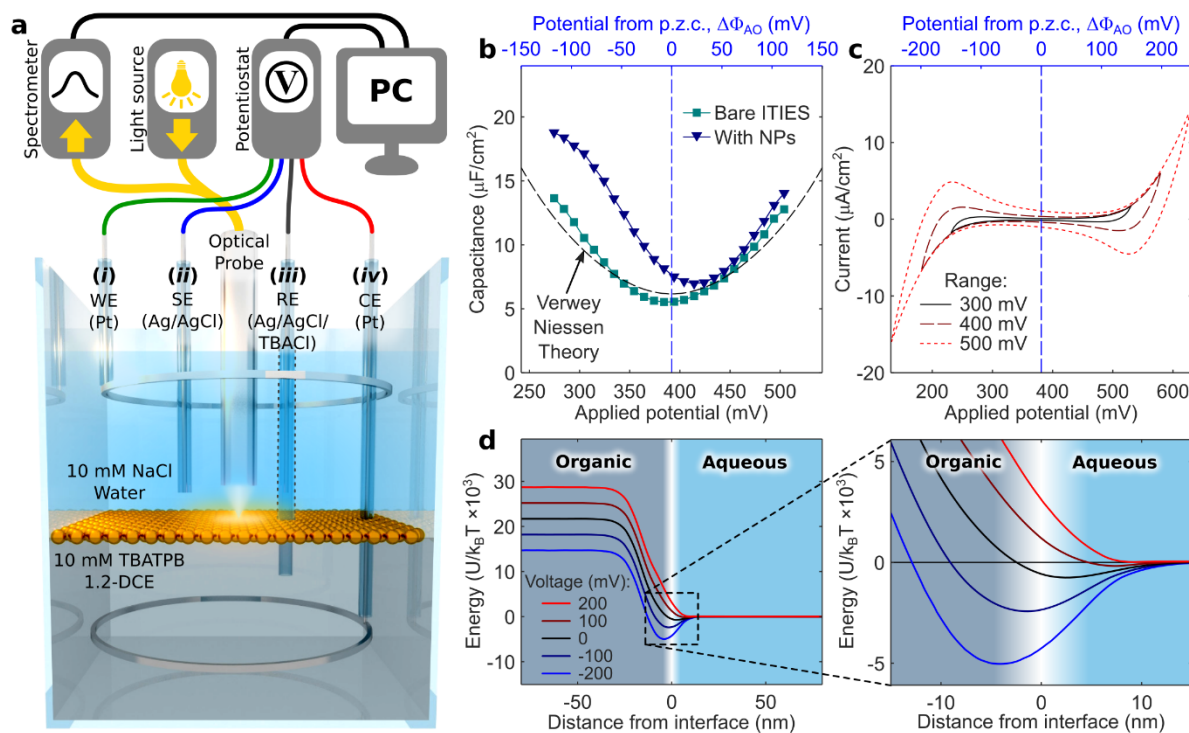


Figure 7.2 **Electrochemical setup and characterization.** (a), Schematic of the ITIES electrochemical cell with an optical probe. The probe shines light onto the interface and transports reflected light to the spectrometer. The potentiostat is connected to the cell through (i) working (WE) and (ii) sense (SE) electrodes in aqueous phase, and (iii) reference (RE) and (iv) counter (CE) electrodes in organic phase. All electrodes are protected with glass capillaries; WE and CE have ring terminals. (b), Capacitances of bare ITIES (\blacksquare) and with NPs (\blacktriangle) in the aqueous phase, $5 \times 10^{12} \text{ cm}^{-3}$. Adsorption of NPs at ITIES increases the capacitance at negative $\Delta\Phi_{\text{AO}}$.³⁶ The bottom, black dashed curve corresponds to Verwey–Niessen (Gouy–Chapman) theory of two back-to-back electrical double layers (without NPs) plotted for the used electrolyte concentrations and solvents.³⁷ The minimum of U-shaped capacitance of a bare ITIES is taken as the potential of zero charge (p.z.c.). (c), Cyclic voltammograms recorded at 5 mV/s over different voltage ranges showing the limits within which there is negligible ionic current across the interface. (d), Calculated potential energy profile of a single NP at the ITIES containing 10 mM TBA-TPB 1,2-DCE and 10 mM NaCl in water, controlled by applied voltage. The blow up highlights the stabilization of the well at negative polarization and its elimination by positive polarization. Curves in (d) are plotted using the equations of Ref.²⁷

Extensive studies of the stability of these nanoparticles were performed in order to ascertain their stability as a function of aqueous electrolyte ionic strength and non-aqueous electrolyte concentration. We found NPs could be stable in 10 mM NaCl in the aqueous solution (c.f. **Chapter 3**) and 10 mM TBATPB in the oil phase. Interestingly, it has been recently reported that for citrate- and short chain-length mercaptopropanesulfonate- stabilized gold nanoparticles, aggregation at the LLI can be induced by low concentrations of tetrabutyl ammonium cations.^{38, 39} We have repeated these experiments for citrate stabilized particles, finding aggregation at concentrations as low as 10^{-5} M TBATPB, and concomitant irreversible formation of aggregated Au particles at the LLI (**Figure 7.3**). The absence of aggregation with our particles is associated with the longer chain surfactants resisting close approach of the nanoparticles.

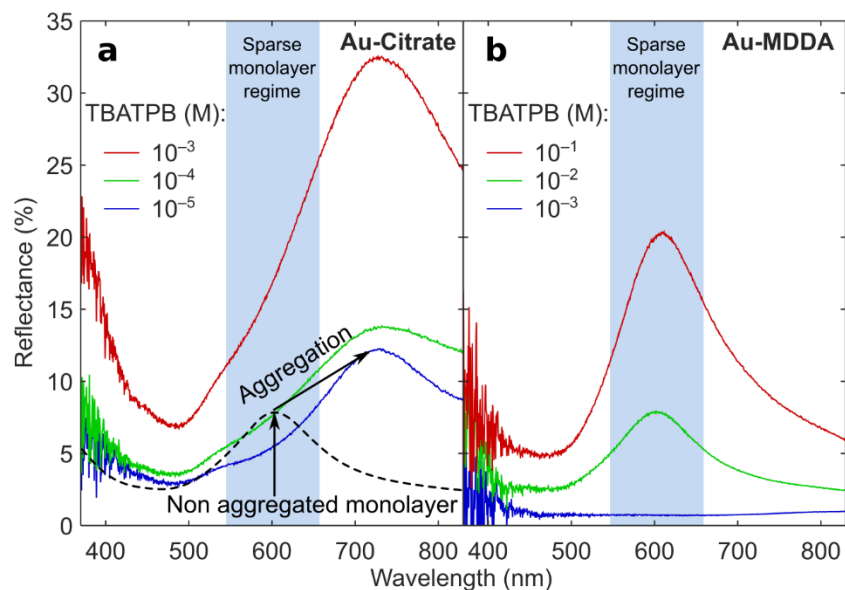


Figure 7.3 Reflectance observed from Au NPs assembled at liquid-liquid interfaces for different molarity of TBATPB at the organic phase and 10 mM of NaCl at aqueous phase. (a) Au-Citrate NPs were tested at concentrations of 10^{-5} M, 10^{-4} M and 10^{-3} M, showing aggregation at very low concentration <10 M. (b) Au-MDDA NPs were tested at larger concentrations of 10^{-3} M, 10^{-2} M and 10^{-1} M without sign of aggregation.

The ITIES was characterized by electrical capacitance (**Figure 7.2b**), obtained from impedance measured at 1 Hz frequency with $1 \text{ mV}_{\text{rms}}$ signal amplitude, over the interval of applied voltage bias, recorded in 5 mV steps. We first checked how well the classical Verwey-Niessen theory of two back-to-back electrical double layers⁴⁰ (black dashed curve) replicates the response for bare ITIES (squares). In the range between -100 mV to +100 mV, the data reproduce theoretical predictions; outside this range, the capacitance rise is steeper. The latter has been explained by voltage-induced undulations of the interface that increase its area and thereby the capacitance.⁴¹ The potential of zero charge (p.z.c.) corresponds to the potential of the minimum of capacitance of the bare ITIES. With NPs at the interface (triangles) the capacitance should be larger, as when NPs pierce the interface the ITIES surface area increases.³⁶ We see this for $\Delta\Phi_{\text{AO}} < 0$, where NPs are pushed towards the ITIES. This effect practically disappears at $\Delta\Phi_{\text{AO}} > 0$ when NPs leave the interface for the aqueous bulk. These trends are similar to the earlier observed ones by Girault's group⁴² and rationalized in Ref. ³⁶.

Cyclic voltammograms without NPs (**Figure 7.2c**) were measured to evaluate the potential window within which no significant ionic current flows across the ITIES. We set a target of $16 \mu\text{A cm}^{-2}$ maximum current at a scan rate of 5 mV s^{-1} to determine a safe electrochemical window at which the interface is not disturbed by ionic transport across it. Using this criterion, we were able to sustain a 500 mV window without excessive ion transfer; all experiments described below were performed inside this range. The low average current and relatively high aqueous electrolyte conductivity mean that any static potential $\ll 1 \text{ mV}$, and so electrophoretic effects may be ignored.

7.4. Dynamics of assembly-disassembly of nanoparticle arrays

The theoretical estimate of the potential energy profile of a single NP at the ITIES as a function of applied voltage, shown in **Figure 7.2d**, depicts the concept of electrical modulation of the capillary well, which plays a vital role in deciding NP population at the ITIES. The curves here were calculated using the approach and equations described in detail in Ref.²⁷, and the parameters correspond to our experimentally studied ITIES cell. The curves in **Figure 7.2d** correspond to different values of $\Delta\Phi_{AO}$. Please note that **Figure 7.2d** bears only a *qualitative* message, because the theory used to plot it is too simplistic for any quantitative predictions. Furthermore, although there is a well for an individual NP at the non-polarised interface (black line), the wells will become shallower for NPs settling close to each other, when forming a dense array. To reversibly control the population of NPs at the interface with the voltage across it, we must first ensure no aggregation of NPs occur in the bulk. This can be achieved by optimizing the NP size, ligand charge/length, Debye screening, and choice of solvent. Adjustment of these parameters offers, simultaneously, a fine balance between the maximal optical reflectivity of NP arrays, and the ease of their assembly/disassembly. The theory²⁷ helps navigating the search for such conditions, but the exact system parameters has to be found experimentally, which has been achieved in the present work.

Crucially, the electric field at the ITIES is localized near the interface, within two double layers – each a Gouy-length thick.⁴³ At the electrolyte concentrations used, the overall width is ~ 4 nm. The *bulk solution will be electroneutral*, with electric field totally screened. There is no one-dimensional drift of NPs in the external field across the bulk, as the field is zero there, as expected from the near-zero current during the potential step, and the very low transference number of the gold particles in solution. Hence, the NPs will only be able to work their way to the ITIES *via random diffusion*, which imposes restrictions on the mirror switching time. We should also ensure that the substantial $\Delta\Phi_{AO}$ is applied to avoid any potential barrier preceding the well. Under these conditions, the switch-‘on’-time is determined by diffusion-controlled adsorption of NPs and can be improved by reducing the average path length via increasing the NP concentration or introducing convection. In our system we have sought to minimise convection by performing experiments under temperature-controlled conditions in order to minimise thermally driven convection in the electrochemical cell. Confirmation that diffusion is the predominant mode of transport is provided by the optical images of the electrolyte adjacent to the ITIES, showing a smooth and graded response over a distance of 1 cm perpendicular to the ITIES during nanoparticle absorption and desorption from the ITIES, **Figure 7.4c**. The lack of any sharp transitions and the significant distance over which the gradient is maintained strongly suggests that diffusion, and not convection, is the major transport mechanism. Without any detailed theory one can obtain an order of magnitude estimate for the time needed to fill the monolayer via diffusion from the bulk. The area which is expected to be occupied by one particle

in a complete monolayer, $\xi\pi R^2 \equiv 1/\Gamma_{\max}$ where R is the NP radius, ξ is a packing factor with the value of the order of 1 (depending on the structure of the layer and the size of the ligands, e.g. for triangular lattice arrangement $\xi = \frac{2\sqrt{3}}{\pi} \left(1 + \frac{\delta}{R}\right)$ where δ is the length of functionalizing ligands) and; Γ_{\max} is the maximal surface coverage. Given the average concentration of NPs in the solution, an average closest distance l from such spot to any NP in the solution is estimated from an equation: $c_{np} \approx \frac{1}{l\xi\pi R^2} = \frac{\Gamma_{\max}}{l}$, hence $l \approx \frac{1}{c_{np}\xi\pi R^2} = \frac{\Gamma_{\max}}{c_{np}}$. The time needed for that particle to reach that spot by Brownian diffusion, is then given by:

$$\tau_a = \frac{l^2}{D_{np}} = \left(\frac{\Gamma_{\max}}{c_{np}}\right)^2 \frac{1}{D_{np}} \quad 7.2$$

Average concentration of NPs in the bulk of the aqueous phase of our sample is estimated as $5.3 \times 10^{12} \text{ cm}^{-3}$; for the diffusion coefficient in water of 16 nm gold NPs with 2.4 nm ligands we take for orientation the data of Ref.⁴⁴: $D_{NP} = 1.53 \times 10^{-7} \text{ cm}^2\text{s}^{-1}$; for dense packing of such NPs (packing of NP centres on a triangular lattice with a lattice constant 18.8 nm, c.f. the next section), $\Gamma_{\max} = 3.26 \cdot 10^{11} \text{ particles/cm}^2$. From Eq. 7.2 we obtain then a disappointingly long time of $\tau_d = 1.93 \cdot 10^4 \text{ s}$. As τ_d is inversely proportional to the square of concentration, the way to decrease the time is to increase concentration in the same sample. We checked this law experimentally, and the inset of **Figure 7.4d-i**, proves that $\tau_d \propto c_{np}^{-2}$ law does work. However for practical applications increasing the NP concentration in our current configuration is not the way to go, as the increase of the NP concentration in the bulk adds to light absorption and the colour change. A clear way to achieve the fast switching time, is to use miniaturise, micro/nano cell. Indeed, incorporating the platform into a microfluidic channel with the height of the aqueous column of 10 μm , i.e. 10^{-3} times smaller than we use it now, but with 10^3 times higher nanoparticle concentration will not increase light absorption, but will bring the switch-on time to the ms time scale.

Noteworthy, as is seen from **Figure 7.4b-iii**, the dynamics of monolayer formation, after abruptly polarizing the aqueous phase negatively with respect to oil, does roughly obey law⁴⁵ of diffusion limited adsorption, which before it reaches saturation is well reproduced by the simple diffusion law:

$$\Gamma(t)/\Gamma_{\max} = \sqrt{\frac{t}{\tau_a}} \quad 7.3$$

These arguments are valid when the NPs in the bulk are in substantial excess above the amount to just cover the surface. They also require the absence of the barrier for the NP at the entrance to their wells. If such barrier exists, more general equations, accounting for adsorption limitations in the adsorption kinetics need to be invoked, but in our case, this did not seem to be necessary. On the other hand, once the NPs are assembled at the ITIES, removing them and switching the mirror ‘off’ will be much faster, if the well at the interface is destroyed completely. According the EMT calculation, it is sufficient for NPs to drift away from the interface some distance $l > 10R$ (R is NP-radius) in order to stop performing the coherent mirror function. The time needed for disassembly by the diffusion drift can then be estimated as:

$$\tau_d \sim \frac{l^2}{D_{\text{NP}}} \sim \frac{(10R)^2}{D_{\text{NP}}} \quad 7.4$$

With $R \sim 8 \times 10^{-7}$ cm, and again $D_{\text{NP}} = 1.53 \times 10^{-7}$ cm²s⁻¹ we get $\tau_d \sim 4.2 \times 10^{-4}$ s. However, such value for the mirror switching-off time will be valid only if the applied potential bias fully removes the well. However, the voltage applied is seemingly insufficient to fully remove the well, because the observed time is of the order of few seconds (**Figure 7.4d-ii**). Where is still a metastable well separated by a barrier, the disassembly time will be determined by the Kramers time of escape from the well. Generally, it might be interesting to describe such case, but the problem is that individual wells for NPs are affected by the presence of neighboring NPs, and once they start leaving the surface, the wells will get deeper and the process will slow down and overall will not be described by the classical Kramers model.^{46, 47} The theory of such a complex process should be left for future research. But interestingly this is what **Figure 7.4d-ii** exactly shows: a fast major initial stage of disassembly taking about 2s and a slower tail. This limitation can be overcome for systems with a larger potential window, as larger voltages will remove the metastable well to reach the sub-millisecond regime of disassembly.

If the wells or barriers are removed by the applied voltage, and the system is rapidly switched on and off, back-and-forth, the assembly time will be decided just by the shorter of the diffusion time and the switching interval. In a macroscopic cell, the shortest time will be the switching-time, but it can be the diffusion-time in a miniaturized cell.

7.5. Optical response during assembly/disassembly process

The results shown below demonstrate the proof-of-the-principle of the electrovariable mirror–window, consistent with these estimates of the time constants. In this work we focus on the physics of the electrovariable effect, demonstrating how it works in a macroscopic cell, unravelling the interplay between voltage-controlled assembly/disassembly and the optical response rather the working towards optimizing the response time.

Optical reflectivity of this electrovariable interface was measured with a spectrometer when illuminated by normal incidence of white unpolarised light through an optical probe. Such measured reflectance data provide typically an estimate of the minimal reflectivity from any surface. **Figure 7.4a** shows the observed evolution of the reflectivity spectra in real time after the application of -200 mV potential drop across the ITIES. This voltage induces the adsorption of NPs at the interface; the reflectance spectra evolve until the process stops. During this assembly process, the reflectance increases and its peak wavelength shifts to the red. The obtained peak reflectance R_{\max} and peak wavelength λ_{\max} are found to be in excellent agreement with theoretically simulated optical reflectance spectra, shown in **Figure 7.4b-i** and **ii**. ‘Theoretical’ spectra were generated using the original theory⁴⁸, under the following two assumptions.

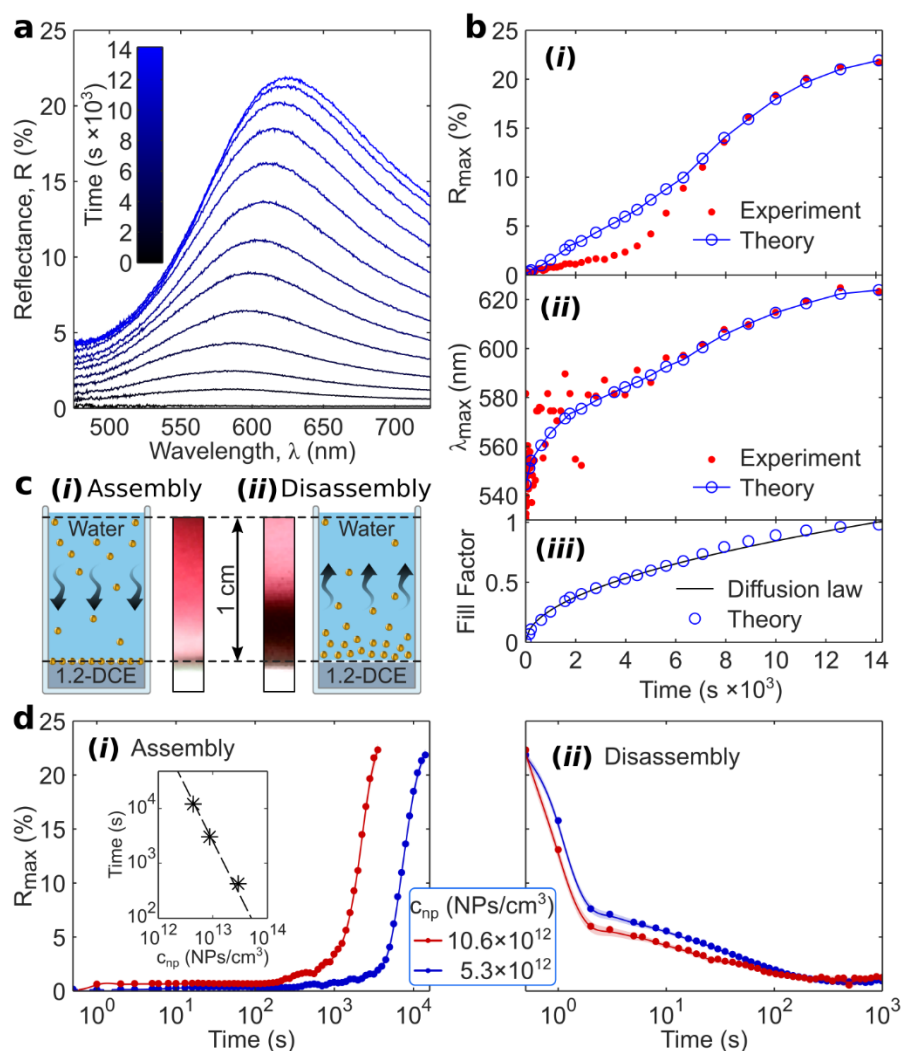


Figure 7.4 Dynamics of assembly and disassembly of 16nm diameter MDDA functionalised gold NPs at the ITIES interface. (a) Optical reflectance spectra observed during assembly process in equally spaced time steps ranging from 1 to 14116 seconds at the potential bias -200 mV (water relative to oil). (b) The peak reflectance R_{\max} (i) and peak wavelength λ_{\max} (ii) measured during the assembly process (red filled circles) are compared against their theoretical estimates (blue open circles connected by a line). (iii) The time dependence of the fill factors – the coverage of the interface by NPs (blue open circles) obtained from theoretical fitting are then compared against those obtained from the diffusion-limited adsorption (Eq. 7.3) law (solid black curve), with a fitted value of the diffusion coefficient, eventually coinciding with $1.53 \times 10^{-7} \text{ cm}^2/\text{s}$ reported in Ref.⁴⁴ and the bulk NP concentration $c_{\text{np}} = 5.3 \times 10^{12} \text{ NP}/\text{cm}^3$. (c) Cartoons of assembly (i) and (ii) disassembly process ‘viewed’ from the side of the container; the middle colour gradients are real photographs of the same view taken during the experiment, with the ITIES at the bottom of the images. The latter correspond to density distributions of NPs in the aqueous phase during (i) assembly and (ii) disassembly each shot after a period of 4 hours. (d) Evolution of reflectance peak R_{\max} during assembly (i) and disassembly (ii) of NPs for two different concentrations. The potential applied for assembly was -200 mV and for disassembly 200 mV. The scaling of the adsorption time as $1/c_{\text{np}}^2$ is well seen in the insert of (i) plotted for three concentrations of NPs – 5.3×10^{12} , 10.6×10^{12} , and $35.4 \times 10^{12} \text{ NPs}/\text{cm}^3$. ITIES: 10 mM NaCl aqueous | DCE + 10 mM TBATPB organic phases.

Firstly, at steady state the NPs are considered to form a homogeneous hexagonally-ordered monolayer. In this formulation, we considered NPs settling right at the interface. The method described in Ref.²⁵ is then applied to find the lattice constant that matches λ_{\max} of the steady-state optical reflectance spectrum (the ‘long time’ data). It is found that the λ_{\max} at steady-state refers to a uniform monolayer with lattice constant 18.8 nm, *i.e.* shortest inter-NP, surface-to-surface, separation of 2.8 nm.

Secondly, for less dense layers it is convenient to use the approach where the filling fraction, $f = \Gamma(t)/\Gamma_{\max}$ of the monolayer is varied, instead of varying the lattice constant. The fill factor $f = 1$ corresponds to a dense hexagonal monolayer in which each lattice-site would have been occupied by an NP with 100% probability. When the assembly process starts, $f \ll 1$. With time, more and more NPs adsorb at the interface, and f increases, and its optical reflectivity reaches saturation. This way we are left with just one fitting parameter f , the value of which can in principle vary between 0 and 1 to match the optical reflectance spectrum at different stages of the monolayer formation. The theoretical model for calculating optical response from an incomplete monolayer follows the same strategy as applied for the complete monolayer. The only difference would be in the effective polarizability expressions, which are affected by the value of f . With this new approach, we can find the fill factors that match the reflectance maximum R_{\max} and peak wavelength λ_{\max} at every time point of the assembly process. As expected and already mentioned, the fill factor evolution follows a diffusion limited adsorption law (Eq. 7.2), up to the times close to the saturation (as shown in **Figure 7.4b-iii**), with the diffusion coefficient of NPs of the value of $1.53 \times 10^{-7} \text{ cm}^2/\text{s}$ Ref.⁴⁴.

The spatial density distribution of NPs in the solution adjacent to the ITIES can be clearly observed from the side windows of the cell. **Figure 7.4c** shows the schematic and actual photographs (colour gradient panels) corresponding to the NP density distribution in the aqueous phase during assembly (i) and disassembly (ii), each after a period of 4 hours.

Evolution of the reflectance peak R_{\max} during assembly and disassembly of NPs for two different concentrations are shown in **Figure 7.4d**. According to Eq. 7.2, the speed of assembly increases quadratically with the concentration of NPs (**Figure 7.4d-i**). The insert in **Figure 7.4d-i** shows data for experiments performed at three concentrations, which clearly demonstrates the $\tau_a \propto c_{np}^{-2}$ law. The disassembly process is practically independent of concentration, c.f. Eq. 7.4 (**Figure 7.4d-ii**).

7.6. Electrotuning of the optical metasurface

A clear advantage of an electroactive TOM is in the ability to fine tune the reflectivity spectrum, including peak reflectance, R_{\max} , and peak wavelength, λ_{\max} , by changing the applied potential. **Figure 7.5a** shows the time-dependence of R_{\max} and λ_{\max} during the disassembly process. In this experiment, first a monolayer was formed at $\Delta\Phi_{AO} = -250 \text{ mV}$, then the potential was increased to the p.z.c. until the spectra stabilized. Noticeably within the first 30 s the system attained a constant reflectivity, although λ_{\max} takes a little longer to stabilize ($\sim 100\text{s}$).

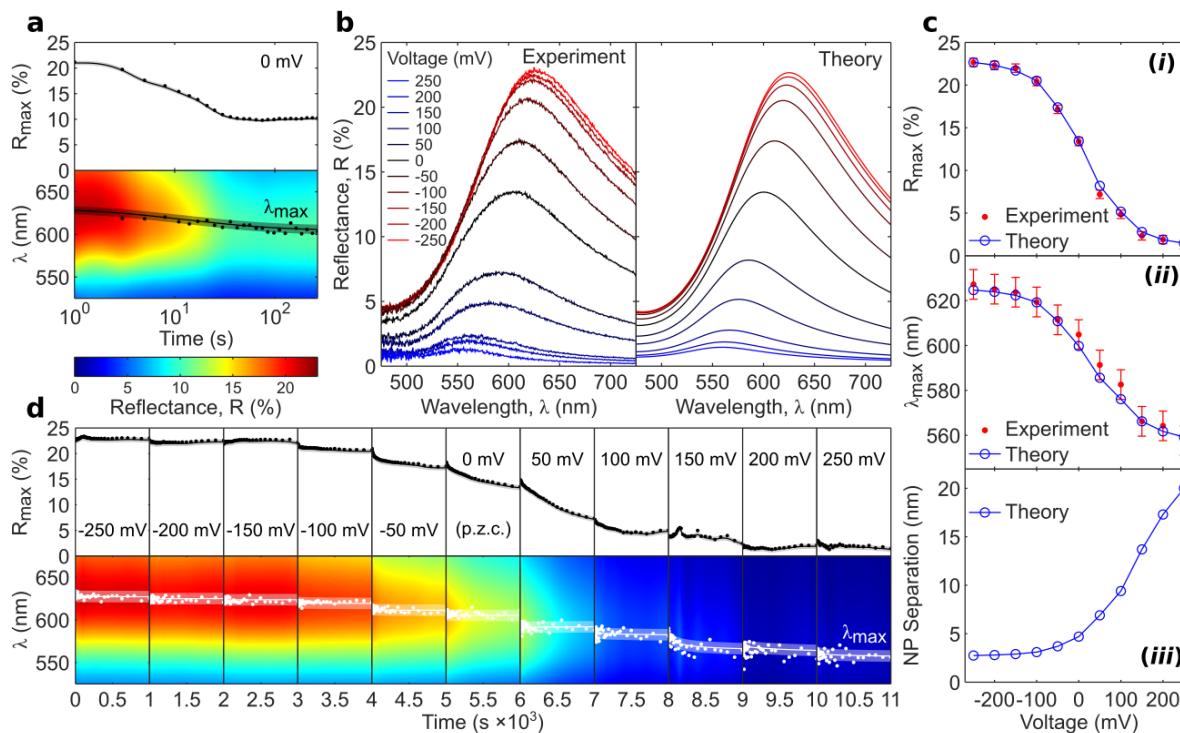


Figure 7.5 **Voltage-controlled plasmon ruler utilizing 16nm diameter MDDA functionalised gold NPs at the ITIES interface.** (a) Evolution of peak reflectance R_{\max} and peak wavelength λ_{\max} of the NP mirror. The experiment was conducted in a two-step process: first, the NP mirror was assembled at a negative polarization (-250 mV) of the aqueous phase relative to the oil phase. Then the potential was increased to the p.z.c. and kept such for 200 seconds, the spectra were recorded until they stabilize. (b) Optical reflectance spectra were recorded at steady-state for different applied electric potentials: experimental (left panel) and theoretical (right panel). (c) Comparison between the experimental data (red circles) and theoretical calculations (blue open circles connected by a line) for (i) R_{\max} and (ii) λ_{\max} for different applied potentials; (iii) shows variation of the inter-NP separation, fitted for the theory to reproduce the experimental reflectance spectra, with applied voltage. (d) Steady states observed when the NP mirror was disassembling in a multi-step process, starting from a fully assembled layer to a state when the majority of NPs leave the interface. Each step, corresponded to indicated voltage, lasted 1000 seconds after which the spectra stabilized. ITIES: 10 mM NaCl aqueous /1,2 dichloro ethane + 10 mM TBATPB organic phases.

In **Figure 7.5b** the equilibrium reflectance spectra are shown, as well as the theoretically calculated ones, for a series of potentials between -250 to 250 mV. In the calculated spectra, for each potential, the adopted lattice constant (NP-surface-to-surface separation) in the NP hexagonal array was different, subjected to the best fit to the measured spectra; **Figures 7.5c-i** and **ii** show fits being in excellent agreement. **Figure 7.5c-iii** shows the dependence of the thus obtained inter-NP separation on voltage; as expected for large negative $\Delta\Phi_{AO}$, a dense monolayer is formed with short inter-NP separation. For less negative voltages the potential well that keeps NPs at the interface becomes less deep, which makes it harder for them to tolerate their mutual electrostatic repulsion, so some NPs will have to leave the interface. As a result, the inter-NP separations increase and the reflectance diminishes, vanishing at large positive potentials.

The variation of inter-NP separation as a function of applied voltage demonstrates the proof-of-concept for a ‘voltage-controlled plasmon ruler’. It allows us to tune inter-NP separation over a range of about 3–20 nm *in-situ* just by altering the applied potential $\Delta\Phi_{AO}$ within a 500 mV window.

Tuning the NP array structure can also be performed consecutively. After inducing the complete assembly at -250 mV we further conducted a multi-step disassembly process (**Figure 7.5d**) with the potential $\Delta\Phi_{AO}$ increased in 50 mV steps, from -250 mV to 250 mV. Each potential step had a duration of 1000 seconds. These experiments once more show that the interparticle distance can be precisely controlled which allows accurate tuning of both reflectance intensity and peak wavelength.

7.7. Reversibility of the electro-tunable device

Switching the liquid-mirror ‘on’ (applying $\Delta\Phi_{AO} = -200$ mV) and ‘off’ ($\Delta\Phi_{AO} = 200$ mV) for two consecutive cycles demonstrates the full reversibility of the designed TOM (**Figure 7.6a–iv**). We fabricated a prototype device (**Figure 7.6b**) of a switchable window–mirror, which can be altered electrovariably between its transmissive and reflective states. To demonstrate this, we placed a coin in front of the liquid mirror and a currency note at the back of the mirror, as shown in the schematic **Figure 7.6c**.

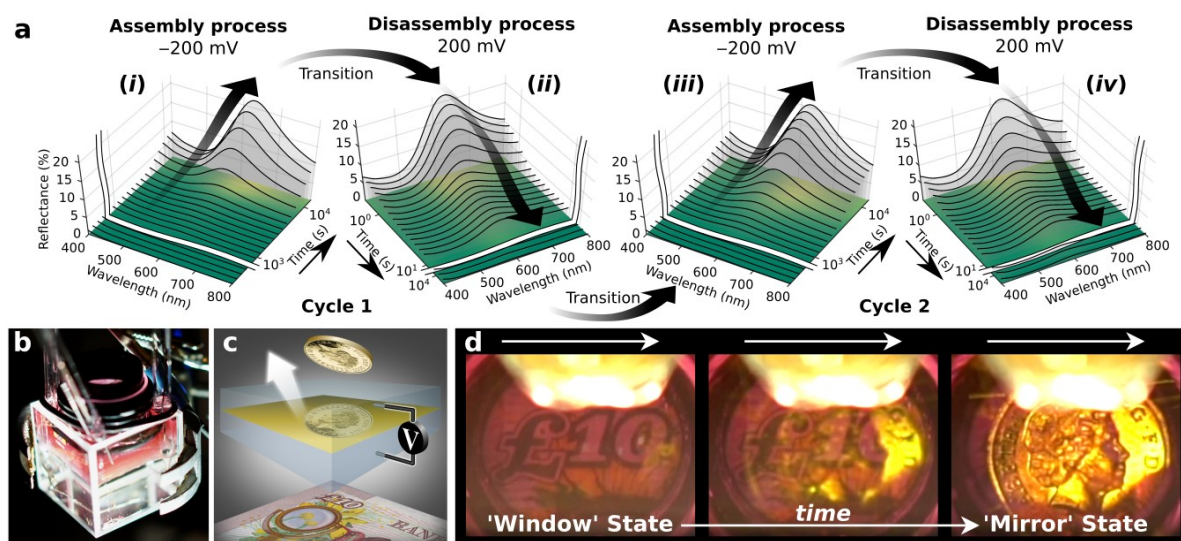


Figure 7.6 Switchable window–mirror. (a) Time dependent study showing two cycles of reversible spectral characteristics of a mirror/window application where NPs (i) assemble at -200 mV and(ii) disassemble at 200 mV, followed by a repetition of those two states in a consecutive cycle – (iii) and (iv). (b) Experimental setup for recording switchable liquid window–mirror application. (c) Schematic showing the setup with a coin facing the liquid mirror and a currency note at the back of the mirror. (d) Real images observed during the transition between a transmissive ‘window’ state (when no NPs are at the interface) to a reflective ‘mirror’ state (when NPs assemble densely at the interface). 16nm diameter MDDA functionalized gold NPs at the ITIES interface which was composed of a 10 mM NaCl aqueous | DCE + 10 mM TBATPB organic phase interface.

The transformation from a ‘window’ to a ‘mirror’ is shown in **Figure 7.6d**. A positive applied potential made the ITIES free of NPs and hence, the interface emulated a transmissive ‘window’ that allows us to see the currency note. After reversing the voltage polarity, NPs gradually adsorb to the interface and form a dense layer that behaves like a reflective ‘mirror’. The reflection of the coin can thus be seen.

7.8. Conclusion

Here we present the first realization of an electrochemical nanoplasmonic platform operating with medium size NPs that provides electrotuneable optical responses. In this platform we reversibly control the interparticle distances in two dimensional arrays of NPs at a liquid-liquid interface, from full assembly to disassembly and back, by varying the potential drop across the interface. This allows us to control the wavelength-dependent reflectivity of the interface. We demonstrated that different potentials produce, correspondingly, different steady-state reflection spectra. The peak reflectance was tailorable both in intensity and wavelength. We show how this system can be used to fabricate a switchable window–mirror device.

The dynamics of the operation is dictated by the diffusion of NPs to/from a polarized liquid | liquid interface. We observe that the assembly time is inversely proportional to the square of the concentration of NPs, as expected from a diffusion driven assembly process. The disassembly time is independent of NP concentration. In a macroscopic electrochemical cell, used in this proof-of-the-principle investigation, the dynamics of assembly is slow determined by diffusion of NPs over, on average, long distances. The dynamics can be sped up by orders of magnitude via miniaturization of the cell.

Experimental results are corroborated by theoretical predictions, demonstrating the simple physics behind the voltage-controlled assembly-disassembly of NPs is correct, as well as our ability to calculate the reflection spectra from NP arrays using transparent, simple theory. This study opens up a wide range of possibilities for designing electrotuneable optical metamaterials including switchable mirrors, filters, displays and SERS sensors.

7.9. References

- (1) Montelongo, Y.; Sikdar, D.; Ma, Y.; McIntosh, A. J. S.; Velleman, L.; Kucernak, Anthony R.; Edel, J. B.; Kornyshev, A. A. Electrotunable Nanoplasmonic Liquid Mirror. *Nat. Mater.* **2017**, *16*, 1127-1135.
- (2) Fan, J. A.; Wu, C. H.; Bao, K.; Bao, J. M.; Bardhan, R.; Halas, N. J.; Manoharan, V. N.; Nordlander, P.; Shvets, G.; Capasso, F. Self-Assembled Plasmonic Nanoparticle Clusters. *Science* **2010**, *328*, 1135-1138.
- (3) Stebe, K. J.; Lewandowski, E.; Ghosh, M. Oriented Assembly of Metamaterials. *Science* **2009**, *325*, 159-160.

- (4) Nie, Z.; Petukhova, A.; Kumacheva, E. Properties and Emerging Applications of Self-Assembled Structures Made from Inorganic Nanoparticles. *Nat. Nanotechnol.* **2010**, *5*, 15-25.
- (5) Lal, S.; Link, S.; Halas, N. J. Nano-Optics from Sensing to Waveguiding. *Nat. Photonics* **2007**, *1*, 641-648.
- (6) Engheta, N. Circuits with Light at Nanoscales: Optical Nanocircuits Inspired by Metamaterials. *Science* **2007**, *317*, 1698-1702.
- (7) Kabashin, A. V.; Evans, P.; Pastkovsky, S.; Hendren, W.; Wurtz, G. A.; Atkinson, R.; Pollard, R.; Podolskiy, V. A.; Zayats, A. V. Plasmonic Nanorod Metamaterials for Biosensing. *Nat. Mater.* **2009**, *8*, 867-871.
- (8) Kawata, S.; Inouye, Y.; Verma, P. Plasmonics for Near-Field Nano-Imaging and Superlensing. *Nat. Photonics* **2009**, *3*, 388-394.
- (9) Shalaev, V. M. Optical Negative-Index Metamaterials. *Nat. Photonics* **2007**, *1*, 41-48.
- (10) Maier, S. A.; Brongersma, M. L.; Kik, P. G.; Meltzer, S.; Requicha, A. A. G.; Atwater, H. A. Plasmonics - A Route to Nanoscale Optical Devices. *Adv. Mater.* **2001**, *13*, 1501-1505.
- (11) Atwater, H. A.; Polman, A. Plasmonics for Improved Photovoltaic Devices. *Nat. Mater.* **2010**, *9*, 205-213.
- (12) Willets, K. A.; Van Duyne, R. P. Localized Surface Plasmon Resonance Spectroscopy and Sensing. *Annu. Rev. Phys. Chem.* **2007**, *58*, 267-297.
- (13) Samec, Z. Electrical Double-Layer at the Interface between 2 Immiscible Electrolyte-Solutions. *Chem. Rev.* **1988**, *88*, 617-632.
- (14) Samec, Z. Electrochemistry at the Interface Between Two Immiscible Electrolyte Solutions. *Pure Appl. Chem.* **2004**, *76*, 2147-2180.
- (15) Jensen, T. R.; Schatz, G. C.; Van Duyne, R. P. Nanosphere Lithography: Surface Plasmon Resonance Spectrum of a Periodic Array of Silver Nanoparticles by Ultraviolet-visible Extinction Spectroscopy and Electrodynamic Modeling. *J. Phys. Chem. B* **1999**, *103*, 2394-2401.
- (16) Jain, P. K.; Huang, W.; El-Sayed, M. A. On the Universal Scaling Behavior of the Distance Decay of Plasmon Coupling in Metal Nanoparticle Pairs: A Plasmon Ruler Equation. *Nano Lett.* **2007**, *7*, 2080-2088.
- (17) Ghosh, S. K.; Pal, T. Interparticle Coupling Effect on the Surface Plasmon Resonance of Gold Nanoparticles: From Theory to Applications. *Chem. Rev.* **2007**, *107*, 4797-4862.
- (18) Su, K. H.; Wei, Q. H.; Zhang, X.; Mock, J. J.; Smith, D. R.; Schultz, S. Interparticle Coupling Effects on Plasmon Resonances of Nanogold Particles. *Nano Lett.* **2003**, *3*, 1087-1090.
- (19) Halas, N. J.; Lal, S.; Chang, W.-S.; Link, S.; Nordlander, P. Plasmons in Strongly Coupled Metallic Nanostructures. *Chem. Rev.* **2011**, *111*, 3913-3961.
- (20) Yogeov, D.; Efrima, S. Novel Silver Metal Liquidlike Films. *J. Phys. Chem.* **1988**, *92*, 5754-5760.
- (21) Flatte, M. E.; Kornyshev, A. A.; Urbakh, M. Electrovariable Nanoplasmonics and Self-Assembling Smart Mirrors. *J. Phys. Chem. C* **2010**, *114*, 1735-1747.
- (22) Edel, J. B.; Kornyshev, A. A.; Kucernak, A. R.; Urbakh, M. Fundamentals and Applications of Self-Assembled Plasmonic Nanoparticles at Interfaces. *Chem. Soc. Rev.* **2016**, *45*, 1581-1596.
- (23) Booth, S. G.; Dryfe, R. A. W. Assembly of Nanoscale Objects at the Liquid/Liquid Interface. *J. Phys. Chem. C* **2015**, *119*, 23295-23309.
- (24) Smirnov, E.; Peljo, P.; Scanlon, M. D.; Gumy, F.; Girault, H. H. Self-Healing Gold Mirrors and Filters at Liquid-Liquid Interfaces. *Nanoscale* **2016**, *8*, 7723-7737.
- (25) Velleman, L.; Sikdar, D.; Turek, V. A.; Kucernak, A. R.; Roser, S. J.; Kornyshev, A. A.; Edel, J. B. Tuneable 2d Self-Assembly of Plasmonic Nanoparticles at Liquid| Liquid Interfaces. *Nanoscale* **2016**, *8*, 19229-19241.
- (26) Turek, V. A.; Cecchini, M. P.; Paget, J.; Kucernak, A. R.; Kornyshev, A. A.; Edel, J. B. Plasmonic Ruler at the Liquid-Liquid Interface. *ACS Nano* **2012**, *6*, 7789-7799.
- (27) Flatte, M. E.; Kornyshev, A. A.; Urbakh, M. Understanding Voltage-induced Localization of Nanoparticles at a Liquid-Liquid Interface. *J. Phys.: Condens. Matter* **2008**, *20*, 073102.
- (28) Edel, J. B.; Kornyshev, A. A.; Urbakh, M. Self-Assembly of Nanoparticle Arrays for Use as Mirrors, Sensors, and Antennas. *ACS Nano* **2013**, *7*, 9526-9532.

- (29) Sikdar, D.; Kornyshev, A. A. Theory of Tailorable Optical Response of Two-dimensional Arrays of Plasmonic Nanoparticles at Dielectric Interfaces. *Sci. Rep.* **2016**, *6*.
- (30) Su, B.; Abid, J. P.; Fermin, D. J.; Girault, H. H.; Hoffmannova, H.; Krtil, P.; Samec, Z. Reversible Voltage-induced Assembly of Au Nanoparticles at Liquid Vertical Bar Liquid Interfaces. *J. Am. Chem. Soc.* **2004**, *126*, 915-919.
- (31) Abid, J.-P.; Abid, M.; Bauer, C.; Girault, H. H.; Brevet, P.-F. Controlled Reversible Adsorption of Core - Shell Metallic Nanoparticles at the Polarized Water/1,2-dichloroethane Interface Investigated by Optical Second-harmonic Generation. *J. Phys. Chem. C* **2007**, *111*, 8849-8855.
- (32) Bera, M. K.; Chan, H.; Moyano, D. F.; Yu, H.; Tatur, S.; Amoanu, D.; Bu, W.; Rotello, V. M.; Meron, M.; Kral, P.; Lin, B.; Schlossman, M. L. Interfacial Localization and Voltage-Tunable Arrays of Charged Nanoparticles. *Nano Lett.* **2014**, *14*, 6816-6822.
- (33) Booth, S. G.; Cowcher, D. P.; Goodacre, R.; Dryfe, R. A. W. Electrochemical modulation of SERS at the liquid/liquid interface. *Chem. Commun.* **2014**, *50*, 4482-4484.
- (34) Fang, P.-P.; Chen, S.; Deng, H.; Scanlon, M. D.; Gumy, F.; Lee, H. J.; Momotenko, D.; Amstutz, V.; Cortes-Salazar, F.; Pereira, C. M.; Yang, Z.; Girault, H. H. Conductive Gold Nanoparticle Mirrors at Liquid/Liquid Interfaces. *ACS Nano* **2013**, *7*, 9241-9248.
- (35) Kondrat, S.; Wu, P.; Qiao, R.; Kornyshev, A. A. Accelerating Charging Dynamics in Subnanometre Pores. *Nat. Mater.* **2014**, *13*, 387-393.
- (36) Marinescu, M.; Urbakh, M.; Kornyshev, A. A. Voltage-Dependent Capacitance of Metallic Nanoparticles at a Liquid/Liquid Interface. *Phys. Chem. Chem. Phys.* **2012**, *14*, 1371-1380.
- (37) Volkov, A. G.; Deamer, D. W.; Tanelian, D. L.; Markin, V. S. Electrical Double Layers at the Oil/Water Interface. *Prog. Surf. Sci.* **1996**, *53*, 1-134.
- (38) Konrad, M. P.; Doherty, A. P.; Bell, S. E. J. Stable and Uniform SERS Signals from Self-Assembled Two-Dimensional Interfacial Arrays of Optically Coupled Ag Nanoparticles. *Anal. Chem.* **2013**, *85*, 6783-6789.
- (39) Xu, Y.; Konrad, M. P.; Lee, W. W. Y.; Ye, Z.; Bell, S. E. J. A Method for Promoting Assembly of Metallic and Nonmetallic Nanoparticles into Interfacial Monolayer Films. *Nano Lett.* **2016**, *16*, 5255-5260.
- (40) Verwey, E. J. W.; Niessen, K. F. XI. The Electrical Double Layer at the Interface of Two Liquids. *Lond. Edinb. Dublin Philos. Mag. J. Sci.* **1939**, *28*, 435-446.
- (41) Daikhin, L. I.; Kornyshev, A. A.; Urbakh, M. Capillary Waves at Soft Electrified Interfaces. *J. Electroanal. Chem.* **2000**, *483*, 68-80.
- (42) Younan, N.; Hojeij, M.; Ribeaucourt, L.; Girault, H. H. Electrochemical Properties of Gold Nanoparticles Assembly at Polarised Liquid Vertical Bar Liquid Interfaces. *Electrochem. Commun.* **2010**, *12*, 912-915.
- (43) Girault, H. H.; Schiffrin, D. H., *Electroanalytical Chemistry, Electrochemistry of Liquid-Liquid Interfaces*. CRC Press: 1988; Vol. 15, pp 1-142.
- (44) Wong, K.; Chen, C.; Wei, K.; Roy, V. A. L.; Chathoth, S. M. Diffusion of Gold Nanoparticles in Toluene and Water as Seen by Dynamic Light Scattering. *J. Nanopart. Res.* **2015**, *17*, 153.
- (45) Miura, T.; Seki, K. Diffusion Influenced Adsorption Kinetics. *J. Phys. Chem. B* **2015**, *119*, 10954-10961.
- (46) Kramers, H. A. Brownian Motion in a Field of Force and the Diffusion Model of Chemical Reactions. *Physica* **1940**, *7*, 284-304.
- (47) Hanggi, P. Escape from a Metastable State. *J. Stat. Phys.* **1986**, *42*, 105-148.
- (48) Sikdar, D.; Hasan, S. B.; Urbakh, M.; Edel, J. B.; Kornyshev, A. A. Unravelling the Optical Responses of Nanoplasmonic Mirror-on-Mirror Metamaterials. *Phys. Chem. Chem. Phys.* **2016**, *18*, 20486-20498.

8. Conclusions and outlook

Tunable metamaterials composed by stimuli-responsive nanostructures are promising for future smart optical devices. In our proof-of-concept studies, functionalized metallic NPs are assembled into plasmonic active arrays at SLI or LLI, and tuned through electric, thermal and chemical methods. The control over the interparticle distance affords these systems tailorable optical outputs such as the intensity and wavelength of the reflectance dip or peak and the enhancement of Raman signals. Future on-demand optical applications require the optimisation of the tuning range, switching speed and reversibility.

8.1. Tuning range

Across all the projects, controlling the interparticle distance is a key factor in tuning the optical output in the terms of wavelength and intensity. The closer NPs, the redder the SPR wavelength shifts and the more intense the reflectance dip (at SLI) and peak (at LLI) become. Moreover, by correlating the reflectance and SERS signal to the interparticle distance, **Figure 8.1** (take the data in Chapter 4 as an example), it can be found that this relationship is non-linear. This is because the SPR coupling among NPs become increasingly stronger when the gap narrows.¹ Therefore, in order to construct a metamaterial with wider tuning range, the further reduce of the interparticle distance could be a promising direction.

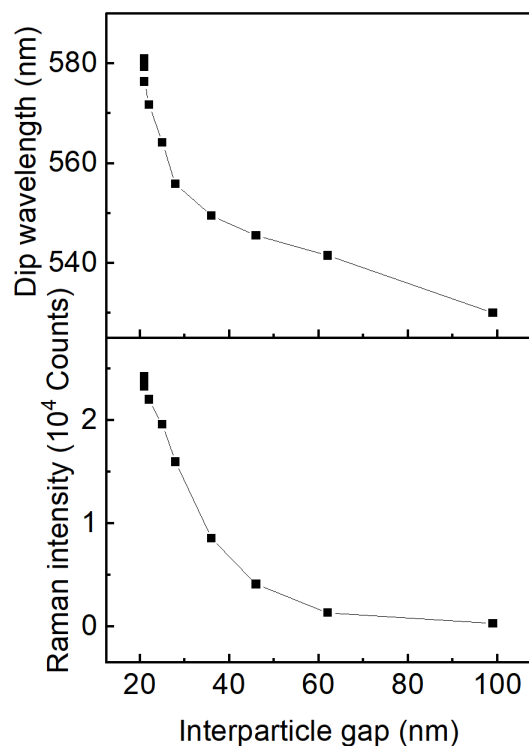


Figure 8.1 Dip wavelength of the reflectance dip (up) and Raman intensity of the peak 1078 cm^{-1} (down) versus calculated interparticle gap, extracted from Figure 4.9.

For electrochemical systems, as explored in **Chapter 3**, both the electrolyte concentration and positive electric potential help with reducing the interparticle distances. The former screens the repelling electrostatic forces between NPs while the later increases the attractive forces between NPs and the substrate, deepens the energy well at the interfaces. However, too much electrolyte will destabilise the NP solution and too high potential will electrolyze the solvent.

It has been demonstrated that ligands with longer chains such as polyethylene glycol (PEG) and polystyrene (PS) can prevent NP aggregation.² NPs covered with polyvinylpyrrolidone (PVP) can even be re-dissolved into mono-dispersed solution after drying. After attaching disassociating moieties on these polymers, the functionalized NPs are expected to be able to tolerate higher salt concentrations while still providing electro-tunable capability. Another alternative is DNA. Carrying huge amount of negative charges on its phosphate backbones, DNA functionalized NPs can withstand electrolyte at mol/L levels.³ However, the increased number of negative charges on DNA potentially hinders the NPs coming close with each other, which needs careful adjustment in future experiments. Furthermore, thanks to the programmable nature of DNA sequences, functionality for sensing can be incorporated.⁴

As to the electrochemical window that currently limited by the aqueous system, an extension is expected by transferring to the ionic liquid system. Compared with water based electrolyte systems, the widely studied 1-Ethyl-3-methylimidazolium dicyanamide, Triethylsulphonium bis(trifluoromethylsulfonyl)imide and N-Butyl-N-methylpyrrolidinium bis(trifluoro-methylsulfonyl)imide provide a much wider electrochemical window ranging from 2.9 V to 6.6 V.⁵ The only concern is the relative high viscosity which could slow down the switching speed of the system.

8.2. Switching speed

The fast 2 s switching speed of thermo-responsive system in **Chapter 5** underscores the need for further speeding up our electro-tunable systems. As mentioned in **Chapter 3** and **7**, the diffusion process plays a key role in the dynamics of the assembly process: its speed has an inverse relationship with the NP concentration in the solution. Thus, using small amount of ultra-high concentration of NP solution in a small cell could greatly speed up the assembly kinetics. We performed preliminarily experiments in this direction. As shown in **Figure 8.2**, our collaborator Klaus Mathwig from University of Groningen, Netherlands fabricated the nanoscale electrochemical cell. The substrate was reduced to a $4 \times 5 \mu\text{m}$ gold electrode, above which a was a 100 nm nano-channel which contained a high concentration NP solution. The reduced diffusion length and increased NP concentration are expected to shorten the switching time to the ms range.

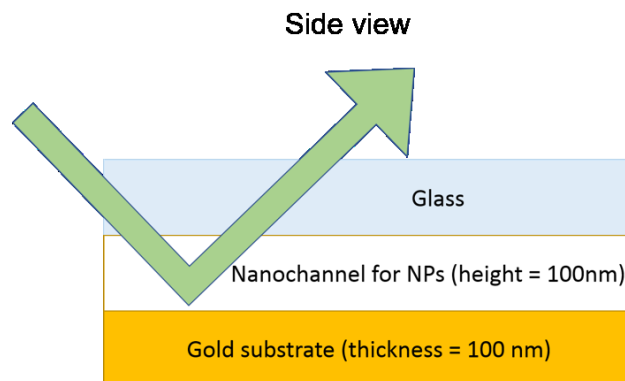


Figure 8.2 The schematic structure of the miniaturized cell.

8.3. Reversibility

Although the reversibility using smaller NPs (16 nm) in this thesis is satisfactory, the 40 nm NP data as shown in **Chapter 4** is still far from ideal, especially during the disassembly process. The main issue is that some NPs cannot be released back into the bulk solution. This is likely due to the van der Waals forces between those NPs and the substrate being too strong when they come closer to each other. The possible existence of some bare gold surface on the NPs and the defects on the TiN films could also provide the chance of merging the NPs onto the exposed Ag substrate. Extra passive layer or self-assembled monolayer (SAM) on the substrate could possibly remedy this. In addition, more negative potential could also increase the repelling force between the NPs and the substrate when disassembling the NP array, but this should be supported by more stable electrolytes and solvents.

In the thermo-responsive system based on pNIPAM factionalized NP array, it was observed that the swelling process during the cooling of the system required much longer time than the shrinking process during the heating. Researchers attributed this to the phase transition hysteresis which could be induced by the hydrophobic interactions and hydrophilic intramolecular interactions.⁶ To tailor these interactions, additional hydrophobic/ hydrophilic groups could be incorporated into pNIPAM molecules, and indeed a vast varieties of derivatives have been designed.⁷ Further screening of these polymers and a balance between switching speed and reversibility could be achieved in later experiments.

8.4. References

- (1) Ghosh, S. K.; Pal, T. Interparticle Coupling Effect on the Surface Plasmon Resonance of Gold Nanoparticles: From Theory to Applications. *Chem. Rev.* **2007**, *107*, 4797-4862.
- (2) Saha, K.; Agasti, S. S.; Kim, C.; Li, X.; Rotello, V. M. Gold Nanoparticles in Chemical and Biological Sensing. *Chem. Rev.* **2012**, *112*, 2739-2779.

- (3) Li, J.; Zhu, B.; Yao, X.; Zhang, Y.; Zhu, Z.; Tu, S.; Jia, S.; Liu, R.; Kang, H.; Yang, C. J. Synergetic Approach for Simple and Rapid Conjugation of Gold Nanoparticles with Oligonucleotides. *ACS Appl. Mater. Interfaces* **2014**, *6*, 16800-16807.
- (4) Jones, M. R.; Osberg, K. D.; Macfarlane, R. J.; Langille, M. R.; Mirkin, C. A. Templated Techniques for the Synthesis and Assembly of Plasmonic Nanostructures. *Chem. Rev.* **2011**, *111*, 3736-3827.
- (5) Hayyan, M.; Mjalli, F. S.; Hashim, M. A.; AlNashef, I. M.; Mei, T. X. Investigating the Electrochemical Windows of Ionic Liquids. *J. Ind. Eng. Chem.* **2013**, *19*, 106-112.
- (6) Osváth, Z.; Iván, B. The Dependence of the Cloud Point, Clearing Point, and Hysteresis of Poly(N-isopropylacrylamide) on Experimental Conditions: The Need for Standardization of Thermoresponsive Transition Determinations. *Macromol. Chem. Phys.* **2017**, *218*, 1600470.
- (7) Roy, D.; Brooks, W. L. A.; Sumerlin, B. S. New Directions in Thermoresponsive Polymers. *Chem. Soc. Rev.* **2013**, *42*, 7214-7243.

Appendix

List of publication during PhD study


- (1). **Ma, Y.**; Zagar, C.; Klemme, D. J.; Sikdar, D.; Velleman, L.; Montelongo, Y.; Oh, S.-H.; Kucernak, A. R.; Edel, J. B.; Kornyshev, A. A., A Tunable Nanoplasmonic Mirror at an Electrochemical Interface. *ACS Photonics* 2018, 5 (11), 4604-4616.
- (2). **Ma, Y.**; Sikdar, D.; Fedosyuk, A.; Velleman, L.; Zhao, M.; Tang, L.; Kornyshev, A. A.; Edel, J. B., An auxetic thermo-responsive nanoplasmonic optical switch. *ACS Applied Materials & Interfaces* 2019, 11 (25), 22754-22760.
- (3). Montelongo, Y.; Sikdar, D.; **Ma, Y.**; McIntosh, A. J. S.; Velleman, L.; Kucernak, Anthony R.; Edel, J. B.; Kornyshev, A. A., Electrotunable Nanoplasmonic Liquid Mirror. *Nature Materials* 2017, 16, 1127-1135.
- (4). Xue, L.; Cadinu, P.; Paulose Nadappuram, B.; Kang, M.; **Ma, Y.**; Korchev, Y.; Ivanov, A. P.; Edel, J. B., Gated Single-Molecule Transport in Double-Barreled Nanopores. *ACS Applied Materials & Interfaces* 2018, 10 (44), 38621-38629.

Certificates of copyright permission

All the copyright permission is attached here unless the documents are open access with a Creative Commons licence. It should be noted that the Figure 1.1 in this thesis is shared under a Creative Commons Attribution-NonCommercial-ShareAlike 4.0 International (CC BY-NC-SA 4.0) licence from the British Museum.

Annual review of physical chemistry

Order detail ID: 71937377
Order License Id: 4621220914879
ISSN: 1545-1593
Publication Type: e-Journal
Volume:
Issue:
Start page:
Publisher: ANNUAL REVIEWS

Permission Status:  **Granted**
Permission type: Republish or display content
Type of use: Thesis/Dissertation

Requestor type Not-for-profit entity

Format Print, Electronic

Portion image/photo

Number of images/photos requested 1

The requesting person/organization Ye Ma

Title or numeric reference of the portion(s) Figure 1, Schematic diagrams illustrating (a) a surface plasmon polariton (or propagating plasmon) and (b) a localized surface plasmon.

Title of the article or chapter the portion is from Localized Surface Plasmon Resonance Spectroscopy and Sensing

Nanoscale

Order detail ID: 71937386
Order License Id: 4621240381055

ISSN: 2040-3372

Publication Type: e-Journal

Volume:

Issue:

Start page:

Publisher: RSC Pub

Author/Editor: National Center for Nanoscience and
Technology ; Royal Society of
Chemistry (Great Britain)

Permission Status: **Granted**

Permission type: Republish or display content
Type of use: Thesis/Dissertation

Requestor type Not-for-profit entity

Format Print, Electronic

Portion image/photo

**Number of
images/photos
requested** 1

**The requesting
person/organization** Ye Ma

**Title or numeric
reference of the
portion(s)** Fig. 3 Reflectance spectra
for NPs assembled at the
water-DCE...reflectance
spectra taken from
different areas on each
sample.

**Title of the article or
chapter the portion is
from** Tuneable 2d Self-Assembly
of Plasmonic Nanoparticles
at Liquid|Liquid Interfaces



Title: Auxetic Thermo-responsive Nanoplasmonic Optical Switch
Author: Ye Ma, Debabrata Sikdar, Aleksandra Fedosyuk, et al
Publication: Applied Materials
Publisher: American Chemical Society
Date: Jun 1, 2019
Copyright © 2019, American Chemical Society

Logged in as:
Ye Ma
Account #:
3001423699

LOGOUT

PERMISSION/LICENSE IS GRANTED FOR YOUR ORDER AT NO CHARGE

This type of permission/license, instead of the standard Terms & Conditions, is sent to you because no fee is being charged for your order. Please note the following:

- Permission is granted for your request in both print and electronic formats, and translations.
- If figures and/or tables were requested, they may be adapted or used in part.
- Please print this page for your records and send a copy of it to your publisher/graduate school.
- Appropriate credit for the requested material should be given as follows: "Reprinted (adapted) with permission from (COMPLETE REFERENCE CITATION). Copyright (YEAR) American Chemical Society." Insert appropriate information in place of the capitalized words.
- One-time permission is granted only for the use specified in your request. No additional uses are granted (such as derivative works or other editions). For any other uses, please submit a new request.



Title: An electromechanically reconfigurable plasmonic metamaterial operating in the near-infrared
Author: Jun-Yu Ou, Eric Plum, Jianfa Zhang, Nikolay I. Zheludev
Publication: Nature Nanotechnology
Publisher: Springer Nature
Date: Mar 17, 2013
Copyright © 2013, Springer Nature

Logged in as:
Ye Ma
Account #:
3001423699

LOGOUT

Order Completed

Thank you for your order.

This Agreement between Ye Ma ("You") and Springer Nature ("Springer Nature") consists of your license details and the terms and conditions provided by Springer Nature and Copyright Clearance Center.

Your confirmation email will contain your order number for future reference.

SPRINGER NATURE

Title: Magnetoelastic metamaterials
Author: Mikhail Lapine, Ilya V. Shadrivov, David A. Powell, Yuri S. Kivshar
Publication: Nature Materials
Publisher: Springer Nature
Date: Nov 13, 2011
Copyright © 2011, Springer Nature

Logged in as:
Ye Ma
Account #:
3001423699

LOGOUT

Order Completed

Thank you for your order.

This Agreement between Ye Ma ("You") and Springer Nature ("Springer Nature") consists of your license details and the terms and conditions provided by Springer Nature and Copyright Clearance Center.

Your confirmation email will contain your order number for future reference.



Title: Thermosensitive Unimolecular
Micelles Surface-Decorated with
Gold Nanoparticles of Tunable
Spatial Distribution

Author: Hangxun Xu, Jian Xu, Xiaoze
Jiang, et al

Publication: Chemistry of Materials

Publisher: American Chemical Society

Date: May 1, 2007

Copyright © 2007, American Chemical Society

Logged in as:

Ye Ma

Account #:

3001423699

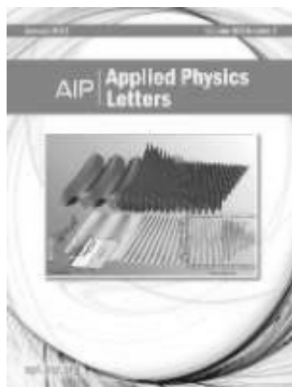
LOGOUT

PERMISSION/LICENSE IS GRANTED FOR YOUR ORDER AT NO CHARGE

This type of permission/license, instead of the standard Terms & Conditions, is sent to you because no fee is being charged for your order. Please note the following:

- Permission is granted for your request in both print and electronic formats, and translations.
- If figures and/or tables were requested, they may be adapted or used in part.
- Please print this page for your records and send a copy of it to your publisher/graduate school.
- Appropriate credit for the requested material should be given as follows: "Reprinted (adapted) with permission from (COMPLETE REFERENCE CITATION). Copyright (YEAR) American Chemical Society." Insert appropriate information in place of the capitalized words.
- One-time permission is granted only for the use specified in your request. No additional uses are granted (such as derivative works or other editions). For any other uses, please submit a new request.

If credit is given to another source for the material you requested, permission must be obtained from that source.



Title: Ultra-thin perfect absorber employing a tunable phase change material
Author: Mikhail A. Kats, Deepika Sharma, Jiao Lin, et al
Publication: Applied Physics Letters
Volume/Issue 101/22
Publisher: AIP Publishing
Date: Nov 26, 2012
Page Count: 5
Rights managed by AIP Publishing.

Logged in as:
Ye Ma
Account #:
3001423699

LOGOUT

Order Completed

Thank you for your order.

This Agreement between Ye Ma ("You") and AIP Publishing ("AIP Publishing") consists of your license details and the terms and conditions provided by AIP Publishing and Copyright Clearance Center.

Your confirmation email will contain your order number for future reference.



Title: Two-Dimensional Active Tuning of an Aluminum Plasmonic Array for Full-Spectrum Response
Author: Ming Lun Tseng, Jian Yang, Michael Semmlinger, et al
Publication: Nano Letters
Publisher: American Chemical Society
Date: Oct 1, 2017
Copyright © 2017, American Chemical Society

Logged in as:
Ye Ma
Account #:
3001423699

LOGOUT

PERMISSION/LICENSE IS GRANTED FOR YOUR ORDER AT NO CHARGE

This type of permission/license, instead of the standard Terms & Conditions, is sent to you because no fee is being charged for your order. Please note the following:

- Permission is granted for your request in both print and electronic formats, and translations.
- If figures and/or tables were requested, they may be adapted or used in part.
- Please print this page for your records and send a copy of it to your publisher/graduate school.
- Appropriate credit for the requested material should be given as follows: "Reprinted (adapted) with permission from (COMPLETE REFERENCE CITATION). Copyright (YEAR) American Chemical Society." Insert appropriate information in place of the capitalized words.
- One-time permission is granted only for the use specified in your request. No additional uses are granted (such as derivative works or other editions). For any other uses, please submit a new request.

If credit is given to another source for the material you requested, permission must be obtained from that source.



Title: Strain Multiplexed Metasurface Holograms on a Stretchable Substrate
Author: Stephanie C. Malek, Ho-Seok Ee, Ritesh Agarwal
Publication: Nano Letters
Publisher: American Chemical Society
Date: Jun 1, 2017
Copyright © 2017, American Chemical Society

Logged in as:
Ye Ma
Account #:
3001423699

LOGOUT

PERMISSION/LICENSE IS GRANTED FOR YOUR ORDER AT NO CHARGE

This type of permission/license, instead of the standard Terms & Conditions, is sent to you because no fee is being charged for your order. Please note the following:

- Permission is granted for your request in both print and electronic formats, and translations.
- If figures and/or tables were requested, they may be adapted or used in part.
- Please print this page for your records and send a copy of it to your publisher/graduate school.
- Appropriate credit for the requested material should be given as follows: "Reprinted (adapted) with permission from (COMPLETE REFERENCE CITATION). Copyright (YEAR) American Chemical Society." Insert appropriate information in place of the capitalized words.
- One-time permission is granted only for the use specified in your request. No additional uses are granted (such as derivative works or other editions). For any other uses, please submit a new request.

If credit is given to another source for the material you requested, permission must be obtained from that source.



Title: Actively Tuned Plasmons on Elastomerically Driven Au Nanoparticle Dimers

Author: Fumin Huang, Jeremy J. Baumberg

Publication: Nano Letters

Publisher: American Chemical Society

Date: May 1, 2010

Copyright © 2010, American Chemical Society

Logged in as:

Ye Ma

Account #:
3001423699

LOGOUT

PERMISSION/LICENSE IS GRANTED FOR YOUR ORDER AT NO CHARGE

This type of permission/license, instead of the standard Terms & Conditions, is sent to you because no fee is being charged for your order. Please note the following:

- Permission is granted for your request in both print and electronic formats, and translations.
- If figures and/or tables were requested, they may be adapted or used in part.
- Please print this page for your records and send a copy of it to your publisher/graduate school.
- Appropriate credit for the requested material should be given as follows: "Reprinted (adapted) with permission from (COMPLETE REFERENCE CITATION). Copyright (YEAR) American Chemical Society." Insert appropriate information in place of the capitalized words.
- One-time permission is granted only for the use specified in your request. No additional uses are granted (such as derivative works or other editions). For any other uses, please submit a new request.

If credit is given to another source for the material you requested, permission must be obtained from that source.

**SPRINGER NATURE LICENSE
TERMS AND CONDITIONS**

Mar 20, 2019

This Agreement between Ye Ma ("You") and Springer Nature ("Springer Nature") consists of your license details and the terms and conditions provided by Springer Nature and Copyright Clearance Center.

License Number	4553401295750
License date	Mar 20, 2019
Licensed Content Publisher	Springer Nature
Licensed Content Publication	Nature Materials
Licensed Content Title	Electrotunable nanoplasmonic liquid mirror
Licensed Content Author	Yunuen Montelongo, Debabrata Sikdar, Ye Ma, Alastair J. S. McIntosh, Leonora Velleman et al.
Licensed Content Date	Sep 11, 2017
Licensed Content Volume	16
Licensed Content Issue	11
Type of Use	Thesis/Dissertation
Requestor type	non-commercial (non-profit)
Format	print and electronic
Portion	full article/chapter
Will you be translating?	no
Circulation/distribution	<501
Author of this Springer Nature content	yes
Title	Tunable nano-plasmonic metamaterials at solid-liquid and liquid-liquid interfaces
Institution name	Imperial college london
Expected presentation date	Jul 2019
Requestor Location	Ye Ma 26 south end row



ACS Publications
Most Trusted. Most Cited. Most Read.

Title: A Tunable Nanoplasmonic Mirror at an Electrochemical Interface
Author: Ye Ma, Cristian Zagar, Daniel J. Klemme, et al
Publication: ACS Photonics
Publisher: American Chemical Society
Date: Nov 1, 2018
Copyright © 2018, American Chemical Society

Logged in as:
Ye Ma

LOGOUT

PERMISSION/LICENSE IS GRANTED FOR YOUR ORDER AT NO CHARGE

This type of permission/license, instead of the standard Terms & Conditions, is sent to you because no fee is being charged for your order. Please note the following:

- Permission is granted for your request in both print and electronic formats, and translations.
- If figures and/or tables were requested, they may be adapted or used in part.
- Please print this page for your records and send a copy of it to your publisher/graduate school.
- Appropriate credit for the requested material should be given as follows: "Reprinted (adapted) with permission from (COMPLETE REFERENCE CITATION). Copyright (YEAR) American Chemical Society." Insert appropriate information in place of the capitalized words.
- One-time permission is granted only for the use specified in your request. No additional uses are granted (such as derivative works or other editions). For any other uses, please submit a new request.



Title: Hybrid Lithographic and DNA-Directed Assembly of a Configurable Plasmonic Metamaterial That Exhibits Electromagnetically Induced Transparency

Author: David B. Litt, Matthew R. Jones, Mario Hentschel, et al

Publication: Nano Letters

Publisher: American Chemical Society

Date: Feb 1, 2018

Copyright © 2018, American Chemical Society

Logged in as:
Ye Ma
Account #:
3001423699

LOGOUT

PERMISSION/LICENSE IS GRANTED FOR YOUR ORDER AT NO CHARGE

This type of permission/license, instead of the standard Terms & Conditions, is sent to you because no fee is being charged for your order. Please note the following:

- Permission is granted for your request in both print and electronic formats, and translations.
- If figures and/or tables were requested, they may be adapted or used in part.
- Please print this page for your records and send a copy of it to your publisher/graduate school.
- Appropriate credit for the requested material should be given as follows: "Reprinted (adapted) with permission from (COMPLETE REFERENCE CITATION). Copyright (YEAR) American Chemical Society." Insert appropriate information in place of the capitalized words.
- One-time permission is granted only for the use specified in your request. No additional uses are granted (such as derivative works or other editions). For any other uses, please submit a new request.

If credit is given to another source for the material you requested, permission must be obtained from that source.